Electrical manipulation of cortical and hippocampal dynamics during slow-wave states

by

Anastasia Greenberg

A thesis submitted in partial fulfillment of the requirements for the degree of

Doctor of Philosophy

Centre for Neuroscience

University of Alberta

Abstract

Oscillations are a fundamental principle of neural operation, organized into a hierarchy of frequency bands with the dominant rhythm alternating within and across behavioral states. During states of sleep and anesthesia, brain activity in forebrain regions displays two major distinct activity patterns: activated states of low voltage fast activity in the neocortex along with theta activity in the hippocampus, and deactivated states of synchronized slow-wave activity in both structures. The signature event during such slow-wave states is the large amplitude slow oscillation (~1 Hz, SO) which is cortically generated through transitions between highly active depolarized (UP, ON) states and hyperpolarized (DOWN, OFF) states of complete quiescence. The SO dynamically propagates across the cortex and reaches the hippocampus, making this rhythm attractive for mediating cortico-hippocampal interactions. It has been demonstrated that such interactions during the SO support the consolidation of declarative (hippocampal-mediated) memories in humans, and that directly manipulating the SO using rhythmic electrical stimulation at a similar frequency to the SO can affect both properties of the SO as well as subsequent memory. However, such evidence is currently lacking a mechanistic explanation for how rhythmic stimulation alters the dynamic properties of the SO, such as its propagation patterns, and how it supports cortico-hippocampal communication that would ultimately lead to the behavioral memory effects. The aim of my thesis was to address these issues using a urethane-anesthetized rat and mouse model and applying slowly alternating rhythmic electrical fields to the frontal portions of the cortex.

In Chapter 2 I examine the influence of sinusoidal electrical stimulation on spontaneous SO propagation dynamics using a simple three-channel linear electrode array

across the anterior-posterior axis of the rat motor cortex. We show that during the spontaneous SO, two major propagation patterns traveling in both directions along the anterior-posterior plane appeared to compete for expression with alternations between these patterns occurring specifically during the OFF state. Applying rhythmic stimulation successfully entrained the local-field potential (LFP) at all recording sites along with gamma and multi-unit activity. The stimulation also biased the SO propagation in favour of the anterior-to-posterior direction in an intensity dependent fashion. Within local networks, cortico-cortical gamma synchrony was enhanced during the stimulation.

In Chapter 3, I extend these findings to a more encompassing cortical network using voltage-sensitive dye (VSD) imaging in a large bilateral window of the mouse cortex. In accordance with findings from Chapter 2, spontaneous SO propagation showed several distinct propagation patterns with two major patterns emerging: anterior-to-posterior and posterior-to-anterior directions; with these patterns traveling along a slightly angled medio-lateral plane. The application of sinusoidal field stimulation entrained the VSD signal at multiple widespread cortical sites and biased SO propagation. Propagation during stimulation showed multiple initiation zones, mainly around anteriorly located regions, with a very specific termination zone in the somatosensory cortex. Importantly, there was no SO propagation detected during the application of neural activity blockers. Surprisingly, following the cessation of stimulation, hemisphere-specific activity was suppressed for a period of time with recovery thereafter.

In Chapter 4 I introduce cortical and hippocampal (linear probe) recordings using rats in an attempt to address the effects of sinusoidal electrical stimulation on cortico-hippocampal interplay. As with the cortex, stimulation successfully entrained hippocampal

LFP activity, likely by way of a specific pathway from the entorhinal cortex to the hippocampus. Stimulation also boosted the occurrence of hippocampal ripples which are implicated in memory replay as well as cortical spindles which are likewise associated with cortical plasticity and learning. Following the cessation of stimulation, cortico-hippocampal coordination at the SO band was enhanced and the flow of information, as assessed using Granger causality, was biased in the hippocampo-cortical direction. Gamma activity between the cortex and hippocampus showed enhanced synchrony following stimulation, with the effect being restricted to the hippocampal pyramidal cell layer, the output layer of the hippocampus, suggesting further that information flow was occurring in the hippocampal-cortical direction.

These results show that rhythmic electrical field stimulation alters forebrain-wide SO dynamics. Changes in cortico-cortical, cortico-hippocampal and hippocampo-cortical interplay as a result of stimulation may all play important roles during sleep. Understanding the mechanisms that are at play during and following the administration of such stimulation can promote the development of targeted protocols for the enhancement and disruption of memory consolidation for use in experimental settings and eventually to affect clinical outcomes.

Preface

In Chapter 2, partial data collection of spontaneous recordings was performed by Justin Barclay. In Chapter 3, all data was collected through a collaborative project in Dr. Majid Mohajerani's laboratory at the University of Lethbridge. Data was collected by Javad Karimi and me, with a portion collected by Javad solely (data presented in Figure 3.9 and 3.10). All craniotomies in Chapter 3 were performed by JianJun Sun. For this project, all analyses were performed by me. In Chapter 4, all data collection and analyses were performed by me except for the method using independent-component analysis (ICA) for artifact removal which was developed and performed by Dr. Tara A. Whitten.

All of the Matlab code used to analyse data that appears in this thesis was created using a combination of built-in functions and custom-written code that I developed. In a few instances my code was adapted from code shared with me by Dr. Jesse Jackson (phase-amplitude modulation), Dr. Jeremy Caplan's laboratory (BOSC) and Dr. Majid Mohajerani's laboratory (preprocessing of VSD data).

In all remaining cases, all of the work presented in this thesis including the ideas presented were developed by me with the invaluable help and guidance of my supervisor Dr. Clayton T. Dickson.

It is not only in music that one produces perfect harmony. The body produces a garland of rhythms, one could say a bouquet, though these words suggest an aesthetic arrangement, as if the artist nature had foreseen beauty…

Henri Lefebvre (Lefebvre, 1992)

Acknowledgements

The work presented in this thesis was supported by several scholarships: Natural Science and Engineering Council of Canada (NSERC) Alexander Graham Bell Canada Graduate Scholarship (CSG M and CGS D3), Alberta Innovates – Technology Futures Scholarship, Queen Elizabeth II Graduate Scholarship and Campus Alberta Neuroscience Trainee Mobility Program.

I would like to acknowledge the support of my supervisor Dr. Clayton T. Dickson who has guided me throughout my graduate degree and has helped me to develop as a scholar. Clayton has taught me invaluable skills such as how to design research in a feasible manner, give engaging public presentations, critique the research of others as well as my own, and write manuscripts in a clear and concise fashion. It is clear that Clayton is a scientist at heart and throughout the time working under his supervision I feel that I inherited a little bit of his research wisdom and insight.

I would also like to thank Dr. Jeremy Caplan, one of my supervisory committee members, who has made me a better scientist through challenging me at every presentation that I delivered and providing encouraging words to keep me going. I would also like to thank Dr. Kyle E. Mathewson who likewise challenged me at presentations and also contributed many useful editorial comments towards now published manuscripts.

Dr. Majid Mohajerani and Javad Karimi also deserve a huge acknowledgement for their efforts towards the collaborative project described in Chapter 3. This project is a very important part of my thesis and without their help and major contributions this thesis would not be the same. I would also like to thank JianJun Sun for his hard work on this project as well.

Additionally, I would like to thank all of my colleagues of the Brain Rhythms laboratory who have been there for me through difficult times and without whose friendships I could not have finished a doctoral degree.

Finally, I would also like to thank my partner Igor Zlobine, who believes in me more than I believe in myself, for his unwavering love and support throughout my entire graduate program.

Table of Contents

Table of Figures

List of Tables

List of Abbreviations

Alternating current	AC
α-amino-3-hydroxy-5-methyl-4-isoxazolepropionic acid	AMPA
Alternating current	AC
Anterior	ANT
Anterior-lateral	AL
Anterior-posterior	AP
Average	AVG
6-cyano-7-nitroquinoxaline-2,3-dione	CNQX
Better oscillation detection method	BOSC
Calcium	Ca^{2+}
Cornu ammonis 1	CA1
Cornu ammonis 2	CA2
Cornu ammonis 3	CA3
Cortex	CTX
Current source density	CSD
Dentate gyrus	DG
Dizocilpine	MK-801
Dorso-ventral	DV
Electrocardiogram	ECG
Electroencephalogram	EEG
Electromyogram	EMG
Electrooculogram	EOG
Entorhinal cortex	EC
γ – aminobutyric acid	GABA
Granger causality connectivity analysis	GCCA
Hippocampal fissure	Fiss
Hippocampus	HPC
Hyperpolarization-activated mixed cation current	I_h
Independent component analysis	ICA
Inter-stimulus-interval	ISI
Intraperitoneal	*i.p.*
Intravenous	*i.v.*
Large-amplitude irregular activity	LIA
Lidocaine	Lido
Local field potential	LFP
Long-term potentiation	LTP
Low-threshold Ca^{2+} current	I_T

Low-voltage fast activity	LVFA
Medial entorhinal cortex	MEC
Medial temporal lobe	MTL
Medio-lateral	ML
Modulation index	MI
Monoamine oxidase	MAO
Multiunit activity	MUA
N-methyl-D-aspartate receptor	NMDA
Non-rapid eye movement	Non-REM
Not significant	n.s./NS
Oscillatory transcranial direct current stimulation	osc-tDCS
Potassium	K^+
Posterior	POST
Post-mortem	PM
Rapid eye movement	REM
Region of interest	ROI
Root-mean-squared	RMS
Sharp-wave ripple	SPW-R
Slow oscillation	SO
Slow wave activity	SWA
Slow wave sleep	SWS
Sodium	Na^+
Standard deviation	SD
Standard error of the mean	SEM
Stimulation	STIM
Stratum granulosum	SGran
Stratum lacunosum moleculare	SLM
Stratum moleculare	SMol
Stratum oriens	SOr
Stratum pyramidale	SPyr
Stratum radiatum	SRad
Subcutaneous	s.c.
Temporoammonic	TA
Thalamic reticular nucleus	RE
Thalamocortical	TC
Tetrodotoxin	TTX
Transcranial alternating current stimulation	tACS
Transcranial direct current stimulation	tDCS
Transcranial electrical current stimulation	TES
Ventrolateral preoptic nucleus	VLPO

Voltage-sensitive dye	VSD

1 Introduction

"The rhythmanalyst …[is] more sensitive to time than to places. [S]he will come to listen to a house, a street, a town, as an audience listens to a symphony". Those were some of the last words French philosopher Henri Lefebvre ever wrote, appearing in his book "*Rhythmanalysis: Space, Time and Everyday Life"* that was published in 1992 following his death (Lefebvre, 1992, 2004). Lefebvre imagined a new kind of scientist-philosopher, the "rhythmanalyst", who systematically explores the rhythms of day-to-day life anywhere from biological rhythms to the cyclic sounds of urban traffic. This idea, that rhythms are omnipresent, can describe many fundamental properties of the world in which we live, such as the familiar cycles of night and day, the lunar cycle, and the cycles of life and death. Less intuitively, even political-economic instability has been shown to cycle with a period length of two to three centuries whereby egalitarianism shifts towards elitism bringing increased economic inequality followed by political collapse and the reinstatement of the cycle anew. A faster fifty-year long cycle of violence and quiescence is superimposed onto the slower cycle (Turchin and Nefedov, 2009). Zooming deep into this broad socio-historical context, we can see that the individual constituent elements – humans (and other animals) – are themselves governed by brain rhythms controlling the temporal scale of behavior and cognition.

The first electroencephalogram (EEG) recordings from a human subject were conducted in 1924 by the German neuropsychiatrist Hans Berger (1873 – 1941) using a string galvanometer and large silver electrodes. Berger was hoping to uncover the secrets of telepathy in his search for "mental energy". The first rhythm that he recorded was a ~10 Hz oscillation over the occipital lobe that appeared when the subject closed their eyes; he thus correspondingly named this first rhythm the alpha (α) rhythm. Berger is also credited with

performing the first ever EEG recordings during sleep, including the detection of sleep spindles (Niedermeyer et al., 2005). These oscillations that Berger recorded are now understood as reflecting the spatiotemporal summation in the extracellular space of mainly synaptic currents (as opposed to action potentials) produced in cortical cells that create voltage dipoles that can be recorded from the scalp due to their parallel arrangement across cortical laminae in an orientation perpendicular to the pia (Niedermeyer et al., 2005).

Although Berger did not realize his dream of discovering mind-to-mind communication, as air is a poor conductor and the electrical signals recorded at the scalp are miniscule, his contribution to understanding "brain states", and as a result stimulus-to-brain interaction, is paramount. The phenomenon of brain states, the fact that EEG activity is markedly different depending on the behavioral state of the organism, such as fast low amplitude activity upon opening of the eyes (named beta (β) by Berger) and the large slow-waves during sleep, suggests that there is an internal world in the brain intermediate to sensory perception and behavior.

Unlike the dark ages of behaviorism theory where the brain was viewed as a simple black box; a mere input-output machine, neuroscientists today are starting to appreciate the complex non-linear interactions between the input parameters and the state of the brain. When a subject is presented with a perceptible stimulus, the brain responds with high inter-trial variability which is typically averaged to create event-related potentials intended to get rid of the "noise" and reveal the true brain response to the stimulus (Buzsáki, 2006). However, while the stimulus may be invariant, the ongoing brain dynamics determine how that stimulus is treated and whether it is amplified or shunned. A particularly exemplifying study showed that the phase of the ongoing posteriorly recorded α oscillation in humans

determined the likelihood of a visual stimulus (a dot on a screen presented for ~12 ms) reaching conscious awareness, with maximum and minimum detection values occurring at opposite phases of α (Mathewson et al., 2009). Such findings of perceptual "gating" led to the idea that the brain operates in discontinuous fragments in which consciousness and perception can perhaps be viewed as being sampled from the analog environment, as if the brain lives in digital space. Given the critical importance of timing to brain operation, as the famous philosopher Friedrich Nietzsche suggested: perhaps living beings are more like verbs than nouns (Goodrich, 2010).

In this introduction section I will discuss the critical importance of oscillations in the organization of neural networks and the various oscillatory patterns that exist during different behavioral states, particularly sleep-like states, as well as the mechanisms of transitions between these states. I will then introduce the neocortical slow oscillation, its mechanisms of generation and synchrony, and its relevance to memory function. I will then touch on cortical anatomy in the context of physiological function. Next, I examine the role of the hippocampus in memory, its specific oscillatory activity and anatomical organization, as well as its interactions with the neocortex to support memory function. I will then move on to various paradigms and mechanisms of electrical stimulation and its effects on cognitive function. Finally, I address the use of the urethane-anesthetized rodent model to study sleep-like brain activity and I present an overview of the findings of this thesis.

1.1 Oscillatory organization of neural networks

Brain activity is organized into a multiplex of oscillations spanning the range from 0.02 Hz to 600 Hz, with various defined oscillatory bands having a natural logarithmic

relationship to each other (Buzsáki and Draguhn, 2004). This is an interesting property of oscillations suggesting that they can never become perfectly phase-locked across bands (since *e* is an irrational number) but rather can come in and out of mutual interactions depending on current cognitive and behavioral conditions. When brain activity is measured through EEG on the scalp or local-field potential (LFP) recordings more locally inside the brain and summated over long time periods, the resulting power spectrum (activity viewed in frequency space) shows a 1/f "pink noise" signal with a predictable inverse relationship between oscillatory frequency and power. However, at any given moment of time, oscillations in a particular band may be dominating a specific network, such as thalamocortical delta activity (0.5 – 4 Hz) during sleep or hippocampal theta (~4 – 8 Hz) activity during active exploration (Buzsáki and Moser, 2013; Steriade, 2006). Even within a given behavioral state such as sleep or anesthesia, brain dynamics alternate between "activated" low-voltage fast activity (LVFA) and "deactivated" slow-wave activity (SWA) (Figure 1.1) thereby displaying a "peak" in the power spectrum – a deviation from the 1/f dynamics (Figure 1.1). This shows two important principles of brain oscillatory dynamics: 1) The activity of the brain is not just "noise" but rather appears as such only when irrationally related oscillatory bands are summed over long time intervals and 2) despite deviations from the 1/f dynamics at any given moment, the general principle holds that the slower the oscillation, the higher the EEG power resulting from the larger recruitment of neural elements (Figure 1.1).

The conduction velocity limitations of axons (max ~120 m/s) and the low-pass filtering properties of the extracellular space are the main reasons that slower rhythms have longer critical time windows, which allow more distant brain areas to come together in

synchrony (Buzsáki, 2006). Therefore, the slow oscillation (SO; ~1 Hz) which occurs during the SWA of slow-wave sleep (SWS) and anesthesia is able to synchronize the entire neocortex while gamma rhythms (~30-50 Hz) reflect local network processing. Oscillations of the same frequency (such as the SO) can interact across regions by phase-phase coupling while oscillations across bands can interact by phase-amplitude coupling such as the nesting of gamma power into a specific phase of the SO (Steriade, 2006) (Figure 1.1C).

Synchronizing activity by oscillatory mechanisms, as well as the anatomical principle of convergence, is considered the most metabolically efficient means for maximizing the probability of successfully activating downstream targets. In a study that examined the theoretical efficiency of synchronization through oscillation, sound recordings were made in an opera theater with microphones placed on the ceiling in order to examine synchronized clapping behavior. The results showed that an audience claps in response to a performance at first incoherently and within several seconds, synchronized clapping emerges. Interestingly, when examined in a laboratory setting, in order to achieve synchronized clapping individuals skipped every second clap when compared to the initial desynchronized clapping phase, yet the synchronized phase resulted in more intense volume gains. Therefore oscillatory behavior allowed for smaller individual effort exertion while maximizing the net result in volume amplification (Neda et al., 2000). A similar mechanism is thought to control neural oscillations which can effectively discharge downstream targets and affect the precision of spike-timing (Buzsáki, 2006; Buzsáki and Draguhn, 2004).

How are such diverse classes of oscillations generated by the brain? At the network level, oscillations result from cell-to-cell interactions mediated by both synaptic connections as well as gap junctions in certain cell types (Lewis and Rinzel, 2000; McCormick and Bal,

1997). The simplest model example of an inter-cell oscillatory mechanism is feedback inhibition (Figure 1.2A). In this scenario a constant depolarizing input is delivered to an excitatory pyramidal cell which excites an inhibitory interneuron which in turn feeds back onto the same pyramidal cell and inhibits its activity. As a consequence, the interneuron then loses its activating input and the cycle restarts.

Oscillations also occur at a single cell level due to certain intrinsic current properties (Figure 1.2B). A classic example is the intrinsic delta oscillation of thalamocortical cells in which at hyperpolarized membrane potential levels a hyperpolarization-activated mixed cation current (I_h) depolarizes the cell and activates a low-threshold Ca^{2+} current (I_T) which in turn causes a wide calcium wave onto which fast sodium (Na^+) spikes ride. The depolarization deactivates I_h and inactivates I_T followed by ensuing hyperpolarization, driven by active K^+ conductance through both delayed rectifying and Ca^{2+} dependent channels, and restarting of this cycle (McCormick and Pape, 1990) (Figure 1.2B). An important point that can be drawn from both the network and single cell examples is that a fine balance between excitation and inhibition is required for oscillation. There is a large diversity of inhibitory interneurons throughout the brain providing autonomy to local cell assemblies and a greater complexity of pyramidal cell function by finely controlling output timing (Freund and Buzsáki, 1996).

Oscillations are fundamental to brain operation and are incredibly highly individualistic. It has been shown that EEG patterns are hereditary with up to 96% concordance rate between monozygotic twins for specific rhythms (Anokhin et al., 1992; De Gennaro et al., 2008). There is also a correlation between spindle density as well as amplitude and standard measures of IQ (Fogel and Smith, 2011). Furthermore, many

neuropsychiatric disorders are associated with abnormal oscillatory patterns such as disrupted gamma synchrony in patients suffering from schizophrenia (Maharajh et al., 2010) and a wide range of EEG peculiarities are seen in depression (Alhaj et al., 2011). Interestingly many neuropsychiatric disorders specifically show irregular patterns of sleep rhythms and sleep architecture including schizophrenia, depression and even eating disorders (Brown et al., 2012; Jauregui-Lobera, 2012; Rockstroh et al., 2007).

1.2 Oscillations of sleep and wakefulness

The most global brain state changes are those observed across sleep-wake cycles as well as within various sleep stages. Wakefulness is marked by low voltage fast activity (LVFA) with cortical EEG predominantly in the beta to gamma frequency ranges (~15 – 50 Hz) and high muscle tone with sustained motor activity in the electromyogram (EMG) (Basheer et al., 2004, Fuller et al., 2006). During quiet wakefulness, when the eyes are closed, the EEG activity displays prominent alpha waves (~ 8 – 12 Hz), especially over the occipital cortex (Fuller et al., 2006). In humans, sleep initially progresses through various stages of non-rapid eye-movement (NON-REM) sleep, followed by REM sleep. In the first stage of NON-REM sleep the EEG transitions from alpha to theta waves (~ 4 - 8 Hz), followed by K-complexes (high-amplitude waveforms) and spindles (transient 7 – 14 Hz activity) during the second stage of SWS sleep, and finally the EEG slows even further to display highly synchronous slow activity known as slow-wave sleep (SWS) during the deepest stage of NON-REM sleep. In rodents, NON-REM sleep is not parsed into separate stages as cortical activity transitions rapidly from the “activated” state of wakefulness to the “deactivated” state of SWS (Brown et al., 2012). The signature cortical event of SWS is the

high amplitude slow oscillation (~ 1 Hz) that reflects alternating periods of highly active, depolarized (UP) states and silent, hyperpolarized (DOWN) states at the cellular level (Steriade et al., 1993b) (see section 1.3). Interestingly, it has been shown that K-complexes likely reflect a single slow oscillation cycle followed by spindle activity (Amzica and Steriade, 1997).

REM sleep is characterized by vivid dreaming along with LVFA in the EEG, rapid eye-movements (shown in the electrooculogram: EOG), and profound skeletal muscle atonia in the EMG, except for muscles controlling eye-movements and breathing (Saper et al., 2010). The similarity in EEG activity between wakefulness and REM sleep is evident by the cortical LVFA as well as hippocampal theta that are present in both states; thus this sleep state has been categorized as an "activated" state.

1.2.1 Mechanisms of sleep-wake transitions

The transition from wakefulness to sleep takes seconds or less in rodents and up to 10 minutes in humans (Takahashi et al., 2010). Following sleep onset, SWS sleep in humans progresses into prominent slow waves within 40 to 60 minutes, while rodents enter SWS sleep within seconds after sleep onset and transition between SWS and REM approximately every 3- 5 minutes (Saper et al., 2010). Early in the sleep period, SWS sleep is deeper and takes up a larger proportion of sleep time in comparison to REM sleep, while in the second half of the sleep period, REM sleep predominates (Datta and Maclean, 2007). While wakefulness transitions into SWS sleep, spontaneous awakening tends to occur after a REM sleep period (Brown et al., 2012).

The pioneering work of Moruzzi and Magoun in 1949 spurred experimental efforts in the dissection of sleep-wake circuitry in order to understand how such major state transitions occur and led to the concept of the "ascending reticular activating system". These authors showed that electrical stimulation of the mesopontine reticular formation in anesthetized cats produced the desynchronized "activated" EEG typical of wake and REM sleep (Moruzzi and Magoun, 1949). On the other hand, electrolytic lesions of this same region in cats caused coma (Lindsley et al., 1949), implicating the upper brainstem in cortical activation. Earlier work by Frederic Bremer (1935) showed that a transection at the junction of the brainstem and spinal cord did not affect sleep-wake states, and therefore the spinal cord was not necessary for controlling state transitions. More recently, specific wake-promoting brainstem, as well as hypothalamic, nuclei within the ascending arousal system and their projections have been identified. The ascending arousal system is composed of predominately cholinergic brainstem nuclei and aminergic cells in the brainstem and posterior hypothalamus (Saper, 1985, Hallanger et al., 1987, Saper et al., 2001, Saper et al., 2005b). On the other hand, the major sleep-promoting area is the ventrolateral preoptic nucleus (VLPO) of the anterior hypothalamus. The VLPO neurons contain GABA and gelanin and send projections to nearly all wake-promoting circuits (Sherin et al., 1998, Saper et al., 2001). In a complementary fashion, the wake-promoting cell groups innervate the VLPO (Chou et al., 2002). It has been shown *in-vitro* that the neuromodulators of these wake-promoting regions, such as serotonin, norepinephrine, and acetylcholine inhibit VLPO neurons (Gallopin et al., 2000). This mutual inhibition, reminiscent of an electrical flip-flop circuit, between sleep and wake circuitry can allow effective switching between sleep and wake states. A similar flip-flop mechanism has been proposed for switching between REM

and SWS sleep states through inhibitory connections between several REM-on regions including cholinergic nuclei of the pons, the laterodorsal and pedunculopontine tegmental nuclei, and REM-off regions including the monoaminergic locus coeruleus and dorsal raphe (Dunmyre et al., 2014).

1.2.3 Sleep and memory

Sleep appears to be a universal phenomenon and the architecture of sleep and sleep-wake transitions is largely phylogenetically preserved (Saper et al., 2010). The evolutionary advantage of the vigilant state of wakefulness is unequivocal, while the functional significance of sleep is perhaps less evident, and is still a matter of great debate. Over the years, strong evidence has accumulated to suggest that sleep may be relevant for cognitive functions such as memory consolidation (Fowler et al., 1973; Marshall et al., 2006; Mölle et al., 2004; Stickgold, 1998).

Müller and Pilzecker (1900) were the first to show that memory is initially labile and a period of consolidation takes place during which the memory is strengthened for long-term storage. They demonstrated that new material presented after initial learning could interfere with the first memory – the phenomenon of retroactive interference (Lechner et al., 1999). Soon after, investigations began to suggest that sleep was particularly beneficial for memory consolidation, with an initial focus on REM sleep (Siegel, 2001). However, animal studies showing memory impairments following REM sleep deprivation were confounded with stress. It also turned out that in depressed patients the administration of monoamine oxidase (MAO) inhibitors, such as phenelzine (Nardil), as a treatment can completely suppress REM

sleep resulting surprisingly in some memory improvement rather than the expected decrement (Siegel, 2001).

Today, evidence for a role of SWS in memory consolidation of a specific memory system - namely declarative or explicit memory - is continually growing (see section 1.6). One of the earliest studies attempting to parse out the individual roles of REM and SWS sleep in memory showed that declarative memories benefitted from early SWS-rich sleep, while procedural memories (memories for skills) benefited from late REM-rich sleep (Plihal and Born, 1997). More recently, the benefit of SWS for declarative memory consolidation has been pinpointed to depend on a specific rhythm during SWS – the cortical slow oscillation (Born et al., 2006; Diekelmann and Born, 2010; Marshall et al., 2006). In the next section I discuss in detail the neurophysiological features of this rhythm and its specific role in memory consolidation.

1.3 The neocortical slow oscillation

In a ground-breaking series of papers in 1993, Steriade and colleagues described for the first time the neocortical slow oscillation (SO) in anesthetized cats (using urethane and other anesthetics) as well as in naturally sleeping humans during SWS sleep (Steriade et al., 1993b; Steriade et al., 1993c, d). The SO is an approximately 1 Hz (and lower) frequency rhythm that is composed of UP (ON at the network level) states of vigorous neuronal activity interleaved with DOWN (OFF at the network level) states of neuronal quiescence (Steriade et al., 1993d). At the cellular level, the membrane potential exhibits a bimodal distribution that on average fluctuates between -62 mV during the UP state and -70 mV during the DOWN state (Timofeev and Chauvette, 2011) (Figure 1.3). All cortical neurons including

glutamatergic and inhibitory interneurons participate in this rhythm with synchronous UP and DOWN states (Contreras and Steriade, 1995). At the network level, ON states appear as positive wave peaks at superficial cortical levels (such as with EEG recordings; Figure 1.3A) and as negative peaks in deep layers due to the dipole created by the large layer V cells with superficially extending apical dendrites. Multiunit (cellular) activity and gamma are phase modulated by the SO recorded at the network level (Chauvette et al., 2010; Contreras et al., 1996a; Steriade et al., 1993d; Timofeev and Steriade, 1996) (c.f. Figure 1.1).

The SO was originally detected in both cortical and thalamic sites with the generation zone shown to be cortical in origin since it remained after thalamic lesions (Steriade et al., 1993c) as well as being present in isolated cortical slabs (Timofeev et al., 2000a) and in cortical slices *in-vitro* under specific conditions (Sanchez-Vives and McCormick, 2000). Furthermore, the SO is absent in the decorticated thalamus (Timofeev and Steriade, 1996) and relies on intact cortico-cortical connections (Amzica and Steriade, 1995a). The SO is also associated with low neuromodulatory tone and can be abolished in favor of low-voltage fast activity by stimulation of brainstem REM-on regions (see section 1.2) such as cholinergic pedunculopontine tegmentum or the noradrenergic locus coeruleus (Steriade et al., 1993a). The SO is globally encompassing and has been recorded in the hippocampus (Isomura et al., 2006; Nir et al., 2011; Wolansky et al., 2006), striatum (Wilson and Groves, 1981), amygdala (Crane et al., 2009) and cerebellum (Ros et al., 2009).

1.3.1 Mechanisms of the slow oscillation DOWN state

The DOWN state of the SO is caused by disfacilitation, or lack of synaptic input, rather than active inhibition as suggested by the high input resistance during the DOWN

state (Contreras et al., 1996b). It was initially shown that fast-spiking inhibitory neurons did not increase their firing rates before the onset of the DOWN state and, unlike during REM activity, intracellular Cl^- infusions did not reverse the membrane potential suggesting that $GABA_A$ mediated conductance was not involved in DOWN state initiation (Contreras and Steriade, 1995; Contreras et al., 1996b; Timofeev et al., 2001). Although still somewhat unclear, it is likely that the termination of the UP state involves the activation of K^+ channels (Timofeev et al., 2001) as well as the gradual depletion of extracellular calcium throughout the UP state (Massimini and Amzica, 2001). If the opening of K^+ channels is outweighed by the closing of synaptically regulated channels, the net effect would still result in an overall increase of input resistance (Neske, 2015). Furthermore, it has been recently suggested that a small subset of inhibitory cortical neurons increase their firing rate ~250 ms prior to the DOWN state onset (Lemieux et al., 2015) and may thus contribute to the DOWN state initiation.

1.3.2 Mechanisms of the slow oscillation UP state

A fascinating question pertaining to SO mechanisms is: how is the UP state initiated when the entire network is simultaneously shut off during the DOWN state? The spontaneous release hypothesis suggests that miniature excitatory post-synaptic potentials (mEPSPs) caused by the stochastic release of synaptic vesicles, eventually summate in time and cause an avalanche reaction bringing the entire network into an UP state (Chauvette et al., 2010; Timofeev et al., 2000a). Layer V neurons are the ideal candidate cells for the spontaneous release theory since they have the highest divergence and convergence due to their extensive axonal arborisations and large dendrites with high spine density, making it

more likely for mEPSP events to summate and for the resultant activity to be effectively broadcasted downstream (Neske, 2015). In support of this, it has been demonstrated that at the onset of an UP state, cells in any layer can respond with the earliest latencies but cells in layer V are typically the earliest to fire (Chauvette et al., 2010).

Another hypothesis is the pacemaker theory which suggests that specific types of cortical cells have intrinsic oscillatory properties that maintain the SO. A specific class of layer V cells has been recently identified with intrinsic rhythmic low-frequency burst firing at ~ 0.2 – 2 Hz that occurs at hyperpolarized membrane potential levels; and this rhythmic firing was resistant to the block of glutamatergic and GABAergic transmission (Lorincz et al., 2015). Another theory implicates glia in UP state modulation since astrocytes release important neurotransmitters such as glutamate and ATP as well as the N-methyl-D-aspartic acid (NMDA) receptor co-activator, D-serine; and blocking astrocytic function disrupts UP state dynamics (Fellin et al., 2009; Halassa, 2011; Newman, 2003; Poskanzer and Yuste, 2011).

Regardless of which theory or combination of theories is correct, there is strong evidence to suggest that layer V cells are the ones responsible for UP state initiation. Blocking layer V with TTX in an *in-vitro* rat model disrupted SO initiation and horizontal SO propagation while blocking superficial layers (II/III) had little impact on SO properties other than slightly delayed propagation, supporting the idea that the layer V cells are necessary and sufficient for SO generation (Wester and Contreras, 2012). In a similar vein, *in-vivo* optogenetic activation of layer V cells evoked SO waves that were indistinguishable from spontaneous waves while the optogenetic silencing of these cells abolished the SO.

Once again, activating or inhibiting the supragranular layers had little effect on SO dynamics (Beltramo et al., 2013).

1.3.3 Involvement of the thalamus in slow oscillation dynamics

Early studies of SO suggested that the thalamus was not necessary for SO generation and maintenance (see section 1.3.1), more recently however, this conclusion has been questioned (Crunelli and Hughes, 2010; David et al., 2013; Lemieux et al., 2014; Neske, 2015). The thalamus plays a role in synchronizing the SO across cortical networks (Amzica and Steriade, 1995b) and in maintaining the SO frequency (David et al., 2013). In a recent study, Lemieux and colleagues (2015) inactivated the thalamus of cats *in-vivo* using lidocaine which caused SO UP states to occur less frequently and less regularly while desynchronizing the remaining isolated slow-wave events in the cortex. Interestingly, the SO activity began to recover 12 hours following thalamic inactivation (Lemieux et al., 2014). A modelling component of this study suggested that the recovery occurred as a result of compensatory mechanisms which enhanced excitatory synaptic activity across long-range intracortical connections. It is important to note that the original study by Steriade and colleagues using thalamic lesions performed recordings 2 days post-lesion (Steriade et al., 1993c). The implications from the Lemieux study would suggest that the SO compensatory mechanisms would have already taken effect in the original Steriade study. Therefore, although the cortex still seems to have a predominant role in SO generation and maintenance, the additional, and perhaps complex, role of the thalamus cannot be disregarded.

1.3.4 Propagation of the slow oscillation

Although the SO appears highly synchronous, a particularly dynamic feature of this activity is that when examined on a finer temporal scale, each wave of the SO originates at a distinct local focus and travels across the neocortex (Amzica and Steriade, 1995a; Massimini et al., 2004). Human studies show that waves tend to originate more often at prefrontal/orbitofrontal regions, with different initiation zones cycle-to-cycle and travel in a mainly anterior-to-posterior direction across the cortex (as well as perhaps involving a cortico-thalamo-cortical loop) and eventually making their way to the hippocampus (Massimini et al., 2004; Nir et al., 2011). The propagation path that SO waves typically follow involve medio-central regions along the frontal gyri, anterior and posterior cingulate and the precuneus, growing in amplitude as they propagate (Murphy et al., 2009). Remarkably, streamline maps for all possible SO propagation trajectories in a given night are highly consistent within individuals across nights (Massimini et al., 2004).

SO propagation has been demonstrated in animal studies as well with somewhat different results since such studies allow the examination of SO propagation on a finer spatial scale (in comparison to using EEG in humans). Using voltage sensitive dye (VSD) imaging in mice it was shown that SO displays multiple peaks of activity, rather than a specific focus, with complex local propagation patterns that were well mirrored across hemispheres likely synchronized by the fibers of the corpus callosum (Mohajerani et al., 2010). Furthermore, complex spiral wave patterns have been reported in an SO slice study (Huang et al., 2004) and in-vivo (Mohajerani et al., 2010). More complex local patterns have been shown in a human study as well using subdural electrode grids in epilepsy patients, showing that SO propagation is non-linear with the presence of reciprocal and circular

patterns (Hangya et al., 2011). There is also a developmental feature to SO propagation as slow-waves during early childhood tend to originate at more posterior cortical locations and progressively move to anterior locations throughout adolescence (Kurth et al., 2010).

Interestingly, it has also been shown that while a propagating wave can pass in more than one direction from the viewpoint of a given location, the inter-cell firing relationships were consistent regardless of the wave direction passing by these local networks (Luczak et al., 2007). This suggests that the activity of local cellular assemblies is not random during the SO but has a predetermined and systematic structure that is reinforced upon being activated by a traveling wave front. In this way, depending on the propagation direction, various local assemblies would be activated in specific orders relative to one another. Since the SO has been specifically implicated in memory consolidation (see section 1.3.5), it is tempting to speculate that waking experience determines which cell assemblies, and relationships between assemblies, will be reinforced during sleep. Importantly, it has been shown that electrically evoked slow-waves in naturally sleeping rats have highly similar features to endogenous slow-waves including propagation of activity from the initial stimulation site (Vyazovskiy et al., 2009). It is therefore theoretically possible to actively manipulate the SO and examine the effects on SO dynamics and potentially behavior.

1.3.5 Role of the slow oscillation in memory consolidation

There is strong evidence implicating a specific role for SO in memory consolidation. For example, in a human study, learning a declarative memory task increased SO coherence across distinct cortical regions during subsequent sleep (Mölle et al., 2004). In another human study, the acquisition of a specific visuospatial task resulted in enhanced SO power

during sleep restricted to the specific cortical region associated with task acquisition, and the local SO power increase was positively correlated with improved task performance the following day (Huber et al., 2004). Furthermore, a daytime nap dominated by SWS and thus, SO activity, resulted in improved declarative memory consolidation without affecting procedural memory (Tucker et al., 2006).

The most direct evidence for a role of the SO in memory comes from two studies by Marshall and colleagues (Marshall et al., 2006; Marshall et al., 2004). In these studies, experimenters applied either oscillating transcranial electrical stimulation at a similar frequency to the endogenous SO (0.75 Hz) (Marshall et al., 2006) or direct current stimulation (Marshall et al., 2004) during SWS sleep in humans and showed that these manipulations boosted SO power and led to improvements on a declarative memory task that was learned the previous day (these studies are discussed in more detail in section 1.8.4). A similar effect of transcranial electrical stimulation was observed by the same group in rats (Binder et al., 2014a), and using rhythmic auditory instead of electrical stimulation in humans (Ngo et al., 2013). It is important to note that in the majority of the discussed studies, it is specifically declarative memories that benefited from the SO and its manipulation (the role of the hippocampus for such memories is discussed in section 1.6). In support of a potential mechanism for SO-dependent memory consolidation, it has been shown that the SO supports NMDA-receptor mediated long-term potentiation which is thought to strengthen specific neural connections (Chauvette et al., 2012).

1.4 Thalamocortical spindles and memory consolidation

As discussed earlier, the SO groups local network activity such as gamma and multi-unit activity. The SO also modulates another important rhythm, the thalamic spindle oscillations that have also been associated with learning and memory. Spindles are waxing and waning oscillations with a frequency of ~ 7 - 14 Hz. The spindle pacemaker is the GABAergic thalamic reticular nucleus (RE) whose cells have intrinsic oscillatory properties and are highly inter-connected through gap junctions. These cells send rhythmic inhibitory post synaptic potentials (IPSPs) to the glutamatergic thalamocortical cells which thereby produce rhythmic firing during the rebound phase, relaying EPSPs to the cortex as well as back to the RE to keep this rhythm going (Contreras and Steriade, 1995). Corticothalamic projections back to the RE are necessary for synchronizing spindles across the thalamus (Contreras et al., 1996a, 1997). Furthermore, the cortex can initiate and control the duration of spindles through the direct projections to the RE (Timofeev and Chauvette, 2011).

Spindles are associated with massive depolarization and Ca^{2+} entry at superficially located cortical dendrites and have thus been implicated in Ca^{2+} triggered intracellular signaling cascades associated with long-term potentiation (LTP) and synaptic plasticity (Neske, 2015; Rosanova and Ulrich, 2005; Timofeev et al., 2002). At the behavioral level, it has been shown that spindle density increases post-learning in rats and humans (Eschenko et al., 2006; Mölle, 2009) and that this increase is correlated with subsequent memory performance (Clemens et al., 2005; Gais et al., 2002). Spindles are also important for integrating new knowledge into pre-existing representations (Tamminen et al., 2010).

1.5 Cortical anatomy and architecture

Francis Crick is famously quoted as saying "if you want to understand function, study structure" (Crick, 1990). Although a literal interpretation of this quote would do little justice to the field of brain rhythms, in order to fully appreciate the complex functional operation of the neocortex it is important to consider its structural organization. Excitatory pyramidal neurons make up ~80 percent of all cortical neurons, the rest being made up of various interneuron (mostly inhibitory) classes, some with long-range connections (DeFelipe and Farinas, 1992; Thomson and Bannister, 2003). The wiring of the cortex is thought to reflect "small-world" principles with mainly local connections and a few interspersed long-range connections which results in a beneficial trade-off between the physical space that would be required to connect all cells to one another (using axons) and the average synaptic path length (Buzsáki, 2006; Watts and Strogatz, 1998). Such small-world organizational principles have been found to exist in the neuronal network of the Caenorhabditis elegans (C. elegans), the only completely mapped neuronal network to date, with an average synaptic path length of ~3 nodes (Watts and Strogatz, 1998). This local organization allows for a large gain in decreased path length while requiring magnitudes of order less long-range connections when compared to a random network where all connections are randomly distributed. Interestingly, small-world networks also represent the US power grid and the social network of collaborations between film actors (Watts and Strogatz, 1998).

The basic neocortical unit of this local organization is the cortical minicolumn (~ 54 μm diameter) made up of vertical interconnections between the layers of cortical cells with several minicolumns forming cortical columns through horizontal connections (Mountcastle, 1997). The pioneering work of Hubel and Wiesel demonstrated the functional properties of

this organization showing that visual cortical cells positioned vertically respond to the same visual features (angle and direction) of slits of light and that there is an orderly transition of preferred angles across horizontally positioned orientation columns (Hubel and Wiesel, 1962, 1963).

1.5.1 Intrinsic and extrinsic cortical connections

The neocortex has six layers with complicated efferent and afferent connections that vary across cortical region. The discussion here will focus on simplified principles that are mostly generalizable across regions. Sensory information from the thalamus projects primarily to layer IV of the relevant sensory region with some connections to layer VI as well (Figure 1.4). The classic model suggests that following the thalamic input, layer IV then sends the information to the superficial layers II and III and from there the information flows to layer V and from layer V to layer VI. Layers III and V have long horizontal projections which distribute information across the cortex (Figure 1.4) (Aroniadou and Keller, 1993; Mountcastle, 1997).

Layers V and VI are the major output layers of the cortex which send projections back to the thalamus and to various subcortical regions including the brainstem and spinal cord (Figure 1.4). The major monoaminergic input to the cortex is fed into the superficial (layer I-III) dendrites. As previously mentioned (see section 1.3.2) layer V cells are the largest cells with some dendrites extending into layer I, therefore receiving some of the same inputs as more superficially located neurons (Figure 1.4). Another aspect of cortical organization that reiterates its highly local structure is the fact that the vast majority of excitatory inputs to the cortex come from other excitatory cortical cells (Mountcastle, 1997).

These structural principles may suggest that the cortex can easily dissociate from the environment, as during sleep, and can continuously reinforce activity through its highly reciprocal connections.

1.6 The role of the hippocampus in memory consolidation

The neocortical SO appears to consolidate memories, however, the cortex does not act alone to achieve this goal; rather its interaction with the hippocampus is imperative for a specific type of memory – declarative memory. There are multiple systems of memory, each following different acquisition rules with the involvement of different brain regions. Declarative memory is an explicit form of memory that is further categorized into semantic and episodic memories. Semantic memories are related to non-contextual information, lacking a specific spatial and temporal context in which such memories were acquired. On the other hand, episodic memory is tied to a spatiotemporal context, such as autobiographical information (Squire, 2004). Declarative memories, especially those that are episodic in nature, are thought to rely on the structures of the medial temporal lobe (MTL) including the hippocampal formation. Procedural memory is a type of nondeclarative memory for skills and habits which is mediated by various brain regions, including the striatum. Other forms of nondeclarative memory are non-associative, classical-conditioning (associative) and priming (Squire, 2004).

The role of the hippocampus in memory processing was first brought to light by William B. Scoville and Brenda Milner who studied the famous amnesiac patient Henry G. Molaison, known as H.M. in the scientific literature. H.M. suffered from intractable epilepsy since childhood and at the age of 29 in 1953 he underwent bilateral resection of the medial

temporal lobes including the hippocampus, entorhinal cortex, parahippocampal and perirhinal cortices in attempt to moderate his symptoms (Scoville, 1954; Scoville and Milner, 1957). While successfully treating his epilepsy, the operation severely impaired his mnemonic abilities. Following the operation, H.M. did not recognize hospital staff and could not find his way to the bathroom. It was established that he had complete anterograde amnesia as he could not form new long-term memories, together with severe temporally graded retrograde amnesia going back about 11 years prior to the surgery (Corkin, 2002), although his episodic memories seemed to be completely abolished, showing a flat gradient (Eichenbaum, 2013). H.M was studied for decades up until his death in 2008 and is arguably the most studied patient in neuroscience with ongoing investigations of his post-mortem brain up until today. The initial brain slicing procedure of his post-mortem brain was live-streamed with over 400,000 people tuning in (Moll, 2014). A 3- dimensional reconstruction of his brain was completed in 2014 (Annese et al., 2014).

The study of H.M. laid the foundation for the study of hippocampal-mediated memory and the distinction between multiple memory systems; prior to which the role of the hippocampus was believed to concern olfactory processing (Scoville, 1954; Scoville and Milner, 1957). Following H.M.'s surgery he did not suffer from any change in personality or general intelligence. Although he could not acquire new long-term memories, he could seemingly recall childhood memories but not memories more recent to the onset of surgery (Scoville, 1954; Scoville and Milner, 1957). Importantly, he could acquire and retain procedural skills such as learning to trace inside the borders of a star using the reflection of his hand in a mirror; showing improvements trial after trial without any explicit memory of having previously encountered the task (Scoville, 1954; Scoville and Milner, 1957). The

suggested temporally graded nature of the memory loss, and the fact that the affected memories were of a specific type, led to a dominant model of memory consolidation which posits that overtime the interactions between the neocortex and hippocampus are essential for reorganizing memory representations – specifically declarative memories, making these memories increasingly less reliant on the hippocampus (Squire and Bayley, 2007).

1.6.1 Hippocampal anatomy and architecture

Prior to discussing how such cortico-hippocampal interactions take place during the SO to support memory consolidation, a look at hippocampal specific anatomical and physiological properties is important for realizing the distinct roles that the cortex and hippocampus may play. The hippocampus proper includes the hippocampus, dentate gyrus, subicular complex, and entorhinal cortex. The hippocampus resembles a seahorse in shape (its name is derived from the Greek *hippo* meaning "horse" and *kampos* "sea monster") and has a long septotemporal axis which runs dorsal to ventral in the rodent, and is called the anterior-posterior axis in the primate as the position of the hippocampus was shifted through evolution with the growth of the cerebral cortex (Figure 1.5A). The septal (ventrally located) end of the hippocampus in the rat is analogous to the anterior end of the primate hippocampus. The axis orthogonal to the septotemporal (anterior-posterior) axis is called the transverse axis and a slice through this axis reveals all of the major hippocampal subregions (Figure 1.5B). This axis is somewhat analogous to the cortical column although divergent connections across the septotemporal axis suggest that there is no true "basic unit" of the hippocampus (Amaral and Lavenex, 2007). The hippocampus has three subdivisions named cornu ammonis, after an Egyptian God (meaning "horns of Ammon"): CA1, CA2 and CA3

(Figure 1.5B). CA2 is the least studied of these regions. Like the neocortex, the hippocampus has a structured laminar organization, but unlike the neocortex, it is an allocortical structure with a single cellular layer that is twisted forming a "C" shape. A transverse slice also reveals another cellular layer, made up of the granule cells of the dentate gyrus (DG), which forms a "V" shape interlocking with the hippocampal "C".

The principal cells of the hippocampus are pyramidal cells with long apical dendrites extending towards the pial surface called the hippocampal fissure, located at the intersection of the CA regions and the DG (Figure 1.5B). Due to the twisted "C" shape of the hippocampus, an electrode penetrating the rat hippocampus from the dorsal surface of the cortex will first encounter the pyramidal cells being "upside down" with the following order of cell layers: the stratum oriens (SOr) which contains the basal dendrites, followed by the pyramidal layer (SPyr) containing the cell bodies, stratum lucidum (only for CA3 cells), stratum radiatum (SRad) which contains the proximal apical dendrites and finally stratum lacunosum-moleculare (SLM) which contains the distal apical dendrites (Figure 1.5C). A deeper penetration, moving ventrally, will cross the hippocampal fissure to enter the molecular layer of the DG which contains the spiny dendrites of the granule cells - the principal cells of the DG (Figure 1.5C). The molecular layer is followed by the granule cell layer, stratum granulosum, containing the cell bodies. The polymorphic layer of the DG lies just below reaching the hilus, and contains mostly interneurons. As in the neocortex, local interneurons are scattered through the hippocampal and DG layers, with more than 20 different typed identified in CA1 alone (Basu and Siegelbaum, 2015).

The subicular complex lies next to CA1 (on the other side of CA3) and includes the subiculum, presubiculum, and parasubiculum. The subicular complex is a major output

source of the hippocampus (see section 1.6.2). The entorhinal cortex (EC) is a six-layered cortical structure with four cellular layers (II, III, V and VI) and lies at the temporal (anterior) end of the hippocampus. The EC brings in highly processed cortical information to the hippocampus (Figure 1.4A; see below).

1.6.2 Hippocampal intrinsic and extrinsic connections

As discussed earlier, the neocortex is organized topographically to represent statistical features of the environment. The hippocampus on the other hand does not show such orderly local organization. The hippocampus is wired based on "random networks" (see section 1.6.1) in which a CA3 neurons for example may contact a neighbouring cell with the same likelihood as a more distant cell (Buzsáki, 2006; Miles and Wong, 1986). The structure of the hippocampus suggests that it is not designed to interact directly with the environment as it receives highly processed multimodal information and its "randomly wired" networks are ideal for creating patterns of abstract relationships. The classic hippocampal trisynaptic circuit is made up of mainly unidirectional excitatory pathways from the EC to the DG, DG to CA3 and CA3 to CA1 (Figure 1.5). Once the information reaches CA1 it then takes several paths which distribute the information from the hippocampus to other brain regions. Information therefore converges to reach the hippocampus and diverges after processing. The intrinsic and extrinsic connections related to this circuit are discussed below.

The hippocampal loop begins at the EC which receives major afferents from the perirhinal and postrhinal (parahippocampal in the primate) cortices which in turn receive both unimodal and multimodal neocortical projections. The EC is separated into the lateral EC, which receives object related "what" information from the perirhinal cortex, and the

medial EC which receives “where” information from the postrhinal cortex (van Strien et al., 2009). Therefore information pertaining to both object features and its spatiotemporal context merge at the level of the hippocampus which receives these inputs from the EC. The EC projects to several regions of the hippocampal formation (Figure 1.6). Layer II of the EC sends projections through the perforant path which travel in the angular bundle and “perforate” the subiculum on their way to the molecular layer of the DG as well as to SLM of CA3 (Amaral and Lavenex, 2007). An alternate route exists from layer III of the EC through the temporoammonic path which travels mainly in the alveus (at more septal hippocampal levels) instead of the perforant path and contacts CA1 at the level of SLM as well as the distal dendrites of the subiculum.

The next step in the trisynaptic path is from the granule cells of the DG to stratum lucidum of CA3 by way of the mossy fibers (Figure 1.6). The DG also contains another major cell type, the mossy cells, which make up the major commissural projection across the DG of both hemispheres. Interestingly these commissural connections are very limited in the primate (Amaral and Lavenex, 2007). The CA3 pyramids form a major recurrent (associational) network whereby they feedback onto themselves at the level of SRad (Figure 1.6). The final projection of the trisynaptic loop is from these same CA3 pyramids to the CA1 by way of the Schaffer collaterals which form synapses at the level of SRad as well as a smaller portion at the level of SOr (Figure 1.6). The CA1 cells are the major output cells of the hippocampus since they make their way to the subiculum and the deep layers (V/VI) of the EC thereby completing the loop. CA1 also has unique connections with the prefrontal cortex since it sends direct efferents to the prefrontal cortex (from the ventral hippocampus)

and receives afferents at the level of SLM from the nucleus reuniens of the thalamus which in turn receives direct input from the medial prefrontal cortex.

The EC is the main source of hippocampal output back to the neocortex, while the subiculum provides the main source of hippocampal afferents to subcortical regions (Figure 1.6). While the superficial layers of the EC feed into the hippocampus and the deep layers receive the processed hippocampal information, there are also connections between layer V of EC back to the layers II/III which fully close the loop (Basu and Siegelbaum, 2015). The EC's projections back to the neocortex are to higher-order associational areas. This complete circuit therefore starts at multimodal cortical areas, funnels into the hippocampus and returns back to the same higher-order cortical areas. Therefore, there is no "top" in this circuit but rather a complex recurrent path which is ideal for modifying inputs.

1.7 Interactions between the neocortex and hippocampus in memory consolidation

The complex cortico--hippocampo-cortical wiring sets up an ideal platform for creating dynamic interregional interactions during SWS, and specifically during the SO. During sleep, hippocampal activity alternates between rhythmic theta activity (4 – 8 Hz) that is concurrent with neocortical REM activity and large-amplitude irregular activity that co-occurs with neocortical SWS. More recently, however, it has been demonstrated that the hippocampus also has a third state that is present during natural SWS and anesthesia, the hippocampal slow oscillation (SO), which is a highly rhythmic oscillation (~0.3 – 1 Hz) that is moderately coherent with the neocortical SO and locally modulates hippocampal multiunit, gamma and ripple (see sections 1.7.1 & 1.7.2) activity (Isomura et al., 2006; Wolansky et al., 2006). The neocortical SO likely interacts with the hippocampal SO via the

EC and creates windows of opportunity for cortico-hippocampal interactions that are thought to support memory consolidation (Dickson, 2010; Wolansky et al., 2006).

1.7.1 Hippocampal ripples

Hippocampal ripples (140 – 200 Hz) which occur during SWS states are associated with memory replay and are therefore particularly relevant in the context of cortico-hippocampal interactions. The so called sharp-wave ripple events (SPW-Rs) are generated by strong depolarization of SRad in CA1 by the CA3 Schaffer collaterals (sharp waves) which trigger interneuron-pyramidal cell interactions (ripples) restricted to the pyramidal cell layer. Sequences of firing patterns between "place cells" during learning of a spatial task are repeated or "replayed" during SPW-Rs (Sutherland and McNaughton, 2000; Wilson and McNaughton, 1994). SPW-Rs occur during cortical UP states , particularly following the DOWN-UP transitions of the cortical SO (Battaglia et al., 2004; Isomura et al., 2006; Molle et al., 2006; Siapas and Wilson, 1998; Sirota et al., 2003). Interestingly, ripples are also nested in individual thalamocortical spindle cycles (Clemens et al., 2007; Siapas and Wilson, 1998) and bursts of activity during SPW-Rs can trigger spindles in the prefrontal cortex (Wierzynski et al., 2009). As with cortical spindles, learning causes increases in ripple occurrence (Mölle, 2009). The most direct evidence for the role of ripples in memory comes from studies that selectively disrupted ripples with a resulting disruption in memory consolidation (Ego-Stengel and Wilson, 2010; Girardeau et al., 2009).

1.7.2 Gamma rhythms

Gamma oscillations (20 – 80 Hz) represent local network interactions and are modulated by the SO in both the cortex and hippocampus. The membrane time constant of neurons is between 10 – 30 ms during which inputs can be successfully integrated. This time frame matches the gamma period and it has therefore been suggested that gamma allows for integration and segregation of individual cell assembles (Buzsáki, 2006; Harris et al., 2003). This timing also concurs with the window for spike-time dependent plasticity during which synaptic strength can be successfully modified (Bi and Poo, 1998; Dan and Poo, 2004). Gamma oscillations are generated by fast rhythmic bursting interneurons which precisely control the output timing of excitatory pyramidal cells (Buzsáki and Wang, 2012; Cardin et al., 2009). Optogenetic stimulation of fast-spiking inhibitory neurons at gamma frequencies generates gamma in the LFP with no such effects for regular-spiking excitatory cells (Cardin et al., 2009), while GABAergic antagonists such as picrotoxin cause gamma desynchronization (Stopfer et al., 1997). Gamma oscillations therefore represent a basic fundamental mode of neural operation and the modulation of gamma by slower rhythms allows for efficient long-range synchronization and communication of distinct assemblies across distant brain regions (Buzsáki, 2006; Buzsáki and Wang, 2012).

1.7.3 Behavioral implications for cortico-hippocampal interactions

As discussed earlier, both the cortex and hippocampus show mutual SO states, with the cortical SO originating at a specific focus and making its way across the cortex and to the hippocampus. Within this framework, it has been shown in rats that replay representing specific learned events co-occurred in the cortex and hippocampus within SO UP state time

frames, with cortical frames leading hippocampal frames by ~ 50 ms (Ji and Wilson, 2007). However, task-related firing sequences appeared to occur in the hippocampus first. Therefore, it is possible that the cortical SO triggers and selects the specific hippocampal replay events that will then be relayed back to the cortex.

The involvement of the hippocampus during SWS-dependent memory consolidation was demonstrated in a study where subjects were presented with an odor during the acquisition of a declarative memory task involving spatial associations between pairs of cards. Odor re-exposure during SWS activated the hippocampus as assessed by functional magnetic resonance imaging (fMRI) and resulted in improved memory performance, without affecting memory for a procedural task (Rasch et al., 2007). Importantly, odor re-exposure during REM sleep did not have an effect on memory (Rasch et al., 2007). Another human study trained healthy and epileptic patients with various degrees of hippocampal lesions on an association task relating auditory cues to specific words. Upon auditory cue re-exposure during SWS to a subset of the learned associations, both of the healthy controls and patients with partial hippocampal damage showed improvements specific to the cued words (Fuentemilla et al., 2013). Notably, the degree of memory improvement negatively correlated with the extent of hippocampal damage, supporting the involvement of the hippocampus in memory reactivation.

An influential proposed model for SWS-mediated memory consolidation suggests that the cortical SO groups hippocampal and thalamocortical events which replay memories and initiate synaptic modifications in cortical networks thereby strengthening memory representations for long-term storage (Born, 2010; Diekelmann and Born, 2010). Recent mechanistic support for this model comes from a study which simulated SO activity in a

physiologically realistic thalamocortical network (Wei et al., 2016). The results showed that the spatiotemporal pattern of SO propagation influenced plasticity in specific cortical networks and in turn when applying input mimicking hippocampal SPW-Rs, the synaptic weights in cortical networks were adjusted resulting in altered spatiotemporal SO propagation patterns. This model therefore links cortico-hippocampal interactions with cortical SO propagation dynamics for the support of plastic modifications.

1.8 Manipulating brain rhythms using electrical stimulation

Since the discovery of electrical neural conduction (then called "animal electricity") by Luigi Galvani in the late 18th century, followed by the advent of the voltaic pile (the first battery) by Alessandro Volta, experiments using direct current stimulation in an attempt to manipulate brain activity and behavior emerged (Zaghi et al., 2010). Giovanni Aldini, Luigi Galvani's nephew, used such "galvanic currents" to treat patients with melancholy at the beginning of the 19th century (Zaghi et al., 2010). Studies of "Electrosleep" began around 1902 with most of the work being performed in Russia using pulsed currents (30 – 100 Hz, monophasic) with electrodes placed over each eye and a return electrode placed on the mastoids to induce sleep-like states in patients (Guleyupoglu et al., 2013). Around the same time, there were also experiments using electroanesthesia intended to induce a generalized anesthetic state by applying very high frequency currents (> 3000 Hz) across various scalp configurations. These techniques are no longer in use as they led to severe side-effects including cardiac arrest (Guleyupoglu et al., 2013).

1.8.1 Mechanisms of tDCS

These earlier studies have led to the modern-day use of electrical brain stimulation techniques which are grouped under the umbrella term: transcranial electrical stimulation (TES). The most common form of TES is called direct current stimulation (tDCS) which generally involves placing an anode and cathode electrode on the scalp and passing constant current using a battery-powered current generator with intensities varying across studies between 0.5 and 2 mA (Barham et al., 2016). tDCS has been used to successfully modulate a wide range of cognitive behaviors, especially in clinical populations, including improvement of working memory in patients with depression (Boggio et al., 2007) and Alzheimer's disease (Boggio et al., 2009), decision making in alcoholism (Boggio et al., 2008) and recognition memory in Alzheimer's patients (Ferrucci et al., 2008).

The mechanisms of tDCS have been shown to involve influence on the membrane potential and modification of the firing rate of individual cells (Zaghi et al., 2010). Anodal tDCS over the target area increases excitability of the underlying cortical tissue while cathodal stimulation decreases excitability (Bestmann et al., 2015). The anodal protocol depolarizes layer V cortical cells while hyperpolarizing the superficial layers. The direct effect of tDCS is likely constrained to the region under the electrode but interpretation of the net effects are complicated by inter-region interactions between the stimulated region and its downstream targets as well as the fact that anodal stimulation increases excitability not only of pyramidal cells but of inhibitory neurons as well (Bestmann et al., 2015; Zaghi et al., 2010). While the effects of tDCS during stimulation seem to involve excitability changes at the level of the membrane potential, the aftereffects of tDCS appear to be at the synaptic level (Stagg and Nitsche, 2011). Certain tDCS protocols affect neuronal firing rate for hours

after a stimulation session (Bindman et al., 1964; Paulus et al., 2013) and these long-term effects include increases in gene-expression mediated by NMDA receptor activation (Stagg and Nitsche, 2011).

1.8.2 Mechanisms of tACS

A more recent form of TES, which is particularly relevant to this thesis, is transcranial alternating current stimulation (tACS). In tACS the applied current varies in a sinusoidal fashion over time between the anode and cathode, making this technique particularly attractive for manipulating oscillatory brain patterns. Slice work has shown that even weak alternating electrical fields can successfully modulate the membrane potential of cells in a sinusoidal manner (Reato et al., 2013). Estimates showed that stimulation resulting in 1 mV/m measured in the extracellular space was sufficient to entrain cells inducing 2-3 mV polarization (Ozen et al., 2010). Unlike tDCS, tACS modulates the timing of cellular discharge without affecting the average firing rate (Reato et al., 2010). It has been demonstrated in both a simulated network model and *in-vivo* in ferrets that tACS shows a resonance phenomenon representing an "Arnold tongue" whereby the closer the stimulation frequency is to the endogenous frequency, the smaller the intensity of stimulation required to entrain the network (Ali et al., 2013; Frohlich and McCormick, 2010). In terms of phase, a tACS simulation showed that the endogenous network was successfully entrained within a few seconds of stimulation initiation regardless of the phase at which the stimulation was initially applied, although the phase determined the time it took initially for the network to phase lock to the stimulation (Ali et al., 2013). tDCS and tACS can be combined by superimposing a direct current onto an alternating current resulting in oscillatory-tDCS (osc-

tDCS). tACS and osc-tDCS have been used to successfully modulate a wide range of rhythms including alpha stimulation during wakefulness to boost alpha power (Neuling et al., 2013), gamma-band stimulation to entrain gamma in hippocampal slices (Deans et al., 2007) and influence SO and spindle power using SO-band stimulation during sleep (see below) (Marshall et al., 2006).

1.8.3 Behavioral implications of electrical stimulation

Although brain stimulation techniques have been around for a long time, the mechanisms of TES in relation to its behavioral consequences, especially for tACS, are poorly understood. Since 2006 there has been a sharp rise in media coverage of the apparent benefits of TES, including headlines such as: "zap your way out of depression", "jump-start your brain" and "zapping brain boosts math skills" (Dubljevic et al., 2014). As a result, entire online communities of "DIY brain hackers" have sprung up where members develop TES devices for as little as $20 inspired by following the latest scientific literature and playing with various current amplitudes, waveforms and electrode montages (Dubljevic et al., 2014; Economist, 2015). There is also a plethora of TES devices on the market with currently little regulatory oversight (Guleyupoglu et al., 2013). Although the scientific community currently considers such devices as far from being safe and effective for commercial use, there is some evidence suggesting that TES may be safe, as there have not been any reports of neuronal damage or pathological EEG waveforms detected in human studies (Stagg and Nitsche, 2011).

1.8.4. Rhythmic electrical stimulation in memory consolidation

TES cannot yet promise to "jump start" our brain in the comfort of our homes, however, recent research in laboratory settings have provided some promising results of TES, particularly in the context of memory function. In a notable study, Marshall and colleagues trained human participants on a declarative paired-associate task (using word pairs) prior to a night of sleep (Marshall et al., 2006). During SWS sleep trapezoidal shaped current oscillating at a similar frequency to the endogenous SO (0.75 Hz; osc-tDCS) was applied to two frontolateral electrode sites (with references at the mastoids) five times for five minutes with one-minute stimulation free intervals in between. This TES protocol resulted in increased SO and spindle band power at frontal recording sites as well as a phase reset of the endogenous SO that was visible following the cessation of stimulation (measured during the stimulation free intervals). Furthermore, SO stimulation resulted in enhanced memory recall for the declarative task the following day, with no change for a procedural task. There were also no memory effects for procedures using sham stimulation or stimulation applied at 5 Hz. Another study from the same group demonstrated that TES applied at 5 Hz during SWS decreased SO power and resulted in memory decrements for a declarative memory task (Marshall et al., 2011).

SO frequency osc-tDCS has also been used during SWS to improve memory in patients with schizophrenia (Goder et al., 2013) and in children with attention-deficit/hyperactivity disorder (ADHD) (Prehn-Kristensen et al., 2014). Similarly, in patients with temporal lobe epilepsy, osc-tDCS (at SO frequencies) applied over the affected cortical region before a day-time nap enhanced spindle density during the nap and improved subsequent memory consolidation for a declarative task acquired prior to the nap (Del Felice

et al., 2015). Although some reports have failed to find an effect of TES on sleep-dependent memory consolidation (Binder et al., 2014b; Sahlem et al., 2015), a recent meta-analysis found that across studies the general conclusion that TES is effective at enhancing declarative memories specifically, has been supported (Barham et al., 2016).

1.8.4 Cortico-hippocampal interactions during rhythmic electrical stimulation

Slowly oscillating TES applied during SWS appears to benefit declarative memories, however, the effects of TES on SO dynamics and cortico-hippocampal interactions, which are considered necessary for declarative memory consolidation (see section 1.7), remain completely unclear. The difficulty lies in the fact that most of these studies were performed in human subjects, making it impossible to directly record from hippocampal regions. Another issue relates to the stimulation artifact which precludes any assessment of cortical and hippocampal dynamics during stimulation.

In attempt to address some of these issues, Ozen and colleagues applied slow frequency tACS to frontal cortical regions *in-vivo* in anesthetized and naturally sleeping rats (Ozen et al., 2010). They showed that tACS (0.7 - 1.7 Hz) can successfully entrain neurons in both the cortex and hippocampus in a state-dependent manner since entrainment was only accomplished during SWS but not during wakeful exploration. Increasing stimulation intensities resulted in increased numbers of units being entrained in both regions. However, beyond simple entrainment of units at individual sites, it remains to be addressed how such stimulation influences cortico-cortical as well as cortico-hippocampal interregional dynamics both during stimulation and following the cessation of stimulation – the aim of this thesis.

1.9 Urethane model for studying sleep dynamics

This thesis uses urethane anesthesia in both rats and mice as a model for sleep activity. Urethane is considered an excellent model for sleep as it has been demonstrated using *in-vivo* recordings in rats that activity recorded in the cortex and hippocampus under urethane transitions between activated and deactivated states in a manner highly resembling recordings from naturally sleeping rats based on EEG signals within each state as well as the alternation dynamics between states. Physiological sleep measures such as heart rate, muscle tone and respiration were also similar across urethane and natural sleep, as well as the dependence of state alterations on intact cholinergic brain signaling (Clement et al., 2008). In terms of its mechanism of action, urethane applied *in-vitro* was shown to decrease membrane excitability, input resistance and firing rate in pyramidal cell recordings by increasing K^+ leak conductance associated with a specific class of K^+ channels (Sceniak and Maciver, 2006). Furthermore, the effects are restricted to intrinsic membrane properties as there was no effect on excitatory or inhibitory synaptic transmission (Sceniak and Maciver, 2006). Nevertheless, there are some differences between urethane anesthesia and natural sleep including differences in the theta peak frequency during activates states, lack of rapid eye movements that are characteristic of REM sleep and the inability to awake animals from anesthetized states (Clement et al., 2008). A detailed analysis comparing another common anesthetic, ketamine-xylazine, has pointed out several electrophysiological differences in comparison to natural sleep which may apply to anesthetics in general (Chauvette et al., 2011). These studies suggest that while urethane is not identical to natural physiological

states, it is an appropriate controlled model for sleep preserving the synaptic relationships and sleep structure of natural sleep.

1.10 Overview of thesis

In Chapter 2, rhythmic electrical stimulation was applied to frontal regions of the rat cortex with recordings performed using a linear 3-channel array across M1. We found the existence of complex spontaneous propagation dynamics during the SO with stimulation entraining cortical activity and biasing the pattern of these dynamics. In Chapter 3, an identical stimulation protocol was applied to a bilateral VSD imaging preparation in mouse, likewise biasing SO propagation dynamics and entraining VSD activity across the cortex. In both chapters I will discuss the specific propagation trajectories that take place during spontaneous conditions and how they change with the application of stimulation. In Chapter 4, hippocampal linear probe recordings were performed in additional to cortical recordings. The application of rhythmic stimulation entrained hippocampal activity and markedly affected cortico-hippocampal interregional relationships. In Chapter 5, I discuss the results from all three studies in the context of SO-related cognitive function.

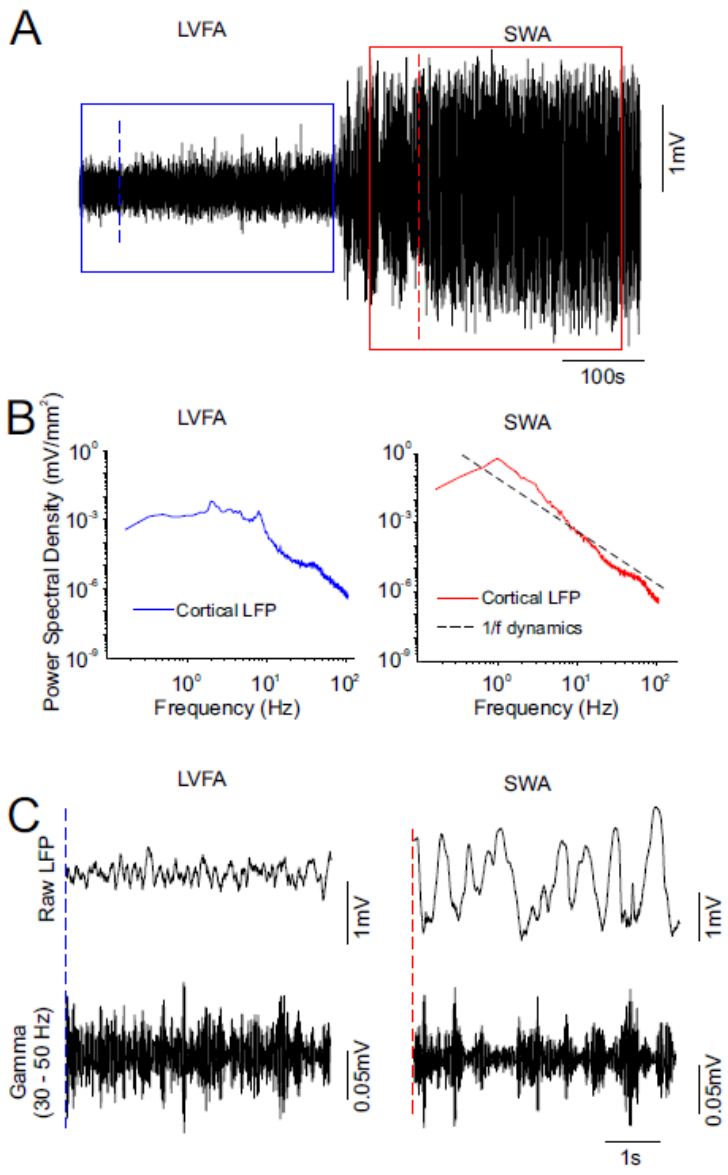

Figure 1.1 Brain state alternations during anesthesia

A. Example cortical trace depth LFP recording in rat showing low-voltage fast activity (LVFA; blue box) alternating to slow-wave activity (SWA; red box). **B.** Power spectra corresponding to time frames outlined with boxes in A. Left power spectrum is for the LVFA (blue) and right is for the SWA (red). Note dramatic deviations from the expected 1/f spectrum (dotted line on right) with peaks at faster frequencies during LVFA and a peak at ~1 Hz during SWA. **C.** Expanded traces for raw data and gamma filtered (30 – 50 Hz) data

starting at the time-points outlined with dotted lines in A (blue for LFA, red for SWA). Note lower amplitude during LVFA and modulation of gamma activity into negative peaks during SWA.

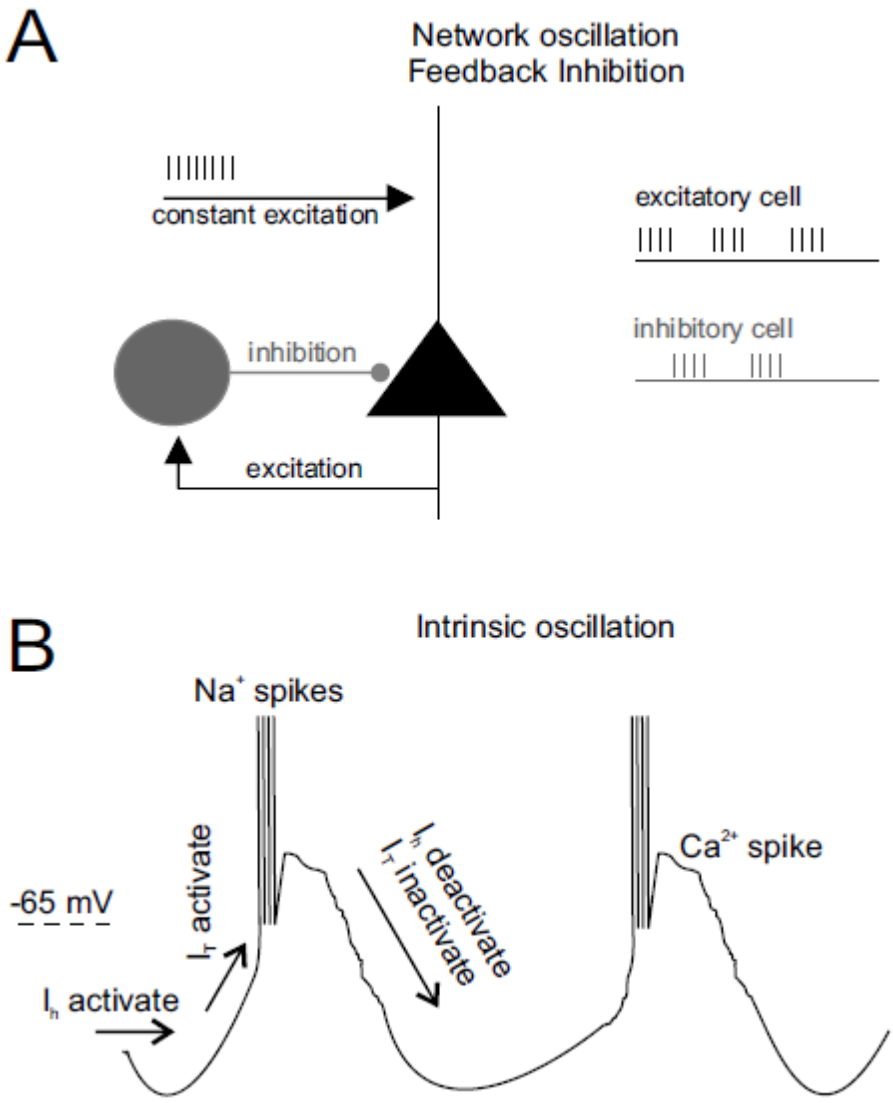

Figure 1.2 Oscillatory neural mechanisms at the network and single cell levels

A. A simplistic model of feedback inhibition. Black triangle represents an excitatory pyramidal neuron receiving constant excitatory input from an external source (e.g. another cell or groups of cells). The pyramidal neuron fires in response to the input and activates an inhibitory cell which in turn inhibits the pyramidal cell. Following inhibition, the pyramidal cell can no longer activate the inhibitory cell and therefore

releases itself from the inhibitory drive allowing the cycle to restart. The oscillatory firing dynamics for both cells is displayed on the left. **B.** Intrinsic oscillation in a thalamocortical (TC) neuron. Hyperpolarization of the cell activates the hyperpolarization-activated channel (I_h) which in turn depolarizes the cell and activated the low-threshold calcium channel (I_T). This initiates a calcium (Ca^{2+}) spike with sodium (Na^+) spikes riding on top. This excitability then deactivated I_h and inactivates I_T allowing the cell to hyperpolarize again and restart the cycle. A is adapted from (Buzsáki, 2006). B is adapted from (McCormick and Pape, 1990). B is a schematic representation, not a real trace recording.

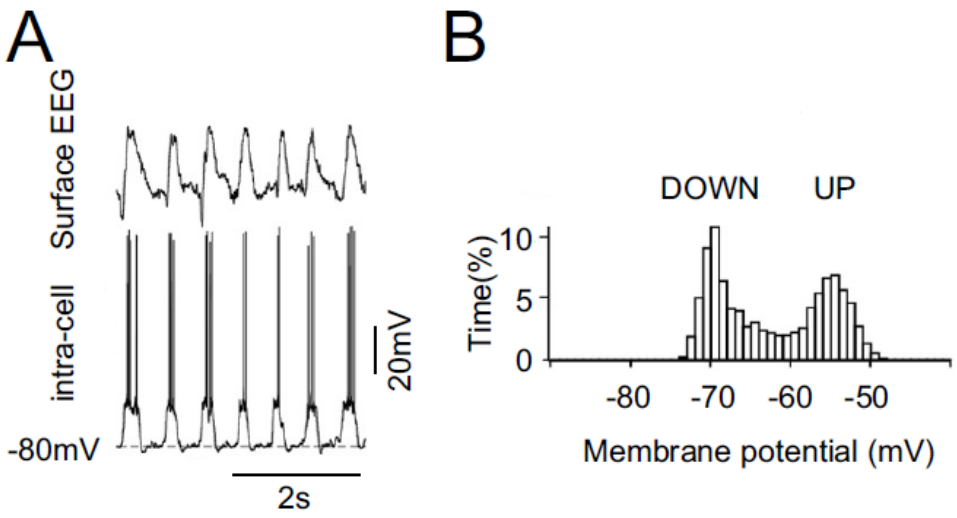

Figure 1.3 UP and DOWN states of the neocortical slow oscillation

A. Example trace of a surface EEG recording from the somatosensory cortex of an anesthetized mouse (top) and a corresponding intracellular recording from the same region (bottom). Note prominent UP and DOWN states of excitability with the intracellular UP states corresponding to the surface EEG positive peaks of the slow oscillation. **B.** Histogram showing the percentage of time a cortical cell spending at various membrane potential levels during the slow oscillation. Note a bimodal distribution that represents UP and DOWN states. Adapted from (Sheroziya and Timofeev, 2015).

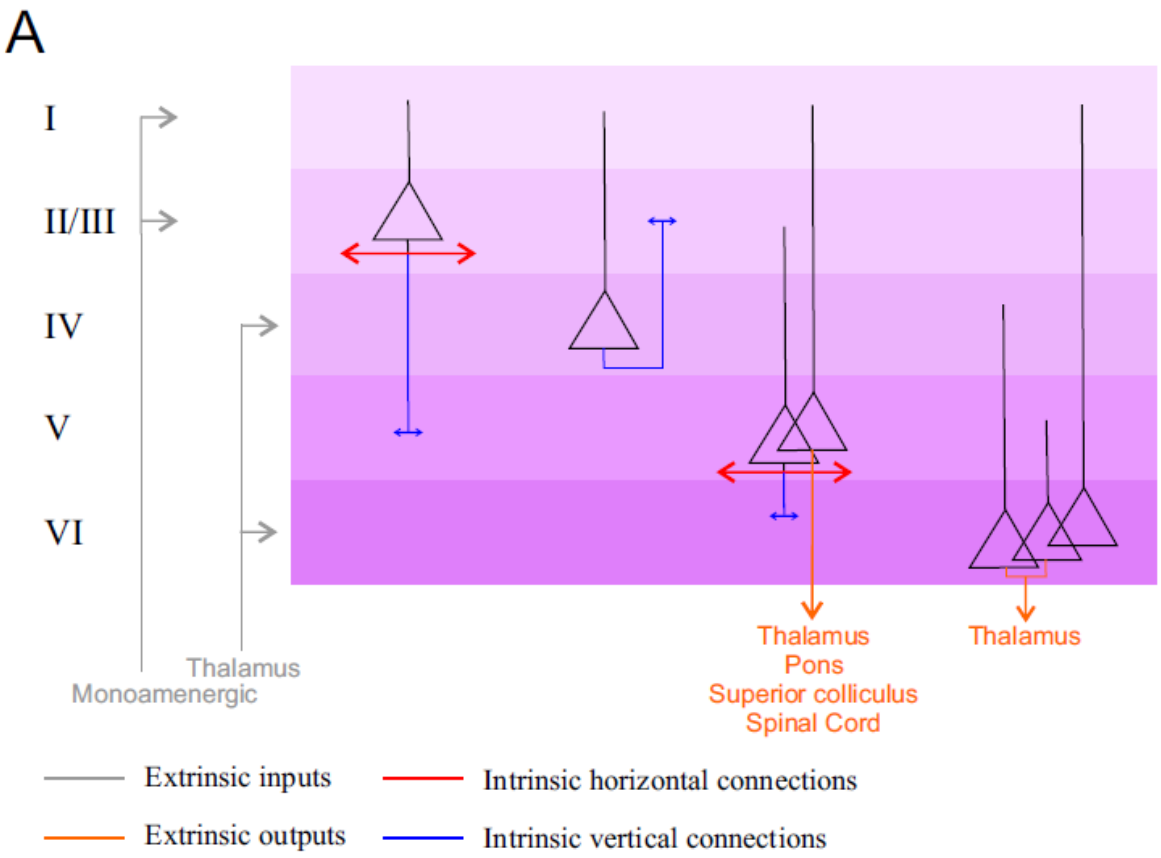

Figure 1.4 Intrinsic and extrinsic cortical connections

A. Simplified schematic representing the intrinsic and extrinsic cortical connections. Pyramidal cells for each cortical layer are represented with triangles and their dendrites are represented with a line extending from the cell body. The dendrites extend to various layers and extra cells within a layer depict the major cell types with different dendritic extensions. The intrinsic connections are depicted in blue for vertical connections (not all possible connections are depicted here) and in red for horizontal connections. The extrinsic afferents (inputs) are depicted in gray and the extrinsic efferents (outputs) are depicted in orange.

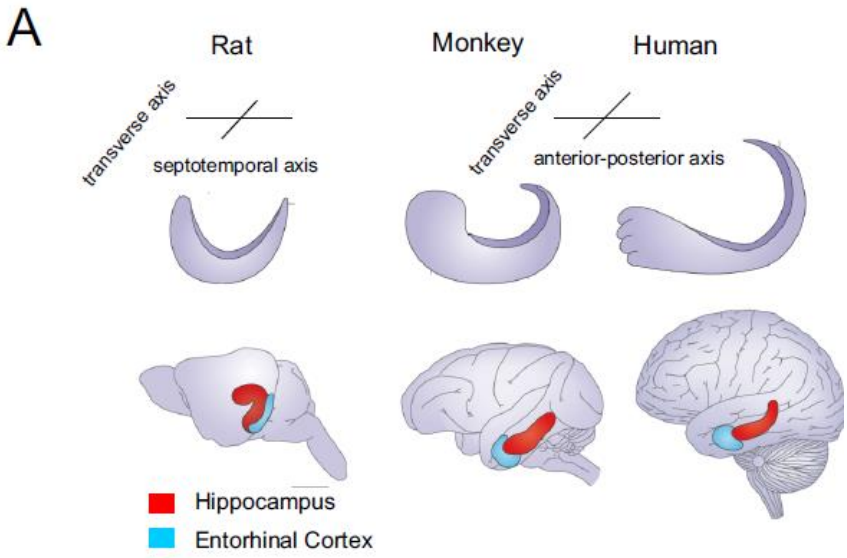
A
Rat
Monkey
Human
transverse axis
septotemporal axis
transverse axis
anterior-posterior axis
Hippocampus
Entorhinal Cortex

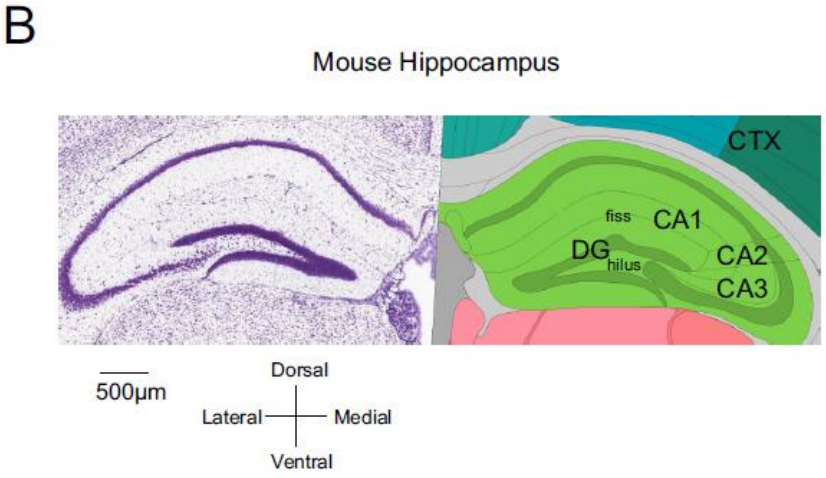
B
Mouse Hippocampus
CTX
fiss
CA1
DG
hilus
CA2
CA3
500µm
Dorsal
Lateral
Medial
Ventral

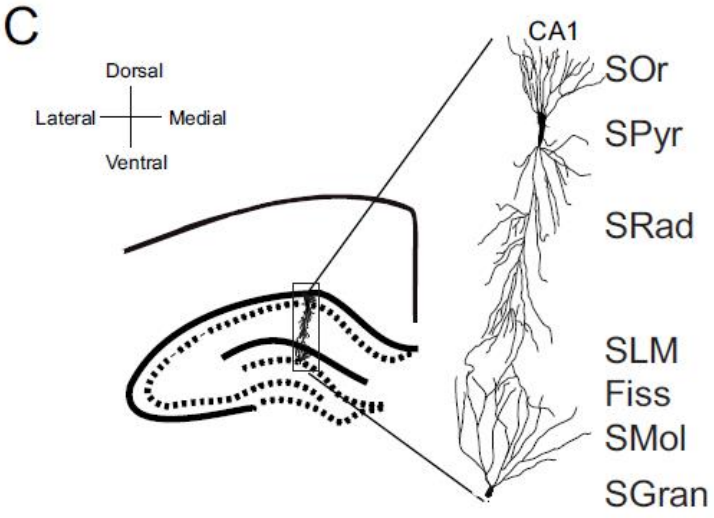
C
Dorsal
Lateral
Medial
Ventral
CA1
SOr
SPyr
SRad
SLM
Fiss
SMol
SGran

Figure 1.5 Hippocampal neuroanatomy

A. Shape and position of the hippocampus (red) and entorhinal cortex (blue) in the rat (left), monkey (middle) and human (right). Legend shows the septotemporal (anterior-posterior in the primates) and transverse axes. **B.** Coronal mouse brain slice showing Nissl stained (left) and region colored and labeled hippocampus (right). **C.** Schematic representation of a transverse rodent hippocampal slice (left) with an expanded cellular layer representation (right) taken from CA1 and the underlying DG. Cellular layers from top to bottom: stratum oriens (SOr), stratum pyramidal (SPyr), stratum radiatum (SRad), stratum lacunosum moleculare (SLM), hippocampal fissure (Fiss), stratum moleculare (SMol) and stratum granulosum (SGran). A is adapted from (Strange et al., 2014). B is adapted from the Allen Mouse Brain Atlas (http://www.brain-map.org/).

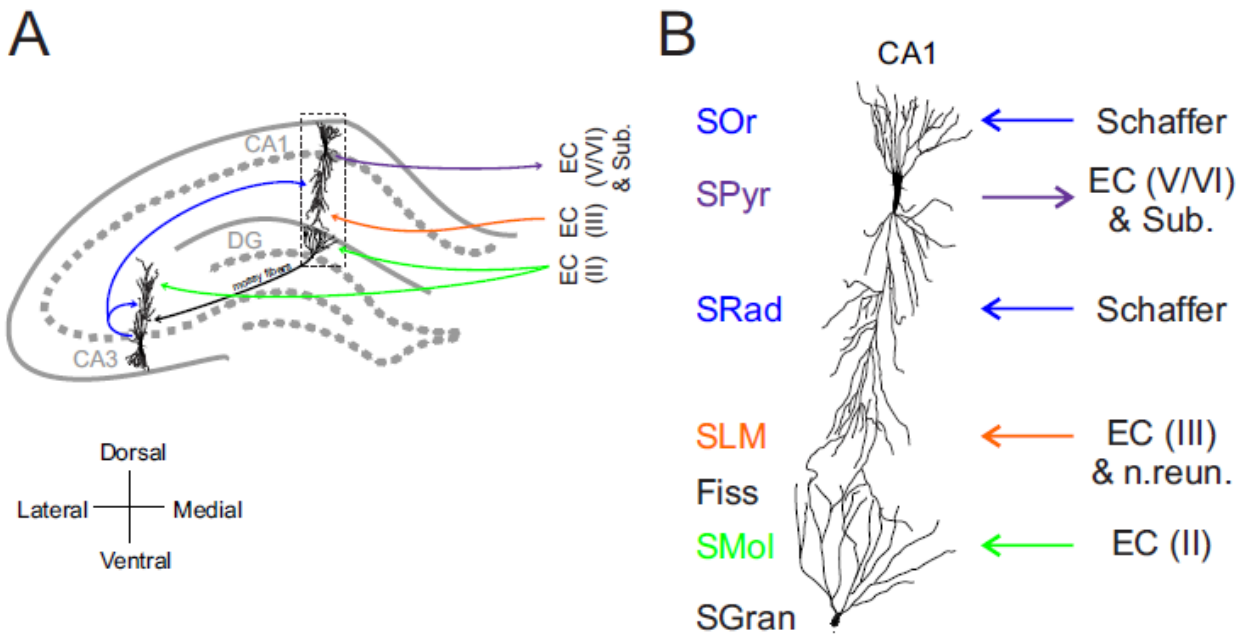

Figure 1.6 Intrinsic and extrinsic hippocampal circuitry

A. Schematic of a rodent hippocampal transverse slice showing the major intrinsic and extrinsic connections (arrows). Depictions of a principal cell is shown for CA1, DG, and CA3. Represented connections are as follows: mossy fiber path from DG to CA3 (black), CA3 recurrent network and schaffer collateral pathway to CA1 (blue), CA1 output pathway to EC and subiculum (purple), EC layer III input path to CA1 (temporoammonic path; orange) and layer II EC perforant pathway to DG and CA3 (green). **B.** Expanded cellular layers from boxed area in A showing the CA1 layers and underlying DG. Input and output pathways are shown for each cellular layer and are color coded as in A. Cellular layers from top to bottom: stratum oriens (SOr), stratum pyramidal (SPyr), stratum radiatum (SRad), stratum lacunosum moleculare (SLM), hippocampal fissure (Fiss), stratum moleculare (SMol) and stratum granulosum (SGran).

2 Spontaneous and electrically modulated spatiotemporal dynamics of the neocortical slow oscillation and associated local fast activity

Authors: Anastasia Greenberg[1] and Clayton T. Dickson[1,2,3]

[1]Centre for Neuroscience, University of Alberta, Edmonton, AB, Canada, T6G 2E1

[2] Department of Psychology, University of Alberta, Edmonton, AB, Canada, T6G 2H7

[3] Department of Physiology, University of Alberta, Edmonton, AB, Canada, T6G 2E9

Acknowledgements: This work was supported by a Natural Science and Engineering Council of Canada (NSERC) grant #249861 to CTD. AG was additionally supported by an NSERC Alexander Graham Bell Graduate Scholarship (CGS M) and an Alberta Innovates Technology Futures Graduate Student Scholarship. We would like to acknowledge Justin Barclay for data collection, Kyle E. Mathewson for helpful data analysis support and advice as well as editorial comments, Jesse Jackson for providing MATLAB code for amplitude-modulation analyses as well as editorial comments, and Tara Whitten and Michelle Yeung for helpful editorial comments.

Published in:

NeuroImage, July 19, 2013

83:782-94

2.1 Abstract

The neocortical slow oscillation (SO; ~ 1 Hz) of non-REM sleep and anesthesia reflects synchronized network activity composed of alternating active and silent (ON/OFF) phases at the local network and cellular level. The SO itself shows self-organized spatiotemporal dynamics as it appears to originate at unique foci on each cycle which then propagates across the cortical surface. During sleep, this rhythm is relevant for neuroplastic processes mediating memory consolidation especially since its enhancement by slow, rhythmic electrical fields improves subsequent recall. However, the neurobiological mechanism by which spontaneous or enhanced SO activity might operate on memory traces is unknown. Here we show a series of original results, using cycle to cycle tracking across multiple neocortical sites in urethane anesthetized rats: The spontaneous spatiotemporal dynamics of the SO are complex, showing interfering propagation patterns in the anterior-to-posterior plane. These patterns compete for expression and tend to alternate following phase resets that take place during the silent OFF phase of the SO. Applying sinusoidal electrical field stimulation to the anterior pole of the cerebral cortex progressively entrained local field, gamma, and multi-unit activity at all sites, while disrupting the coordination of endogenous SO activity. Field stimulation also biased propagation in the anterior-to-posterior direction and more notably, enhanced the long-range gamma synchrony between cortical regions. These results are the first to show that changes to slow wave dynamics cause enhancements in high frequency cortico-cortical communication and provide mechanistic clues into how the SO is relevant for sleep-dependent memory consolidation.

2.2 Introduction

Since the brain is the organ of behavior and consciousness, the function of complex and self-organized activity that occurs during unconscious states such as sleep remains a mystery. Activity during such offline states might be related to the neuroplastic processes underlying the solidification of prior learning episodes during wakefulness through the reactivation of newly-formed neuronal ensembles. The repeated offline "rehearsals" of these ensembles could engender spike-timing dependent solidification of inter-connections amongst participating members (Buzsáki, 1998; Dan and Poo, 2004; Gais and Born, 2004; Marshall and Born, 2007). Interestingly, this very type of offline replay or rehearsal has been shown to occur most prominently during deep non-REM or slow wave sleep (Ji and Wilson, 2007; Luczak et al., 2009; Pavlides and Winson, 1989; Wilson and McNaughton, 1994) and has been directly related to memory consolidation in rats (Ego-Stengel and Wilson, 2010; Girardeau et al., 2009; Ramadan et al., 2009) as well as humans (Rasch et al., 2007).

The signature event of non-REM sleep (and anesthesia) is the large-amplitude (~1 Hz) slow oscillation (SO) that involves synchronized periods of alternating activity and silence (ON/OFF phases) at the neuronal level (Contreras and Steriade, 1995; Steriade et al., 1993d; Timofeev et al., 2001; Volgushev et al., 2006). The slow oscillation is neocortical in origin as demonstrated by its presence and maintenance in isolated cortex (Steriade et al., 1993c; Timofeev and Steriade, 1996) as well as its absence in the thalamus of decorticated animals (Timofeev and Steriade, 1996). The SO provides a temporal window for grouping locally generated, faster rhythms (Buzsáki and Draguhn, 2004) such as gamma activity (Steriade, 2006; Timofeev and Steriade, 1997), thalamocortical spindles (Mölle, 2009; Mölle et al., 2002; Nir et al., 2011; Steriade et al., 1993c), and hippocampal ripples (Grenier et al.,

2001; Mölle, 2009). These faster rhythms have been described as "network ON phases" and their grouping into common temporal frames across the cortical mantle and the hippocampus (Isomura et al., 2006; Wolansky et al., 2006) has been suggested to constitute a platform for brain-wide activity-dependent synaptic plasticity (Dickson, 2010).

Supportive of a role in memory processes, the spatiotemporal dynamics of the SO, which typically appear as traveling waves in the anterior-to-posterior direction (Amzica and Steriade, 1995b; Massimini et al., 2004; Volgushev et al., 2006) are influenced by prior waking experience (Huber et al., 2004; Luczak et al., 2009). Perhaps more convincingly, boosting the SO by slow alternating transcranial electrical field stimulation applied to frontal regions during slow wave sleep improved subsequent mnemonic performance (Marshall et al., 2006). Although electrical field stimulation has been demonstrated to entrain cortical cellular activity in a state-dependent manner (Ozen et al., 2011), its influence on long-range spatiotemporal dynamics of the SO and related local fast activity remain unknown. Given the importance of the SO to memory consolidation, a complete understanding of the spontaneous and electrically-modulated spatiotemporal dynamics of SO expression is paramount.

In the present study we show that the spontaneous SO dynamics under urethane anesthesia are neither random, nor entirely stereotyped, and display competing propagation patterns which surprisingly tend to alternate following phase reset-like events that occur during the silent OFF phase of the SO. Electrical field stimulation entrains activity and biases spatiotemporal SO dynamics in an intensity-dependent fashion while also dramatically enhancing long-range gamma coordination across sites. This fast coupling of neuronal ensembles across widespread brain regions suggests a neurophysiological

mechanism by which SO activity and its modulation could affect offline memory consolidation.

2.3 Methods

2.3.1 Subjects

Spontaneous recordings were obtained from 9 male Sprague Dawley rats with a mean (±SEM) weight of 255 ± 19 g. Field stimulation and recordings were obtained from an additional 5 male Sprague Dawley rats with a mean weight of 281 ± 24 g.

2.3.2 Surgery and implantation

All surgical procedures conformed to the guidelines of the Canadian Council on Animal Care (CCAC) as well as the Society for Neuroscience and were approved by the Biological Sciences Animal Policy and Welfare Committee of the University of Alberta.

Rats were initially anesthetized in a gas chamber with a 4% concentration of isoflurane in 100% 0_2 (Benson Medical Industry Inc., Markham, ON) and then later maintained at 2% administered via nose cone. Rats were implanted with a jugular vein catheter through which urethane (0.8 g/ml) was gradually administered (0.03 – 0.08 ml per minute) to a final anesthetic dose of 1.7 ± .01 g/kg, following cessation of isoflurane delivery. Atropine methyl nitrate (0.05 mg/kg, s.c.) was administered to minimize respiratory complications. Rats were then transferred to a stereotaxic apparatus and body temperature was maintained at 37 °C throughout the experiment via a servo-controlled system which coupled rectal temperature to a heating pad placed under the rat (TR -100, Fine Science Tools, Vancouver, BC). Bipolar Teflon-coated stainless-steel electrodes (125 μm bare diameter; 0.75 – 1.20 mm stagger between electrode tips) were implanted at 3

neocortical sites spaced 3 mm apart in an anterior-to-posterior (AP) linear plane. The respective AP and ML coordinates from bregma were: +3.0, +2.0 mm (site 1); 0.0, +2.0 mm (site 2); and -3.0, +2.0 mm (site 3) (Figure 2.1 A). The longest contact of each pair was targeted just past the deepest neocortical cell layer (approximately at cortical layer VI; -1.4 ± 0.2 mm dorsoventral (DV) to cortical surface). All three sites were located in primary motor cortex (M1; Figure 2.1 A). For 3 of the 9 animals from which spontaneous recordings were collected, we also implanted a fourth electrode along the same anterior-posterior plane, 3 mm posterior to site 3 (from bregma: -6.0 mm AP; +2.0 mm ML) which was located in the visual cortex (V2MM). For the 5 animals that received field stimulation, three Teflon-coated stainless steel microwires (277 μm bare diameter) were lowered to pial surface and implanted in a triangular configuration anterior to the three recording sites, with a central pole located on the midline (+7.0 mm AP and 0.0 mm ML) and two lateral poles more posterior and lateral (+5.0 mm AP; ±3.5 mm ML) (Figure 2.4 A). All recording and stimulating electrodes were secured to the skull using dental acrylic mounted to a jeweler's screw that was fastened in the skull.

2.3.3 Recordings

Spontaneous recordings were wide-bandpass filtered between 0.1 Hz and 10 kHz and amplified at a gain of 1000 using a differential AC amplifier (model 1700; A-M Systems, Sequim, WA). Signals were digitized using an A-D board (Digidata 1322a; Axon Instruments/Molecular Devices, Sunnyvale, CA) and sampled at 1000 Hz (with anti-alias filtering at 500 Hz) for extraction of local field potentials (LFP) and at 10 kHz (with anti-alias filtering at 5 kHz) for extraction of both LFP and multi-unit activity (MUA). Data were

acquired and stored using AxoScope (Axon Instruments/Molecular Devices) on a PC system for later offline analysis. Multiple samples in the same experiment were then analyzed and combined across different epochs of SO activity (Clement et al., 2008; Wolansky et al., 2006).

2.3.4 Field stimulation

Sinusoidal stimulation was applied using an analogue function generator (Hewlett Packard; 3310A) to the three stimulation poles with the two lateral poles receiving opposite polarity stimulation to the central pole (Figure 2.4 A). This configuration was adapted from Ozen et al. (2010) and was intended to create a relatively homogenous electrical field across the frontal pole of the brain. The stimulation generator output was also digitized using the same system as that used for brain signals to obtain stimulation phase and voltage intensity information for later offline analysis.

Control (spontaneous) data was acquired for all stimulation experiments as described previously. Stimulation was then applied at various voltage intensities (defined as peak-to-peak amplitude) ranging from 0.86 to 16.51 V (low = 0.87±0.00 V; n = 4; medium = 11.9±1.20 V; n = 2; high = 16.42±0.10; n = 2). The frequency of stimulation was either 1.25 Hz or 1.67 Hz. These frequencies are faster than the typical SO frequency range (~ 1 Hz) and were chosen for two reasons: 1) to demonstrate phase reset and entrainment to the stimulation frequency and 2) to analyze separately the influences of stimulation on dynamics at the endogenous SO frequency range. Stimulation was applied during SO states (detected visually and later confirmed offline using power spectral density analysis) and the duration of stimulation lasted from 3 to 12 minutes continuously (2 trials per condition) with 1 min

stimulation-free periods between stimulation trials. Multiple samples using the same stimulation parameters within subjects (amplitude and frequency) were analyzed separately and then combined.

At the end of all experiments animals were euthanized with a lethal injection of urethane. Immediately after animals were euthanized, post-mortem recordings were obtained using the same stimulation parameters used previously to obtain channel-specific estimates of stimulation artifact waveform amplitude and shape. These recordings were then used to generate estimates for artifact subtraction (detailed below).

2.3.5 Data analysis

All analyses were performed using a combination of built-in functions and custom written code in MATLAB (MathWorks, Natick, MA). All means are reported as mean ± standard error of the mean. Significance for all statistical tests was defined as $p < .05$ and all *t* tests were performed within-subjects (paired) unless otherwise specified.

2.3.5.1 Stimulus artifact subtraction

Subtraction of the stimulation artifact from the LFP recordings was conducted on a cycle-by-cycle basis using an average estimate of the stimulus artifact obtained during post-mortem recordings (above). A single stimulation cycle was defined as the artifact waveform that was aligned from one negative peak of the sine wave output to the next. For each SO cycle, we estimated the actual amplitude of the online artifact by calculating a raw average LFP using the 5 cycles prior and following the cycle of interest (for a total of 11 cycles). This value, less the standard deviation (SD) of the 11 cycle average, was used to scale the

amplitude of the pure (post-mortem) artifact since the online artifact amplitude represented the largest portion of the raw LFP signal during stimulation. This scaled waveform was then subtracted from the LFP for each cycle by matching the phase of stimulation in both cases (see Figure 2.4 B for example of artifact subtracted trace). To avoid potential distortion to the artifact waveform that may be due to changes in tissue properties and body temperature associated with brain death, we ensured that post-mortem recordings were collected immediately after cessation of brain activity (within 10 seconds; with stimulation lasting 20 sec). Data was discarded for cases in which the LFP amplitude was not reduced to control amplitudes after application of our subtraction algorithm (< 90% reduction relative to post-mortem artifact amplitude). In total, we discarded 3 cases (low stimulation condition in 1 subject and medium stimulation condition in 2 subjects).

2.3.5.2 Spectral analyses

Spectral analyses were performed using Welch's averaged modified periodogram method for power spectral density estimation and coherence (6 sec window; 2 sec overlap) calculated on continuous 60 second epochs of data that were then averaged based on subject and condition. The SO LFP activity was characterized by spectra showing a prominent power spectral density peak between 0.5 and 1.5 Hz and data that did not meet these criteria for control recordings were not analyzed further. Spectral analysis on MUA data was computed in a similar way using a detrended and SD normalized root-mean-square (RMS; 100 ms window) transform of the MUA filtered (750 – 1250 Hz) signal.

For comparing spectral coherence of signals to the stimulation frequency, the coherence value corresponding to the exact stimulation frequency was selected from the

coherence spectrum (1.25/1.67 Hz). To assess the degree of coupling to the stimulation sine wave that is expected by chance, an arbitrary sine wave of the same stimulation frequency was matched to control LFP segments.

2.3.5.3 Phase-amplitude modulation

The cross-frequency coupling of faster frequencies to slower components in the LFP as well as the stimulation frequency was computed by using a modified phase-amplitude coupling procedure (Canolty et al., 2006; Canolty and Knight, 2010; Kramer et al., 2008; Schroeder and Lakatos, 2009). In brief, instantaneous phase (obtained from the Hilbert transform) for low frequency signals was extracted from LFP or stimulation output (i.e., the x-axis of modulation plot; e.g. Figure 2.1 E) by bandpass filtering the raw LFP signal (FIR filter, 512^{nd} order) from 0.5 Hz to 10 Hz in 0.5 Hz steps (width of bandpass) for spontaneous recordings and between 0.1 and 4.1 Hz in 0.2 Hz steps to obtain a higher resolution for stimulation experiments in order to dissociate endogenous SO and stimulation frequencies. For the amplitude component (i.e. the y-axis of modulation plot; e.g. Figure 2.1 E), the LFP was bandpass filtered from 5 Hz to 120 Hz on a base 10 logarithmic scale in log steps of 0.05. For each of these phase signals, an amplitude value was determined from the Hilbert transform and then binned in 10° bins across the phase variable (e.g. Figure 2.1 F). A modulation index (MI; z-axis, adapted from (Kramer et al., 2008)) was computed for each comparison in the total matrix (e.g. Figure 2.1 E) to test whether the average amplitude of the y-axis signal is uniformly distributed across the phase of the x-axis signal. The modulation index is an entropy measure with a value from 0 to 1; 1 indicating all high-frequency amplitude in only one bin of the phase signal, and 0 indicating a completely

uniform distribution of amplitude across all bins of the phase signal. The significance of above average MI values was assessed by shifting the amplitude component in question with respect to the corresponding phase component by a random time value. Values 3 SD ($p \leq .001$, one-tailed) outside the distribution constructed by 200 randomized shifted trials were considered to be significant. To determine mean angles, Rayleigh's circular statistics for individual experiments and Hotelling's test for second order analyses were used (Zar, 1999). The MI values for each experiment were used as the measure of radial consistency (R value; inverse of dispersion). For the amplitude signal, strongest modulation tended to occur in the gamma frequency ranges of 12-25 Hz as well as 56 – 70 Hz. Although the lower bandwidth may represent beta or low gamma ranges, we will refer to it as low gamma throughout the manuscript.

2.3.5.4 Inter-site SO dynamics and propagation

The inter-site dynamics of the SO were analyzed on a cycle-by-cycle basis using Hilbert phase. The Hilbert transform can be used to extract "instantaneous" measures of phase and amplitude of a signal and is considered to be a useful method for tracking changes in phase with high temporal resolution (Freeman et al., 2003; Le Van Quyen and Bragin, 2007). Furthermore, the more common signal analysis methods using the Fourier and/or the wavelet transform can be considered mathematically equivalent to the Hilbert transform when setting similar parameters for the three methods (Bruns, 2004). In brief, LFP signals were bandpass filtered between 0.5 Hz and 1.9 Hz using a 2^{nd} order Butterworth (zero phase distortion) filter before extracting the instantaneous phase angle from the Hilbert transform. One cycle corresponded to a change in the Hilbert phase angle from $-\pi$ to π (see figure 2.2

A). The onset of a cycle for a particular channel was defined as the time at which the Hilbert phase flipped from positive to negative π, which corresponded to the negative peak of the filtered LFP signal (see figure 2.2 A for an example). A channel was designated as an "origin" channel if the cycle onset began for that channel before all others (within a window of at least 300 ms prior). A propagating wave was inferred if the remaining channel signals had cycle onset delays of ≥ 1 ms and < 300 ms relative to the onset of the origin. These detection criteria ensured that propagation was defined on a single cycle basis. By ordering the cycle onset delays of the other channels, a spatiotemporal propagation pattern for each SO cycle could be inferred. Propagation velocity was calculated as the time difference of cycle onset between channel pairs divided by the distance between channel pairs (3 mm).

2.3.5.5 Ongoing phase adjustments and alternations between propagation patterns

In order to understand the alternations between various propagation patterns, we assessed relative changes in phase between pairs of channels that were responsible for propagation pattern onsets (Figure 2.3 A). We used the wrapped phase angle of the Hilbert transform and detected crossover points between the given channels (see Figure 2.3 A). These crossover points reflect phase advances/delays in the ongoing oscillation which result in a reversal of the lead/lag relationship across a pair of channels, and thus a switch in propagation pattern.

To determine whether phase crossovers tended to occur during specific phases of the ongoing SO, we grouped these events based on their occurrence within each channel's respective SO phase (20º bins; see Figure 2.3 B). The non-uniformity of the distributions across the SO cycle was determined using Rayleigh's circular statistics for individual

experiments and Hotelling's second order test for combining across experiments (Zar, 1999). Distributions that appeared bimodal were analyzed using a doubling of angles procedure (Zar, 1999) . Briefly, angles were collapsed along the 180º axis (e.g., 0º bin combined with 180 º bin; 40º bin combined with 220º bin) and redistributed between 0º and 360º (e.g., for a bimodal distribution with a mean angle of 180°, the individual mean angles are 90° and 270°).

Long-range gamma synchrony. We assessed whether long-range gamma synchrony was influenced by field stimulation. Continuous wavelet coherence was performed across channel pairs using the Morlet wavelet (5 cycle width; 150 and 60 second window for low and high gamma respectively). Coherence values were averaged across scales corresponding to the low (12 – 25 Hz) and high (56 – 70 Hz) frequency ranges of gamma. To extract coherence corresponding to ON and OFF phases of the SO or stimulation, we selected coherence values based on gamma RMS for each range that displayed threshold values ≥ 97.5^{th} percentile and ≤ 2.5^{th} percentile of the amplitude distribution, respectively. We also extracted coherence for ON and OFF phases based on the ≤ 2.5^{th} and ≥ 97.5^{th} percentile of the SO filtered LFP values. Visual inspection revealed that both methods selected coherence values that corresponded to the ON phase in the LFP. Wavelet coherence values were averaged within these windows to obtain channel-pair and phase-specific (ON vs. OFF) measures of long-range coherence for low and high gamma.

2.4 Results

2.4.1 The neocortical slow oscillation under urethane is broadly coherent and coupled to local gamma and multi-unit activity

As previously described (Clement et al., 2008; Wolansky et al., 2006), local field potential recordings in our urethane-anesthetized rats showed spontaneous alternations of state resembling those apparent during non-REM and REM sleep. Non-REM-like states were characterized by the SO; a high-amplitude, slow (~1 Hz) rhythm, at all cortical sites (Figure 2.1 B). Across experiments, the SO state lasted a minimum of 2.7 minutes to a maximum of 17.5 minutes (average 13.2±1.1 minutes). Spectral analyses revealed a large power spectral density peak (0.29 ± 0.07 mV^2) in the SO frequency band (0.97 ± 0.05 Hz; Figure 2.1 C, top left) that was highly coherent across all electrode pairs (0.85 – 0.91; Figure 2.1 C, bottom left and right). In the subset of experiments that included a fourth electrode in a different functional region (V2) coherence across channel pairs decreased for all comparisons involving this site, even for comparable distances to the other channel pair comparisons (3 mm distance: 095 ± 0.02 within motor cortex vs. 0.88 ± 0.05 across motor to visual; 6 mm distance: 0.94 ± 0.02 within motor cortex vs. 0.85 ± 0.06 across motor to visual; data not shown), suggesting some independence across functionally defined cortical regions.

As previously shown (Chauvette et al., 2010; Contreras et al., 1996b; Timofeev and Steriade, 1996), faster components of the LFP (gamma and MUA) tended to occur during the peak negativity of the raw SO recordings. High gamma activity (56 – 70 Hz) was strongly modulated by the phase of local SO across all channels (mean angles: 258.9 – 267.5°; $p < .001$ for all; Figure 2.1 D, E, F - left), and a similar pattern of results was obtained for low gamma (12 – 25 Hz) activity (mean angles: 236.9 - 260.4°; $p < .001$ for all;

data not shown) as well as MUA (750 – 1250 Hz; mean angles: 257.7 - 269.1°; $p < .001$ for all; Figure 2.1 D, F – right, G). These results show that under our conditions, like those of natural sleep, the SO is broadly coherent across widespread cortical sites, although showing some intra-areal specificity, and groups faster frequency activity into its ON (local negative) phase.

2.4.2 The slow oscillation appears as a dynamic traveling wave

We were interested in tracking the spatiotemporal propagation dynamics of SO on a continuous cycle to cycle basis. We achieved this by computing the Hilbert transform on SO filtered traces (0.5 -1.9 Hz) and extracting continuous phase information in order to precisely determine relative timing relationships across cortical sites (Figure 2.2 A). The minimum number of SO cycles detected within experiments was 544 and the maximum was 1088 (approximately 1 cycle/sec for every experiment), with the large majority of cycles affecting all three electrode sites (90.28 ± 0.01 %). Figure 2.2 C shows the histogram of all possible propagation patterns (6 possible patterns given 3 electrodes) which was non-uniformly distributed (χ^2 goodness-of-fit test; $p < .001$ for all experiments). There were two propagation patterns that appeared significantly above chance: the anterior-to-posterior (A-P) pattern (pattern 1-2-3; significant in 7 out of 9 experiments; $p < .001$) and the opposite posterior-to-anterior (P-A) pattern (pattern 3-2-1; significant in 8 out of 9 experiments; $p < .001$) (Figure 2.2 C). The average velocity of propagation collapsed across the major propagation patterns was 89.2±4.5 μm/ms (0.089±0.004 m/s) and did not differ between these two major patterns (paired t-test, $p > .05$ for all experiments).

Given that our recordings were made within the broad confines of the motor cortex, we assessed if the same dynamics of spontaneous SO activity existed beyond this region. In the cases in which we made an additional placement (site 4), located on the same anterior-posterior axis but in a different functional region of the cortex (occipital/visual), we considered whether propagation dynamics were region-specific or whether these dynamics were more global, traversing across functional regions. We assessed what percentage of the propagation patterns in the rostral-caudal axis traversed across all 4 electrode sites. For the anterior-to-posterior propagation pattern, only 53 ± 8 % of cases involved electrode 4 in a linear pattern after traveling from site 1 to 3 (compared to 98 ± 5% of cases involving channel 3 after travelling from site 1 to 2, $p < .05$). Likewise, for the posterior-to-anterior pattern, only 43 ± 14 % of cycles were initiated at site 4 (the most posterior) and traveled linearly through sites 3 to 1 (compared to 97 ± 6% of cases involving channel 3 after travelling from site 2 to 1, $p < .05$). Therefore, these findings along with our finding of lower SO coherence across sites involving this fourth site located in a different functional region, suggest that SO propagation dynamics appear to some extend region specific and highlight the highly local property of SO dynamics that has been recently noted by others (Huber et al., 2006; Huber et al., 2004; Nir et al., 2011; Vyazovskiy et al., 2011) .

2.4.3 Major propagation patterns repeat

Given that in most (6 out of 9) experiments both anterior-to-posterior (A-P) and posterior-to-anterior (P-A) directional patterns occurred with probabilities significantly above chance, we examined the ongoing interactive expression of these opposing patterns. We assessed whether the appearance of one pattern predicted the subsequent occurrence of

any other. To do this, we computed a ratio of observed to expected patterns for each cycle following the occurrence of either major pattern (Figure 2.2 D). This showed that the exact same pattern was significantly more likely to re-occur on the subsequent cycle (A-P followed by A-P: mean ratio = 1.18 ± 0.02; $p < .01$; Figure 2.2 D – left; P-A followed by P-A: mean ratio = 1.10 ± 0.04, $p < .04$; Figure 2 D - right), whereas the opposing pattern was significantly less likely to occur on the subsequent cycle (A-P followed by P-A: mean ratio = 0.84 ± 0.06; $p < .05$; Figure 2.2 D – left. P-A followed by A-P: mean ratio = 0.90 ± 0.04, $p < .04$l Figure 2.2 D - right). The likelihood of occurrence of any of the other possible patterns was not significantly influenced on subsequent cycles ($p > .05$; Figure 2.2 D). These results suggest that the particular directional propagation of a slow wave biases the occurrence of a similar propagation direction on the next cycle and inhibits the expression of the opposing directional propagation pattern. Thus, we show for the first time that opposing propagation patterns are mutually exclusive and likely antagonistic.

By computing an inter-event-interval histogram for each major propagation pattern we assessed whether the bias for major pattern repetition tended to occur in pairs or larger clusters. For both the A-P and P-A patterns, the only interval occurring above chance was at 1 second (Figure 2.2 E; A-P: all experiments; P-A: 7 out of 8 experiments). This suggests that directional pattern repetition tended to occur on just the subsequent cycle, and was not a factor in lengthier effects.

2.4.4 Propagation pattern alternations tend to occur during the OFF phase of the slow oscillation

Our observation of alternating and competing propagation patterns suggested that phase adjustments or resets across sites are important for determining such ongoing pattern alternations. We assessed changes of relative phase across sites that would be directly relevant for altered propagation patterns. Such a characteristic was the phenomenon of SO phase crossover, where the relative Hilbert phase reversed its lead/lag relationship across a pair of channels (Figure 2.3 A). Such crossover events reflect a phase reset in which the SO cycle has been advanced or delayed and specifically result in a switch between propagation patterns.

Detection of phase crossovers for the most anterior and posterior sites (channels 1 and 3, respectively) indicated a reversal of SO propagation in this plane (Figure 2.3 A). Interestingly, both anterior-to-posterior (ANT-POST; 18.55±0.67 crossovers/min; reflecting a switch from the A-P pattern to the P-A pattern) and posterior-to-anterior (POST-ANT; 18.93±0.82 crossovers/min; reflecting a switch from the P-A pattern to the A-P pattern) phase crossovers (Figure 2.3 A – left and right panels, respectively) tended to occur at or near the middle of the OFF phase (i.e., at the positive peak of the LFP; ANT-POST: mean angle = 42.3°, $p < .01$; POST-ANT: mean angle = 74.9°, $p < .01$; Figure 2.3 C left and right respectively). These findings suggest, for the first time, that alternations between propagation patterns are manifested, paradoxically, during the silent OFF phase of the SO.

2.4.5 Field stimulation entrains local field and multi-unit activity

Our spontaneous recordings revealed complex spatiotemporal propagation dynamics of the SO under urethane anesthesia. Our next major aim was to determine what influence, if any, sinusoidal electrical field stimulation had on these dynamics (Figure 2.4 A). We carefully evaluated our artifact removal algorithm by ensuring that residual LFP traces had no evidence of stimulation artifact and that average amplitudes were consistent with limits expressed before and after stimulation was delivered (Figure 2.4 B). The length of data used for analysis in each condition ranged between 5.8 – 13.8 minutes (10.73 ± 8.77 min) for control conditions, 4.2 – 8.9 minutes (7.46 ± 1.03 min) for low stimulation conditions, 5.4 – 7.0 minutes (6.23 ± 0.80 min) for medium stimulation conditions, and 4.2 – 8.9 minutes (6.55 ± 2.38 min) for high stimulation conditions.

Figure 2.4 C shows an example LFP trace as well as corresponding MUA obtained during the high stimulation condition in a single experiment. It can be noted that on every cycle, the MUA bursts as well as the associated positive peaks of the multiunit RMS were tightly locked to the positive peaks of the stimulation sine wave. Furthermore, the negative deflections (ON phase) of the artifact subtracted LFP were also similarly locked to the positive component of the stimulation (and MUA activity; Figure 2.4 C, F). This suggested that field stimulation entrained both LFP and cellular activity as has been shown previously (Ozen et al., 2010).

Spectral analyses revealed a prominent peak at SO frequency during control and low stimulation conditions for both the LFP (control: 0.87 – 1.0 Hz, low stim: 0.88 – 1.0 Hz for all channels; Figure 2.4 D - top) and multiunit RMS (control: 0.93 – 1.17 Hz, low stim: 1.0 – 1.21 Hz for all channels; Figure 2.4 D - bottom). For both medium and high stimulation

intensities, spectral peaks for both the LFP and multiunit RMS signals for all channels corresponded to the exact stimulation frequencies used in each experiment (1.25/1.67 Hz), suggesting strong and consistent entrainment across distance (see Figure 2.4 D for example spectra for one channel). Furthermore, in all cases, there was also a second spectral peak at all recording sites in both the LFP and multiunit RMS at exactly double the stimulation frequency (2.5/3.33 Hz; Figure 2.4 D). This frequency doubling effect has been found in previous studies using transcranial electrical stimulation during slow-wave sleep in humans (Marshall et al., 2006) and during slow-wave states in rats (Ozen et al., 2010). It is likely that the arrangement of opposing polarities across stimulation sites has a more complex and non-homogenous influence in terms of the electrical field evoked.

To assess the degree of entrainment across sites to the stimulation, coherence measures were taken between channel pairs as well as between each channel in comparison to the actual applied sine wave for both the LFP and multiunit RMS signals. For coherence with the stimulation sine wave, there was a positive linear association between stimulation intensity and coherence for all channels in both the LFP as well the multiunit RMS signals (Figure 2.4 E - left). Interestingly, stimulation intensity was negatively associated with coherence across all channel pairs at the endogenous SO frequency (0.83 – 1.0 Hz; selected from cross-spectral peaks) for the LFP signal (Figure 2.4 E – top right). Although no significant relationship was observed between stimulation intensity and coherence at the SO frequency range for the multiunit RMS signals (Figure 2.4 - E bottom right), there was certainly a trend for coherence to drop at endogenous SO frequencies as a function of stimulus intensities in individual experiments. In general, these results suggest that as stimulation intensity was increased, so was entrainment of local field and cellular activity to

the stimulation sine wave, while coherence between regions at the endogenous SO frequency was disrupted.

2.4.6 Field stimulation biases propagation dynamics

Since electrical field stimulation entrained LFP and MUA at each site (as previously shown (Ozen et al., 2010)), we assessed (for the first time) whether it altered or biased the inter-site SO relationships as reflected in the distribution of propagation patterns. During stimulation trials, the number of SO cycles detected across experiments varied between 379 - 923 cycles during control, 271 - 579 cycles during low stimulation, 434 - 492 cycles during medium stimulation, and 243 - 760 cycles during high stimulation. We confirmed that the distribution of propagation patterns during control conditions was highly similar to that obtained previously (c.f. Figs 2.2 C and 6 A). As before, there were two major propagation patterns: the anterior-to-posterior and the posterior-to-anterior pattern (A-P: $p < .001$ for all experiments; P-A: $p < .001$ in 4 out of 5 experiments; Figure 2.5 A). The anterior-to-posterior pattern increased in frequency relative to control for most low stimulation intensity conditions (based on standardized residuals; $p < .05$ for 3 out of 4 experiments) and all medium and high stimulation intensity conditions ($p < .001$ for all; Figure 2.5 C, D). The posterior-to-anterior pattern showed either no change in frequency or a significant decrease in frequency relative to control for all stimulation conditions (3 out of 4 low stimulation experiments; all medium and high experiments; Figure 2.5 C). Furthermore, the degree of increase in frequency of the anterior-to-posterior pattern was positively related to the intensity of stimulation ($R^2 = 0.53$, $p < .03$, one-tailed, Figure 2.5 D).

Next, we assessed whether field stimulation influenced the clustering dynamics of propagation patterns that were observed during spontaneous recordings. The inter-event-interval histogram for the anterior-to-posterior pattern was computed using a bin width that was a natural divisor of the stimulation period (119.2 ms for 1.67 Hz stimulation and 160 ms

for 1.25 Hz stimulation given a 1 kHz sampling rate) in order to detect possible temporal entrainment of this enhanced propagation pattern. For the control condition, similar to spontaneous recordings, there was a peak in the inter-event-interval histogram corresponding to the 1 second (bin center = 1.02 ± 0.12), suggesting a tendency of the anterior-to-posterior pattern to re-occur on the subsequent cycle (c.f. Figs 2.2 E and 2.6 B). For the low stimulation condition, there was no clear peak in the histogram for any experiment (Figure 5 B). For the medium and most robustly for the high stimulation conditions, peaks in the histogram appeared to re-occur at intervals corresponding to the precise stimulation periods used (e.g., every 600 ms for the 1.67 Hz stimulation; Figure 2.5 B). This shows that the occurrence of the anterior-to-posterior propagation pattern was systematically entrained to the stimulation frequency, corresponding with the increasing appearance of this propagation pattern with increasing stimulation intensity.

Unexpectedly**,** the velocity of propagation was also influenced by field stimulation, with increasing intensity of stimulation associated with a linear decrease in velocity (R^2 = 0.83, $p < .001$; Figure 2.5 E). This result may be due to an interference effect of the OFF phase of the endogenous SO, thereby preventing an efficient ON state initiation or a mismatch between neuronal resonance properties and our stimulation frequencies. These results indicate that this stimulation-related activity is likely not the same as normal propagating SO and that there is some discrepancy between exogenous and endogenously initiated SO mechanisms.

2.4.7 Field stimulation disrupts ongoing phase crossovers between channels

Given that field stimulation biased propagation patterns, we hypothesized that ongoing phase crossovers, which are critical for propagation pattern alternations, would be affected as well. We found that crossovers were disrupted by field stimulation and with higher intensity stimulation, completely eliminated. Low intensity stimulation showed similar numbers of phase crossovers relative to control conditions ($p > .05$), while the medium stimulation condition showed a non-significant reduction in such phase modulations. High intensity stimulation reduced the phase crossovers by 73% (combined ANT-POST and POST-ANT = 4.48 crossovers/min versus 16.68 crossovers/min).

Therefore, increasing intensity of field stimulation appears to progressively abolish the occurrence of phase crossovers. During control conditions, ongoing phase crossovers are characteristic of dynamically occurring resets of SO activity that are important for mediating alternations between propagation patterns. However, during field stimulation, these phase modulations are disrupted (or eliminated) due to the highly stereotyped and consistent anterior-to-posterior propagation pattern produced by the stimulation itself.

2.4.8 Field stimulation modulates gamma and multi-unit amplitude while disrupting endogenous slow oscillation modulation

Given that field stimulation entrained low frequency LFP and MUA and biased the direction of SO propagation, we also assessed the influence of field stimulation on cross-frequency relationships. We examined the low (12 – 25 Hz) and high (56 – 70 Hz) gamma bandwidths as well as MUA (750 – 1250 Hz) amplitude modulation by the phase of the endogenous SO as well as the phase of the stimulation sine wave. As previously shown

(Figure 2.1 F), amplitude-phase modulation plots computed for control LFP recordings revealed the strongest degree of amplitude modulation based on the phase of the SO (0.7 – 1.1 Hz) for the low gamma frequency range of 12 – 25 Hz as well as the high gamma frequency range of 56 - 70 Hz (Figure 2.6 A - left). With increasing stimulation intensity, both low and high gamma as well as MUA amplitude coupling to the SO phase was severely attenuated, while the amplitude coupling of these faster frequencies to the stimulus waveform increased (Figure 2.6).

During the baseline and low stimulation condition there was strong phase modulation of fast frequency activity (low gamma, high gamma and MUA) to the endogenous SO frequency (0.7 – 1.1 Hz) across all channels with a phase preference close to the negative peak (ON phase) of the SO (Table 2.1; Figure 2.6 A). In contrast and as expected, there was no fast frequency amplitude modulation by the phase of stimulation frequency for any channel during these conditions (Table 2.1; Figure 2.6 B).

For the medium and high stimulation conditions, the amplitude – SO phase modulation for all activity was disrupted at the most frontal location (channel 1; Table 2.1; Figure 2.6 A) but was still significant at the middle (channel 2) and most posterior (channel 3) sites for low and high gamma (except for low gamma for the high stimulation condition which showed disruption at all sites; Table 2.1). The coupling of MUA to SO remained significant only for channel 2 (Table 2.1). In contrast to control and low stimulation conditions, there was prominent phase modulation to the frequency of stimulation which appeared bimodal, suggesting that gamma and MUA amplitude was modulated at double the stimulus frequency for both medium and high stimulation conditions (analyses were performed on doubled angles; Table 2.1). The mean angles for low gamma were close to the

negative-to-positive zero crossing at the doubled frequency suggesting phase preferences at both negative-to-positive and positive-to-negative zero crossings of the actual stimulation sine wave (Table 2.1). For high gamma and MUA, mean doubled angles for all channels were located close to the positive-to-negative zero crossing suggesting modulation at both the positive and negative peaks of the actual stimulation sine wave (Table 2.1; high gamma shown in Figure 2.6 B).

These results suggest that as stimulation intensity increases, there was a progressive disruption of low gamma, high gamma, and MUA amplitude modulation by the endogenous SO, while these faster frequencies were increasingly modulated by the phase of stimulation. Regression analyses confirmed these linear relationships by showing a negative association between stimulation intensity and modulation to the endogenous SO (based on MI values) for low gamma across all channels ($R^2 = 0.38 – 0.44$, $p < .03$ for all; Figure 2.6 C - left), as well as for high gamma for the most frontal and middle sites (channels 1 and 2; $R^2 = 0.56 – 0.61$, $p < .01$; Figure 2.6 C - left) but not for the furthest channel (channel 3; $p > .05$). For MUA, the regression was not significant for any channel ($p > .05$), but the negative association between stimulation intensity and amplitude – SO modulation was still apparent in the slope of the regression line (Figure 2.6 C – left).

For the association between stimulation intensity and modulation to the phase of stimulation, there was a significant positive association for low gamma across all channels ($R^2 = 0.74 – 0.92$, $p < .001$ for all; Figure 2.6 C - right), as well as high gamma for the most frontal and posterior sites (channels 1 and 3; $R^2 = 0.35 – 0.76$, $p < .03$; Figure 2.6 C - right) but not for the middle site (channel 2; $p > .05$). For MUA, the positive relationship between stimulation intensity and modulation by the stimulation phase was significant for all

channels (R^2 = 0.36 – 0.53, $p < .04$ for all; Figure 2.6 C - right). Overall, these results are the first to separately examine the influence of field stimulation on the modulation of faster frequencies by both the endogenous slow LFP and the stimulation phases. We show that field stimulation entrained faster frequency activity at the expense of severe disruptions to the endogenous SO dynamics.

2.4.9 Field stimulation enhances long-range synchronization of low and high gamma

Given that field stimulation entrained low and high gamma while disrupting gamma modulation to the endogenous SO, we assessed the influence of field stimulation on the long-range coordination of both low and high gamma. Figure 2.7 A shows an example of high gamma traces for control (top) and high stimulation (bottom) conditions across the phase of SO (black) and stimulation (cyan) waves respectively. For the control condition, stronger long-range gamma coherence was apparent for the ON in comparison to the OFF phase of the SO; while during the high stimulation condition there was a dramatic enhancement in long-range gamma coherence for both ON and OFF periods of the stimulation phase, suggesting that slow field stimulation enhanced long-range network communication at fast frequencies.

During control and low stimulation recordings, there was moderate low and high frequency gamma coherence which was stronger for ON than for OFF periods (*t* tests, $p < .05$ for all channel pairs for low and high gamma for both conditions; Figure 2.7 A - top, B) which fell off with increased distance between recording sites (3 mm distance for channels 1-2 and 2-3 vs. 6 mm distance for channels 1-3, $p < .05$; Figure 2.7 B). For the medium stimulation condition, there was an increase in low and high gamma coherence across all

channel pairs for both ON periods as well as OFF periods (Figure 2.7 B), although coherence was still stronger for the ON periods (*t* tests, $p < .05$ for all channel pairs). For the high stimulation condition, results were similar to the medium condition, but showed more dramatic increases in coherence across all channels pairs. Coherence values were particularly robust for the ON periods, with some values reaching close to perfect coherence (Figure 2.7 A – inset and bottom traces, B – top). Therefore, for control and low intensity stimulation conditions, there was moderate long-range gamma coupling restricted to the ON periods, as expected. For medium and high stimulation conditions, there was an enhancement in gamma coherence for both ON and OFF periods in comparison to control conditions.

Regression analyses revealed that the increase in ON phase coherence was positively associated with increased stimulation intensity for all channel pairs for both low gamma (Figure 2.7 B – top left) and high gamma (Figure 2.7 B – top right) bands. For the OFF phase, stimulation intensity was similarly positively associated with increase in coherence across all channel pairs for both low gamma (Figure 2.7 B – bottom left) and high gamma (Figure 2.7 B - bottom right). Furthermore, the increases in low and high gamma coherence could not be explained by increases in gamma power (based on cross-spectral power) since the variance in power could only explain up to 10% (across experiments) of the variance in coherence relative to control conditions. These results causally demonstrate for the first time that slow field stimulation can act to dramatically enhance long-range network communication of fast gamma frequencies, a function that may be relevant for spike-time-dependent plasticity mechanisms (Bi and Poo, 1998; Dan and Poo, 2004; Sejnowski and Destexhe, 2000; Sejnowski and Paulsen, 2006).

2.5 Discussion

Our results demonstrated that spontaneous SO activity under urethane anesthesia has complex propagation dynamics that can be manipulated and shaped by electrical field stimulation. We showed that the SO acts like a traveling wave mainly in the rostral-caudal plane as has been shown previously (Amzica and Steriade, 1995b; Massimini et al., 2004; Nir et al., 2011; Volgushev et al., 2006), and extend this work by demonstrating opposing directional propagation patterns which alternate and appear to compete for expression. We also demonstrated that the phase resets and adjustments across sites that are required for the switching of propagation directions tend to occur during the OFF phase of SO. These propagation dynamics were altered monotonically by applying increasing intensities of sinusoidal electrical field stimulation at frontal regions. Perhaps most importantly for the enhancement of memory consolidation with this type of stimulation, we provide the first evidence showing that slow sinusoidal field stimulation enhanced inter-site gamma frequency coupling, revealing the improved fast coordination of neuronal ensembles across wide-spread cortical regions. These data unveil the complex dynamics of slow, sleep-related oscillatory forebrain activity and the influence of electrical field stimulation on SO and gamma coupling that can be used to test the role of spontaneous non-REM activity states in unconscious neural processes.

2.5.1 Complex spontaneous propagation dynamics under urethane anesthesia

We examined the spatiotemporal propagation dynamics of SO using instantaneous measures of phase across all sites. As with prior work, our results were most parsimoniously

consistent with the interpretation of the SO as travelling or propagating waves (Amzica and Steriade, 1995a; Massimini et al., 2004). The velocity of propagation (89.2±4.5 μm/ms) that we determined based on our continuous wave-by-wave analysis is within the range of previous studies using rats (Fucke et al., 2012; Vyazovskiy et al., 2009). Our additional finding that each instance of the slow oscillation can be composed of different initiation sites and directions is reasonably consistent with previous findings in human (Massimini et al., 2004) and is highly consistent for rodent (Mohajerani et al., 2010) and cat (Amzica and Steriade, 1995a; Volgushev et al., 2006) studies. Although dynamic, we also found that the ongoing inter-site relationships of the SO were partially predictable. In particular, we showed that slow waves are not initiated and propagated randomly on every cycle contrary to previous interpretations (Massimini et al., 2004). The occurrence of a given directional pattern predicted its own re-occurrence on the subsequent cycle and also predicted the reduced likelihood of its opposing pattern, suggesting that these patterns are mutually exclusive and likely competitive. These results highlight that urethane anesthesia does not only display dynamic alternations across states that resemble natural sleep (Wolansky et al., 2006), but also shows non-stereotyped and complex interactions within the SO state itself and further support urethane as a good model for studying sleep-like neural activity. Nevertheless, some differences in SO dynamics between natural sleep and urethane are expected, and future work should confirm these findings under natural sleep conditions.

2.5.2 Importance of the OFF phase of the slow oscillation for ongoing phase adjustments and propagation pattern alternations

Perhaps somewhat paradoxically, we found that the occurrence of SO inter-site phase reversals (or phase crossovers, that reflect propagation pattern switches), tended to occur during the OFF phase. Given that the OFF phase has traditionally been regarded as a passive state associated with large-scale neuronal silence caused by disfacilitation of synaptic inputs (Contreras and Steriade, 1995; Timofeev et al., 2000b, 2001), our data reinforces the idea that this phase is more important than previously thought for inter-site interactions, local pacing, entrainment, and synchrony. With respect to this, it has been previously shown that the onset of the silent (OFF/DOWN) state is more synchronized than the onset of the active (ON/UP) state (Volgushev et al., 2006). Since all neuronal cell types are silent during the OFF phase, a non-neuronal mechanism, such as gliotransmission (Halassa, 2011), may be implicated in mediating these types of active processes during the OFF phase. It has been shown that blocking the release of neurotransmitters by astrocytes reduces the duration of UP states and prolongs DOWN states (Fellin et al., 2009), while electrical stimulation of single astrocytes increases the frequency of UP states (Poskanzer and Yuste, 2011), implicating astrocytes in SO expression and modulation. Since astrocytes release essential neurotransmitters and precursors such as glutamate, lactate, and d-serine (an NMDA receptor co-activator) (Newman, 2003) they may play an important role in determining the precise location and time of an OFF to ON state transition, thus influencing phase-related changes and alternations between propagation patterns.

Another possibility is that active (ON) state onsets are caused by spontaneous release of neurotransmitters by cortical layer V neurons, which cause miniature excitatory-post

synaptic potentials (mEPSP). This excitation can ramp up to an avalanche reaction, since layer V cells have the largest projection fields and are most effective at spreading excitation throughout the network, thereby igniting an UP state (Beltramo et al., 2013; Chauvette et al., 2010; Sanchez-Vives and McCormick, 2000; Timofeev et al., 2000a; Wester and Contreras, 2012). In this model, phase resets and propagation pattern alternations may occur as a result of probabilistic factors in which active state transitions occur in various location (causing pattern alternations/crossovers) as well as at various time lags following OFF state onset (causing phase resets). Certain layer V cells may be more likely to ignite an active state as a result of persistent Na^+ current, giving those cells pacemaker-like properties (Crunelli and Hughes, 2010; Le Bon-Jego and Yuste, 2007). Furthermore, certain cortical regions (local "hubs") may be more likely to initiate an UP state due to experience-dependent strengthening of synaptic connections. Therefore, an integrated model would suggest that the UP state onset is a combined function of probabilistic factors (mEPSPs) as well as intrinsic and experience-dependent properties of single neurons and networks. Our findings suggest that OFF states of the slow oscillation provide critical windows of opportunity for ongoing active processes, such as ongoing phase resets and alternations between propagation patterns. Future research will be important for elucidating the mechanisms mediating these processes during the OFF state.

2.5.3 Influence of field stimulation on SO-related neural activity and dynamic coordination

Comparable to previous work (Ozen et al., 2011), we found that sinusoidal field stimulation applied to the brain entrained cortical neural activity. More importantly, we

provide the first evidence (to the best of our knowledge), that field stimulation also influenced the expression of inter-cortical site interactions and the propagation of the SO. Both effects were positively associated with stimulation intensity, and were robust across distance (~6 mm) suggesting that field stimulation can efficiently recruit and synchronize neural populations, presumably by exciting chains of interconnected cortical regions (Frohlich and McCormick, 2010). Indeed, the inter-site propagation during high intensity stimulation became much more stereotyped, with a strong bias for the anterior-to-posterior direction (likely as a result of the frontal location of stimulation electrodes) and the elimination of phase crossovers.

While entrainment across and between sites was enhanced with increased stimulation intensity, the propagation dynamics of the spontaneous SO were increasingly disrupted. We showed that inter-site endogenous coherence, as well as the modulation of faster network activity (gamma and MUA) to the endogenous SO frequency was negatively associated with stimulation intensity. This suggests that at moderate and high intensities, respectively, stimulation could be used to disrupt or enhance the ongoing neocortical interplay during SO states. The moderate stimulation intensity poses an interesting condition in which faster frequency amplitude modulation was present for both the endogenous SO and well as stimulation phases. The moderate stimulation condition might therefore operate to disturb ongoing neural coupling within and across activated cell assemblies during the SO and this disorganization of offline neural dynamics could result in synaptic depotentiation of otherwise normally coupled ensembles. Conversely, high stimulation intensities might operate to enhance neural coupling and function to promote synaptic potentiation (Dickson, 2010; Wolansky et al., 2006). We suggest that future studies using field stimulation in an

attempt to modulate sleep-dependent memory consolidation should consider the influence of various stimulation intensities on the complex recruitment of network activity and its presumed effects on consolidation.

2.5.4 Influence of field stimulation on long-range gamma synchrony

A major finding of the current study is the dramatic enhancement of long-range gamma synchrony for both low (11-25 Hz) and high (56-70 Hz) gamma bands during stimulation. During spontaneous recordings, gamma was moderately coherent during ON phases and only weakly coherent during OFF phases, with coherence falling off substantially for the most distant recording sites (6 mm). These results are consistent with previous findings showing that inter-site gamma coherence is a local and transient phenomenon (Buzsáki and Wang, 2012; Le Van Quyen et al., 2010; Steriade et al., 1996; Valderrama et al., 2012). The inverse relationship between inter-site coherence and frequency of oscillation is a fundamental property of neural networks and is attributed to conduction velocity delays (Buzsáki, 2006; Buzsáki and Draguhn, 2004). Nevertheless, transient strong synchrony in the gamma band can occur across relatively large distances, (Buzsáki and Wang, 2012) and this synchrony may be achieved by long-range connections that can temporally link distant networks (Buzsáki et al., 2004; Buzsáki and Wang, 2012).

With increasing stimulation intensity, gamma coherence across all channel pairs was substantially strengthened. The stimulation paradigm likely induced a phase-reset of gamma resulting in a systematic phasing of gamma across all sites (Dickson and de Curtis, 2002). Long-range gamma synchrony of neuronal ensembles may play a role in activity-dependent synaptic reinforcement, such as spike-time-dependent plasticity (Dan and Poo, 2004;

Sejnowski and Destexhe, 2000; Sejnowski and Paulsen, 2006), that could strengthen local connections and lead to memory consolidation. Consistent with this idea, millisecond precision of cell firing has been shown to occur at particular phases of gamma during slow wave sleep (Le Van Quyen et al., 2010). In a parallel fashion, declarative learning enhances long-range gamma coupling during slow wave sleep in humans (Mölle et al., 2004). Therefore, our results suggest that slow electrical stimulation during deactivated states of sleep and anesthesia may enhance memory consolidation by way of enhancing long-range gamma synchrony.

2.5.5 Conclusion

We have shown that the SO in rat neocortex under urethane anesthesia exhibits non-stereotyped spontaneous dynamics and that can be significantly altered by the application of electrical field stimulation. This study sheds light on the neural mechanisms that could be involved in local production and synchronization of this archetypal non-REM sleep activity and furthermore specifies how entraining stimulation may affect its memory function.

Condition	Control (SO/STIM)	Low (SO/STIM)	Medium (SO/STIM)	High (SO/STIM)
Low gamma				
Channel 1	232.8*/NS	246.0*/NS	NS/64.1*	NS/48.4*
Channel 2	254.3*/NS	262.3*/NS	271.0*/49.3*	NS/44.8*
Channel 3	258.3*/NS	265.3*/NS	267.3*/52.4*	NS/52.4*
High gamma				
Channel 1	255.6*/NS	261.1*/NS	NS/173.6*	NS/186.6*
Channel 2	268.1*/NS	269.1*/NS	260.6*/179.1*	259.4*/184.5*
Channel 3	261.2*/NS	264.3*/NS	255.5*/176.7*	253.4*/191.5*
Multi-unit				
Channel 1	274.2*/NS	268.6*/NS	NS/207.9*	NS/221.8*
Channel 2	272.9*/NS	273.7*/NS	270.9*/181.3*	294.0/224.3*
Channel 3	270.9*/NS	274.3*/NS	NS/198.7*	NS/222.0*

Table 2.1 Mean angles (in º) for phase-amplitude modulation plots for each channel and stimulation condition for low gamma, high gamma, and multi-unit activity. Values on left of dash correspond to SO phase (extracted from LFP) while values on right of dash correspond to stimulation phase. Mean angles for medium and high conditions are based on doubled angles (To obtain the two mean angles: 1st angle = doubled angle/2; 2nd angle = doubled angle/2 + 180). Mean angles are not reported for non-significant modulation. * = $p < .001$; NS = non-significant.

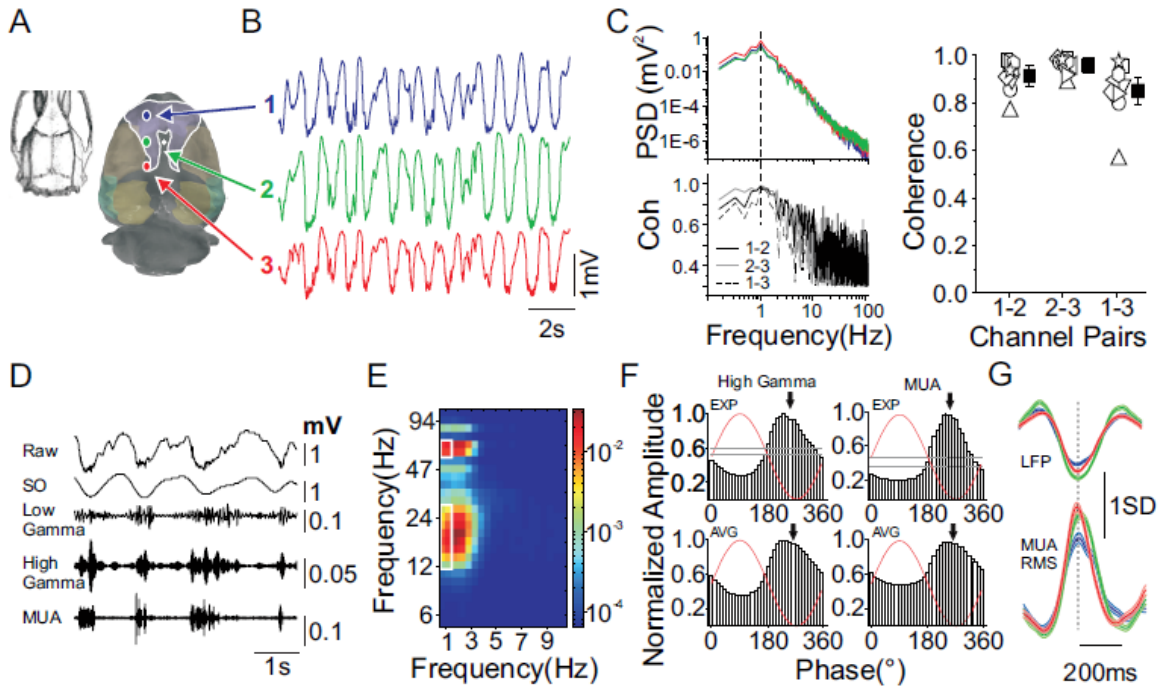

Figure 2.1 The neocortical slow oscillation (SO) in the urethane anesthetized rat is broadly coherent and is coupled to local gamma and multi-unit activity

A. Rat skull (left) and brain (right) in aerial view (nose upwards). White outline shows primary motor cortex (M1). Shaded regions on brain indicate primary cortical areas. The colored dots indicate the 3 electrode positions numbered 1, 2 and 3 and the white dot indicates bregma. **B**. Example raw local field potential (LFP) traces from each electrode site for a single experiment. Color coding corresponds to electrode position as in A. **C**. Left: power spectrum overlaid for all recording sites (top) and coherence spectrum for all channel pairs (bottom) for the experiment shown in B. Note prominent spectral peaks at 1 Hz in both plots, characteristic of SO activity. Right: Average coherence at SO frequency across channel pairs in every experiment. Open symbols indicate individual experiments and solid symbol indicates grand mean (± SEM). **D**. Raw and filtered LFP traces for same experiment as in B show phase coupling of fast activity to the SO. From top to bottom: raw, and filtered for SO (0.5 – 1.5 Hz), low gamma (12 – 25 Hz), high gamma (56 – 70 Hz), and multiunit activity MUA (750 – 1250 Hz). Note grouping of faster frequencies at the negative peak of

the raw and SO filtered traces. **E**. Amplitude-phase modulation plot for traces from the same experiment as in D. X-axis of plot indicates phase component of slow activity, and y-axis indicates amplitude component of high frequency activity. The color scale corresponds to the degree of cross-frequency phase coupling based on the modulation index (MI). White outlines indicate bins with strongest MI values across SO phase (0.5 – 1.5 Hz) which correspond to low (12 – 25 Hz) and high (56 – 70 Hz) gamma amplitude. **F**. Left: Phase histogram showing distribution of high gamma amplitude across SO phase for the same experiment as in E (top) and the grand average across all experiments (bottom). Right: Phase histogram showing histogram for MUA amplitude (750 – 1250 Hz; not shown in modulation plot) across SO phase for the experiment shown in E (top) and the grand average across all experiments (bottom). Grey lines indicate 95% confidence intervals for individual experiments. Arrows indicate mean angle of distribution. Note that all mean angles fall close to the negative peak of SO. **G**. SO-triggered averages for raw LFP (top) and the root mean square (RMS) of MUA (bottom) for the same experiment as in B. Note that the peak of multiunit RMS occurs just before the peak negativity of the SO. Rat skull in A was adapted from: (Paxinos and Watson, 1998).

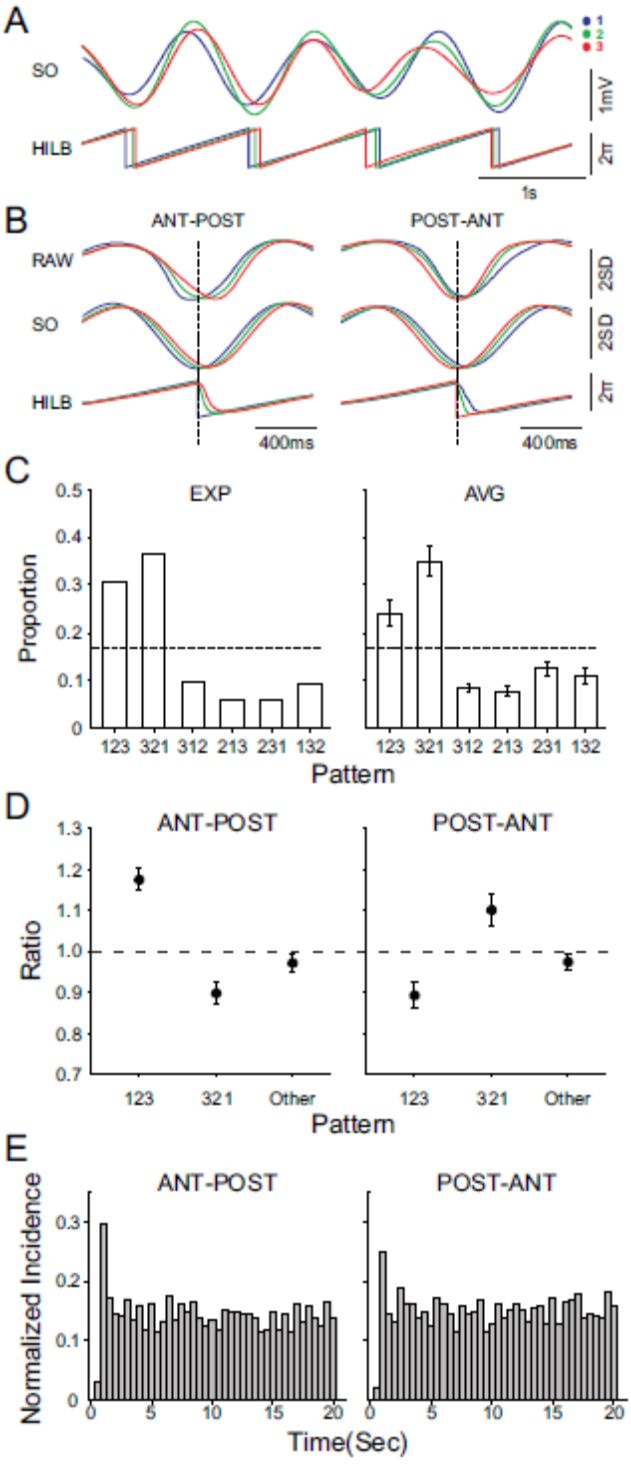

Figure 2.2 The neocortical SO acts as a traveling wave in the rostral-caudal plane and its propagation direction tends to repeat in clusters

A. Superimposed SO filtered (0.5 – 1.9 Hz) LFP traces (top) and corresponding superimposed Hilbert phase (bottom) for all channels for a single experiment. Color coding corresponds to channel positions as noted in Figure 1 A. Note changing phase lags across channels at cycle onsets (i.e., timing of occurrence of negative pi values of Hilbert phase) which suggests changing propagation patterns. Diagonal arrows show the Hilbert phase progression equal to one cycle for the blue channel (channel 1). Circled regions show an example of propagation patterns 1-2-3 (left) and 3-2-1 (right) on a given cycle detected by time lags in the Hilbert phase across channels. **B**. Hilbert phase-triggered averages of raw LFPs (top) and phase values (bottom) for all traces during the anterior-to-posterior (1-2-3; left) and the posterior-to-anterior (3-2-1; right) propagation directions for the experiment shown in A. Note correspondence of propagation pattern in raw LFP (based on negative peak) and Hilbert phase angle. **C**. The histogram of relative proportions of all possible phase sequences (propagation patterns) demonstrates that the majority of patterns occur in the rostral-caudal plane (patterns 1-2-3 and 3-2-1) for both the experiment shown in A (top) and across all experiments on average (bottom). Dotted lines indicate chance level for each propagation pattern given 6 possible patterns. **D**. Conditional proportional scatterplot demonstrating that the occurrence of a major propagation pattern is likely to repeat on the subsequent cycle while the opposite directional pattern is less likely to occur on the subsequent cycle. Left panel shows the relative (to the expected probability) proportional occurrence given the anterior-to-posterior (1-2-3) pattern while the right panel shows the same for the posterior-to-anterior (3-2-1) pattern. Dotted lines indicate no change in pattern expression on the subsequent cycle relative to the prior cycle. Significance was assessed with one-sample *t* tests. **E**. Inter-event-interval histogram for anterior-to-posterior (1-2-3; left) and posterior-to-anterior (3-2-1; right) patterns in 500ms bins for a single experiment. Note peak in the 1 second bin - corresponding to the average SO period - suggesting an enhanced probability of the occurrence of the same directional pattern exactly one cycle later.

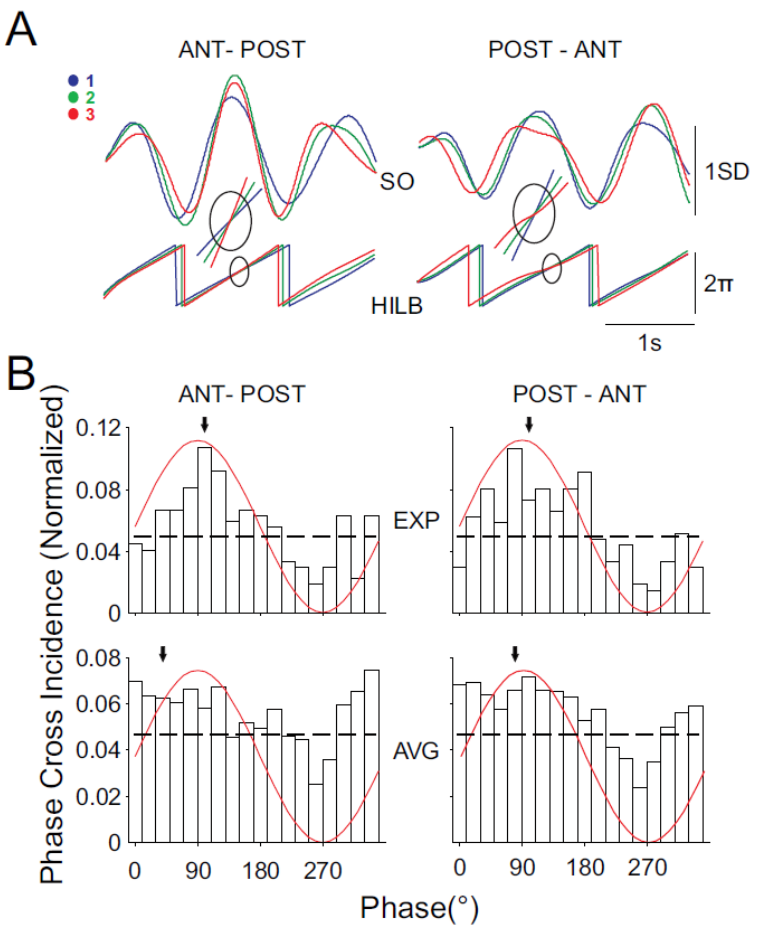

Figure 2.3. Propagation pattern alternations occur during the OFF phase

A. Sample SO filtered traces (0.5 – 1.9 Hz; top) and corresponding Hilbert phase angle (bottom) for all channels in a single experiment. Black circles (magnified above) highlight relative phase angle inversion (crossover) between channels 1 and 3. The left-most example shows a crossover reflecting a switch from the anterior-to-posterior (1-2-3) pattern to the posterior-to-anterior (3-2-1) pattern. The right-most example shows the opposite switch. Color coding corresponds to channel positions as noted in Figure 1A. **B**. Phase histogram showing distribution of the occurrence of phase crossovers across the SO cycle for both anterior-to-posterior inversions (left) and posterior-to-anterior inversions (right). Top graphs show results from the experiment shown in A and bottom graphs show the grand averages across each experiment. Arrows indicate the mean angle of the distribution. Dotted lines

indicate chance level of phase crossover occurrence per bin. Note tendency of phase reversals to occur during the positive peak of SO, corresponding to the OFF phase.

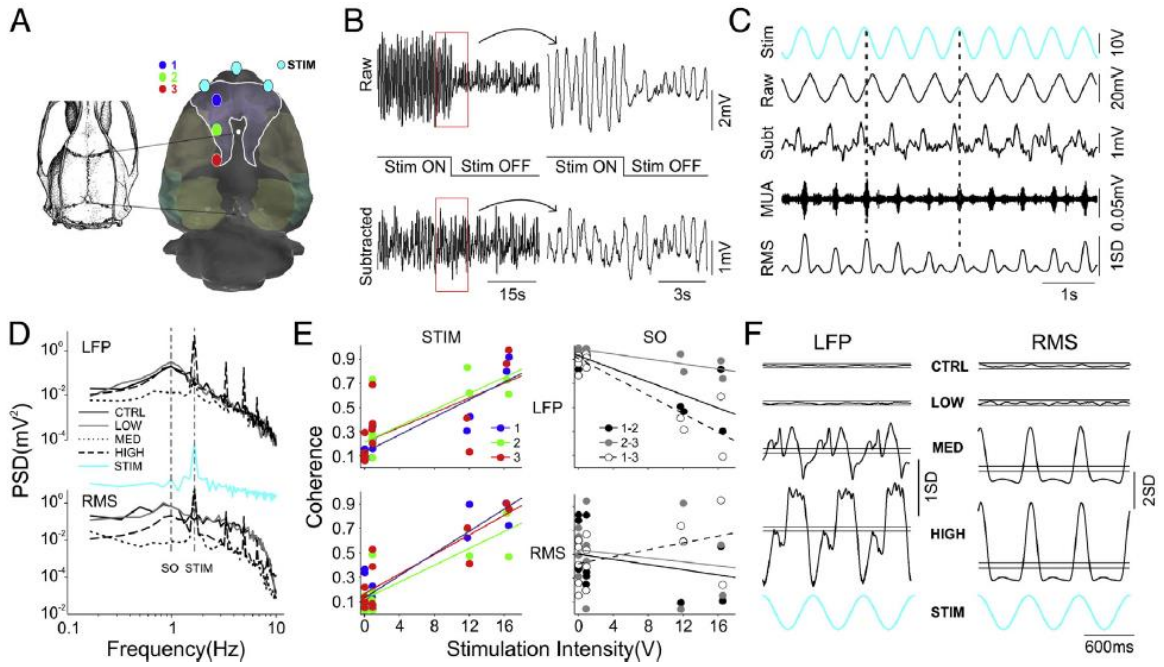

Figure 2.4. Sinuisoidal electrical field stimulation entrains LFP and multi-unit activity

A. Rat skull (left) and brain (right) in aerial view (nose upwards). Shaded regions on brain indicate primary cortical areas. White outline shows primary motor cortex (M1). Recording sites and bregma are as noted in Figure 1 A and cyan-colored dots indicate stimulation sites. **B**. Example recording traces from a single channel (channel 1) during a stimulation trial before (top) and after (bottom) artifact removal. The right panels show expanded traces from outlined regions shown on the left. Note the similar amplitudes pre- and post-stimulation following artifact removal. **C**. Sample traces during stimulation for the same experiment and channel as in B. From top to bottom: stimulation sine wave output, raw LFP before artifact subtraction, raw LFP after artifact subtraction, filtered MUA (750 – 1250 Hz), and multiunit RMS. Note strong entrainment of LFP and MUA to stimulation sine wave. **D**. Power spectrum for LFP (top) and multiunit RMS (bottom; filtered 0.1-10 Hz) during control, low, medium and high stimulation conditions. Cyan trace shows stimulation spectrum (arbitrary scale). Note prominent spectral peaks within the SO frequency range for control and low stimulation conditions that are replaced by peaks at the frequency of stimulation (1.67 Hz in

this case) for medium and high conditions. **E**. Left: coherence between each recording channel and the stimulation sine wave at the frequency of stimulation across all stimulation intensities for the LFP (top) and multiunit RMS (bottom) for all experiments. A significant positive linear regression is present suggesting that an increase in stimulation intensity is associated with an increase in coherence across sites at the stimulation frequency (LFP: R^2 = 0.45 – 0.82, $p < .02$ for all channels; multiunit RMS: R^2 = 0.73 – 0.83, $p < .001$ for all channels). Right: coherence between recording channel pairs at the SO frequency across all stimulation intensities for the LFP (top) and RMS (bottom) for all experiments. A significant negative linear regression is present for all LFP signals suggesting that an increase in stimulation intensity is associated with a decrease in coupling at the natural SO frequency (R^2 = 0.67 – 0.82, $p < .001$ for all channel pairs). Linear relationships for multiunit RMS were not significant ($p > .05$ for all channel pairs). **F**. Stimulation-cycle triggered averages for LFP (left) and multiunit RMS (right). From top to bottom: control, low, medium, and high stimulation conditions, and the stimulation sine wave. LFP averages were obtained from artifact subtracted traces. Lines represent 95% confidence intervals obtained by randomizations of control traces for the LFP and RMS respectively. Note strong entrainment of LFP and RMS to the stimulation sine wave for medium and high stimulation conditions.

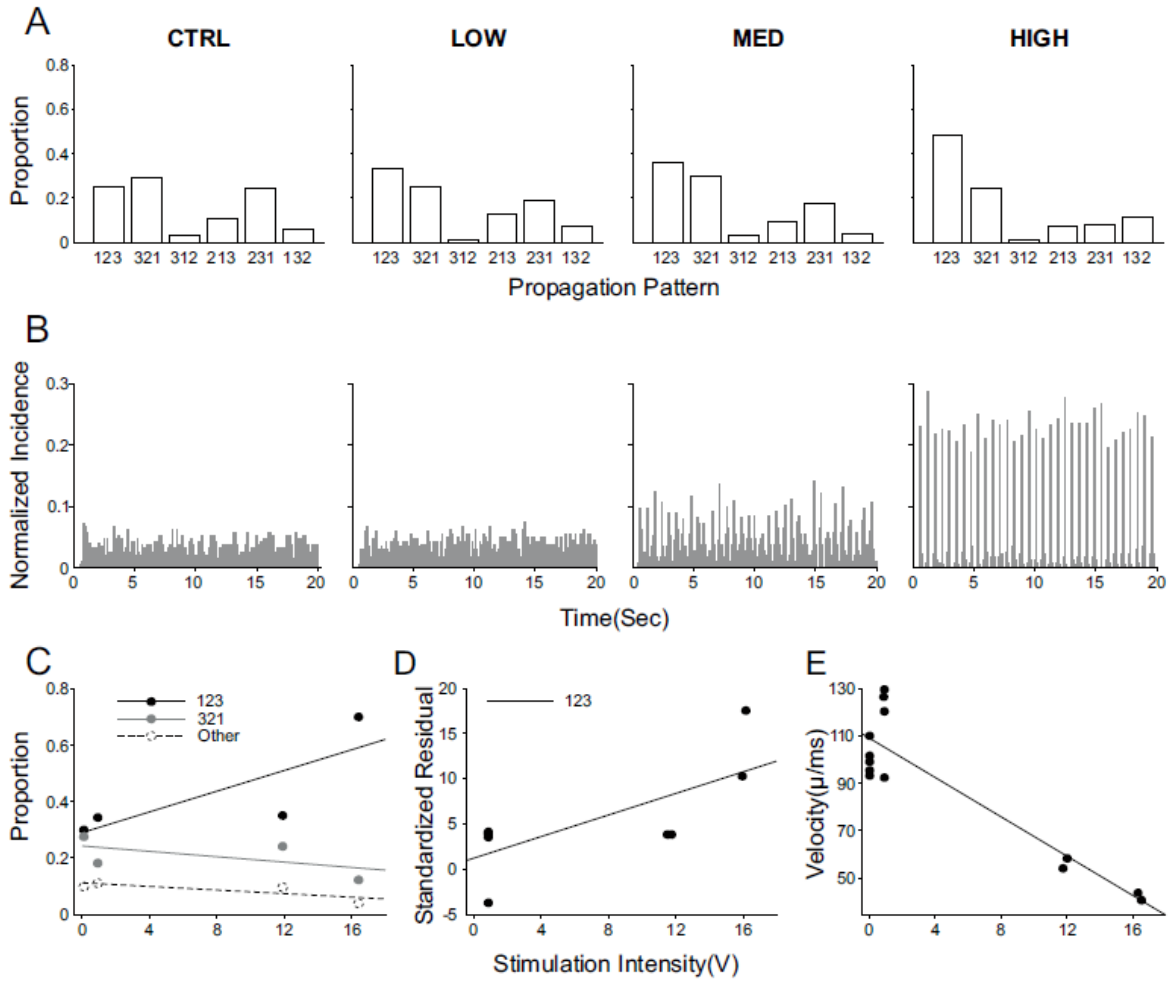

Figure 2.5. Electrical field stimulation biases SO propagation dynamics towards the anterior-to-posterior propagation pattern

A. Histogram showing proportion of all possible SO (0.5 – 1.9 Hz) propagation patterns for control, low, medium, and high stimulation conditions in a single experiment. Note the increase in the anterior-to-posterior pattern (1-2-3; grey bars) with increased stimulation intensity. **B**. Inter-event interval histogram in 119.2ms bins (a dividend of the stimulation period) for pattern 1-2-3 during control, low, medium, and high stimulation conditions for the experiment in A. Note elevated occurrence of pattern repetition every 600ms for strong stimulation conditions, corresponding to the period of the stimulation frequency (1.67 Hz).

C. Grand average proportions of propagation patterns 1-2-3, 3-2-1 and all other patterns across all stimulation intensities. Note increase in the 1-2-3 pattern and a decrease in the 3-2-1 and all other patterns with increased stimulation intensity. **D**. Standardized residuals (compared to control) for pattern 1-2-3 across stimulation intensities for all experiments. Note positive regression slope indicating increase in pattern 1-2-3 with increased stimulation intensity. **E**. Velocity of propagation across stimulation intensities for all experiments. Note negative slope of regression line signifying a decrease in velocity of propagation with increased stimulation intensity.

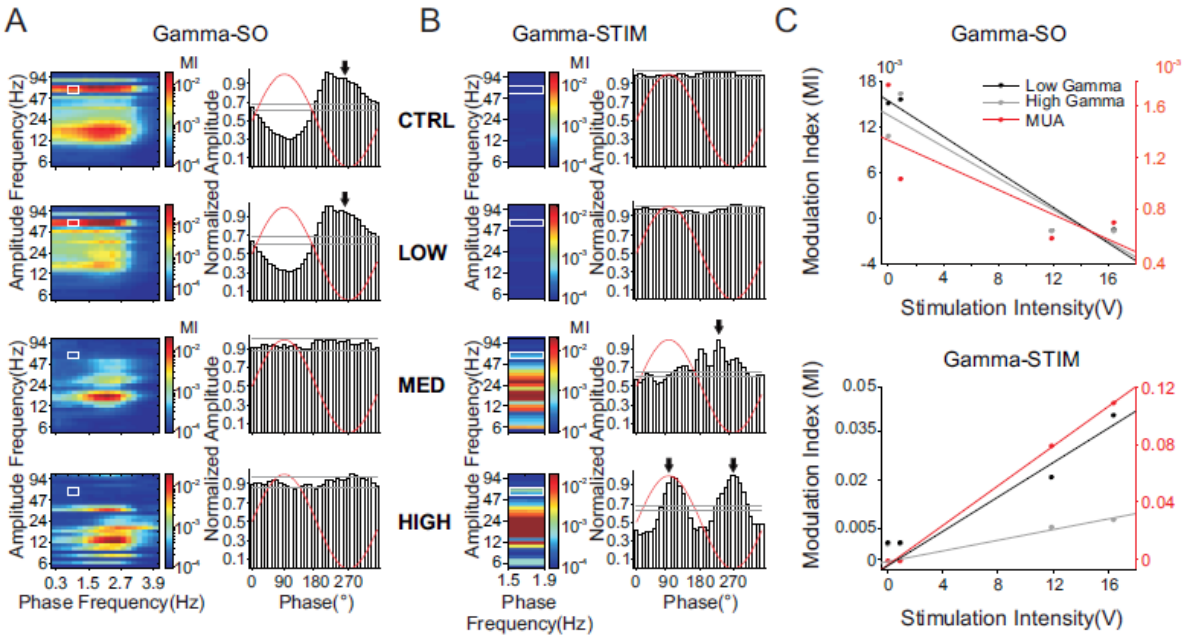

Figure 2.6. Electrical field stimulation entrains local gamma activity while disrupting spontaneous SO-gamma relationships

A. Left panels: Amplitude-phase modulation plots relating ongoing spontaneous slow LFP (x-axis) to faster frequencies (y axis) for control, low, medium, and high stimulation conditions for channel 1 in a single experiment. Color represents degree of cross-frequency phase coupling based on the modulation index (MI). White boxes outline the amplitude-phase intersection of the high gamma frequency range (56 - 70 Hz) to the SO frequency range (0.7 – 1.1 Hz). Right: Phase histograms showing distribution of high gamma amplitude across the SO cycle for amplitude-phase frequency ranges outlined by white box in A. **B**. As in A, with the stimulation sine wave used as the phase variable. White boxes outline the intersection of high gamma amplitude frequencies (56 – 70 Hz) with the stimulation frequency (1.67 Hz). Arrows indicate the mean angle (or bimodal angles) of the phase distribution for histograms. Grey lines indicate 95% confidence interval obtained from randomization procedure using surrogate amplitudes. Note disruptions in SO cycle cross-frequency coupling and increase in STIM cycle cross-frequency coupling with increasing

stimulation intensity. **C.** Left: MI for low (12 – 25 Hz) and high (56 – 70 Hz) gamma and MUA (750 – 1250 Hz) amplitudes across the phase of LFP SO (0.7 – 1.1 Hz) for all stimulation intensities. Right: same as on left but for STIM phase. Note negative association between MI and stimulation intensity at the SO frequency range and a positive association at the STIM frequency. See Table 1 for mean angles and significance of modulation for all fast activity across channels (low gamma, high gamma, MUA).

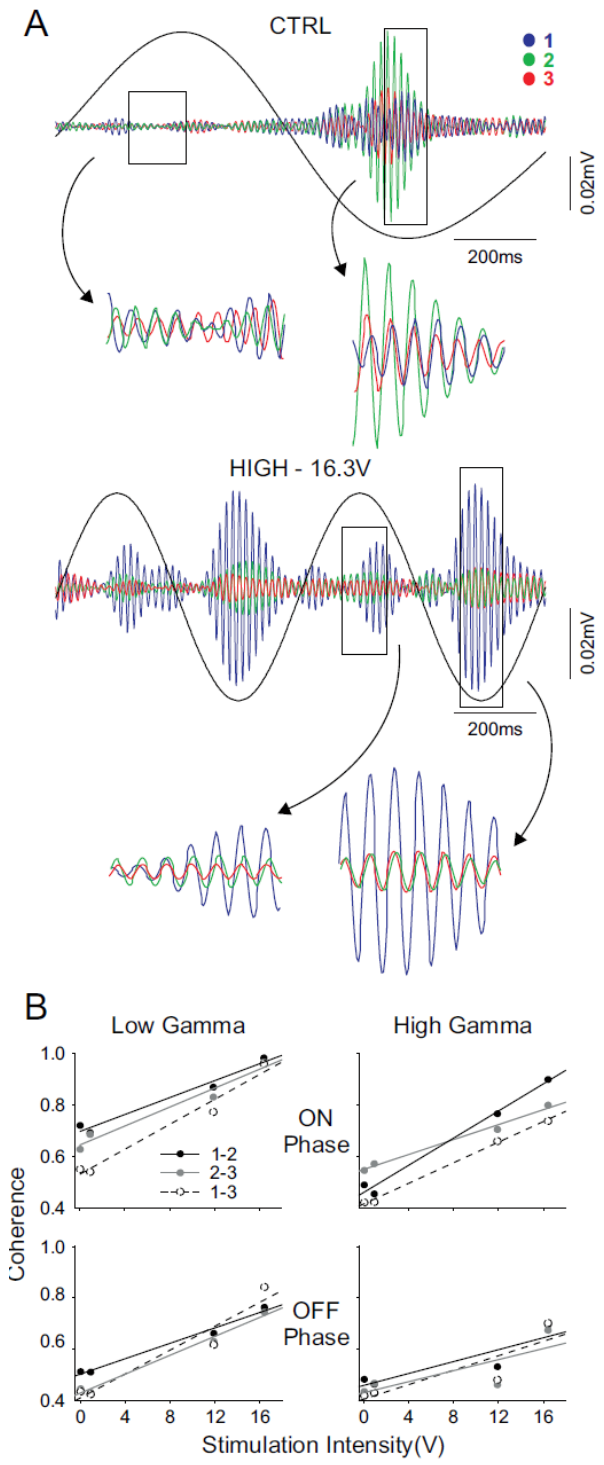

Figure 2.7. Field stimulation enhances long-range synchronization of low and high gamma

A. High gamma (56 – 70 Hz) filtered traces for control (top) and high (bottom) stimulation intensity conditions. Black boxes show regions that are magnified below each trace. Colors correspond to electrode positions, as in Figure 1A. Over-laid waveforms show corresponding SO (black; 0.5 – 1.9 Hz) and stimulation (cyan; 1.67 Hz) traces for control and high stimulation conditions respectively. Note stronger inter-site gamma coherence for the ON phase of SO in comparison to the OFF phase for the control condition and a dramatic increase in inter-site coherence at both ON and OFF phases for the high stimulation condition. Inset shows average ON and OFF high gamma coherence across channels 1 and 3 (6 mm distance) for control and high stimulation conditions for a single experiment. Error bars are too small to be visible. **B**. Coherence grand averages between channel pairs across stimulation intensity for low (12 - 25 Hz) and high (56 – 70 Hz) gamma bands separated for ON and OFF phases (based on gamma RMS). Note increase in coherence in all cases with increasing stimulation intensity (ON phase: low gamma - $R^2 = 0.58 - 0.79$, $p < .01$ for all channel pairs; High gamma - $R^2 = 0.41 - 0.84$, $p < .02$ for all channel pairs; OFF phase: $R^2 = 0.87 - 0.97$, $p < .001$ for all channel pairs; high gamma - $R^2 = 0.44 – 0.57$, $p < .0.2$ for all channel pairs).

3 Changing waves: Rhythmic electric field stimulation systematically alters spontaneous slow dynamics across neocortex

Authors: Anastasia Greenberg[1], Javad Karimi[2], Clayton T. Dickson[1,3,4] and Majid H. Mohajerani[2]

[1]Neuroscience and Mental Health Institute, University of Alberta, Edmonton, AB, Canada, T6G 2E1

[2]Department of Neuroscience, University of Lethbridge, Lethbridge, AB, Canada, T1K 3M4

[3] Department of Psychology, University of Alberta, Edmonton, AB, Canada, T6G 2H7

[4] Department of Physiology, University of Alberta, Edmonton, AB, Canada, T6G 2E9

Acknowledgments: This work was supported by a Natural Science and Engineering Council of Canada (NSERC) grant # 249861 to CTD. AG was additionally supported by an NSERC Alexander Graham Bell Canada Graduate Scholarship – Doctoral (CGS D) and a grant from the Campus Alberta Neuroscience Trainee Mobility Program. We would like to acknowledge Jianjun Sun for performing craniotomies in all animals.

3.1 Abstract

The signature rhythm of slow-wave sleep and anesthesia is the large amplitude, cortical slow oscillation (SO, ~1 Hz) made up of synchronous periods of depolarization (ON, UP states) and hyperpolarization (OFF, DOWN states) at the single cell and network levels. On any given wave, the SO originates at varied cortical foci and propagates across large parts of the neocortex and to the hippocampus, entraining local faster rhythms into its ON phase. These dynamic yet globally encompassing features highlight the potential for the SO to enhance cross-network functional relationships, such as those that would be relevant for memory consolidation. Indeed, attempts to manipulate SO activity using alternating electrical fields have successfully entrained cortical networks and resulted in enhanced hippocampal-dependent memory performance. However, a mechanistic explanation for such memory enhancing effects is lacking, and in particular how electrical stimulation influences cortical SO propagation dynamics. Here we took advantage of the high temporal and spatial resolution of the voltage-sensitive dye (VSD) imaging technique in a bilateral cortical preparation of urethane-anesthetized mice to track SO cortical propagation dynamics and their influence under rhythmic electrical field stimulation applied to frontal regions. We show that under spontaneous conditions, the SO propagates in two main opposing directional patterns along an anterior lateral – posterior medial axis. The application of sinusoidal field stimulation alters propagation to reflect stereotyped activity that repeats itself cycle by cycle with distributed initiation zones and a consistent termination zone in the posterior somatosensory cortex. Following the cessation of stimulation, activity appears suppressed for several minutes followed by the resumption of normal activity. Our results suggest that

electrical field stimulation may be used to alter and target specific propagation patterns in attempts to enhance or disrupt memory consolidation.

3.2 Introduction

Synchronized brain rhythms during distinct behavioral states such as sleep and wakefulness are increasingly recognized as paramount for physiological processing and function (Buzsáki, 1998, 2006; Buzsáki and Draguhn, 2004). Within sleep, as well as anesthesia, slow-wave activity is marked by the large amplitude highly rhythmic cortical slow oscillation (SO; ~ 1 Hz) at the network level which is generated by toggling between depolarized (ON, UP) and hyperpolarized (OFF, DOWN) states at the cellular level (Amzica and Steriade, 1995b; Contreras and Steriade, 1995; Steriade et al., 1993d). This sleep rhythm has been implicated in hippocampal-dependent memory consolidation across both human (Huber et al., 2004; Marshall et al., 2006; Marshall et al., 2011; Mölle et al., 2004; Ngo et al., 2013; Rasch et al., 2007) and animal studies (Binder et al., 2014a; Eschenko et al., 2006; Eschenko et al., 2008). The SO has several properties that make it highly suitable for such a role including its grouping of faster local gamma rhythms (Steriade, 2006; Timofeev and Steriade, 1997), thalamocortical spindles (Mölle, 2009; Mölle et al., 2002; Nir et al., 2011; Steriade et al., 1993c) and the classic hippocampal memory replay events – the so called sharp-wave ripples (Grenier et al., 2001; Mölle, 2009; Sirota et al., 2003) – into its active (ON) state, creating the opportunity for wide-range cross-network interactions. The SO originates in the cortex, is likely driven by activity in deep layer V pyramids, and relies on cortico-cortical connections for synchronization (Amzica and Steriade, 1995a, b; Beltramo et al., 2013; Steriade et al., 1993d; Timofeev et al., 2000a; Timofeev and Steriade, 1996). It has

been shown that on any given cycle, the SO originates at a specific cortical focus and propagates in a traveling wave across the cortex (Massimini et al., 2004; Volgushev et al., 2006) all the way to the hippocampus (Isomura et al., 2006; Nir et al., 2011; Wolansky et al., 2006). This activity generally propagates in an anterior-to-posterior direction from many possible initiation zones with many complex pattern variations (Chan et al., 2015; Hangya et al., 2011; Massimini et al., 2004; Mohajerani et al., 2013; Mohajerani et al., 2010) suggesting that the SO shows non-stereotyped dynamics.

Attempts to manipulate the SO during slow-wave sleep using alternating electrical stimulation applied at frontal regions of the cortex following hippocampal-dependent learning have resulted in improved memory performance in both humans (Marshall et al., 2006; Marshall et al., 2011) and rats (Binder et al., 2012). However, the mechanism by which such stimulation affects SO dynamics in favour of improved mnemonic performance is not well understood. It has been demonstrated that this type of rhythmic field stimulation boosts SO power and effectively entrains both cortical and hippocampal local-field and unit activity (Greenberg and Dickson, 2013; Marshall et al., 2006; Ozen et al., 2010). Recently, we have shown using a three-electrode linear array across the motor cortex that field stimulation in rats can bias and stereotype SO propagation dynamics favoring a specific propagation motif (Greenberg and Dickson, 2013). However, using such a simple array does not allow for a complete representation of complex propagation patterns across multiple cortical regions.

In the current study, we employed voltage-sensitive dye imaging (VSD) of a large bilateral cortical window in urethane-anesthetized mice and systematically assessed the effects of sinusoidal field stimulation applied to frontal regions of the brain on the

spontaneous SO propagation dynamics. We show here that under spontaneous conditions, the SO shows two major opposing propagation directions along an anterior lateral – posterior medial axis. The application of field stimulation entrains VSD activity across wide areas of the cortex and alters propagation away from the spontaneous patterns towards one that can originate at many focal points but with a common termination zone in the somatosensory region. This effect was not observable during field stimulation under the influence of activity blockers (lidocaine and CNQX+MK-801) or in post mortem recordings. Activity during stimulation was also highly stereotyped with the same propagation pattern repeating cycle after cycle unlike the dynamically changing spontaneous SO. Following the cessation of field stimulation, hemisphere-specific VSD activity was briefly suppressed followed by the resumption of normal spontaneous activity.

3.3 Methods

3.3.1 Subjects

Spontaneous VSD recordings were conducted in 14 adult mice (M = 1, F = 13; C57BL6J = 11, YFP (-) = 3) with a mean (± standard error of the mean; SEM) weight of 22.8 ± 0.51 g. Of these animals, 8 were used for delivery of sinusoidal field stimulation and for recordings following the cessation of stimulation (≥ 8 min post-stim). Of these 8 animals, 3 were used for assessing post-stimulation effects on a longer timescale (up to 75 min). Sensory evoked potentials were obtained for all animals.

Animals were housed on a 12 hour light/dark cycle and fed a standard mouse diet *ad libitum.* All housing and surgical procedures conformed to the guidelines of the Canadian

Council on Animal Care (CCAC) and were approved by the Animal Welfare Committee of the University of Lethbridge.

3.3.2 Surgery

Mice were initially anesthetized in a gas chamber with a 4% concentration of isoflurane in 100% O_2 and injected (s.c.) with an initial dose of urethane (1.25 g/kg) and HEPES-buffered saline (100 µL/g). Animals were then transferred to a stereotaxic apparatus and maintained at 0.5-1% isoflurane administered via nose cone. The body temperature was maintained at 37 °C throughout the experiment via a servo-controlled heating pad placed under the mouse. For field stimulation, 4 Teflon-coated stainless steel wires (277 µm bare diameter; 0.4 Ω resistance) were lowered to pial surface and implanted in a triangular configuration with the two central poles located just offset from the midline (+3.5 mm AP and ±0.3 mm ML) and the two lateral poles more posterior and lateral (+2.5 mm AP; ±2.5 mm ML) (see Figure 3.1A). The electrodes were secured to the skull using dental acrylic and super glue.

Mice were then transferred to a metal plate that could be mounted under the VSD camera lens. A steel head plate was then mounted onto the skull and an 8 X 8 mm craniotomy window was created by removing the skull (Figure 3.1A). The dura was either removed (n = 7) or kept intact (n = 7). A tracheotomy was performed to aid breathing. Isoflurane delivery was then eliminated and additional top-up doses of urethane (10% of initial dose; 0.125 g/kg) were administered every few hours as necessary to maintain a consistent level of anesthesia.

3.3.3 VSD Imaging

Following craniotomy, the exposed brain surface was bathed in the dye RH1692 (Optical Imaging, New York, NY), which was dissolved in HEPES-buffered saline solution (1 mg ml^{-1}). The staining procedure resulted in a dark purple appearance of the cortex which indicated sufficient dye incorporation (Mohajerani et al., 2010). The staining time required for reaching proper incorporation was 30 min – 1 hour for the animals in which the dura was removed and 2.5 – 3 hours for the animals with an intact dura. Following washout of the unbound dye animals were transferred to the VSD recording rig. The exposed cortex was coated with 1.5% agarose made in HEPES-buffered saline and covered with a glass coverslip to minimize recording artifacts associated with respiration and heartbeat.

VSD images were collected with a CCD camera (1M60 Pantera, Dalsa, Waterloo, ON) and EPIX E4DB frame grabber with XCAP 3.8 imaging software (EPIX, Inc., Buffalo Grove IL). The camera was focused ~1 mm dorsoventral to cortical surface to avoid distortion from blood vessels. VSD was excited with a red LED (Luxeon K2, 627 nm centre) and excitation filters (630±15 nm). Images were taken through a macroscope composed of front-to-front video lenses (8.6 X 8.6 mm field of view, 67 µm per pixel). VSD fluorescence was filtered using a 673–703-nm bandpass optical filter (Semrock, New York, NY). Images were acquired in 12-bit resolution at 150 Hz sampling rate for sensory-evoked data and 100 Hz or 200 Hz for spontaneous recordings. The camera-clock output of the EPIX system was recorded for offline alignment of EEG and VSD data.

VSD images were preprocessed using custom-written code in Matlab (Mathworks, Natick, MA). The VSD images were first subjected to principal-component analysis (PCA) and the leading components were retained (15-50 components). The data were then filtered

using a second-order Chebyshev bandpass filter (zero-phase filter; 0.2 – 50 Hz). VSD responses were expressed as percent change relative to the baseline response calculated as: F-F0/F0 x 100 where F represents the fluorescence signal for each pixel for a given frame and F0 represents the mean response in each pixel across all frames.

3.3.4 EEG and ECG recordings

For all experiments a cortical EEG electrode was inserted into the conductive agar solution close to the craniotomy window on the right hemisphere near the visual cortex (Figure 3.1A). EEG recordings were stable throughout the experiment and were well correlated with the VSD signal (Figure 3.2). An electrocardiogram (ECG) electrode was inserted subcutaneous into the back. An electrode inserted on the nasal bone served as a reference for both EEG and ECG signals. All electrodes were teflon-coated silver wires (0.127 mm bare diameter). Signals were wide-bandpass filtered between 0.1 Hz and 1 kHz and amplified at a gain of 1000 using a differential AC amplifier (P5 series Grass, Natus Neurology Inc., Warwick, RI). Signals were digitized using an A-D board (Digidata 1550; Axon Instruments/Molecular Devices, Sunnyvale, CA) and sampled at 2000 Hz to prevent aliasing. Data were acquired and stored using AxoScope (Axon Instruments/Molecular Devices) on a PC system for offline analysis.

3.3.5 Sensory stimulation

Sensory-evoked potentials were collected for all animals to map the cortex. For primary hind limb (HLS1) and fore limb (FLS1) evoked-potentials, brief current pulses (20 µA, 1 ms; 10 s inter-stimulus interval) were delivered through acupuncture needles (0.14

mm) inserted into all 4 paws. For visual evoked potentials (V1), LED light stimulation (1 ms, green and blue light) was delivered to each eye separately. For barrel cortex stimulation (C2) a single whisker was identified and placed under a piezoelectric device (Q220-A4-203YB, Piezo Systems, Inc., Woburn, MA) that delivered a single tap using a square pulse (1 ms) which moved the whisker 90 μm in an anterior-to-posterior direction. For each type of sensory stimulation, an average of 10 trials was used to locate the position of the primary region. Based on mapping of cortical regions in each animal, VSD data could be represented on a standardized mouse cortical map adapted from the Allen Brain Institute (Seattle, WA) (c.f. Figure 3.5 E).

3.3.6 Sinusoidal field stimulation

Sinusoidal stimulation was applied using an analogue function generator (Hewlett Packard; 3310A) to the 4 stimulation poles with the two lateral poles receiving opposite polarity stimulation to the two central poles (see Figure 3.1A; see (Greenberg and Dickson, 2013; Greenberg et al., 2016)); adapted from (Ozen et al., 2010)). The stimulation generator output was also digitized using the same system as that used for EEG and ECG signals to obtain stimulation phase and voltage intensity information for later offline analysis. The intensity of stimulation was 10 V (defined as peak-to-peak amplitude). The frequency of stimulation was 1.67 Hz, slightly faster than the endogenous SO frequency (~ 0.5-0.8 Hz). We chose this faster frequency in order to spectrally separate the effects of stimulation and endogenous SO as well as in an attempt to successfully entrain networks by providing a faster putative pacemaking stimulus. Stimulation was applied during SO states identified visually in the online EEG recording and was applied for 3-4 min consecutively for one trial.

VSD and EEG recordings were obtained during stimulation as well as following the cessation of stimulation.

In order to measure the amount of current delivered to each hemisphere, we connected a resistor to the frontal stimulation electrode of each hemisphere and the second end of the resistor was connected to one of the stimulation outputs (Figure A.1). The second stimulation output was connected to the posterior stimulation electrode of each hemisphere (Figure A.1). Therefore, the circuit was in series allowing a direct measurement of the amount of current passing across the brain which is equal to the amount of current passing across the resistor. The current passing across the resistor is equal to the amount of voltage across the resistor divided by the resistivity.

3.3.7 Pharmacology

In order to ensure that field stimulation did not contaminate the VSD recordings with electrical artifact we obtained control experiments in which field stimulation was applied under the influence of three activity suppressing/abolishing conditions: the application of lidocaine (Na^+ channel blocker, n = 4), combined application of CNXQ (AMPA receptor antagonist) and MK-801 (NMDA receptor antagonist) (n = 3), as well as during post-mortem recordings following brain death (n = 5). All drugs were dissolved in HEPES-buffered saline solution. For CNQX, a stock solution was created by dissolving CNQX in DMSO, with a final DMSO concentration of 4% in the experimental solution. After collection of baseline and field stimulation recordings, the agarose was removed from the surface of the brain (for the dura-intact animals) and lidocaine (2%) was applied for ~30 min (until suppression was evident in the EEG) before the trial began. Lidocaine was then washed out for ~60 min (until

resumption of normal EEG activity) and then the mixture of CNQX (2 mM) and MK-801 (0.1 mM) was applied for ~45 min (until suppression was evident in the EEG). Following the CNQX+MK-801 condition animals were euthanized with euthasol (0.05 – 0.1 mL) and the final control trial began immediately after flattening of both the EEG and ECG signals. For each of these activity suppressing conditions the trial began with 3-4 min of spontaneous VSD and EEG recording followed by 3-4 min of field stimulation. For all drug conditions imaging took place while the cortex was bathed in the drug solution to maintain consistent suppression effects and agarose was not reapplied. Movement artifacts were thus present during drug trials at ~ 8 Hz but did not affect our frequency of interest containing the slow oscillation and stimulation frequencies (~0.5-2 Hz) (Figure 3.2C).

3.3.8 Data analysis

All analyses were performed using a combination of built-in functions and custom written code in Matlab (MathWorks). All means are reported as mean ± standard error of the mean (SEM). Significance for all statistical tests was defined as $p < 0.05$ and all *t* tests were performed two-tailed and between-subjects (due to uneven subject numbers per condition) unless otherwise specified.

3.3.8.1 Spectral analyses

Spectral analyses were performed using Welch's averaged modified periodogram method for power spectral density estimation (6 s window; 2 s overlap) calculated on continuous 120 second epochs of data that were then averaged based on subject and

condition. For VSD data, this method was performed on data taken from a given region of interest (ROI) after averaging activity from 25 pixels (5 x 5 window) (Figure 3.2C).

RMS. The root-mean square (RMS) level was computed for each pixel of the VSD data over a 3-minute period for each condition within each experiment. To create group averages, RMS values were first averaged across all pixels for either one (Figure 3.9) or both (Figure 3.2, 3.3) hemispheres within each experiment and condition.

3.3.8.2 Entrainment

For assessing the level of VSD activity entrainment to the delivered stimulus sine-wave, stimulus-triggered VSD averages were created. The phase angle of the Hilbert transform yields a measure of instantaneous phase over time and was used to identify trigger points. To obtain a baseline measure of VSD activity entrainment to the endogenous slow oscillation, the positive peak of the slow oscillation (90º) at a given ROI was used to trigger VSD traces across all cycles (Figure 3.4A – left). For the field stimulation conditions, the positive peak of the delivered sine-wave was used as the trigger point. The peak-to-trough amplitude (in SD units) was taken as a measure of entrainment for all conditions.

3.3.8.3 Propagation patterns

The main aim of the current work was to use VSD imaging to identify slow oscillation propagation pattern dynamics under baseline conditions and observe how such dynamics may be altered during the application of sinusoidal field stimulation. In order to identify propagation patterns on a cycle-by-cycle basis, the phase angle of the Hilbert transform was used to identify positive peaks in the VSD signal taken at the ROI of HLS1

(identifying cycles from the EEG SO instead yielded identical results) or taken from the positive peaks of the stimulation sine wave for stimulation conditions. Using this trigger point, VSD images were separated into single activation (ON state) cycle periods defined as ±135º from the positive peak. The phase angle of the Hilbert transform was then computed for every pixel within each cycle and the positive peak of the given pixel was identified. Thus, for every cycle, a "propagation" image could be created which shows the time (ms) at which each pixel reached its positive peak (peak activation) relative to the triggered peak taken at the ROI (time = 0). By assessing the earliest and latest peak onsets in this image a propagation pattern could be inferred (c.f. Figure 3.5A – gray images). These single cycle propagation images were then subjected to a hierarchical clustering algorithm (built-in Matlab toolbox) in order to group patterns with similar spatial profiles. To create a similarity measure used for grouping, each pair of patterns was spatially correlated and these correlation measures were used in the algorithm. A pattern group was defined as one in which any 2 patterns within the group had a spatial correlation of > 0.08 (above the 99th percentile from 1000 trials of randomized data) resulting in the identification of ~14 pattern groups during baseline (Figure 3.5B; Figure 3.8A). Patterns across all conditions were subjected simultaneously to the clustering algorithm in order to identify overlapping pattern groups across conditions if such existed.

Start and end points of propagation for each cycle were defined as the center of mass of the pixels with the earliest and latest Hilbert positive peak detections (< 2SD and > 2SD respectively) and directional vectors could be drawn from start to end point for those patterns with a relatively linear propagation direction. A measure of propagation strength (propagation index) was calculated as the change in area of activation (> 2SD above baseline

fluorescence) from frame to frame (Δmm^2/frame). The velocity of propagation for any given cycle was calculated as total distance traveled from start to end point over time (mm/s).

3.4 Results

3.4.1 Sensory evoked responses and spontaneous slow activity are abolished by lidocaine and glutamate receptor antagonism

We mapped the functional surface of the cortex by recording the evoked VSD (and EEG) response to stimulation of the hind limb, fore limb, whiskers, and to light flashes. These stimuli activate, respectively, the representations for hind limb (HLS1), fore limb (FLS1), barrel (C2), and visual (V1) areas of the cortex. Strong evoked VSD responses were apparent (Figure 3.1 B-D) and activity corresponded well with the simultaneously recorded EEG (data not shown). The application of lidocaine or glutamate receptor antagonists (CNQX+MK-801) abolished these evoked responses in the VSD (lidocaine: $p = 0.001$; CNQX+MK-801: $p = 0.004$; Figure 3.1 B,C) and largely eliminated evoked potentials in the EEG as well ($p < 0.05$, not shown).

Following initial mapping, we made recordings of VSD and EEG during spontaneous conditions. Consistent with previous observations (Chan et al., 2015; Mohajerani et al., 2010), we observed large slow (<1 Hz) fluctuations in VSD signals that corresponded to similar fluctuations in the EEG (Figure 3.2 A,B). Applications of lidocaine and glutamate receptor antagonism likewise eliminated the spontaneous VSD power (for SO frequency: lidocaine, $p = 0.029$; not significant for CNQX+MK-801, $p = 0.091$) and RMS (lidocaine: $p = 0.008$; CNQX+MK-801: $p = 0.005$) as well as severely depressed spontaneous EEG (lidocaine: $p = 0.014$; CNQX+MK-801: $p = 0.017$) (Figure 3.2 C-F). In post-mortem

recordings, there was severe spectral power loss in both EEG and VSD recordings as well as in RMS analyses (EEG: $p < 0.001$, VSD: $p = 0.007$, RMS: $p < 0.001$; Figure 3.2).

It was apparent that in the EEG, spectral power was reduced across all frequency ranges except during the CNQX+MK-801 condition which showed a shift in the spectral power to a slower frequency (~ 0.3 Hz) (Figure 3.2A-C). It is likely that residual EEG activity post-drug is volume conducted from sources deeper in the brain structures which are not perfused to the same extent.

3.4.2 Field stimulation alters and entrains VSD slow-wave activity

We confirmed that applications of rhythmic electrical fields could successfully alter and entrain VSD activity in a similar fashion to that previously described in EEG studies (Greenberg and Dickson, 2013; Ozen et al., 2010). Rhythmic field stimulation suppressed VSD spectral power and RMS at the SO frequency in comparison to spontaneous recordings (0.5 – 0.8 Hz; VSD: $p = 0.03$, RMS: $p = 0.002$; Figure 3.3A-C) and spectral power had a tendency to increase at the exact frequency of stimulation (1.67 Hz) for every experiment, although this increase was not significant on average (VSD: $p = 0.054$, RMS: $p = 0.19$; Figure 3.3A,B,D). When applying field stimulation under the influence of lidocaine, glutamate receptor antagonism and post-mortem, VSD spectral power and RMS level were expectedly low compared to baseline (VSD: lidocaine: $p = 0.016$; CNQX+MK-801: $p = 0.035$; Dead: $p = 0.008$; RMS: lidocaine: $p = 0.004$; CNQX+MK-801: $p = 0.003$; dead: $p < 0.001$; Figure 3.3B,C). However, spectral peaks at the frequency of stimulation did appear for all activity suppressing conditions but were significantly lower compared to baseline power for that same frequency (VSD: lidocaine: $p = 0.003$; CNQX+MK-801: $p = 0.004$;

dead: $p < 0.001$; RMS: lidocaine: $p = 0.004$; CNQX+MK-801: $p = 0.004$; Dead: $p < 0.001$; Figure 3.3B,D) and thus this small artifact component is unlikely to affect interpretation of the results.

Given the tendency for VSD spectral power to be boosted at the frequency of stimulation, we assessed the level of VSD activity entrainment to the phase of stimulation. There was strong entrainment of VSD activity to the stimulus sine wave during stimulation for all ROI locations (based on randomized trigger points, $p < 0.001$; Figure 3.4B). The level of entrainment to the sine wave was equal in magnitude to the baseline VSD entrainment to the spontaneous SO for most ROI locations (left: HLS1, $p = 0.43$; V1, $p = 0.165$; right: HLS1, $p = 0.351$; V1, $p = 0.11$; Figure 3.4B) except for FLS1 where the entrainment was weaker than the baseline-SO entrainment (left: $p = 0.01$; right: $p = 0.005$) (Figure 3.4 A,B).

When applying stimulation during activity-suppressing conditions, triggered averages showed significantly lower sine-wave entrainment values during lidocaine compared to the unsuppressed stimulation condition for ROI locations of HLS1 and FLS1 (HLS1: left, $p = 0.018$, right, $p = 0.016$; FLS1: left, $p = 0.019$, right, $p = 0.018$) but not for V1 (condition (left: $p = 0.165$, right: $p = 0.11$) (Figure 3.4B). Similar results were observed for glutamate receptor antagonism (CNQX+MK-801) at HLS1 (left, $p = 0.011$, right, $p = 0.009$), FLS1 in the left hemisphere only (left: $p = 0.015$; right: $p = 0.062$), and V1 (left: $p = 0.046$, right: $p = 0.05$) (Figure 3.4B). During post-mortem stimulation, all entrainment values were significantly lower than during unsuppressed stimulation (HLS1: left, $p = 0.001$, right, $p < 0.001$; FLS1: left, $p = 0.001$, right, $p < 0.001$; V1: left, $p = 0.01$, right: $p = 0.009$) (Figure 3.4B). Overall, these findings show that field stimulation entrains VSD activity across

multiple cortical regions, with little to no artifact apparent during activity suppressing conditions.

3.4.3 Spontaneous slow oscillation VSD propagation dynamics fall into major pattern motifs

The main aim of the current work was to examine the influence of field stimulation on SO propagation dynamics. Therefore, it was imperative to first systematically describe SO propagation under spontaneous conditions. We tracked propagation patterns on a cycle-by-cycle basis using the Hilbert transform and clustered these cycles into propagation pattern groups (see Materials and Methods). During the spontaneous slow oscillation (baseline) two major propagation patterns emerged across all experiments (Figure 3.5A-D) out of an average of 14±1 patterns detected. These pattern were the anterior lateral-to-posterior medial (AL-PM) pattern, which showed activity starting in anterior lateral portions of the brain and propagating in a linear fashion to posterior medial regions, and the opposite pattern with a posterior medial-to-anterior lateral (PM-AL) direction of propagation (Figure 3.5A-D). For most experiments (n = 9) the AL-PM pattern was the most common with the PM-AL pattern appearing as the second major pattern, and the opposite was true for the remaining experiments (n = 5) (Figure 3.5B-D).

When examining the start (initiation) and end (termination) points of propagation for every cycle (across all experiments) for each major pattern, the spatial distribution of both start and end points was highly variable (Figure 3.5E). The AL-PM pattern showed a high proportion of start points in the somatosensory areas (0.81 across S1), especially in FLS1 (0.32), and end points mainly in posterior regions (0.64 across V1, V2, pTLP, RS) (Figure

3.5F – left). For the PM-AL pattern on the other hand, the start points were more broadly distributed across posterior medial areas with the majority of start points residing outside of the somatosensory areas (S1, 0.73) while end points were mainly within the somatosensory region (S1, 0.87) (Figure 3.5F – right). Pattern likelihood was not correlated with the strength of the VSD SO on individual cycles ($r^2 = 1.4e^{-5}$ $p > 0.05$; Figure 3.5G).

We noted several unique propagation patterns under spontaneous conditions that were less common but nevertheless present across experiments: patterns with multiple start (initiation) points, those with multiple end (termination) points, those with both start and end points located in posterior regions of the brain and asymmetrical patterns with start and end points appearing with a time lag across hemispheres (Figure 3.6). The most common of these patterns was the multiple end point pattern representing 0.13±0.02 proportion of all patterns (Figure 3.6B) with the other three patterns appearing less frequently (0.03 – 0.06; Figure 3.6B).

In order to make a comparison of propagation dynamics in the mouse VSD model with our rat recordings, we constrained propagation analysis to three cortical sites across M1 analogous to our electrode array in Chapter 2. In accordance with the rat results, we noted two major propagation patterns across M1 along an anterior-posterior plane (Figure A.2, see appendix A). Also in line with the rat data, during the application of sine wave stimulation we noted an increase in the anterior-to-posterior pattern although this increase was not significant on average (Figure A.2, see appendix A), likely due to the already higher proportion of the anterior-to-posterior pattern during baseline conditions in comparison to the rat results (c.f. Figure 2.2).

3.4.4 Field stimulation dramatically alters and stereotypes slow oscillation propagation dynamics

We tracked cycle-by-cycle propagation during field stimulation in the same fashion as for spontaneous data (filtered to include stimulation range: 1.1 – 1.9 Hz; c.f. Figure 3.5). During stimulation, propagation was altered and the major propagation pattern did not overlap with any existing patterns during baseline (Figure 3.7). On any given cycle, activity could initiate at multiple variable locations but consistently terminated within the somatosensory region (S1; 0.65), with the largest proportion in the posterior somatosensory area (S1p, 0.32) (Figure 3.7A,B). This region includes the somatosensory trunk area (TrS1) and an unassigned area (UnS1) (Figure 3.7B – S1p, dark purple). For stimulation during lidocaine, glutamate receptor antagonism and post-mortem, VSD activity was substantially weaker than during unsuppressed stimulation (Figure 3.7A) and had a very different spatial profile (Figure 3.7A - inset) with start and end points distributed around the edges of the craniotomy window, reflecting a pure artefactual component of stimulation (Figure 3.7B).

Field stimulation did not only alter SO propagation patterns but also stereotyped its activity creating a less dynamic oscillation. During baseline conditions, our clustering algorithm detected 14±1 propagation patterns which decreased significantly during stimulation to 7.6±1 patterns ($p < 0.001$; Figure 3.8A – left). Likewise, the proportion of all patterns that is represented by the single major pattern doubled during stimulation (0.52±0.05) compared to baseline (0.25±0.02) ($p < 0.001$; Figure 3.8A – right). There was no change during stimulation in the propagation index (change in area of activation per frame; $p = 0.34$) or velocity of propagation ($p = 0.44$) (Figure 3.8B). Importantly, stimulation applied during lidocaine, glutamate receptor antagonism and post-mortem showed significantly

lower propagation index values (lidocaine: $p = 0.02$; CNQX+MK-801, $p = 0.043$; dead: $p = 0.002$) compared to baseline (Figure 3.8B). This suggests that there was no true propagation of activity during activity suppression and that the stimulation artifact does not propagate.

When examining propagation pattern evolution in time, under baseline conditions any given propagation pattern could repeat in doublets above what is expected from a randomized dataset and up to a maximum of 4 cycles in a row (Figure 3.8C – left). However, during field stimulation activity was less dynamic with patterns more likely to appear in long sequences, up to 40 consecutive cycles (Figure 3.8C – right).

3.4.5 Decoupling of interhemispheric VSD activity following the cessation of field stimulation

Immediately following the cessation of field stimulation (0-8 min post-stim) we noted suppression of EEG activity ($p = 0.008$) and VSD activity specifically in one of the two hemispheres (VSD spectra: $p = 0.021$; RMS: $p = 0.015$) with recovery of activity appearing from 30 minutes onwards (30 and 75 min; VSD: $p > 0.05$; RMS: $p > 0.05$) and no change at any time-point for the opposite hemisphere following the cessation of stimulation (VSD: $p > 0.05$; RMS: $p > 0.05$) (Figure 3.9A-E). In order to understand this suppression effect we used resistors across our stimulation configuration to measure the amount of current that was delivered across each hemisphere (see Materials and Methods section). In all experiments for which this measure was obtained, the hemisphere demonstrating suppression received a greater amount of current than the other (Figure 3.9F) and there was a significant decaying exponential relationship between the amount of current delivered per

hemisphere and the VSD RMS activity (r^2 =0.35, $p < 0.001$; Figure 3.9G), thus showing that the suppression effect was correlated with the amount of current delivered.

When examining SO propagation following the cessation of field stimulation, activity appeared similar to baseline for the unsuppressed hemisphere with a predominantly AL-PM direction of propagation for all time-points post-stim (Figure 3.10 A-C). For the suppressed hemisphere on the other hand, very little activity propagation was apparent immediately following the cessation of stimulation with the resumption of a normal pattern of activity at 30 and 75 minutes (Figure 3.10A). There was no difference from baseline in the number of pattern groups detected following the cessation of stimulation for any time point ($p > 0.05$ for all; Figure 3.10D – left). However, the single major pattern identified (the AL-PM) represented a higher proportion of all patterns immediately following the cessation of stimulation ($p = 0.029$) but not for any other time point ($p > 0.05$ for all) (Figure 3.10D – right). The propagation index was significantly decreased compared to baseline specifically in the suppressed hemisphere immediately following the cessation of stimulation ($p = 0.038$) but not for later time points in the same hemisphere or any time point in the opposite hemisphere ($p > 0.05$ for all) (Figure 3.10E). Propagation velocity was decreased in 6 out of 7 experiments in the suppressed hemisphere immediately after the cessation of stimulation and this effect was marginally significant on average ($p = 0.052$; Figure 3.10F) with no change compared to baseline for any other time point in either hemisphere ($p > 0.05$ for all; Figure 3.10F). These results suggest that even with a symmetrical stimulation electrode implantation configuration (c.f. Figure 3.1A), it is possible to deliver uneven amounts of current to each hemisphere and to decouple the interhemispheric activity following stimulation.

3.5 Discussion

We show here that the application of sinusoidal field stimulation at frontal regions in the urethane-anesthetized mouse entrains VSD activity across the cortex and alters spontaneous SO propagation dynamics. Under spontaneous conditions, SO propagation was dynamic with two major opposing propagation pattern directions appearing along an anterior lateral – posterior medial plane. When applying field stimulation, SO propagation was altered to reflect a new propagation pattern that was not present under spontaneous conditions. Field stimulation also stereotyped propagation causing many repetitions of the same pattern cycle after cycle with less available alternate patterns. Following the cessation of field stimulation, we observed a hemisphere specific silencing of activity and decoupling of interhemispheric propagation. Given that field stimulation has been used to enhance sleep-dependent memory consolidation our results highlight important mechanistic considerations for how such stimulation may be used to target and alter relevant cortical interactions.

3.5.1 Entrainment of VSD activity with sinusoidal field stimulation

We observed entrainment of VSD activity to the stimulation sine-wave which was applied at a faster frequency (1.67 Hz) than the endogenous SO (~ 0.5 – 0.8 Hz). Activity was entrained across the entire cortex with somewhat weaker effects at locations further (more posterior) to the stimulation sites. This is in line with previous work from our group and others showing that field stimulation entrains electrical activity at cortical and hippocampal sites, including local-field and unit activity (Greenberg and Dickson, 2013;

Marshall et al., 2006; Ozen et al., 2010). Cortical SO activity has also been successfully entrained using transcranial magnetic fields (TMS) (Massimini et al., 2007), optogenetic (Beltramo et al., 2013; Kuki et al., 2013) and auditory (Ngo et al., 2013) stimulation. We also found that during stimulation there was an increase in spectral and RMS activity at the exact stimulation frequency, and a decrease in spectral power and RMS level for the endogenous SO frequency. We have previously shown that during field stimulation cortical power and cortico-cortical coherence at the SO frequency decreases compared to baseline conditions (Greenberg and Dickson, 2013). This suggests that the applied faster rhythm recruits cortical networks away from their natural participation in the SO rhythm, perhaps creating competition between the external and internal rhythm generators. When applying field stimulation under the influence of lidocaine, glutamate receptor antagonism and post-mortem, entrainment of the VSD signal to the stimulation phase was observed but this entrainment was magnitudes of order weaker than under unsuppressed stimulation and is thus attributed to a negligible artifact component.

3.5.2 Complex spontaneous SO propagation dynamics

We tracked spontaneous SO propagation on a cycle by cycle basis and applied a clustering algorithm to separate patterns into groups. Spontaneous propagation showed ~14 pattern groups with two opposing patterns along an anterior lateral – posterior medial plane being the most common within and across experiments. Of these two patterns, the anterior-to-posterior direction (AL-PM) was more prevalent in the majority of experiments (9/14) which is consistent with previous research showing mainly anterior-to-posterior SO propagation (Massimini et al., 2004; Nir et al., 2011; Stroh et al., 2013). Our observation of

multiple possible initiation and termination zones is also highly consistent with previous work in human (Massimini et al., 2004; Nir et al., 2011) and animal studies (Amzica and Steriade, 1995a; Mohajerani et al., 2010; Volgushev et al., 2006; Vyazovskiy et al., 2009). The finding of opposing directional patterns matches well with our previous work using a simple electrode array in rat motor cortex where we showed that patterns of opposing direction compete for expression (Greenberg and Dickson, 2013). We also demonstrate that there is a level of predictability in SO propagation whereby a specific pattern is more likely to repeat on the subsequent cycle, which is also in congruence with our previous work (Greenberg and Dickson, 2013). Beyond the two major patterns, we describe less common patterns with unique complex features such as multiple initiation and termination zones on a given cycle, propagation constrained to posterior regions and asymmetrical propagation. This finding is partially consistent with previous work showing that SO propagation examined on a finer spatial scale exhibits many complex non-linear features (Hangya et al., 2011; Huang et al., 2004; Mohajerani et al., 2010).

The velocity of propagation under spontaneous conditions in our mouse model was ~ 18 mm/s which is slower compared to SO propagation reported for rats (~25-140 mm/s) (Fucke et al., 2012; Greenberg and Dickson, 2013; Vyazovskiy et al., 2009), and even more dramatic, compared to humans (> 2 m/s) (Massimini et al., 2004). This velocity difference across species can be interpreted as an evolutionary scalable property whereby larger brains make use of disproportionally more long-range cortical connections to compensate for increased distance (but unchanging maximal axonal conduction) between cortical regions (Buzsáki, 2006; Buzsáki et al., 2013).

3.5.3 Effect of field stimulation on SO propagation dynamics

The main aim of the current work was to assess how sinusoidal field stimulation influences SO propagation dynamics. We show here that field stimulation drastically alters propagation, introducing a stereotyped pattern with distributed initiation zones and a consistent termination zone in the posterior primary somatosensory cortex. The pattern detected during stimulation was not present during baseline conditions, represented a larger proportion of all detected patterns, and tended to repeat for many consecutive cycles. To our knowledge, this is the first demonstration of field stimulation influence on SO propagation across multiple cortical regions. Previously, we have demonstrated that field stimulation biases SO propagation in an anterior-to-posterior direction using a three-electrode array in M1 (Amzica and Steriade, 1995a; Greenberg and Dickson, 2013). Our current findings are consistent with a general interpretation of an anterior-to-posterior direction of propagation during stimulation. However, the limited cortical information in our previous work occluded the description of the complex spatial trajectory of such propagation and its comparison with the spontaneous trajectories across widespread functional regions.

3.5.4 Implications for memory consolidation

Given that electrical field stimulation during SWS has been shown to improve memory consolidation (Binder et al., 2014a; Marshall et al., 2006), an understanding of how stimulation might alter SO propagation dynamics may influence memory function is mechanistically relevant for memory processes. During spontaneous SO conditions we showed a dynamic SO with constantly alternating propagation patterns cycle to cycle, while during stimulation, propagation was altered in both its pattern trajectory and its stereotypy.

These results may suggest that while spontaneous SO is well suited to consolidation a variety of memories reflected in the activation of many various network interactions from cycle to cycle, perhaps the application of field stimulation can select specific motifs and strengthen their relevant functional associations (and underlying memories).

In line with this idea, it has been suggested that on every wave the cortical SO may select specific hippocampal cell assemblies, and associated experiences, that will be replayed across hippocampo-neocortical networks in that given window of activity (Battaglia et al., 2004; Bendor and Wilson, 2012; Dickson, 2010; Isomura et al., 2006; Ji and Wilson, 2007; Rolls, 2000; Sirota et al., 2003). Field stimulation may be suited to bias these interactions since it has been shown by us and others (Ozen et al., 2010) to successfully entrain hippocampal activity likely by way of direct entorhinal input from the temporoammonic path. Even more strikingly, we have recently demonstrated that field stimulation increases hippocampal sharp-wave ripple events and cortical spindles and enhances cortico-hippocampal synchrony for both slow and gamma range networks (Greenberg et al., 2016). Therefore, altering cortical SO propagation using field stimulation likely selects which cortico-hippocampal assemblies are able to participate in and strengthen their interplay. Future work may determine how various stimulation locations may elicit distinct propagation patterns and how those patterns may relate to the targeting of specific memories.

3.5.5 Hemisphere specific suppression following the cessation of field stimulation

An unexpected finding of the current study was the suppression of VSD activity specific to a single hemisphere immediately following the cessation of stimulation with a recovery of activity within ~30 min. Under spontaneous conditions, VSD activity shows

very high inter-hemispheric concordance (Chan et al., 2015; Mohajerani et al., 2013; Mohajerani et al., 2010) which likely relies on the long-range connections of the corpus callosum (Mohajerani et al., 2010). In accordance with this, we show here that under spontaneous conditions, SO propagation was well mirrored across hemispheres with non-symmetrical patterns representing only a small minority of all patterns (~5%). During field stimulation, activity was also symmetrical and only lost its symmetry following the cessation of stimulation due to suppressed activity in one hemisphere with surprisingly unaffected propagation in the left hemisphere. This suppression likely corresponded to stronger current delivery to the suppressed hemisphere during the stimulation epoch. This was a surprising finding since our stimulation electrode implantation was symmetrical across the two hemispheres and was adapted from previous studies (Binder et al., 2014a; Greenberg and Dickson, 2013; Marshall et al., 2006; Ozen et al., 2010). Therefore future studies should use current instead of voltage generators to ensure more homogenous current delivery across hemispheres.

3.5.6 Conclusion

We demonstrate here for the first time the ability of sinusoidal electrical field stimulation to entrain cortical VSD networks and alter SO propagation dynamics both during and following such manipulation. These results bring us closer to understanding how such stimulation can be used in a targeted manner to enhance or disrupt hippocampal-dependent memory consolidation during offline states.

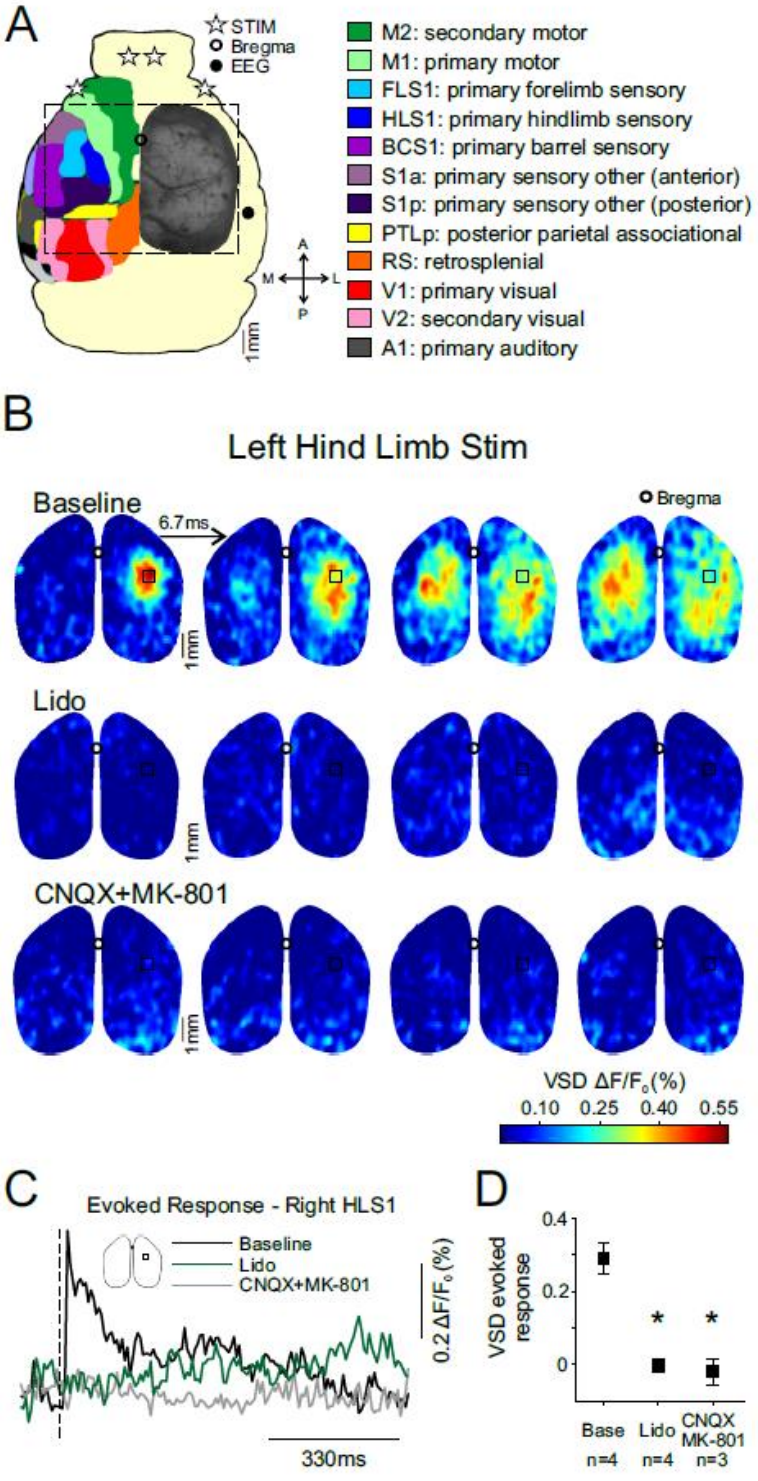

Figure 3.1 Sensory evoked responses are abolished with the activity blockers lidocaine and CNQX+MK-801

A. Standardized mouse cortical map with colored regions indicating cortical areas specified in the legend on the right. Open circle indicates position of bregma. Stars indicate positions of sine-wave stimulation electrodes. Solid circle indicates position of EEG electrode. Gray image overlaid on the right hemisphere shows brain surface in one experiment obtained with the VSD camera. Dotted box shows craniotomy window used for VSD. **B.** VSD images for a single experiment showing evoked response to the stimulation of the left hind limb for baseline, lidocaine and CNQX+MK-801 conditions. Note that the evoked response is abolished after application of the activity blockers. Black box indicates pixels used for the ROI shown in C. **C.** Evoked response shown over time for a ROI taken around HLS1 in the right hemisphere for the same experiment as shown in B for the three conditions. Brain inset shows location of ROI. Dotted line shows time of current delivery to the left hind limb. **D.** Average peak evoked response across experiments for each of the conditions.

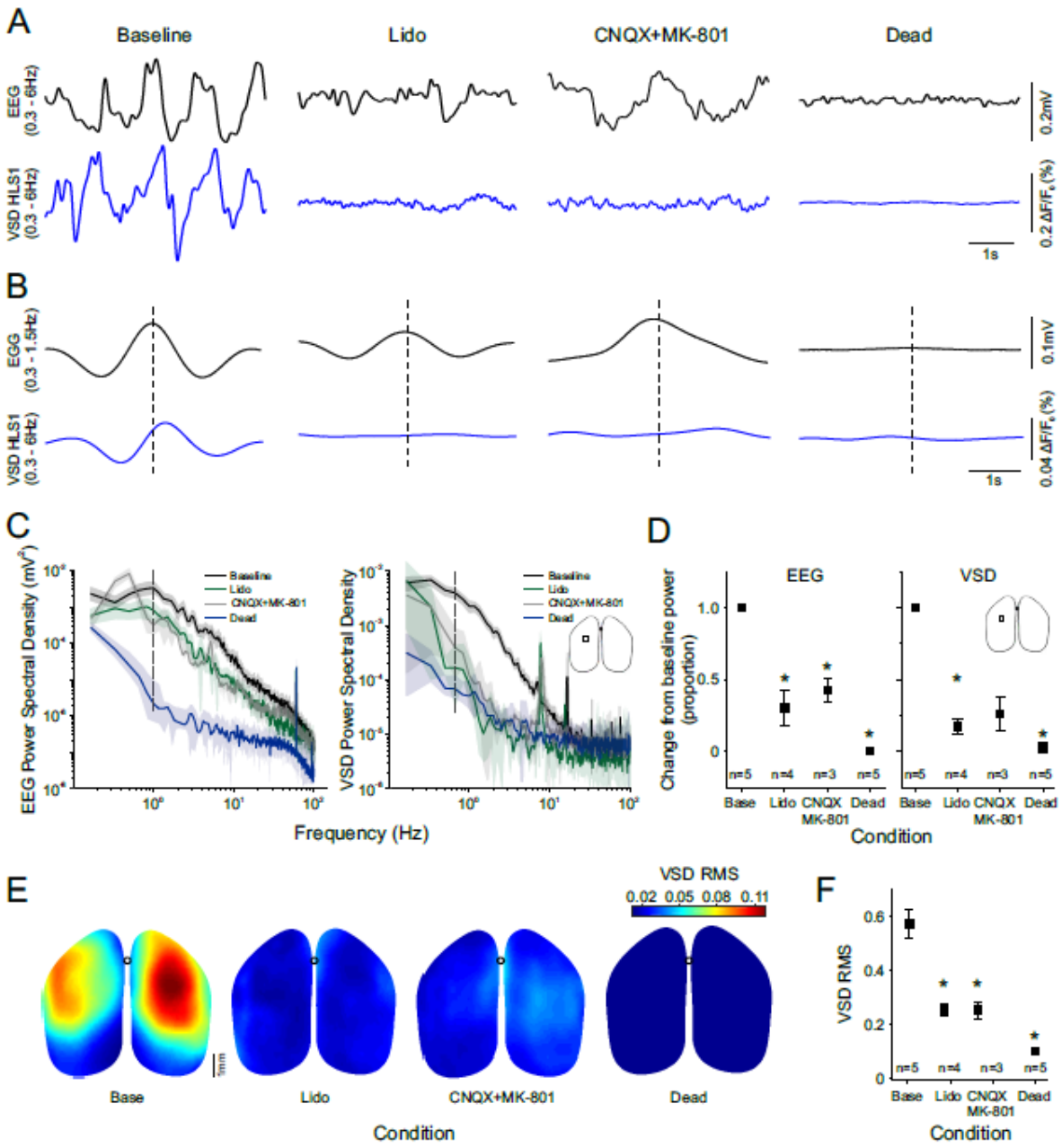

Figure 3.2 Spontaneous EEG and VSD signals are suppressed with the activity blockers lidocaine and CNQX+MK-801

A. Example EEG (black) and VSD (blue) traces filtered in the slow/delta range (0.3-6 Hz) for a single experiment during baseline, lidocaine, CNQX+MK-801 and following death. VSD traces are obtained from the HLS1 ROI in the left hemisphere. Note strong slow-wave correspondence between the EEG and VSD traces during baseline and disruption of both

signals for the drug and dead conditions, especially in the VSD signal. **B.** Slow oscillation triggered EEG and VSD traces (0.3 – 1.5 Hz) for all conditions. Triggering was performed on the peak positivity of the EEG slow-wave. Note correspondence between the EEG and VSD traces and suppression of the VSD slow-wave during the application of activity blockers and death. Slow wave detection was still possible in the EEG trace for the drug conditions. **C.** EEG and VSD power spectra for all conditions for the same experiment as in A and B. Brain inset shows ROI location for the VSD power spectra. Note wide-band power suppression in the EEG and VSD spectra with the application of activity blockers and following death. Dotted lines indicate slow oscillation frequency of 0.8 Hz. **D.** Proportion of change in power from baseline for the slow oscillation frequency (0.5 - 0.8 Hz) across experiments for all conditions. Brain inset shows location of ROI for VSD power. **E.** RMS VSD maps for each condition for the same experiment as in A, B and C. RMS measures for each pixel were taken for three-minute segments. **F.** Average RMS for all pixels across experiments for each condition.

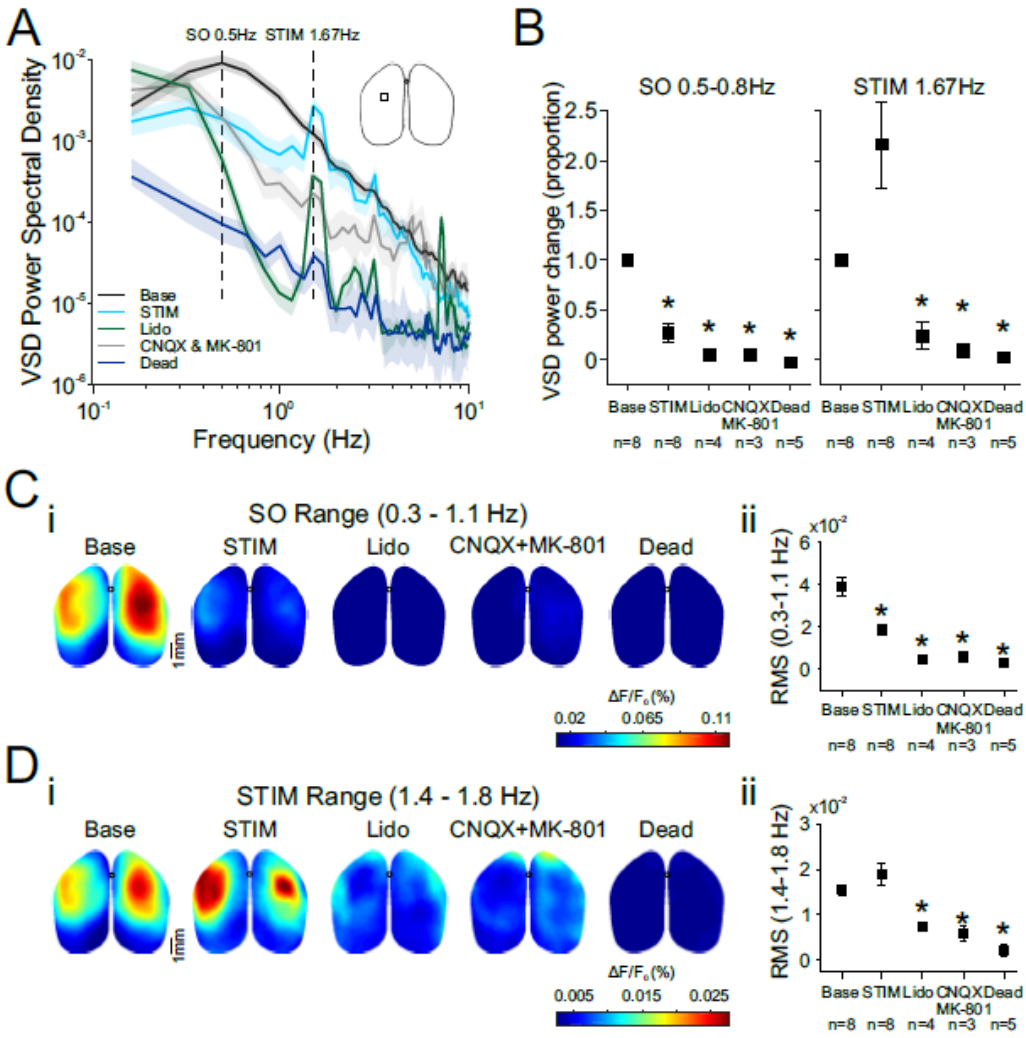

Figure 3.3 Sinusoidal field stimulation alters slow-wave EEG and VSD spectral properties

A. VSD power spectra during baseline as well as during the application of field stimulation under 4 conditions: unsuppressed (STIM), application of lidocaine, application of CNQX+MK-801 and following death. Brain inset shows location of ROI used for power calculation. Dotted lines indicate peak baseline slow oscillation frequency (0.5 Hz in this experiment) and the sinusoidal stimulation frequency (1.67 Hz). Note spectral peaks at the exact frequency of stimulation for all stimulation conditions with lower power in the drug and death conditions compared to the STIM condition. Stimulation frequency peaks during activity suppression conditions can be attributed to sole artifact, with magnitudes of order

weaker power compared to the unsuppressed STIM condition. **B.** Proportion of VSD power change from baseline across experiments for the peak slow oscillation frequency (0.5 – 0.8 Hz depending on the experiment) and for the stimulation frequency (1.67 Hz) for all conditions. Note weaker slow oscillation power for all stimulation conditions and a non-significant boost in the stimulation frequency power specific to the STIM condition (without activity suppression). **C.i**. RMS VSD maps computed for the slow oscillation range (0.3 – 1.1 Hz) on three-minute segments for all conditions in the same experiment as in A. **ii.** RMS for the slow oscillation range across experiments. **D. i.** RMS VSD maps computed for a frequency range (1.4 -1.8 Hz) that includes the stimulation frequency (1.67 Hz) for the same experiment as in A and C. **ii.** RMS for the stimulation range across experiments. Note weaker slow oscillation RMS during sine-wave stimulation (STIM) and non-significant boost in RMS during for the stimulation range. Also note that the artifact component RMS that appears for the stimulation range during activity suppression conditions is much weaker and spatially distinct when compared to the unsuppressed STIM condition.

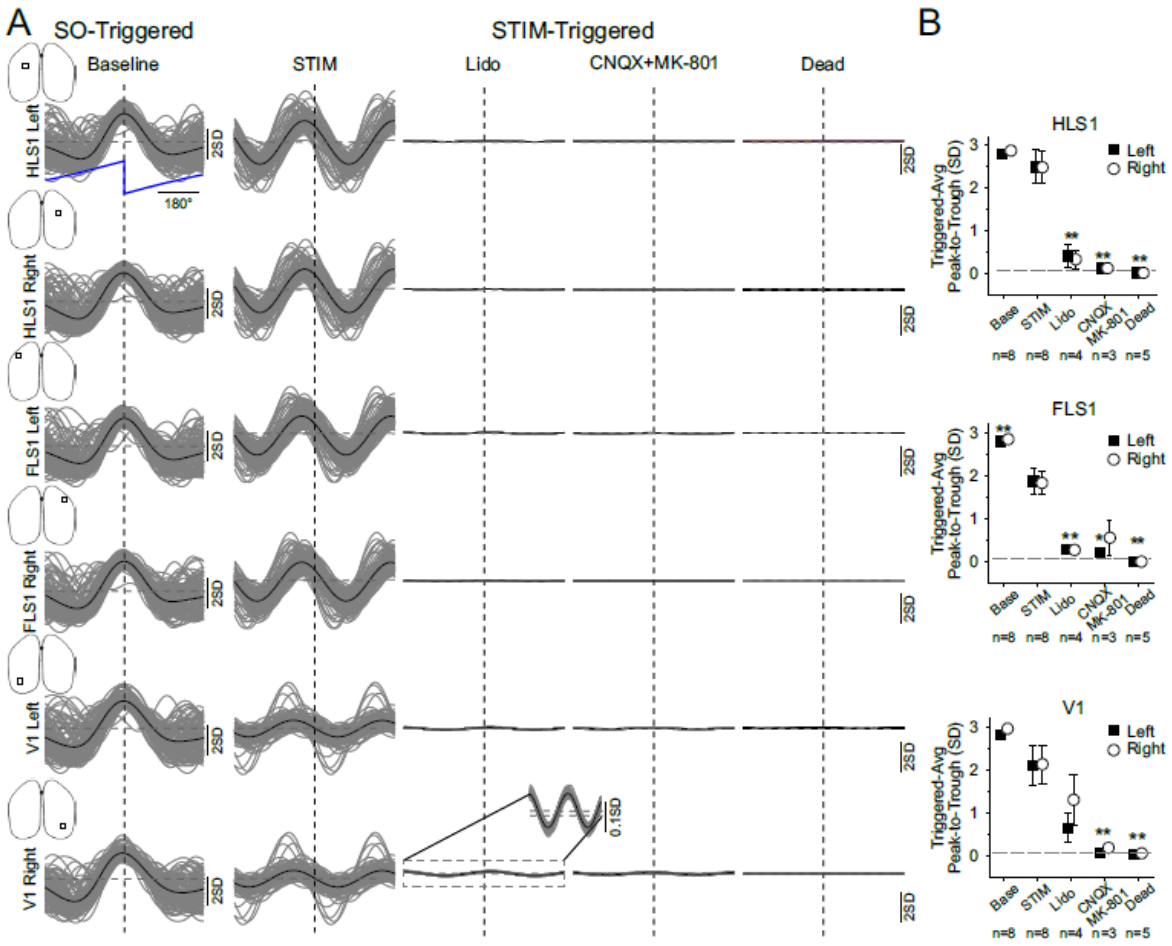

Figure 3.4 Sinusoidal field stimulation entrains VSD activity at multiple sites

A. Single VSD traces (gray) and average trace (black) taken from ROIs indicated by brain insets triggered on the slow oscillation peak for baseline and on the peak of the stimulation sine-wave during stimulation (STIM) as well as during activity suppression conditions using lidocaine, CNQX+MK-801 and following death. All traces are from the same experiment. Vertical dotted line indicates trigger time point at the peak of the slow-oscillation during baseline and at the positive peak of the stimulation wave for all other conditions. Horizontal dotted lines indicate 95th percentile confidence intervals based on triggered-averages of randomized time points. Inset for lidocaine in the right V1 shows expanded trace. Note that entrainment to stimulation wave is visible during lidocaine in expanded trace due to stimulation artifact, but the strength of the signal is weaker than during the unsuppressed STIM condition. **B.** Peak-to-peak SD values from the triggered-averages (same triggering

method as in A) for each condition across experiments for the three ROIs indicated in A, for both right and left hemispheres. Note that entrainment of VSD to the stim wave during stimulation is similar to the baseline entrainment to the SO but weaker for the activity suppression conditions (except for lidocaine condition in V1).

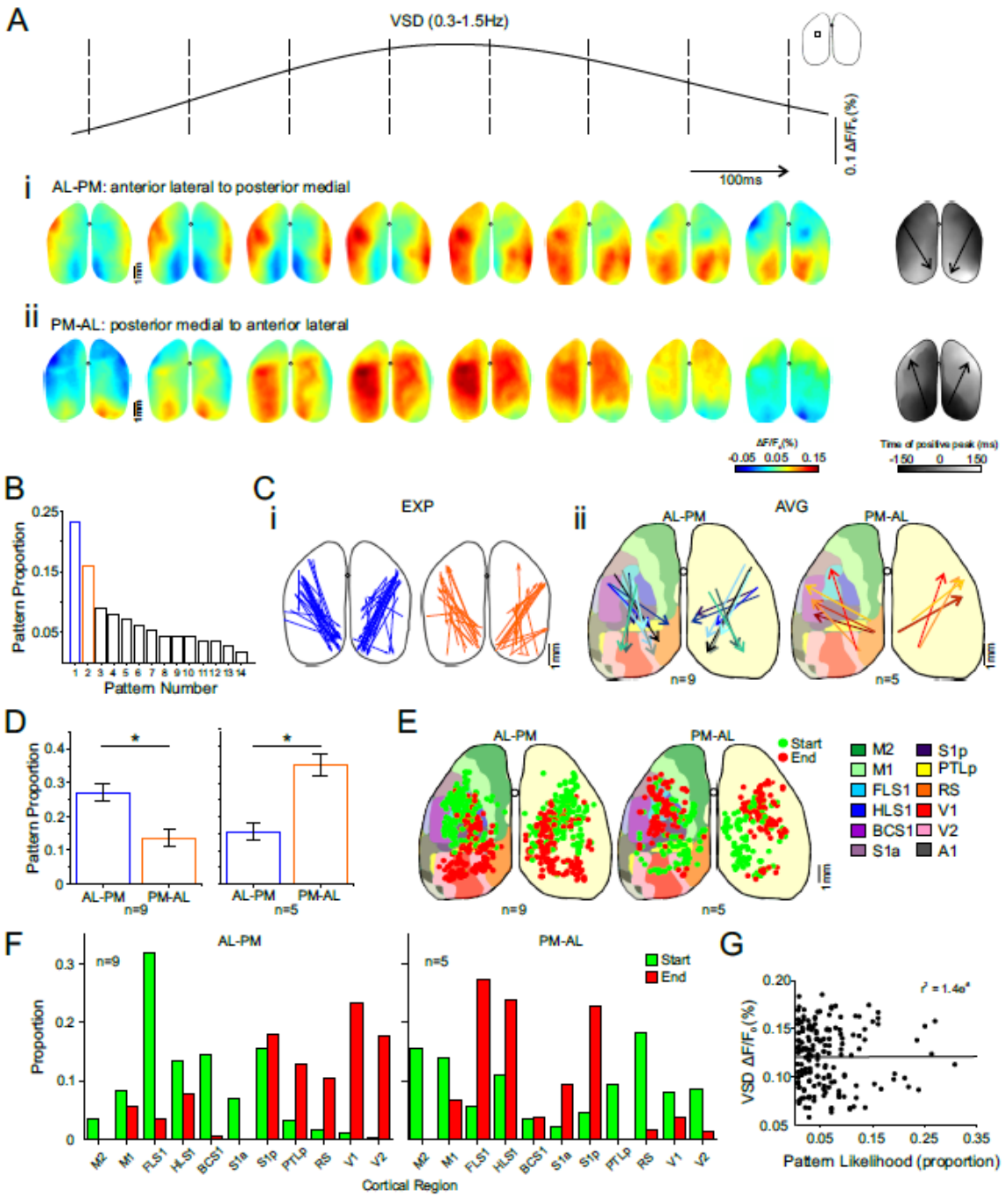

Figure 3.5 The spontaneous slow oscillation propagates in two major opposing directional patterns along an anterior-lateral – posterior-medial axis

A. Top: VSD trace showing positive peak of a single slow oscillation cycle for a ROI indicated in brain inset. Dotted lines indicate 8 time points along the cycle. Bottom: colored images show VSD maps filtered for the slow oscillation range (0.3 – 1.5 Hz) taken at the 8

time points indicated along the VSD trace at the top during a single cycle for i and ii. In i the given cycle showed a propagation pattern with activity (positive; warm colors) starting from anterior-lateral regions and ending in posterior-medial regions. In ii the opposite pattern is apparent with activity starting in posterior-medial regions and ending in anterior-lateral regions. Grey images on the right show time lags of positive peaks in VSD signals for each pixel for the given propagation cycle. Positive peaks were identified using Hilbert phase and a lag of zero indicates positive peak at the ROI of HLS1 (top brain inset). Arrows show average gradient direction from the earliest to latest time lags. **B.** Proportion of each propagation pattern group identified for a single experiment by a hierarchical clustering algorithm. Blue bar indicates the major anterior-lateral to posterior-medial (AL-PM) pattern shown in Ai and the orange bar indicates the second major opposite pattern in the posterior-medial to anterior-lateral (PM-AL) direction (as in Aii). **C.** i. Trajectory arrows as in A plotted on brain mask for every cycle of each of the two major patterns: AL-PM in blue and PM-AL in orange. ii. Average trajectory arrows across cycles for the single major pattern for every experiment plotted on standardized cortical map. Left map shows arrows for 9 experiments in which the AL-PM pattern was the major pattern, and right map shows the remaining 5 experiments in which the PM-AL pattern was the major pattern. **D.** Proportion of all patterns that the major and second major patterns represent across experiments separated by whether the major pattern was an AL-PM or PM-AL pattern. **F.** Proportion of start and end points from D represented in each cortical region. **E.** Start and end points of activity propagation plotted on standardized cortical maps for every cycle of the major pattern in every experiment separated by whether the major pattern was an AL-PM or PM-AL pattern (left and right maps respectively). Legend indicates cortical areas represented in color on standardized maps. **G.** Pattern likelihood for every pattern group detected for each experiment against the average peak VSD signal strength taken at HLS1 ROI for each pattern group. There was no correlation and thus the strength of a given SO cycle does not appear to relate to the observed propagation pattern.

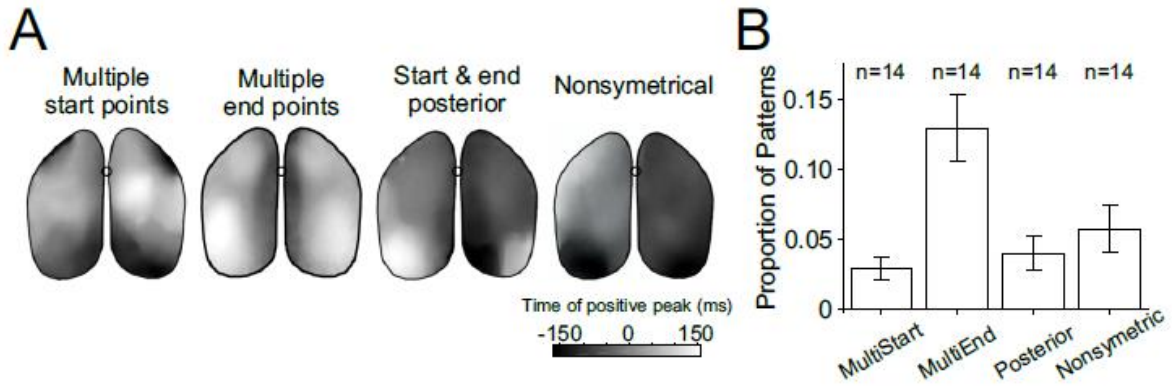

Figure 3.6 Spontaneous slow oscillation propagation patterns that are uncommon show distinct features

A. Hilbert phase time-lag average maps showing propagation patterns for a single experiment that fall into 4 groups: multiple start locations, multiple end locations, both start and end locations in posterior regions of the brain and asymmetrical propagation with activity starting earlier in one hemisphere. **B.** The 4 patterns from A as proportion of all patterns across experiments. Note that the most common of these patterns is the multiple end point pattern.

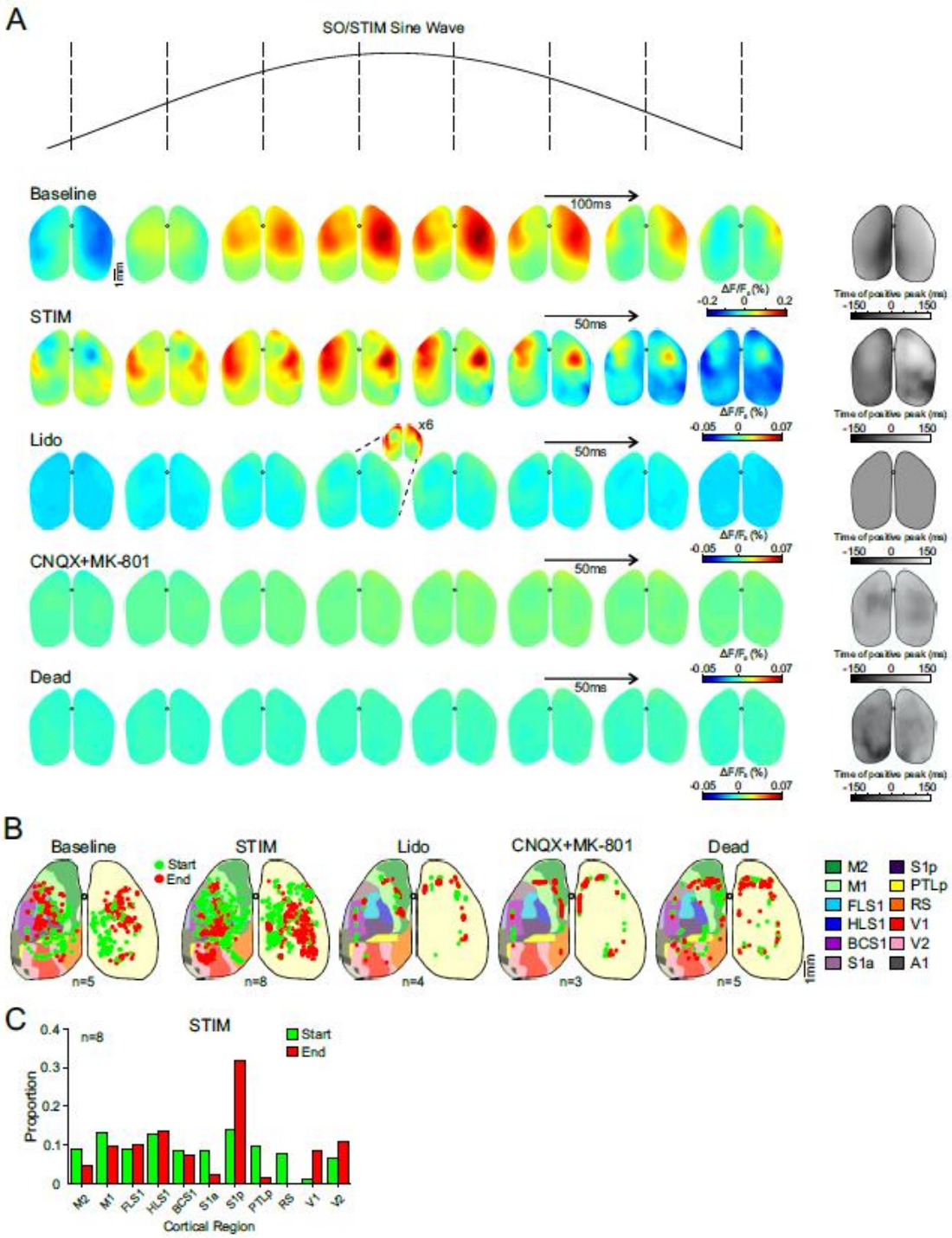

Figure 3.7 Sinusoidal field stimulation alters slow oscillation propagation dynamics

A. Top: example sine-wave trace representing the positive peak of a single slow oscillation or stimulation cycle. Dotted lines indicate 8 time points along the cycle. Bottom: colored images show VSD maps filtered for the slow oscillation range (0.3 – 1.5 Hz) for baseline or

for the stimulation range (1.5 – 2.0 Hz) for the stimulation conditions taken at the 8 time points indicated along the trace at the top during a single cycle. For each condition the cycle depicted is taken from the major pattern group detected. The baseline cycle shows a PM-AL propagation pattern which was the major pattern in this experiment. During stimulation, the major propagation pattern appears altered. The lidocaine, CNQX+MK-801 and dead conditions show activity that is on a weaker scale compared to STIM and with a markedly different spatial pattern with little visible change (propagation) from frame to frame. Grey images on the right show time lags of positive peaks in VSD signals for each pixel for the given propagation cycle. Positive peaks were identified using Hilbert phase and a lag of zero indicates positive peak at the ROI of HLS1 for baseline and peak of stimulation sine wave for all other conditions. **B.** Start and end points of activity propagation plotted on standardized cortical maps for every cycle of the major pattern for each condition in every experiment. The baseline map is the same as shown in Figure 5 for the PM-AL pattern and chosen to reappear here as this was the major pattern for the experiment shown in A. Note altered distribution of start and end points for the STIM condition that does not resemble either of the two major baseline patterns (c.f. Figure 5). The start and end points for the activity suppression conditions are scattered around the craniotomy edges and reflect the artifact spatial configuration. Legend indicates cortical areas represented in color on standardized maps. **C.** Proportion of start and end points from B represented in each cortical region for the stimulation condition.

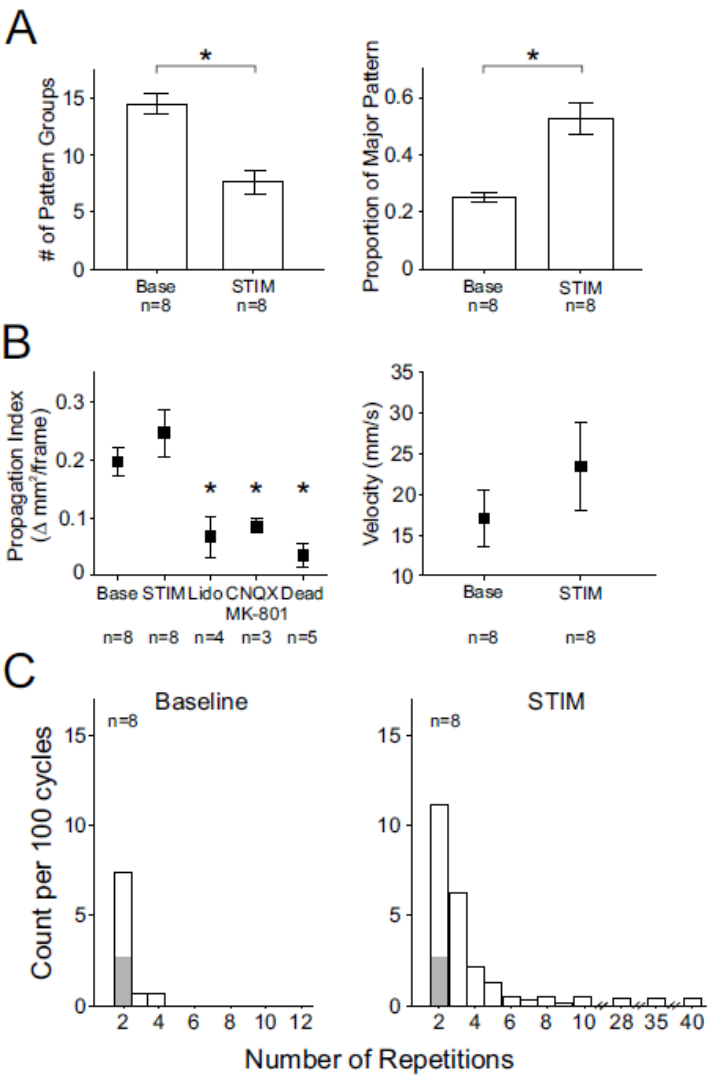

Figure 3.8 Sinusoidal field stimulation stereotypes propagation patterns

A. Left: The number of pattern groups identified with the hierarchical clustering algorithm across experiments for the baseline and stimulation conditions. Right: The proportion of all patterns that the major pattern represents across experiments for the baseline and stimulation conditions. **B.** Left: propagation index as a change in area of activation (number of pixels >2SD of VSD signal) per frame across experiments for baseline, stimulation and the three activity suppressing conditions. Note significantly lower propagation index values in the activity suppressing conditions suggesting that these conditions show static artifact which does not propagate over time. Right: Velocity of propagation calculated as mm/s traveled by the center of mass of activity (> 2SD) for baseline and stimulation conditions. **C.** Number of

repetitions on a next cycle basis per 100 cycles of any propagation pattern for baseline (left) and stimulation (right) conditions across experiments. Note that during baseline a given pattern did not repeat in succession more than four times but repeated up to 40 times in the stimulation condition. Grey area indicated pattern repetition expected by chance. Note that a pattern occurring in larger numbers than a doublet never occurred in our randomized dataset.

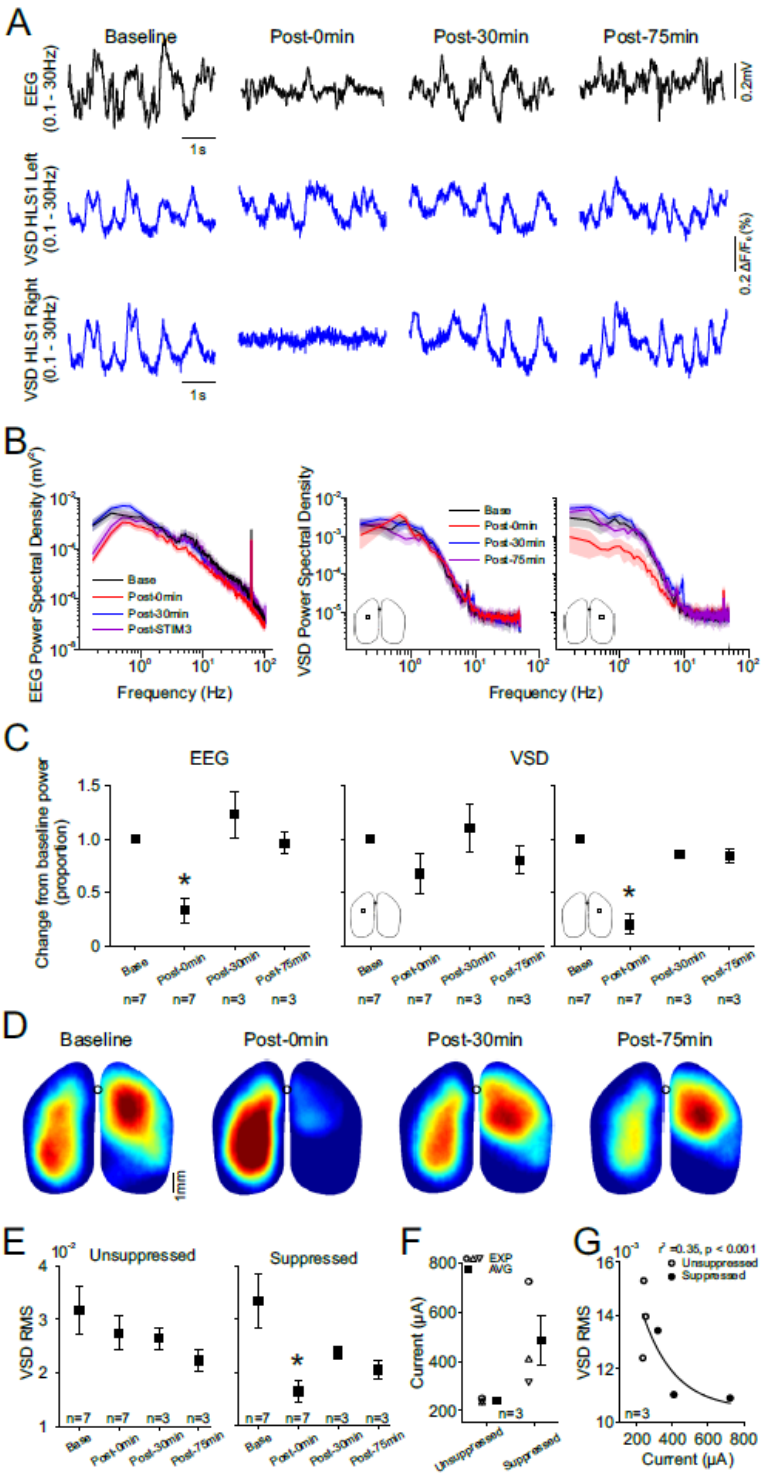

Figure 3.9 VSD activity in one hemisphere is suppressed immediately following the cessation of field stimulation

A. Example EEG (black) and VSD (blue, for left and right hemisphere) traces (0.1 – 30 Hz) for a single experiment during baseline, as well as for three time points following the cessation of stimulation: 0 min (immediately after), 30 and 75 min. Note activity suppression appearing in the EEG (positioned in the right hemisphere) as well as specifically in the right hemisphere in the VSD trace. VSD traces were taken from left and right ROIs in HLS1. **B.** Power spectra for EEG and VSD activity for baseline and for the three time points following the cessation of stimulation for the same experiment as in A. Spectra were computed on four-minute segments. Brain insets show the ROI locations used for VSD power spectra (left and right HLS1). Note spectral power suppression most visible in the VSD power spectrum for the right hemisphere. **C.** Proportion power change for the slow oscillation peak (0.5-0.8 Hz) from baseline for EEG and VSD data across experiments for all time points following cessation of stimulation. Note significant power suppression in the EEG and right hemisphere VSD specific to the time point immediately following the cessation of stimulation (0 min). All spectra from which power values were obtained were computed on four-minute segments as in B. **D.** RMS values for each pixel computed on four-minute segments for the same experiment as in A and B for baseline and for the three time points following the cessation of stimulation. Note lower RMS in the suppressed hemisphere at the 0 min time point. **E.** RMS values across experiments averaged across an entire hemisphere (unsuppressed and suppressed respectively) for baseline and the three time points following the cessation of stimulation. Note significant RMS suppression in the suppressed hemisphere immediately following the cessation of stimulation (0 min). Brain insets show portion of brain used to average RMS values. **F.** Amount of current delivered during stimulation for each of the three experiments for which we had current measures (open symbols) and on average (solid symbols) for the each hemisphere. Note higher current delivery for the suppressed hemisphere in all cases. **G.** VSD RMS for each hemisphere correlated against the amount of current delivered in each hemisphere. Open symbols indicate unsuppressed hemisphere and solid symbols indicate suppressed hemisphere. Note significant exponential decay where higher current delivery results in more RMS suppression in the given hemisphere.

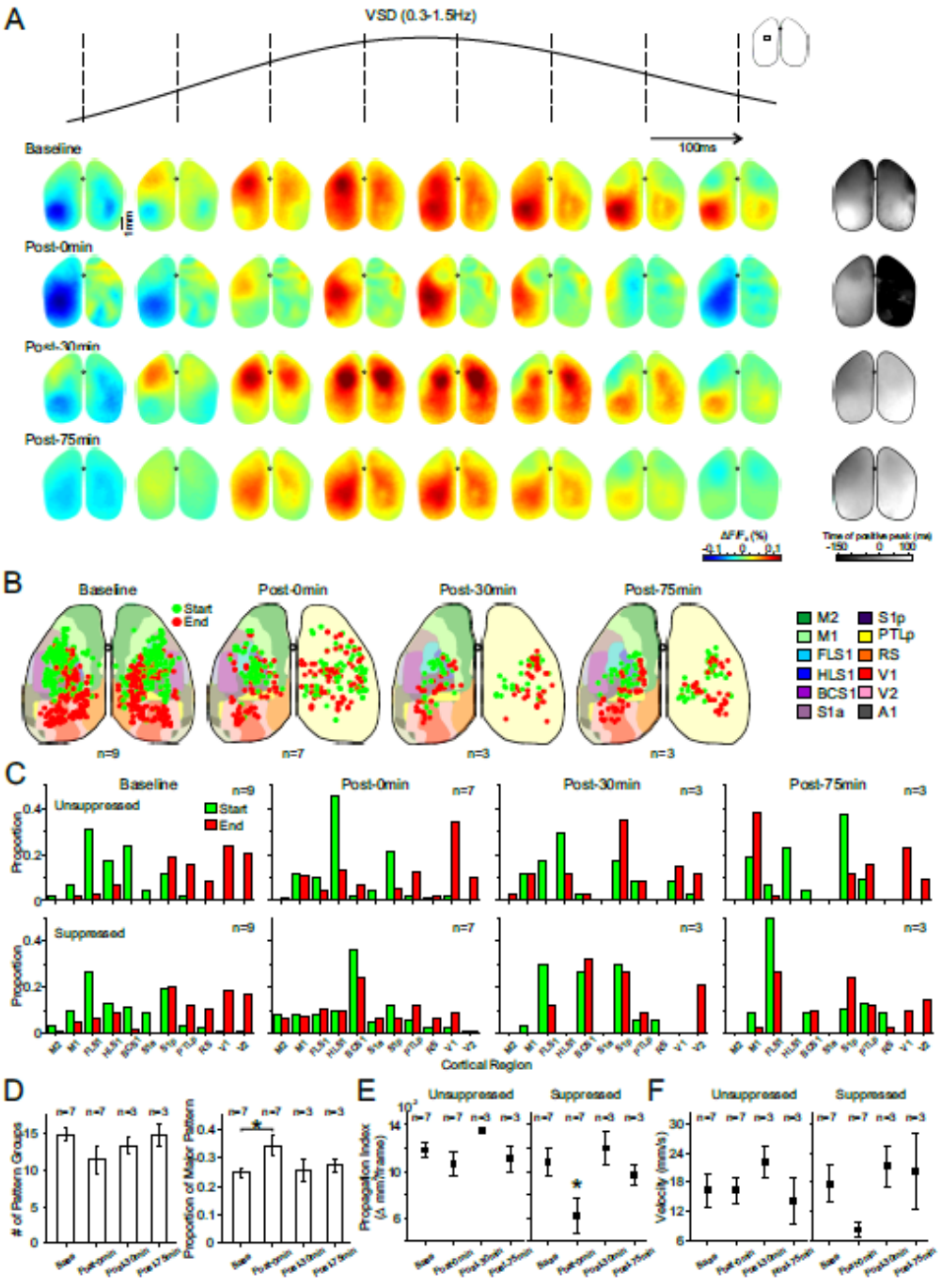

Figure 3.10 Slow oscillation propagation dynamics are altered following the cessation of sinusoidal field stimulation

A. Top: VSD trace showing positive peak of a single slow oscillation cycle for a ROI indicated in brain inset. Dotted lines indicate 8 time points along the cycle. Bottom: colored images show VSD maps filtered for the slow oscillation range (0.3 – 1.5 Hz) for baseline

and following the cessation of stimulation at 0, 30 and 75 min. Frames are taken at the 8 time points indicated along the VSD trace at the top during a single cycle. For each condition the cycle depicted is taken from the major pattern group detected. The baseline cycle shows an AL-PM propagation pattern which was the major pattern in this experiment. Note suppression of propagation in the right hemisphere immediately following the cessation of stimulation (0min) with a return to a normal appearing AL-PM pattern for the 30 and 75 min time points. Grey images on the right show time lags of positive peaks in VSD signals for each pixel for the given propagation cycle. Positive peaks were identified using Hilbert phase and a lag of zero indicates positive peak at the ROI of HLS1. **B.** Start and end points of activity propagation plotted on standardized cortical maps for every cycle of the major pattern for each condition in every experiment. The baseline map is the same as shown in Figure 5 for the AL-PM pattern and chosen to reappear here as this was the major pattern for the experiment shown in A. Note highly dispersed distribution of start and end points immediately following the cessation of stimulation (0 min). Legend indicates cortical areas represented in color on standardized maps. **C.** Proportion of start and end points from B represented in each cortical region for baseline and following the cessation of stimulation for the three time points. Start and end points were separated by hemisphere (unsuppressed and suppressed respectively; indicated by inset). **D.** Left: The number of pattern groups identified with the hierarchical clustering algorithm across experiments for baseline and for the three time points following cessation of stimulation. Right: The proportion of all patterns that the major pattern represents across experiments for baseline and for the three time points following cessation of stimulation. Note an increased proportion of representation by the major pattern for the 0 min time point compared to baseline. **E.** Propagation index as a change in area of activation (number of pixels >2SD of VSD signal) per frame across experiments for baseline and for the three time points following cessation of stimulation for each hemisphere (unsuppressed and suppressed respectively; indicated by brain inset). There was a significant reduction for the 0 min time point in the suppressed hemisphere compared to baseline suggesting that propagation in the suppressed hemisphere was hindered immediately following the cessation of stimulation. **F.** Velocity of propagation calculated as mm/s traveled by the center of mass of activity (> 2SD) for each hemisphere (unsuppressed and suppressed respectively; indicated by inset).

4 Stimulating forebrain communications: Slow sinusoidal electric fields over frontal cortices dynamically modulate hippocampal activity and cortico-hippocampal interplay during slow-wave states

Authors: Anastasia Greenberg[1], Tara A. Whitten[1] and Clayton T. Dickson[1,2,3]

[1]Neuroscience and Mental Health Institute, University of Alberta, Edmonton, AB, Canada, T6G 2E1

[2] Department of Psychology, University of Alberta, Edmonton, AB, Canada, T6G 2E9

[3] Department of Physiology, University of Alberta, Edmonton, AB, Canada, T6G 2H7

Acknowledgments: This work was supported by a Natural Science and Engineering Council of Canada (NSERC) grant # 249861 to CTD. AG was additionally supported by a Queen Elizabeth II Graduate Scholarship and a NSERC Alexander Graham Bell Canada Graduate Scholarship – Doctoral (CGS D). TAW was additionally supported by an Izaak Walton Killam Memorial Graduate Scholarship, an Alberta Innovates – Technology Futures Graduate Scholarship and an NSERC Alexander Graham Bell Canada Graduate Scholarship – Doctoral (CGS D). We would like to acknowledge Jesse Jackson and Kyle E. Mathewson for helpful editorial comments.

Published in:

NeuroImage, March 3, 2016

133:189-206

4.1 Abstract

Slow-wave states are characterized by the most global physiological phenomenon in the mammalian brain, the large amplitude slow oscillation (SO; ~ 1 Hz) composed of alternating states of activity (ON/UP states) and silence (OFF/DOWN states) at the network and single cell levels. The SO is cortically generated and appears as a travelling wave that can propagate across the cortical surface and can invade the hippocampus. This cortical rhythm is thought to be imperative for sleep-dependent memory consolidation, potentially through increased interactions with the hippocampus. The SO is correlated with learning and its presumed enhancement via slow rhythmic electrical field stimulation improves subsequent mnemonic performance. However, the mechanism by which such field stimulation influences the dynamics of ongoing cortico-hippocampal communication is unknown. Here we show - using multi-site recordings in urethane-anesthetized rats - that sinusoidal electrical field stimulation applied to the frontal region of the cerebral cortex creates a platform for improved cortico-hippocampal communication. Moderate intensity field stimulation entrained hippocampal slow activity (likely by way of the temporoammonic pathway) and also increased sharp-wave ripples, the signature memory replay events of the hippocampus, and further increased cortical spindles. Following cessation of high-intensity stimulation, SO interactions in the cortical-to-hippocampal direction were reduced while the reversed hippocampal-to-cortical communication at both SO and gamma bandwidths was enhanced. Taken together, these findings suggest that cortical field stimulation may function to boost memory consolidation by strengthening cortico-hippocampal and hippocampo-cortical interplay at multiple nested frequencies in an intensity-dependent fashion.

4.2 Introduction

Patterned synchronized oscillatory activity in the nervous systems has been suggested to play a role in neural information processing and storage (Buzsáki, 1998, 2006; Buzsáki and Draguhn, 2004). While the primary research focus has been on conscious states and online brain function, the importance of activity during offline states such as sleep has also been recognized. Specifically, slow-wave patterns during sleep have been pinpointed as an important element in aiding hippocampal-dependent memory consolidation (Born et al., 2006; Diekelmann and Born, 2010; Rasch and Born, 2013; Rauchs et al., 2005).

The signature event of slow-wave states (during both sleep and anesthesia) is the slow oscillation (SO; ~ 1 Hz). This rhythm is composed of alternations between active (UP/ON) and silent (DOWN/OFF) phases (Amzica and Steriade, 1995b; Steriade et al., 1993d). The SO has global influence across the forebrain, and organizes faster, local rhythms, such as gamma (Steriade, 2006; Timofeev and Steriade, 1997), spindles (Mölle, 2009; Nir et al., 2011; Steriade et al., 1993c), and even hippocampal ripples (Battaglia et al., 2004; Mölle, 2009; Sirota et al., 2003) into its active ON phase. This nesting of fast rhythms may allow for spike-timing-dependent synaptic modifications relevant for memory consolidation (Dan and Poo, 2004; Ji and Wilson, 2007). Indeed, during SWS, region-specific dynamics of the SO are also modulated by prior learning (Huber et al., 2004; Mölle et al., 2004).

Given that declarative memory consolidation is assumed to rely on communication between the hippocampus and cortex (Rasch et al., 2007; Sirota et al., 2003; Walker and Stickgold, 2004; Wierzynski et al., 2009), investigations of the spatiotemporal dynamics of the SO and its manipulation are critical for gauging how such interactions may influence

cortico-hippocampal interplay. The SO propagates from local foci across the cortex (Amzica and Steriade, 1995b; Massimini et al., 2004; Volgushev et al., 2006) and makes its way to the hippocampus likely via the entorhinal cortex (Isomura et al., 2006; Nir et al., 2011; Wolansky et al., 2006). The SO is known to group hippocampal sharp-wave ripples events (SPW-R) which can "replay" prior wake-related correlated cellular discharge (Ji and Wilson, 2007; Sirota et al., 2003; Wilson and McNaughton, 1994) and in turn can reciprocally influence the same cortical targets that initiated the sequence (Battaglia et al., 2004; Lee and Wilson, 2002; Logothetis et al., 2012; Peyrache et al., 2011; Wierzynski et al., 2009). Interestingly, replay during cortical UP states is coordinated across the hippocampus and cortex resembling prior behavioral cell pair correlations (Ji and Wilson, 2007). Importantly, boosting the SO using rhythmic electrical or sensory stimulation enhances future memory performance (Marshall et al., 2006; Ngo et al., 2013). However, what remains to be determined is how slow electrical field stimulation might actually alter hippocampal activity, and perhaps more importantly, cortico-hippocampal interplay.

Here we show that the application of slowly alternating sinusoidal electrical fields over the frontal cortex in urethane anesthetized rats alters inter-regional communication by entraining hippocampal activity and enhancing the occurrence of hippocampal sharp-wave ripples and cortical spindles at moderate intensities of stimulation. Unexpectedly, we found that in the period following high-intensity field stimulation there was a disruption of coherence in the cortical-to-hippocampal direction while coherence in the reversed direction was enhanced for both slow and fast (gamma) network rhythms. These results are the first to show that rhythmic field stimulation applied to the frontal regions of the brain can alter

network dynamics in the hippocampus as well as hippocampal-cortical interactions, an effect that could be critical for declarative memory consolidation.

4.3 Methods

4.3.1 Subjects

Recordings and stimulation (Figure 1A-C) were conducted in 18 male Sprague Dawley (SD) rats with a mean (± standard error of the mean; SEM) weight of 266.7 ± 8.6 g. Of these animals, 7 were used for recordings with 3 cortical sites and one hippocampal site (protocol 2; Figure 1A&B), a separate group of 7 were used for recordings with a single cortical site (site 2) and a linear probe in the hippocampus (protocol 3; Figure 1A) and a final separate group of 4 animals were used for recordings following the cessation of high-intensity stimulation using a single cortical electrode (site 3) and a linear probe in the hippocampus (protocol 1; Figure 1A&C). Spontaneous (baseline) recordings were obtained for all animals in all recording conditions.

4.3.2 Surgery and implantation

All surgical procedures conformed to the guidelines of the Canadian Council on Animal Care (CCAC) and were approved by the Biological Sciences Animal Policy and Welfare Committee of the University of Alberta.

Rats were initially anesthetized in a gas chamber with a 4% concentration of isoflurane in 100% O_2 (Benson Medical Industry Inc., Markham, ON) and later maintained at 2% administered via nose cone. Rats were implanted with a jugular vein catheter through which urethane (0.7 g/ml) was gradually administered (at ~0.03 – 0.08 ml per minute) to a final anesthetic dose of 1.6 ± .01 g/kg, after cessation of isoflurane delivery. Atropine methyl

nitrate (0.05 mg/kg, s.c.) was administered to minimize respiratory complications. Rats were then transferred to a stereotaxic apparatus and body temperature was maintained at 37 °C throughout the experiment via a servo-controlled heating pad placed under the rat (TR -100, Fine Science Tools, Vancouver, BC).

For the bipolar recording group, bipolar Teflon-coated stainless-steel electrodes (125 μm bare diameter; 0.6 – 1.0 mm stagger between electrode tips) were implanted at 3 neocortical sites spaced 3 mm apart in an anterior-to-posterior (AP) linear plane, and at one contralateral hippocampal site (see Figure 1A,C). All cortical sites were positioned + 2.0 mm medio-lateral (ML) to bregma and the respective AP coordinates were: +3.0 mm (cortical site 1), 0.0 mm (cortical site 2), and -3.0 mm (posterior cortical site). The hippocampal electrode was positioned at -2.2 mm ML and +3.3 mm AP. For cortical placements, the longest contact of each pair was targeted just past the deepest neocortical cell layer (approximately at cortical layer VI; -1.6 ± 0.1 mm dorso-ventral (DV) to cortical surface) and the shorter contact (reference) was in the superficial layers (approximately at cortical layers II-III). All three cortical sites were located in primary motor cortex (M1; see Figure 1B). For hippocampal placements, the deepest contact was at or about the hippocampal fissure (DV: -3.3 ± 0.1 mm), with the shorter contact above the CA1 pyramidal cell layer.

For the linear probe recording groups, a 16-channel linear array (U-probe, Plexon, Dallas, TX) with 100 μm contact separation was lowered into the hippocampus at the same coordinates as the bipolar electrodes (-2.2 mm ML and +3.3 mm AP). The final depth of the linear probe was determined by visually examining the theta signal at each contact and ensuring a visible theta signal reversal at approximately the 5th contact from the superficial

(towards the cortex) portion of the probe as well as stronger theta amplitude in the deeper (near the fissure) contacts (see Figure 1C). This ensured that the probe was optimally lowered to obtain recordings along the cellular axis of CA1 from approximately stratum oriens to the molecular layer of the dentate gyrus. The final probe depth (deepest contact) across experiments was -4.07 ± 0.07 mm. All linear probe recording animals also had a bipolar cortical electrode contralateral to the probe hemisphere positioned at cortical site 2 (see above for depth information) for the field stimulation (low and moderate intensity) animals or cortical posterior cortical site (see Figure 1C; as described above) for evoked potential and field stimulation (high-intensity) animals.

For all field stimulation experiments, three Teflon-coated stainless steel wires (277 μm bare diameter; 0.4 Ω resistance) were lowered to pial surface and implanted in a triangular configuration anterior to the recording sites, with a central pole located on the midline (+6.0 - +7.0 mm AP and 0.0 mm ML) and two lateral poles more posterior and lateral (+4.0 - +5.0 mm AP; ±3.5 mm ML) (see Figure 1B&C). The lateral poles served as a reference to the midline pole. All recording and stimulating electrodes were secured to the skull using dental acrylic mounted to a jeweler's screw that was fastened to the skull.

4.3.3 Recordings

Bipolar field recordings. Spontaneous recordings were wide-bandpass filtered between 0.1 Hz and 10 kHz and amplified at a gain of 1000 using a differential AC amplifier (model 1700; A-M Systems, Sequim, WA). Signals were digitized using an A-D board (Digidata 1322a; Axon Instruments/Molecular Devices, Sunnyvale, CA) and sampled at 1000 Hz (with software-controlled anti-alias filtering at 500 Hz) for extraction of local field

potentials (LFP). Data were acquired and stored using AxoScope (Axon Instruments/Molecular Devices) on a PC system for offline analysis.

Linear probe recordings. The linear probe was attached to a headstage (Plexon) with unity gain and signals were then amplified at a gain of 1000 (PBX-2 amplifier, Plexon) and wide bandpass filtered between 0.07 Hz and 8 kHz. Signals were digitized as reported above (DigiData 1322a; Axon Instruments) and sampled at 1000 Hz (with anti-alias filtering at 500 Hz). All channels were referenced to the stereotaxic apparatus (which was itself connected to ground) and signals were stored for offline analysis as described above.

4.3.4 Field stimulation

Sinusoidal stimulation was applied using an analogue function generator (Hewlett Packard; 3310A) to the three stimulation poles with the two lateral poles receiving opposite polarity stimulation to the central pole (see Figure 1B; see Greenberg and Dickson, 2013; adapted from Ozen et al., 2010). The stimulation generator output was also digitized using the same system as that used for brain signals to obtain stimulation phase and voltage intensity information for later offline analysis.

Stimulation was applied at various voltage intensities (defined as peak-to-peak amplitude) ranging from 0.86 to 19.97 V to test the effect of increasing stimulation intensity on ongoing SO dynamics. For both the bipolar and linear probe recording experiments the intensities were separated into low, moderate and high conditions (bipolar: low = 0.89 ± 0.01 V, n = 6, moderate = 7.28 ± 0.69 V, n = 3, high = 15.24 ± 0.32 V, n = 4; linear probe: low = 0.87 ± 0.01 V, n = 7, moderate = 4.57 ± 0.67 V, n = 7, high = 17.11 ± 2.07 V, n = 4) (Figure 1A). There were no differences between baseline and low-intensity stimulation for any

analysis and therefore this condition will not be discussed further. The frequency of stimulation was 1.67 Hz, slightly faster than the endogenous SO frequency (~ 1 Hz). We chose this faster frequency in order to spectrally separate the effects of stimulation and endogenous SO as well as in an attempt to successfully entrain networks by providing a faster putative pacemaking stimulus. Stimulation was applied during mutual cortical and hippocampal SO states (detected visually and later confirmed offline using spectral analyses). The duration of stimulation lasted from 3 to 6 minutes continuously per condition (one trial per condition) with 1 to 6 minute stimulation-free periods between stimulation trials (Figure 1A). The duration of the stimulation-free period depended on the length of time until the return of stable SO activity.

At the end of all experiments animals were euthanized with a lethal dose of urethane. Immediately after being euthanized (within 5 seconds of the cessation of brain activity), post-mortem recordings were obtained using the same stimulation parameters used previously to obtain channel-specific estimates of stimulation artifact waveform amplitude and shape. These recordings were then used to generate estimates for artifact subtraction (detailed further below; see also Greenberg and Dickson, 2013).

4.3.5 Evoked potentials

To determine whether our cortical field stimulation configuration was capable of eliciting evoked-potentials at the level of the hippocampus we delivered constant-current pulses (500 µA, 1 ms duration) during both theta and SO states to the same stimulation electrodes and configuration as those used for field applications (see Figure 1A&C) and recorded evoked potentials using the linear probe. The applied current pulses were delivered

every 10.3 sec using an isolated constant current pulse generator (model 2100; A-M Systems). We obtained 100 stimulation trials per condition.

4.3.6 Data analysis

All analyses were performed using a combination of built-in functions and custom written code in MATLAB (MathWorks, Natick, MA). All means are reported as mean ± standard error of the mean (SEM). Significance for all statistical tests was defined as $p < 0.05$ and all *t* tests were performed two-tailed and within-subjects (paired) unless otherwise specified.

4.3.6.1 Linear probe depth normalization

In order to perform group analyses for the linear probe experiments, we normalized the depth profile for each experiment by setting a depth value of 0 for the contact at which the theta reversal occurs and expecting a 400 μm separation between the reversal channel and the contact with maximal theta and SO power which is found to be at stratum lacunosum moleculare (SLM; Wolansky et al, 2006) (see Figure 1C). The ratio between this expected distance and the actual separation in channels from the reversal to the maximal theta (400 μm/true separation) was multiplied by the expected depths from the 0 reversal channel (expected depths given 14 contacts and 100 μm separation: -900 to 400) to yield a "standardized" depth. This normalized depth for each experiment was then interpolated (using cubic spline interpolation) to obtain equivalent depths across experiments. Only interpolated data was included, no extrapolation was performed. Therefore, starting from 14 channels per experiment we ended up with 11 normalized channels.

4.3.6.2 Stimulus artifact subtraction

Subtraction of the stimulation artifact from the LFP recordings was performed using two separate methods: independent component analysis (ICA) as well as our previously described post-mortem subtraction method (PMA; Greenberg and Dickson, 2013).

For ICA artifact subtraction, the runica algorithm (Bell and Sejnowski, 1995; Delorme and Makeig, 2004; Makeig et al., 1996) was applied to the combined baseline and stimulation time series, including all hippocampal channels and the neocortical channel. Components representing the artifact were identified based on their distinctive temporal and spectral characteristics during stimulation compared to baseline. In addition, artifact components had irregular spatial profiles (relative weightings across multiprobe channels) that did not resemble the smooth profiles of ICA components with physiological origins (Fernandez-Ruiz and Herreras, 2013; Schomburg et al., 2014). Based on these criteria, between 2 and 6 components (4.8 ± 1.4) were identified as artifact, and these were summed to create the artifact time series. This time series was then filtered using a zero-phase lag 2^{nd} order Butterworth filter to retain the main stimulation frequency and all visible harmonics while avoiding the inclusion of any non-artifact signal that may have contaminated the ICA-separated components (Castellanos and Makarov, 2006). Filter parameters were specific for each subject and stimulation condition based on the variation in artifact characteristics: 10 Hz low-pass filter (n=4); 20 Hz low-pass filter (n=6); 1-3 Hz bandpass filter (n=1). This processed artifact signal was then subtracted from the raw data to yield the cleaned, artifact-free signal for further analysis. The similarity of the time series and spectra for the raw baseline signal and the artifact-subtracted baseline signal (which should be identical given

no artifact during the baseline) was assessed to ensure that the true neural signal had not been altered by the subtraction procedure.

The PMA method was conducted on a cycle-by-cycle basis using an average estimate of the stimulus artifact obtained during post-mortem recordings (see Greenberg and Dickson, 2013 for detailed explanation). In brief, post-mortem stimulation recordings were scaled to match the amplitude of the artifact-enhanced LFP and subtracted from each cycle by matching the phase of stimulation across both. Data were discarded for cases in which the LFP amplitude was not reduced to control amplitudes after subtraction (< 90% reduction relative to post-mortem artifact amplitude). In total, we discarded 5 cases for the bipolar recordings (low stimulation condition in 1 subject and moderate stimulation condition in 4 subjects) and 2 cases for the linear probe recordings (moderate stimulation condition).

High-intensity stimulation could not be subtracted using either method since the artifact was large enough to saturate the amplifier. Therefore, all analyses for the high-intensity stimulation examined the signal immediately following the cessation of the high-intensity stimulation (post high-intensity). Following cessation of stimulation we noted a stimulation artifact that lasted approximately 50 ms and thus this period was not used in post-stimulation data analysis.

4.3.6.3 Comparison of field stimulus artifact removal using two distinct methods

In order to ensure that we were removing the stimulus artifact consistently, the two subtraction methods were systematically compared in Figure 2 in their ability to extract the stimulation artifact with highly similar results obtained from both. The ICA method was only possible in the situations where we had large numbers of independent contacts using the

hippocampal linear probe which allowed us to systematically evaluate our previously used PMA method.

Visual examination and spectral analyses show that both methods produce nearly identical signals which appear similar to the baseline spectrum (Figure 2A). The only difference to the baseline condition is a spectral peak at the stimulation frequency of 1.67 Hz for the PMA subtraction method; a peak that was not present for the ICA method (Figure 2Aii). There was significantly higher power at 1.67 Hz for the PMA method at SLM (Figure 2Aiii – bottom left, $p = 0.048$) but not in the cortex (Figure 2Aiii top left). This suggests that the ICA method may perform a more complete artifact subtraction. However, there were no spectral power differences at other frequency ranges such as SO (0.6 – 1.5 Hz) and gamma (30 – 40 Hz) (Figure 2Aiii). The coherence for the signals extracted with the two methods was high at all sites for both the SO and gamma bands (Figure 2Aiii – right) but dropped off for the exact stimulus frequency (Figure 2Aiii – right) suggesting that the ICA method removes the artifact entirely, while some artifact is likely left over using the PMA method.

As for the subtracted signals themselves, the extracted artifact (which was used in subtraction) was nearly identical for the two methods (Figure 2B). When comparing the power difference in the two artifacts at the main stimulation frequency (1.67 Hz), there was no difference in the cortex (Figure 2Biii – top left) and the coherence was nearly perfect between the two signals (0.95 ± 0.03; Figure 2Biii – top right). For the SLM site, the power difference was significantly higher for the PMA method (Figure 2Biii – bottom left, $p = 0.005$) suggesting that the PMA method slightly overestimated the artifact power on average. Nevertheless, the coherence between the two extracted artifact signals was nearly perfect at SLM (0.997 ± 0.001; Figure 2Biii bottom right) and at all other hippocampal sites

(coherence > 0.95; data not shown). Furthermore, the phase difference between the two artifact signals did not significantly differ from 0 for any contact (data not shown). Overall, these results suggest that the ICA and PMA subtraction methods are highly similar in their extraction of the stimulus artifact, lending validity to our previously described PMA method (Greenberg and Dickson, 2013). Furthermore, all of our analyses results described below did not show any differences across subtraction method.

4.3.6.4 Spectral analyses

Spectral analyses were performed using Welch's averaged modified periodogram method for power spectral density estimation and coherence (6 sec window; 2 sec overlap, significance threshold based on time-shifted randomization procedure = 0.2) calculated on continuous 120 second epochs of data that were then averaged based on subject and condition. As previously shown (Wolansky et al., 2006), The SO LFP activity for cortical and hippocampal signals was characterized by spectra showing a prominent peak power between 0.3 and 1.5 Hz.

4.3.6.5 Current source density analysis

In order to assess stimulus induced changes at specific hippocampal layers, current source density analysis (CSD) was computed on the raw LFP recordings from the linear probe as well as trial averaged linear probe traces from the evoked-potential recordings. The CSD was estimated as the second spatial derivative of voltage traces using a 3-point difference across contacts (Freeman, 1975; Ketchum and Haberly, 1993; Rodriguez and Haberly, 1989). Therefore, CSD = $[f(pi\ -1)\ -\ 2f(pi)\ +\ f(pi\ +\ 1)]/d^2$, where $f(pi)$ is the field

signal from probe channel *i* (i =2, 3, . ., 14), and *d* is the distance between adjacent channels (100 μm) and the resulting units of the CSD are in mV/mm^2.

4.3.6.6 Ripple, spindle and gamma detection

We determined whether field stimulation influenced hippocampal ripples (130 – 200 Hz), hippocampal gamma (30 – 45 Hz), and spindles (7 – 12 Hz) which are all local network processes that have been implicated in memory consolidation and plasticity. Since ripples are high frequency events, it was important to ensure that we were selecting true ripple oscillations and not simply non-rhythmic spectral bleeding of multi-unit activity (Scheffer-Teixeira et al., 2013). To accomplish this, we used the robust Better OSCillation detection method (BOSC; (Caplan et al., 2001; Hughes et al., 2012; Whitten et al., 2011)) which isolates oscillatory episodes in a signal by using a combined power and duration threshold specific for each frequency. In brief, we computed power spectra for the hippocampal linear probe signals (for ripples and gamma) or the cortical signal (for spindles) for each condition using Morlet wavelets (6 cycles; 0.6 – 300 Hz range; in log-sampled scales). A linear regression (for cortical signals) and a curved regression (for hippocampal signals since their spectra deviate from the 1/f linear relationship) were fitted to each spectrum plotted in log-log coordinates. To find the power threshold, the fit was used to estimate the mean power for each frequency in a χ^2 distribution, and the 99^{th} percentile was chosen as the significant power threshold. The duration threshold was defined as 6 cycles for ripples, 3 cycles for gamma and 4 cycles for spindles for which the power threshold was exceeded (the most strict criteria was applied for ripples to ensure detection of true ripples and not spectral bleeding). Therefore, the BOSC has a binary output, for each time point in the analyzed

signal an oscillation for a given frequency is either detected or not detected (see Figure 4A for an example). For each frequency band described above (ripples, gamma and spindles) we collapsed the BOSC results across the chosen frequency band. For each frequency band we then computed P-episode which is the proportion of time that the oscillation is present out of the total time of the analyzed epoch (Caplan et al., 2001; Hughes et al., 2012; Whitten et al., 2011). The modulation of gamma, spindle and ripple count to slow-band phase was calculated using Rayleigh's test for circular statistics (Zar, 1999).

4.3.6.7 Granger causality

Our hypothesis states that field stimulation is likely to alter cortico-hippocampal interactions. To understand causal interactions across regions during spontaneous SO as well as during field stimulation, we computed the Granger causality with the Granger Causality Connectivity Analysis (GCCA) MATLAB toolbox (Seth, 2010). Given two signals, X and Y, if knowing past values of signal Y improves the prediction of future values of X better than knowing the past values of X alone, then Y is said to "cause" X (Granger, 1969). Mathematically, this can be described by two autoregressive models: the restricted model (including only variable X) and the unrestricted model (including variables X and Y). Granger causality is the log ratio of the prediction error variance for the restricted and unrestricted models. Therefore, a value of 0 indicates no causal link, while high values indicate large reductions in the prediction error by the inclusion of signal Y, thus inferring that Y causes X. This logic can be extended for the multivariate case (with more than two signals), using multivariate autoregressive (MVAR) models. In this case, causality is inferred if prediction error in the model is reduced by including signal Y above and beyond

the inclusion of all other signals (i.e., signal X itself, X_2, X_3...X_n). By performing this analysis spectrally, it is possible to infer causal relationships between given regions for specific frequency bandwidths. The frequency-domain Granger causality can be realized with Fourier decomposition of the time-domain MVAR model.

We also measured causal flow which is computed for each channel as the sum of its Granger outputs minus the sum of its Granger inputs. Therefore, for a given channel a value of zero would suggest a net neutral Granger connectivity while a positive value would suggest the given channel is a net source (sending information) and a negative number would suggest this channel is a net sink (receiving information).

We tracked causal interactions for the SO frequency (0.8 – 1.2 Hz) range as well as the gamma range (30 - 45 Hz). This allowed us to infer causal inter-site interactions for specific cortical and hippocampal recording sites and test the prediction that stimulation alters cortico-hippocampal functional interactions in order to facilitate memory consolidation.

4.3.6.8 Long-range gamma coherence

To track any possible changes in coherence during stimulation and following cessation of stimulation for each condition, we selected 40 second time windows during control recordings, during stimulation and immediately post-stimulation (for each stimulation condition). Continuous wavelet coherence spectrograms (5 cycle width; 1 sec window) were created for wavelet scales corresponding to the frequency ranges of 0.6 – 200 Hz (53 log-sampled scales). Control coherence distributions were created for each frequency by collapsing wavelet coherence across time. Wavelet spectrograms were then z-normalized

to control coherence to reveal any apparent stimulation-related changes. These spectrograms were used to examine coherence in the bipolar experiments between each cortico-cortical channel pair as well as each cortical site and the hippocampus (6 overall comparisons). For the linear probe experiments the one cortical site was compared to each hippocampal probe contact, creating a profile of changes in cortico-hippocampal coherence. These were computed for the LFP as well as CSD recordings. For all experiment types, each spectrogram was then collapsed across time to reveal any overall coherence boosts between specific site-to-site comparisons and within specific frequency ranges (see Figure 10 for example).

4.4 Results

4.4.1 Spontaneous SO activity shows moderate coherence across cortico-hippocampal sites

As previously reported for rats and mice under urethane anesthesia, cortical LFP recordings showed spontaneous transitions between activated (REM-like low amplitude, fast activity) and deactivated/SO (NON-REM-like high amplitude, ~1 Hz) states (Clement et al., 2008; Pagliardini et al., 2013; Wolansky et al., 2006). In the hippocampus, theta co-occurred with cortical activated states, while alternations between large-amplitude irregular activity (LIA) (Vanderwolf, 1975) and the hippocampal slow oscillation were concomitant with cortical SO states (Figure 4.1C).

In the present study, we were interested in epochs in which SO was present in both cortical and hippocampal LFPs. These epochs were visually selected and confirmed using

spectral analyses (Figure 4.1). Simultaneous cortical and hippocampal SO epochs lasted between 3.6 and 23.3 minutes (12.6 ± 2.8 min) across all examples and experiments. When visually examining cortical and hippocampal traces we noted that the SO appeared highly coherent across cortical sites (Figure 4.1B) and while hippocampal SO appeared highly coherent across hippocampal depth (Figure 4.1C), it was noticeably distinct from the cortical SO (Figure 1B&C). Spectral analyses confirmed this observation by showing that the rhythmic cortical SO had a large power spectral peak (0.05 – 0.58 mV^2) at approximately 1 Hz (0.83 – 1.17 Hz; Figure 4.1D) which was highly coherent across cortical sites (coherence values: 0.78 – 0.99, $p < 0.001$; Figure 4.1E). Hippocampal SO, on the other hand, tended to have a broader peak that included slower frequencies (centred at ~ 0.4 Hz and ranging between 0.33 and 0.50 Hz) in addition to the SO peak at approximately 1 Hz (0.83 – 1.17 Hz) (Figure 4.1D). While there was significant average coherence (significance threshold computed as described in Methods section = 0.2, $p = 0.01$, Figure 1E) observed between cortico-hippocampal sites at the cortical SO frequency (coherence values: 0.16 – 0.67; Figure 4.1E), this coherence was weaker on average than that expressed between cortico-cortical sites ($p < 0.001$). In contrast, there was no significant coherence for the slower (~ 0.4 Hz), hippocampal bandwidth (0.09 – 0.1; $p = 0.19$ - 0.23).

As previously shown for both cortical (Chauvette et al., 2010; Contreras et al., 1996b; Timofeev and Steriade, 1996) and hippocampal SO (Isomura et al., 2006; Wolansky et al., 2006), gamma activity was strongly modulated to the active ON phase (negative peak in depth recordings) of the LFP at each site (mean angle = 261.57º, $p = 0.04$; Figure 4.1F). These findings confirm the likelihood that both the cortical and hippocampal SO are generated locally and are not simply a result of volume propagation from alternate sites.

4.4.2 Electric stimulation of frontal cortical sites elicits evoked potentials in the hippocampus

Our main objective was to test the idea that rhythmic field application over the frontal cortex during sleep-like states alters hippocampal activity as well as cortico-hippocampal interactions. Prior to applying rhythmic electric field stimulation, we initially applied brief (1 ms, 500 μA) direct current pulses to the same frontal sites used for the application of electric fields (protocol 1). In this way, we could assess whether stimulation of this region had the ability to influence distant hippocampal sites. Baseline CSD plots showed strong sink/source alternations at the level of SLM (Figure 4.3A, SO on left, theta on right) and indeed we observed evoked potentials at SLM during both SO and theta states when applying current pulses (Figure 4.3). The initial component of the evoked potential showed a large sink (SO: 3.87 ± 2.15 mV/mm^2; theta: 3.43 ± 1.87 mV/mm^2) with an average lag from stimulus offset of ~20 ms (SO: 21.5 ± 0.65 ms; theta: 20.0 ± 1.68 ms) followed by a large source (SO: -4.74 ± 2.69 mV/mm^2; theta: -5.77 ± 3.34 mV/mm^2) with an average lag of ~40 ms from stimulus offset (SO: 44.5 ± 2.53 ms; theta: 41.5 ± 2.22 ms; Figure 4.3B). Neither latencies nor amplitudes of sinks and sources showed any difference across states ($p = 0.11 - 0.75$). As expected, the evoked potential was present in the cortical site as well with an earlier latency (12.25 ± 2.65 ms) followed by a triggered slow-wave (118.25 ± 9.14 ms) (Figure 3C) which is consistent with previous findings for stimulation-triggered slow oscillations (Vyazovskiy et al., 2009). Thus, electrical stimulation applied at the surface of frontal cortical regions appears to evoke synaptic responses in hippocampus.

4.4.3 Hippocampal entrainment to sinusoidal electric field application

Given that frontal stimulation could elicit evoked potentials in the hippocampus, we asked whether applying time varying electric stimulation and/or fields could entrain ongoing hippocampal activity. Using increasing duration trains of the same brief current pulses that evoked synaptic activity in the hippocampus (as described in the previous section) at train intervals of 600, 700 or 800 ms (1.67, 1.42, and 1.25 Hz respectively; Figure 4.1A – protocol 1) we could not detect any slow wave entrainment effects in either LFP or CSD traces in the hippocampus, even with progressively longer trains of stimulation (data not shown). Since we did not monitor the ongoing phase of cortical SO activity online during stimulation, this failure to entrain might have been due to the variation in excitability of both the cortical and hippocampal networks across the SO cycle itself (Schall et al., 2008). Thus, in an attempt to modulate ongoing cortical slow activity (e.g. (Greenberg and Dickson, 2013)), and assess its influence on hippocampal LFP and CSD we applied moderate voltage (7.28 ± 0.69 V) slow (1.67 Hz) sinusoidal electric fields to the same frontal regions (protocol 3). We observed an increase in the artifact-subtracted CSD spectral power for the stimulus frequency of 1.67 Hz at stratum radiatum (SRad) compared to the baseline condition ($p = 0.025$) with no change at SLM ($p = 0.063$) or stratum pyramidal (SPyr; $p = 0.087$). Interestingly, we also observed an increase in the CSD power at double the stimulus frequency (3.33 Hz) compared to baseline at SRad ($p = 0.005$), SLM ($p = 0.03$) and SPyr ($p = 0.009$). When examining the artifact-subtracted LFP traces, we detected this increase in power during stimulation compared to baseline at the SLM site for the doubled stimulus frequency ($p = 0.04$) but there were no changes at any site for the stimulus frequency or at the doubled frequency for any other site ($p = 0.06$ - 0.37).

Given that the moderate stimulation intensity used might not have evoked consistent entrainment, we assessed whether stimulus phase-locking of hippocampal CSD could occur on average as a function of the artifact stimulus waveform (extracted with ICA from the cortical site), as it does with the cortical SO waveform (e.g., Wolansky et al, 2006) (Figure 4.4). We found evidence for CSD entrainment locked to the stimulus waveform in 5 of 7 experiments ($p = 0.001 - 0.04$ in each of the 5 experiments). In three of these cases, entrainment occurred in a time- and frequency-locked fashion to the fundamental of the stimulation sinusoid (1.67 Hz, Figure 4.4A) and in the two remaining cases it occurred at double this frequency (3.33 Hz, Figure 4.4B), as evident in the CSD and LFP power increases (see above). Most convincingly, the profile of the entrained activity appeared similar to, although in some cases more robust than, the coherence of hippocampal activity to the cortical SO during baseline conditions (Figure 4.4A&B). In both spontaneous and stimulated cases, the strongest sink-source alternations occurred at SLM and SRad (depths of -100 and -400; Figure 4.4).

It was also apparent that activity in strata other than SLM was also altered during electric field application as compared to baseline conditions. We computed the root-mean square (RMS) of the continuous CSD traces before and during stimulation to track alterations in extracellular current flow across all laminae. Although there was significantly higher RMS across all laminae during field stimulation in comparison to baseline ($p = 0.001 - 0.05$, data not shown), the largest effect sizes for this RMS difference were at the channels corresponding to SRad (Cohen's $D = 1.2$) and SPyr (+100 depth) (Cohen's $D = 1.4$), indicating that activity and current flow were robustly enhanced at these locations. Since

these are the laminae at which sharp-waves and ripples are generated, we hypothesized that field stimulation might be modulating the expression of these events.

4.4.4 Moderate intensity field stimulation boosts hippocampal ripples and cortical spindles

We detected LFP ripple events (130 – 200 Hz) at the level of SPyr using BOSC (Caplan et al., 2001; Hughes et al., 2012; Whitten et al., 2011) and compared the number of detections during stimulation and baseline conditions. We confirmed that detected ripples co-occurred with sharp-waves in SRad (Figure 4.5A&C) and were localized to SPyr (Figure 4.5B). Indeed, and as suggested by our RMS analysis, the application of rhythmic field stimulation dramatically increased hippocampal sharp-wave ripple events as compared to baseline conditions for both the ICA and PMA subtraction methods (Figure 4.5B – top; ICA: $p = 0.035$; PMA: $p = 0.031$). The average duration of each ripple event corresponded to ~ 8 cycles and did not differ across conditions (baseline: 7.68 ± 0.45 cycles; ICA: 7.66 ± 0.25 cycles; PMA: 7.94 ± 0.25 cycles, $p = 0.68$ - 0.98). Following the cessation of moderate intensity stimulation, the magnitude of the ripple increase at SPyr was comparable to that found during stimulation and was significantly elevated in 6 out of 7 experiments, although on average across experiments this increase was not significant ($p = 0.07$; Figure 4.5B – bottom). The average length of ripple events was similar to that during moderate stimulation and again did not differ from baseline (8.37 ± 0.48 cycles; $p = 0.15$). The sharp-wave amplitudes during and following stimulation also did not differ from the baseline condition ($p = 0.16$ - 0.95; Figure 4.5C). We also detected hippocampal gamma activity (30 – 45 Hz)

which was present most strongly just above SLM (depth = -300) and gamma count did not differ between baseline and stimulation conditions ($p = 0.16 - 0.26$, not shown).

Since interactions between hippocampal ripples and cortical spindles have been reported to occur during slow-wave sleep (Siapas and Wilson, 1998; Sirota et al., 2003) we examined whether rhythmic field application enhanced cortical spindle (7 – 12 Hz) activity as well. Using BOSC to detect spindles in cortical traces we found a parallel increase in the occurrence of spindling activity during stimulation (P-episode: proportion of time oscillation is present; Baseline: 0.07 ± 0.02; ICA: 0.14 ± 0.04; PMA: 0.14 ± 0.04; $p = 0.015$). Following the termination of rhythmic field application, there was a continuing increase in spindle activity in 5 of 7 experiments but this increase was not significant across experiments (P-episode: 0.08 ± 0.02, $p = 0.75$). We also assessed whether there was a correspondence between the occurrence of ripples and spindles. Using the center of ripple detections to assess the co-dependence of spindle events, we found that spindles tended to co-occur with ripples within a 1 second window around the ripple above what is expected from a randomized distribution ($p < 0.001$), although a specific lead/lag relationship was not apparent ($p = 0.45$). Furthermore, both ripple and spindles were phase-modulated by the cortical SO (ripple mean angle = 2.83.3º, $p = 0.03$; spindle mean angle = 253.6º, $p = 0.045$) consistent with previous findings (Mölle, 2009; Peyrache et al., 2011; Sirota et al., 2003). However, neither ripples nor spindles showed phase modulation to the stimulation sine wave during (or following) stimulation ($p = 0.15 - 0.77$). We also detected spindles in the hippocampus itself which were strongest at SLM and were phase modulated by the cortical SO (mean angle: 300.4º, $p = 0.042$). Hippocampal spindles have been previously reported for natural sleep (Staresina et al., 2015; Sullivan et al., 2014) and in our own hands under

urethane anesthesia (Whitten & Dickson, in preparation). However, we did not find any change in spindle count between baseline and stimulation conditions ($p = 0.17 - 0.22$, not shown). Following high-intensity stimulation, there were no changes in ripple count compared to baseline (P-episode: baseline = 0.002±0.001, post-high stim = 0.001±0.001; $p = 0.51$) while cortical spindle count was significantly reduced (P-episode: baseline = 0.0035±0.0005, post-high stim = 0.001±0.0008; $p = 0.02$). Our novel demonstration of a boost in hippocampal ripples (and confirmation of an increase in cortical spindle activity - (Marshall et al., 2006)) does suggest that slow sinusoidal electrical field applications can influence both hippocampal and cortical dynamics.

4.4.5 Rhythmic field stimulation alters directional interactions between the cortex and hippocampus at the slow oscillation frequency

Since rhythmic electric field application could entrain and alter the expression of hippocampal-specific network rhythms, we evaluated the potential influence of this stimulation on cortico-hippocampal interactions. We did not observe any significant changes to cortico-hippocampal SO (~ 1 Hz) coherence (using SLM and SRad LFP) during moderate levels of stimulation as compared to baseline ($p = 0.07 - 0.42$). However, we speculated that more subtle alterations to cortico-hippocampal interactions might be taking place. To examine this possibility, we employed spectral Granger measures which allow specification of directional interactions at the SO frequency (0.8 - 1.2Hz) between cortical and hippocampal sites. For this, we compared activity at the most posterior cortical site to 3 different hippocampal channels from the multi-probe; specifically sites corresponding to SLM, SRad and SPyr (Figure 4.6). We found that during and following moderate intensity

stimulation the cortico-hippocampal directional interactions were unchanged, while following high-intensity stimulation there was an enhancement in the hippocampal-to-cortical direction of influence.

During baseline recordings, Granger interactions appeared strongest in the direction from the cortical region towards all 3 selected hippocampal sites (Figure 4.6Ai). During moderate intensity stimulation, there was an enhancement from SLM towards the other hippocampal sites (Figure 4.6Aii, Aiii). These results were identical for both ICA and PMA subtraction methods (Figure 4.6A). Most interestingly, following the cessation of high-intensity stimulation there was a reduction in Granger interactions from the cortex towards the hippocampus and a reversed enhanced interaction from SPyr towards the cortex (Figure 4.6C).

In order to summarize how these directional flows were changing with stimulation we used a measure of causal flow which describes for each channel whether it is a net causal source (sending information; positive values) or net sink (receiving information; negative values). As was apparent from the site-to-site Granger values, the cortex is a causal source during both baseline and stimulation conditions with no significant differences between baseline and stimulation (ICA: $p = 0.14$; PMA: $p = 0.08$; Figure 4.6Aiv). For the SLM site, during baseline and stimulation conditions this region was a net sink but showed a significantly enhanced Granger outflow during stimulation perhaps reflecting enhanced SLM influence onto other hippocampal layers (i.e., becoming less of a sink; ICA: $p = 0.013$; PMA: $p < 0.001$) (Figure 4.6Aiii&Aiv). SRad and SPyr showed no changes in flow with moderate stimulation ($p = 0.12$ - 0.76; Figure 4.6Aiv). When examining 40 seconds immediately following the cessation of moderate intensity stimulation, all of the Granger

results showed identical trends to those during moderate intensity stimulation with an increased SLM outflow present in 6 out of 7 experiments, although these effects were no longer significant on average ($p = 0.14 - 0.96$; Figure 4.6B).

Due to saturation of signals during higher intensity field applications we were unable to successfully eliminate the artifact, thus we analyzed 40 second epochs immediately following its cessation. The directional influence from the cortex to all hippocampal sites was reduced (Figure 4.6Ci, ii and iii). Furthermore, there also appeared to be an enhanced influence from SPyr towards the cortex. Neither of these effects appeared during or following the moderate stimulation condition (Figure 4.6Cii and iii). When examining the causal flow results (Figure 4.6Civ) there was a significantly decreased cortical source following high intensity stimulation ($p = 0.03$) and a significant reversal in causal flow in SPyr which was a slight causal sink during baseline conditions and became a causal source following high intensity stimulation ($p = 0.05$). This suggests that SPyr showed its enhanced outflow most strongly towards the cortex. There were no differences in causal flow following high intensity stimulation for SLM or SRad ($p = 0.20 - 0.22$).

Taken altogether, the Granger analysis shows that the main directional interactions at the SO frequency during baseline conditions are from the cortex towards the hippocampus. This directional influence is maintained during and following moderate stimulation conditions with an enhancement in SLM influence onto other hippocampal layers. Surprisingly, following high-intensity stimulation there was a reduced cortical influence onto the hippocampus along with a boost and reversal in directional flow from the hippocampus (specifically SPyr) towards the cortex.

4.4.6 Field stimulation alters temporoammonic pathway input to the hippocampus

The Granger analysis revealed altered interactions in the cortico-hippocampal direction following high-intensity stimulation. We therefore asked whether the temporoammonic input to the hippocampus shows similar disruptions. Using ICA we identified the component with maximal activity at SLM (Figure 4.7) as previously described by others (Benito et al., 2014; Schomburg et al., 2014). This component may correspond to the direct temporoammonic pathway from the entorhinal cortex layer III to CA1 although a thalamic-hippocampal route by way of the nucleus reuniens is also a candidate. During moderate intensity stimulation, the power spectra at SLM for this extracted component were similar for the baseline and stimulation conditions, although the stimulation condition appeared to have higher power at the stimulation frequency of 1.67 Hz (Figure 4.7A, top). When examining the grand average power profiles normalized to baseline for this ICA component at the SO frequency, there were no differences in power between baseline and stimulation conditions ($p = 0.75$, Figure 4.7B, top). However, the power profile during stimulation at the stimulus frequency showed higher power at SLM (-400 normalized depth) and this effect was marginally significant ($p = 0.056$, Figure 4.7B, top).

Following high-intensity stimulation, the power spectra for the temporoammonic ICA component showed reduced power at the SO frequency range (Figure 4.7A, bottom). When examining the grand average power profiles, this reduced power following stimulation was significant compared to the baseline condition at SLM ($p = 0.04$, Figure 4.7B, bottom). These results suggest that during moderate intensity stimulation while there is no effect on the temporoammonic pathway at the SO frequency, there seems to be a boost at the stimulus frequency in line with our results showing hippocampal CSD entrainment to the stimulus

wave. Conversely, following high-intensity stimulation there is an apparent disruption in the SO temporoammonic input to the hippocampus corroborating the Granger results which show disrupted cortico-hippocampal directional interactions for this stimulus intensity.

4.4.7 Transient slowing of cortical SO and increases in hippocampo-neocortical SO coherence are observed following cessation of high intensity stimulation

Although we did not observe any obvious SO-related spectral changes to cortical LFP during or following moderate intensity stimulation ($p = 0.61 - 0.65$), we noted a prominent and consistent ($n = 4$) slowing of cortical LFP following high-intensity stimulation (Figure 4.8). The cortical SO during baseline conditions was approximately 1 Hz, and following high-intensity stimulation this peak was slower (~ 0.5 Hz; for all channels in 3 out of 4 experiments; Figure 4.8). However, there was no change in the peak spectral frequency of the hippocampal signal ($p = 0.42$; Figure 4.8B, D). Since the largest component in the hippocampal signal during control recordings was slower than the cortical SO (cf. Figure 1C, D), the slowing of the cortical signal post-stimulation now appeared much more coherent with the hippocampal signal (Figure 4.8A – bottom).

In terms of SO coherence, the peak in the coherence spectra for cortico-cortical channel pairs was also shifted to a lower frequency post-stimulation, in line with a slowing of the signal fundamental (Figure 4.8C – left). Cortico-cortical coherence values were already high during control conditions, and did not significantly change post-stimulation (repeated ANOVA for channel-pair by stimulation condition, $p = 0.35 - 0.91$ for all main effects and interaction term; Figure 4.8C – left, E – left). On the other hand, for cortico-hippocampal channel pairs, the peaks in the coherence spectra (and cross-spectra; not

shown) were not only shifted to lower frequency values (although not significant on average, $p = 0.12$; Figure 4.8C – right), but also showed significant coherence increases across channel pairs at these lower frequencies (repeated-measures ANOVA for channel-pair by stimulation condition, main effect for stimulation condition, $F(1,3) = 10.63$, $p = 0.047$ with no significant channel-pair effect or interaction term; Figure 4.8C – right, E – right). These results are the first to show transient effects following electrical field stimulation on cortical EEG spectral properties as well as on hippocampo-cortical SO coherence. This result is in accordance with our findings from the Granger and temporoammonic ICA component analyses reported above showing disrupted cortical influence onto hippocampal networks and thus suggests that the cortical slowing and boosted hippocampo-cortical coherence is likely due to an enhancement in the reversed hippocampal-to-cortical directional influence.

4.4.8 Influence of field stimulation on hippocampal-to-cortical gamma band interactions

In our previous work (Greenberg and Dickson, 2013), cortico-cortical gamma coherence was enhanced during slow sinusoidal electrical field stimulation and this finding was replicated in the current work (data not shown, see (Greenberg and Dickson, 2013)). Here we similarly assessed if cortico-hippocampal gamma coherence was affected following high intensities of field stimulation. We found that gamma coherence was enhanced between a specific cortical site and the hippocampus and this enhancement appeared to be in the hippocampal-to-cortical direction (Figure 4.9).

We computed wide bandwidth wavelet coherence on 40 second epochs of data immediately following the cessation of stimulation and compared these to baseline

conditions. For the baseline condition, epochs used for coherence normalization were compared to a randomly chosen epochs of baseline from different time-points (see Methods section). In all cases there was a significant increase in cortico-hippocampal gamma-band coherence for the caudal cortical site following stimulation as compared to the baseline condition ($p < 0.001$; Figure 4.9A). When using spectral Granger analysis, this same channel pair showed enhanced gamma band Granger connectivity following high (but not moderate; Figure 9B) intensity stimulation (Figure 4.9Ci – iii). There was an increase in Granger flow for the hippocampal (HPC) site in comparison to baseline in 4 out of 4 experiments, although this was not significant on average ($p = 0.21$; Figure 4.9Civ). We did not observe this increase in gamma coherence ($p = 0.26$-0.69) of Granger connectivity for any other stimulation condition.

We further explored enhanced cortico-hippocampal gamma coherence across the intra-hippocampal laminar contacts of the linear probe following high intensity stimulation. As shown in Figure 4.10A, LFP wavelet z-coherence increased in the gamma range (~30 – 50 Hz) for almost all hippocampal contacts across depth ($p < 0.001$) except for the region just below the theta phase reversal (-100 μm normalized depth; SRad; $p = 0.15$ - 0.95) (Figure 4.10A – right). Interestingly, there was also a decrease in coherence in approximately the theta band (~ 4 – 8 Hz) specific to the superficial half of the probe contacts (stratum oriens to SRad) ($p < 0.001$). These changes were specific to the post stimulation period since baseline epochs did not show any changes in coherence ($p = 0.2$ - 0.98; Figure 4.10 A). By computing CSD across probe traces we attempted to isolate intra-hippocampal generative zones for gamma and then recomputed wavelet coherence to the posterior cortical site in the cortex. As shown in Figure 4.10B, a similar boost in coherence

emerges but appears more spatially specific with the strongest values at SPyr (+100 normalized depth; $p < 0.001$). Thus, it appears that high intensity stimulation dramatically enhances gamma synchrony between the hippocampus and the cortex in a region-specific manner and most strongly between SPyr and the posterior cortical site. Interestingly, SPyr was also the site that showed enhanced SO range Granger connectivity towards the cortex (cf. Figure 4.6C).

To ensure that the increased gamma coherence between the hippocampal pyramidal layer and the posterior cortical site was not due to volume conduction from homotopic points in the contralateral hippocampus, we separated the combined neocortical and hippocampal signal into neocortical and hippocampal components using ICA. Hippocampal components were those that had a phase reversal within the CA1-dentate axis. This yielded a hippocampal signal with neocortical volume conduction removed, and a neocortical signal with hippocampal volume conduction removed. Coherence analysis on these ICA-processed signals showed highly similar results to the analysis of the raw signals, suggesting that our results were not due to volume conduction. Taken together with the SO and gamma band Granger analysis (cf. Figure 4.7C and 4.8B), this enhanced coherence following electric field application appears to be directed, perhaps somewhat surprisingly, from hippocampus towards cortex.

4.5 Discussion

We have shown that the application of slow sinusoidal electrical fields to frontal regions of the neocortex altered hippocampal-specific activity and created altered cortico-hippocampal interactions at multiple time scales (both slow and fast) in an intensity-dependent fashion. During moderate intensity stimulation we observed entrainment of

hippocampal CSD activity to field stimulation that paralleled the coherence of hippocampal CSD to spontaneous neocortical SO activity, as well as a robust increase in hippocampal ripples and cortical spindles, hinting at enhanced communication between these regions. These effects also persisted following moderate intensity stimulation, albeit at slightly weaker levels. Following cessation of high-intensity stimulation, the dynamics of neocortico-hippocampal interactions were unexpectedly biased in the hippocampal-to-cortical direction. This reversed communication flow was associated with spectral cortical slowing and enhanced hippocampo-neocortical coherence at a frequency that matched the typically slower peak frequency in the hippocampus. Similarly, following high-intensity stimulation, there was an enhancement in hippocampal-to-cortical gamma causal interactions as well as robust increases in gamma synchrony across these regions. These results clearly show that electrical fields applied to a distant cortical region have the ability to alter internal hippocampal dynamics and perhaps more importantly, hippocampo-cortical dynamics. While during (and following) moderate intensities of stimulation cortico-hippocampal communication appeared enhanced by way of the spontaneously dominant cortico-hippocampal route, following high-intensity stimulation this directionality reversed to reflect hippocampo-cortical influence.

4.5.1 Entrainment of hippocampal activity to electrical fields

Consistent with previous findings (Ozen et al., 2010), we observed entrainment of HPC network activity to the phase of both the fundamental and its double of rhythmic field stimulation. Frequency doubling of neural activity in response to rhythmic alternating electric field application has been previously reported by us and others (Greenberg and

Dickson, 2013; Marshall et al., 2006; Ozen et al., 2010) and may be a result of the complex field waveform produced across the spatial arrangement of the stimulation electrodes. This differential field may produce entrainment of networks at different spatial locations to alternate phases of the stimulus. These speculations, however, remain to be tested experimentally.

While we showed that entrainment occurred with a stimulus frequency faster than that of the spontaneous SO (1.67 Hz versus 1.0 Hz), it may also be the case that lower frequencies approaching the natural resonance of forebrain networks might have induced stronger effects. Indeed, it has been noted that optogenetic stimulation during slow-wave states applied at 2 Hz has also been shown to be effective at entraining slow-wave activity, however; it is somewhat less effective than when applied at 1 Hz (Kuki et al., 2013). Our logic for using a faster frequency was to ensure separation of spontaneous versus evoked frequencies and to be able to isolate these potential changes during the stimulation itself.

When using the stimulation sites to deliver brief current pulses we observed a large evoked-potential at the level of SLM, suggesting the involvement of a cortico-temporoammonic pathway in entrainment at the level of the HPC. Given that the anterior-most stimulation site was located above the olfactory bulb, it might have also been the case that this entrainment was elicited by stimulation of olfactory pathways via the piriform cortex. However, this possibility is highly unlikely since direct stimulation of the olfactory bulb produces a very different depth profile, with strong activity at the level of the dentate and no response at SLM, in stark contrast with our results (Cragg, 1960; Yanovsky et al., 2014). Nevertheless, another potential route that cannot be ruled out is a cortico-thalamic

route via the nucleus reuniens which also projects to SLM and receives strong input from frontal regions of cortex (Varela et al., 2014; Vertes et al., 2007).

4.5.2 Influence of field stimulation on hippocampal ripples and cortical spindles

During moderate-intensity stimulation, stronger CSD activity at SRad and SPyr coincided with a dramatic boost in the number of hippocampal sharp-wave ripple events. Ripple oscillations reflect CA1 pyramidal-interneuron interplay that is initiated by intense excitatory input from CA3 collaterals – the so called sharp-wave ripple (SPW-R) phenomenon (Buzsáki et al., 1992; Buzsáki and Silva, 2012). These events are paramount for offline memory replay and consolidation (Bendor and Wilson, 2012; Ji and Wilson, 2007; O'Neill et al., 2008; Wilson and McNaughton, 1994). An increase in ripple density has been shown to occur during post-learning slow-wave sleep (Eschenko et al., 2008; Mölle, 2009), and is correlated with subsequent memory recall in both rats (Ramadan et al., 2009) and humans (Axmacher et al., 2008). In support of this, selective inactivation of ripples during post-training sleep disrupts memory consolidation (Ego-Stengel and Wilson, 2010; Girardeau et al., 2009). Thus, our findings suggest that a simple potential mechanism by which frontal electric field application can enhance hippocampal-dependent memory consolidation is through increased SPW-R incidence.

Similarly to previous research (Marshall et al, 2006), we found that electrical field application also enhanced cortical spindle activity. Sleep spindles (~ 7-15 Hz) are generated through a thalamocortical circuit synchronized by the reticular thalamic nucleus and are grouped into the active phase of the slow oscillation (Nir et al., 2011; Steriade et al., 1993d). There is a close temporal relationship between spindles and SPW-R during slow-wave sleep

in which SPW-Rs precede cortical spindles and are thought to represent hippocampal-to-cortical communication (Peyrache et al., 2011; Siapas and Wilson, 1998; Wierzynski et al., 2009). In line with this idea, spindle density is enhanced by prior learning (Gais et al., 2002; Mölle, 2009) and is associated with subsequent improvement in memory performance (Fuentemilla et al., 2013; Gais et al., 2002).

4.5.3 Bias of hippocampal-to-cortical SO coordination by field stimulation

Consistent with previous work, (Hahn et al., 2012; Isomura et al., 2006; Sirota et al., 2003; Wolansky et al., 2006) there was moderate coherence of cortical and hippocampal SO under spontaneous conditions. Our directionality (Granger) analysis showed that this coherence indicated flow from the cortex to the hippocampus. This finding is in accordance with previous research showing that hippocampal activity tends to follow the cortical SO (Isomura et al., 2006; Ji and Wilson, 2007; Nir et al., 2011; Sirota et al., 2003; Wolansky et al., 2006). This is assumed to occur via excitatory cortico-cortico connections that converge in the entorhinal cortex and provides the hippocampus with both perforant and temporoammonic inputs. During (and following) moderate intensity stimulation, the cortical-to-hippocampal interaction in the slow band was still predominant while internal hippocampal information flow was enhanced from SLM to other hippocampal regions. Immediately following high intensity stimulation, cortical-to-hippocampal communication was dramatically decreased and there was a reversal in the predominant direction of information flow from the hippocampus, specifically from SPyr, towards the cortex.

Using ICA to extract the temporoammonic pathway input to CA1, we found a slight increase of power in this component at the stimulus frequency during moderate intensity

stimulation, while directly following high intensity stimulation this component showed reduced power compared to the baseline condition. These findings suggest that during moderate-intensity stimulation the cortex has enhanced influence upon the hippocampus specifically at the stimulation frequency (together with hippocampal CSD entrainment to the stimulus wave) while following high intensity stimulation cortical influence is suppressed.

Interestingly, post-high intensity stimulation, we also observed a slowing of cortical LFP at all sites, shifting to match the spontaneous slow hippocampal fundamental (~ 0.4 Hz). Indeed, this slower frequency bandwidth showed higher coherence across hippocampo-neocortical sites, suggesting improved hippocampal-to-cortical communication that outlasted the stimulation period. We are the first to report such cortical slowing and the mechanism by which this might occur is unclear. However, our data suggest that in this post-stimulation period, the hippocampus may be having a more prominent influence on cortical activity since cortical influence onto the hippocampus also appeared to be weakened. This weakened cortical influence following high-intensity stimulation is reminiscent of a stimulation induced effect in cardiac tissue in which an artificial pacemaker can cause arrhythmia and ventricular fibrillation due to interference with internal pacing mechanisms (Tavel and Fisch, 1964; Wiggers and Wegma, 1940).

The finding of a slower hippocampal SO fundamental is in line with previous research showing that while the hippocampal SO is influenced by the cortical SO, likely by way of the temporoammonic pathway (which sends direct projections to CA1), it shows some independence in its initiation and coordination with the cortical SO (Isomura et al., 2006; Wolansky et al., 2006). One suggested mechanism for this partial decoherence between cortical and hippocampal SO is the persistent activity of medial entorhinal cortex

layer III cells which delay DOWN state onset and result in a slower frequency of the hippocampal SO in CA1 (Hahn et al., 2012). However, we have been unable to find evidence for persistence in the population activity of the TA input to CA1 at SLM, either in the raw LFP, the CSD trace, or even the component corresponding to the TA extracted by ICA (Whitten et al., 2014). This suggests that persistent activity in individual MEC cells may not reflect the aggregate (synchronized) network activity and thus may not be sufficient for explaining the independent slower hippocampal SO.

4.5.4 Influence of field stimulation on long-range hippocampo-neocortical gamma synchrony

Previously we have shown that rhythmic field stimulation improves cortico-cortical gamma synchrony (Greenberg and Dickson, 2013). A major finding of the current study is that high intensity field stimulation enhances hippocampo-neocortical gamma coherence following the cessation of stimulation. This enhancement was specific to our posterior-most cortical region and the hippocampus, and was strongest at SPyr. This result follows the Granger analysis for the slow frequency range showing enhanced interaction from SPyr to the cortex as well as for the gamma range showing enhanced interaction specifically from the hippocampus to the posterior cortical region. Interestingly, the cortical site at which this contact was located was the only cortical site that was located at the border between the motor and somatosensory cortices. The somatosensory cortex is the most prominent source of sensory information in the rat brain (Burwell et al., 1995) and therefore may be a more likely region for cortico-hippocampal connections.

Cortical and hippocampal gamma is generated by fast-spiking inhibitory interneurons (Cardin et al., 2009; Colgin and Moser, 2010) and long distance coherence is likely achieved through long-range interconnections (Buzsáki et al., 2004; Buzsáki and Wang, 2012). In the current work, our evoked-potential analysis suggests that the initial influence of stimulation onto the hippocampus may arrive at the SLM by way of the temporoammonic pathway. However, hippocampo-neocortical gamma rhythms were presumably linked by way of the hippocampal output via deep entorhinal cortex layer cells.

Gamma rhythms have been implicated in many cognitive functions such as linking distributed cell assemblies that are processing related information – the "binding" hypothesis of gamma (Fries et al., 2007; Harris et al., 2003; Singer et al., 1990; Singer and Gray, 1995). Highly relevant to the current findings, gamma coordination within and across hippocampal and cortical regions is important for all stages of memory processing including memory formation (Fell et al., 2001; Sederberg et al., 2007), consolidation-related replay (Carr et al., 2012), and retrieval (Montgomery and Buzsáki, 2007).

4.5.5 Conclusion

We demonstrate here for the first time that the application of slowly-fluctuating rhythmic electric fields to the brain during slow wave states can be used as a tool to robustly enhance and bias cortico-hippocampal interplay across different bandwidths (such as slow, gamma and ripple frequencies) and in a bidirectional fashion, depending on stimulus intensity. These results can help shed light on the potential mechanisms by which slow oscillations and slow rhythmic electrical fields at the level of frontal cortical regions mediate

improved memory consolidation and how they might be used as a future therapeutic treatment for memory impairment.

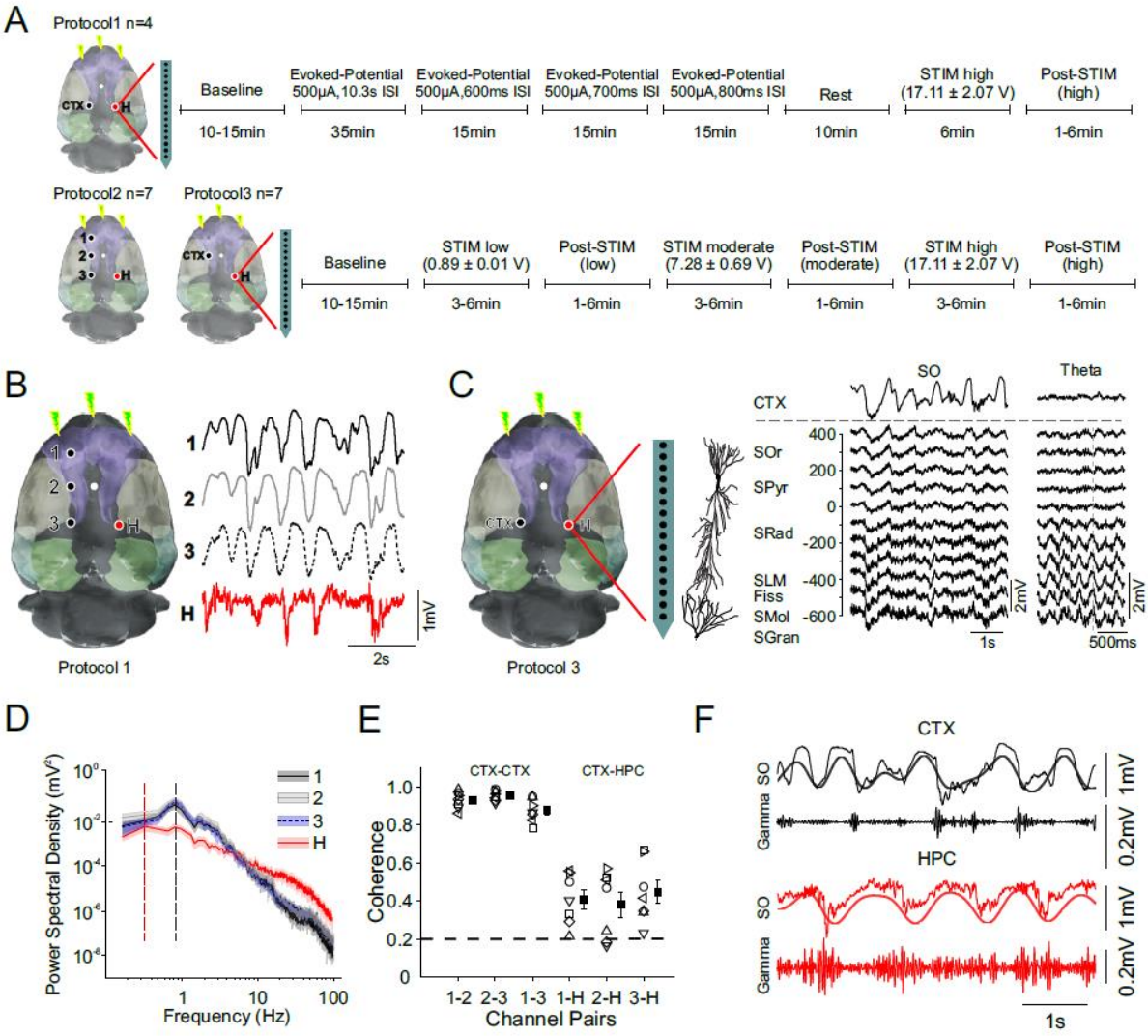

Figure 4.1 Hippocampal SO is moderately coupled to neocortical SO

A. Overview of the three experimental protocols. Rat brain images (dorsal view, nose upwards) show locations of electrodes depicted relative to the position of bregma. The black dots indicate the cortical electrode positions numbered 1, 2 and 3 for protocol 1 and labeled as "CTX" for protocols 1 and 3. The red dot indicates the hippocampal electrode position (H) for the bipolar experiments (protocol 2) or for the location of the linear probe (protocols 1&3), and the white dot indicates bregma. The lightning bolt symbols indicate stimulation electrode positions. Note that cortical electrode position for protocols 1 and 3 correspond to the cortical electrode locations numbered 2 and 3 respectively for protocol 2. Timeline of experiment was identical for protocols 2 and 3. ISI in protocol 1 refers to inter-stimulus

interval. Note that the STIM low condition in protocols 2 and 3 are not discussed in the results section as there were no differences from baseline for any analysis. **B**. Left: Brain in aerial (dorsal) view (nose upwards) with locations of electrodes depicted relative to the position of bregma as in A. Color shaded regions on brain indicate primary cortical areas. The black dots indicate the 3 cortical electrode positions numbered 1, 2 and 3, the red dot indicates the hippocampal electrode position (H) for the bipolar experiments, and the white dot indicates bregma. The lightning bolt symbols indicate stimulation electrode positions. Right: Example raw local field potential (LFP) traces from each electrode site for a single experiment. **C.** Left: Same as in A but for the linear probe experiments. Black dot indicates single cortical site and red dot indicates position of linear probe in the hippocampus. Red expansion lines show a 16-channel linear probe. Right: Spontaneous raw LFP traces from the cortical site and the linear probe for one experiment during SO and theta states. Anatomical representation of cell layers across CA1 maps onto specific normalized depths for the recorded traces. Dotted line along theta traces shows a theta trough in the superficial layers being reversed at the normalized depth of 0 and turning into a theta peak for deeper contacts. **D**. Power spectrum overlaid for all bipolar recording sites for the experiment shown in A. Black dotted line shows spectral peak for cortical SO and red dotted line shows spectral peak for HPC SO. **E.** Average coherence at SO frequency across channel pairs in every bipolar experiment. Open symbols indicate individual experiments and solid symbol indicates grand mean (± SEM). Note strong coherence across cortico-cortical comparisons with substantially lower values for cortico-hippocampal comparisons. Dotted line shows significance cutoff. **F**. Raw and filtered LFP traces for cortical site 1 and HPC from the same experiment as in A show phase coherence of fast activity to the SO. From top to bottom: raw overlaid with SO filtered (0.6 – 1.9 Hz) for cortex (CTX), gamma (30 – 45 Hz) for cortex, raw overlaid with SO filtered for HPC, and gamma (30 – 45 Hz) for HPC. Brain maps in A and B were adapted from: ((Paxinos and Watson, 1998) in BrainNavigator, Elsevier, 2010).

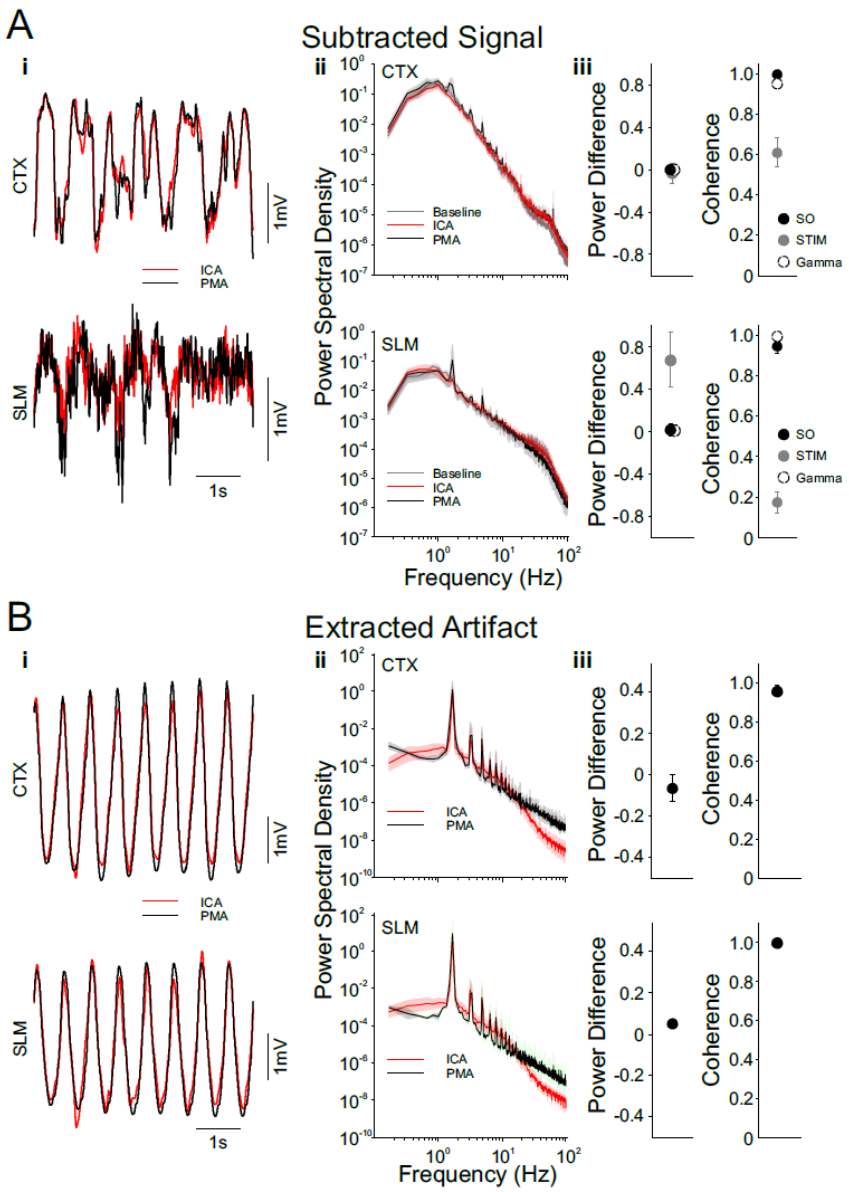

Figure 4.2 Comparison of artifact subtraction for ICA and PMA methods

A. Comparison of spectral properties of subtracted signals during field stimulation for both methods. Top is for the CTX signal and bottom is for SLM. i shows LFP traces overlaid for both subtraction methods (PMA – black, ICA – red). ii shows grand average (shading representing ±SEM) power spectra for baseline, PMA, and ICA subtraction methods. iii left: power difference in the subtracted signals between the two methods for the SO (0.6 – 1.5 Hz), stimulation frequency (1.67 Hz) and gamma (30 – 45 Hz). Note no power differences except for the exact stimulation frequency at SLM. iii right: coherence between the two

subtracted signals at the same frequency bands as for the power comparison. Note strong coherence at all frequency bands expect for the exact stimulation frequency. **B.** Same as in A but for comparing the extracted artifact component. Note strong correspondence in power and coherence for the artifact signals extracted by the two different methods.

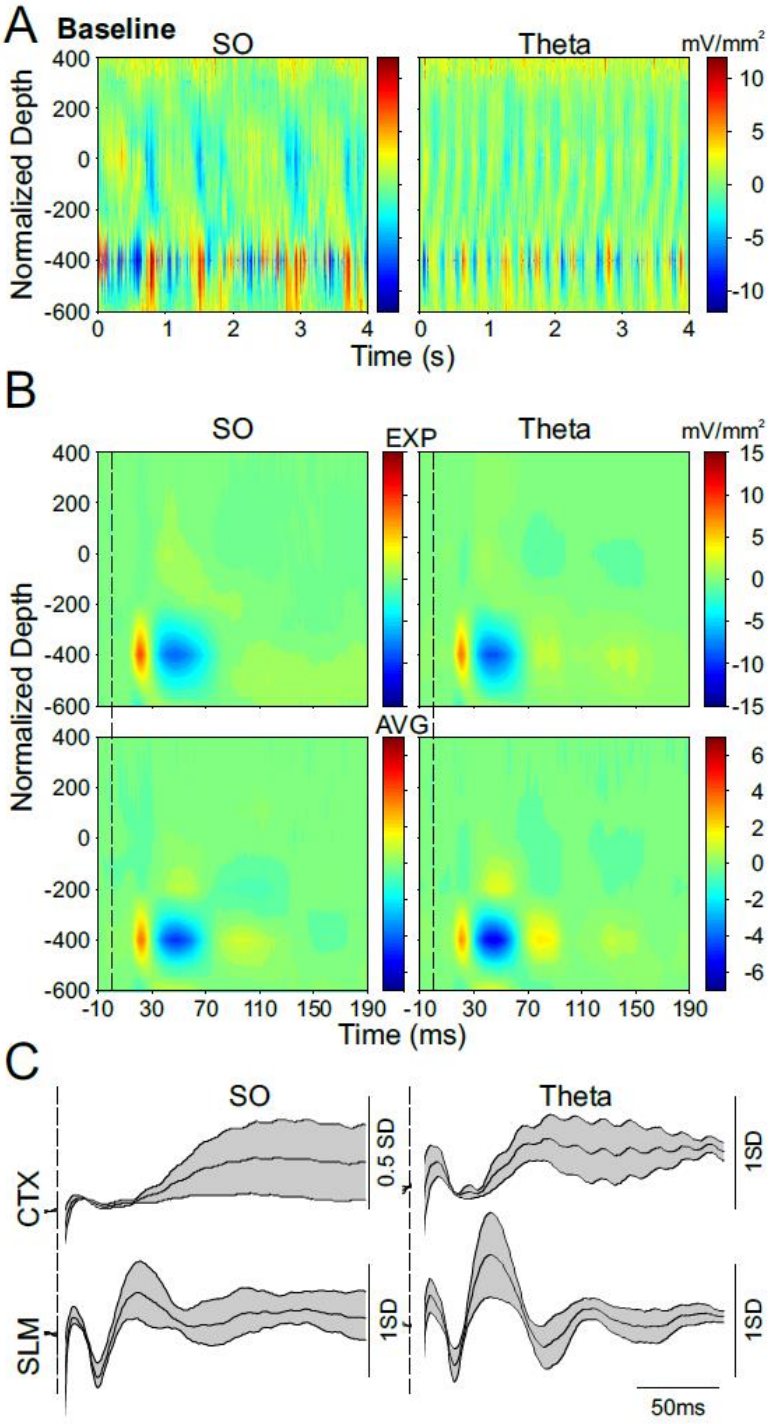

Figure 4.3 Stimulation of frontal regions elicits evoked potentials in the hippocampus

A. Spontaneous CSD plots along normalized hippocampal depth during SO (left) and theta (right). Positive values (warm colors) indicate sinks. Note strongest sink and source alternations at a normalized depth of -400 corresponding to SLM. **B.** CSD plots following

500 µA current application (1 ms) for a single experiment (top) and on average (bottom) during both SO (left) and theta (right). Dotted line indicates onset of current pulse. Note large evoked potentials elicited at SLM for both SO and theta states. **C.** Grand average LFP traces (shading represents ±SEM) showing evoked potentials in CTX (top) and at SLM (bottom) during both SO (left) and theta (right). Dotted line represents onset of current pulse. Current artifact is blanked out.

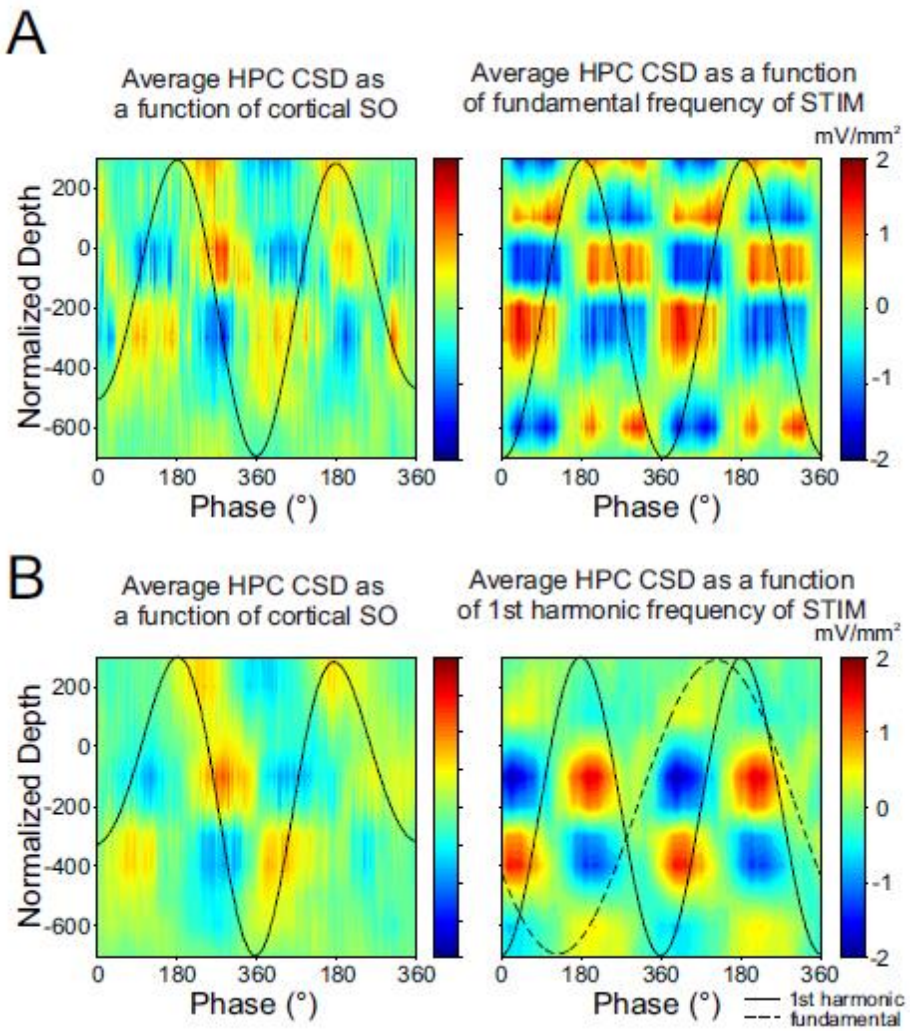

Figure 4.4 Sinusoidal field stimulation entrains hippocampal sink-source alternations

A. Single-experiment example of CSD triggered on peak negativity (0 time) of the filtered cortical SO (0.6 – 1.5 Hz) during baseline spontaneous conditions (left) and of the filtered stimulus artifact waveform (extracted from the cortical site; 1.0 – 1.9 Hz to include the 1.67 Hz fundamental) during moderate-intensity stimulation (right). **B.** Same as in A but for an experiment in which the entrainment occurred to the stimulus frequency doublet. The stimulus artifact was filtered to include the doublet (3.0 – 3.9 Hz). Solid wave shows the artifact for the doublet and the dashed wave shows the artifact filtered for the fundamental as in A. Phase scale corresponds only to the 1st harmonic. Note similarity of sink-source alternations during stimulation to the baseline condition.

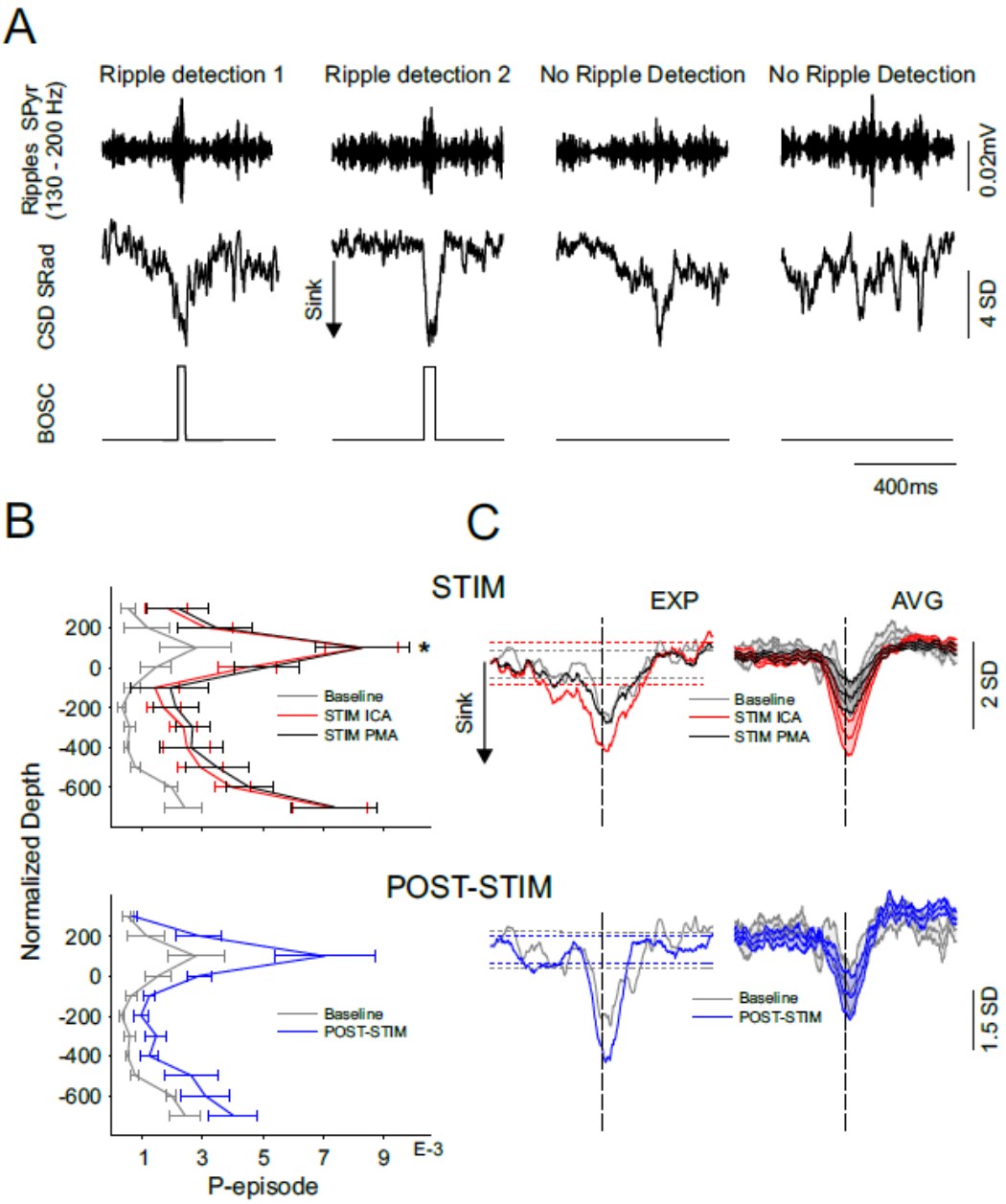

Figure 4.5 Moderate intensity field stimulation boosts sharp-wave ripple events detected by BOSC

A. Single experiment examples of 2 BOSC ripple detections and 2 non-detections. From top to bottom: ripple filtered LFP trace (130 – 200 Hz) at SPyr, corresponding raw CSD trace at SRad and BOSC detection at SPyr. Note detections corresponding to large amplitude bursts in SPyr with clear associated sharp-waves at SRad. Non-detections occurred for clear sharp-waves with no associated ripple, as well as a high-amplitude event at SPyr with no clear

sharp-wave (likely multi-unit activity). **B.** BOSC detections in P-episode along normalized hippocampal depth for baseline as well as during moderate intensity stimulation (top; showing subtracted data from both ICA and PMA methods) and post-moderate intensity stimulation (bottom). Note significant increase in ripple detections at a normalized depth of +100 μm corresponding to SPyr during stimulation and a similar magnitude (non-significant) increase following stimulation. **C.** Single experiment (left) and grand average (right; shading represents ±SEM) ripple triggered average CSD at SRad for baseline, moderate intensity stimulation (top) and post-moderate intensity stimulation (bottom) conditions. Note clear sharp-waves for all conditions corresponding to the BOSC detected ripples at SPyr.

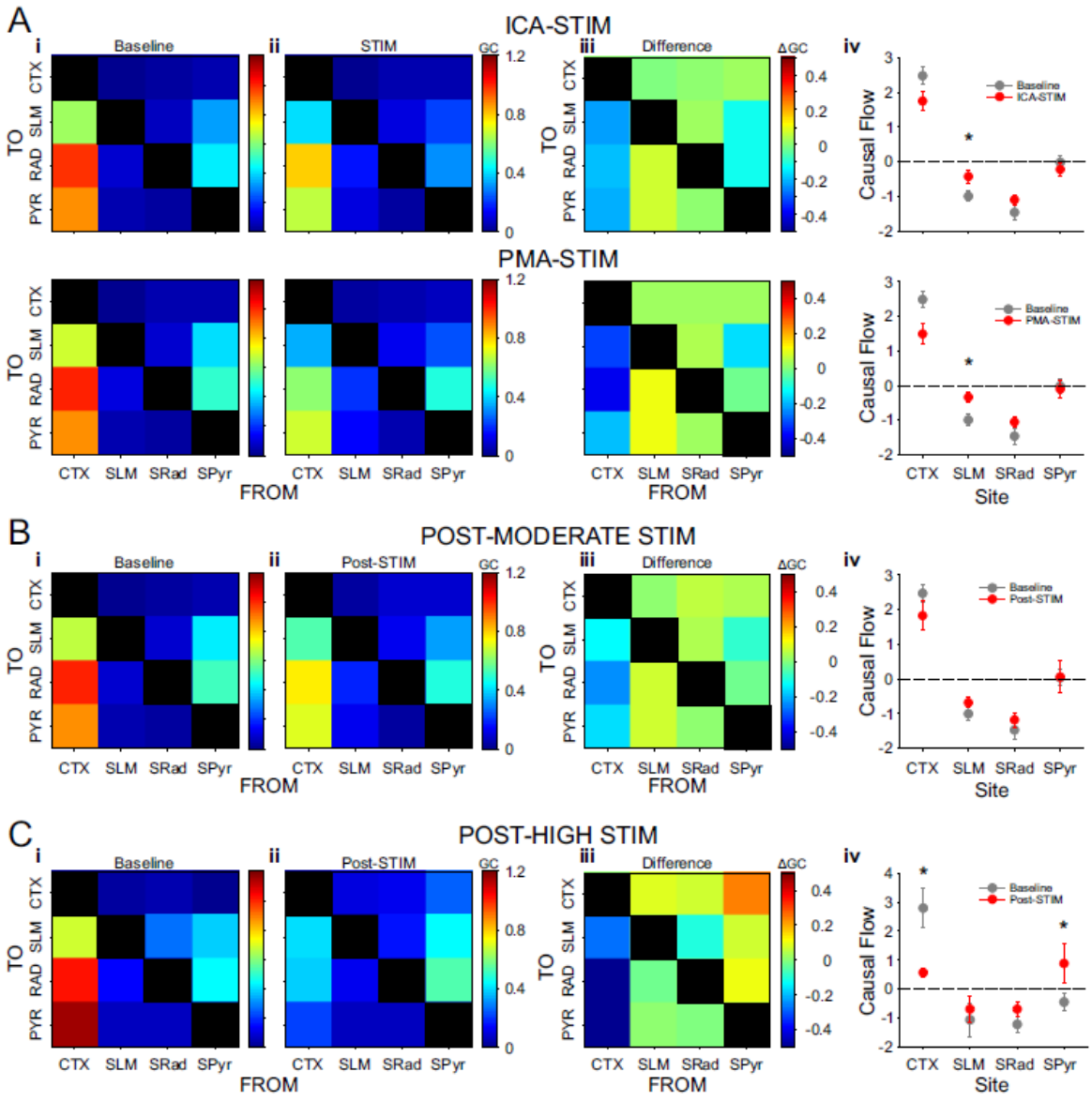

Figure 4.6 Field stimulation alters cortico-hippocampal Granger SO relationships across sites

A. Granger connectivity relationships at the SO frequency (0.8 – 1.2 Hz) during moderate intensity stimulation for CTX, SLM, SRad and SPyr. Top is for ICA subtracted data and bottom is for PMA subtracted data. i shows the grand average Granger causality matrix during the baseline condition, ii shows the Granger matrix during stimulation and iii is the difference between the two. Note reduction in Granger values from the CTX to all HPC sites as well as an increase from SLM to the remaining HPC sites. iv shows average Granger flow

(± SEM) for each site for both baseline and stimulation conditions. Note slight decrease in cortical flow and significant increase in SLM flow during stimulation. Also note similarity between ICA and PMA results. **B.** Same as in A but immediately following the cessation of moderate intensity stimulation. Note similar trend as during stimulation. **C.** Same as in A and B but immediately following the cessation of high intensity stimulation. Note dramatic decrease in Granger connectivity from CTX to all HPC sites and increase in SPyr Granger to CTX. Granger flow (iv) shows a significant decrease in CTX flow and a significant increase and reversal in SPyr flow suggesting a bias towards hippocampal-to-cortical flow.

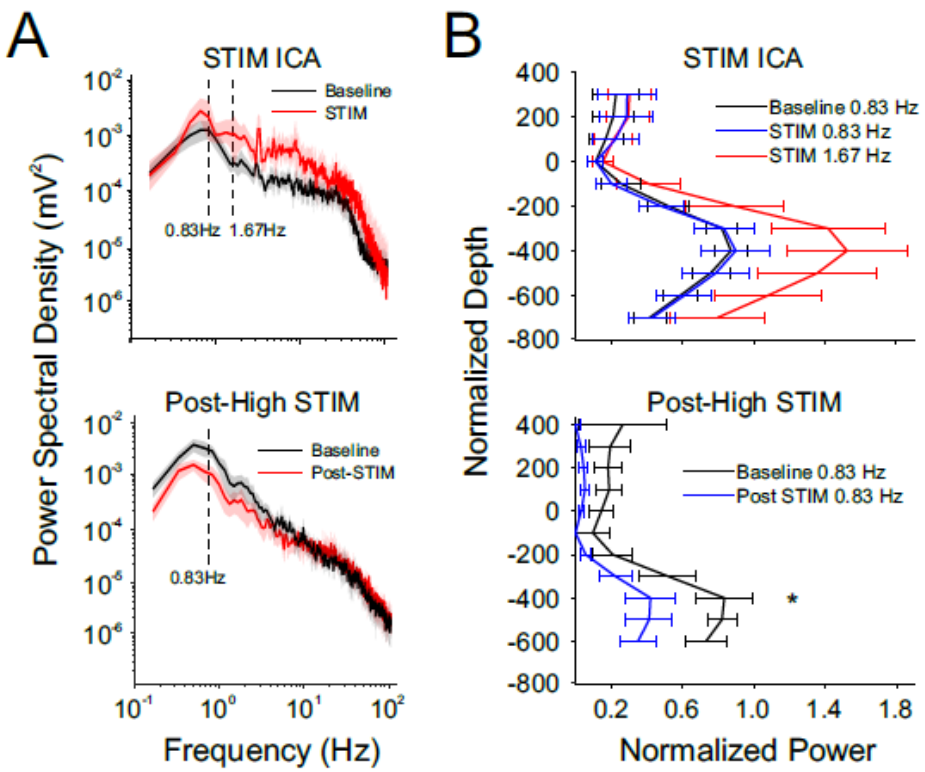

Figure 4.7 Field stimulation alters the temporoammonic input to the hippocampus

A. Power spectra for the ICA component likely representing the temporoammonic pathway input to CA1 for the baseline and the ICA artifact subtracted moderate stimulation condition (top) and following high-intensity stimulation (bottom) for a single experiment in each case. **B.** Power profile for the temporoammonic ICA component across subjects for the SO frequency (0.83 Hz) during baseline and moderate stimulation condition as well as for the stimulation frequency during stimulation (1.67 Hz) (top) and following high-intensity stimulation (bottom). Note reduced SO power at SLM following high-intensity stimulation.

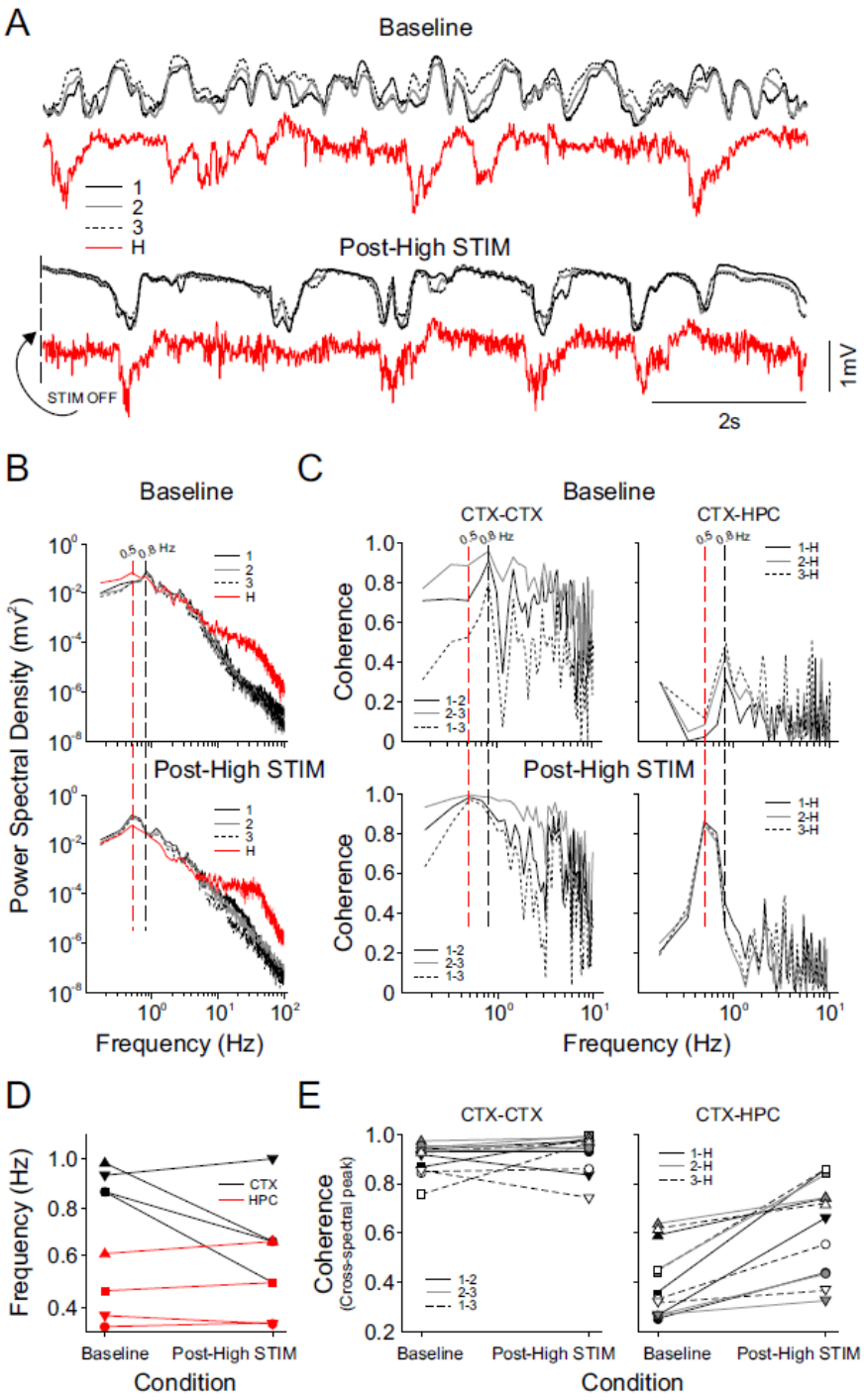

Figure 4.8 Transient slowing of cortical SO and increase in cortico-hippocampal SO coherence is observed following cessation of high intensity stimulation

A. Raw LFP traces for all bipolar channels during baseline recordings (top) and immediately after cessation of high intensity stimulation (bottom). Color coding corresponds to electrode

positions as depicted in Figure 1A. **B.** Power spectra for all channels for the baseline (top) condition and post-high intensity stimulation (bottom) for the same experiment as in A. Red dotted vertical line highlights peak HPC SO frequency and black dotted vertical line depicts peak cortical SO frequency during baseline conditions. Note shift of cortical SO peak frequency to match the slower hippocampal SO frequency post-stimulation. **C.** Coherence spectra for cortico-cortical (left) and cortico-hippocampal (right) channel pair comparisons for baseline (top) and post-high intensity stimulation (bottom) for the same experiment as in A. Red and black vertical dotted lines depict the same frequencies as in B. Note enhanced cortico-hippocampal SO coherence after cessation of stimulation. **D.** Peak spectral frequencies for a single cortical site (posterior site, black) and the hippocampal site (red) during baseline and post-high intensity stimulation for all experiments. **E.** SO coherence selected from peaks in cross-spectra for cortico-cortical (left) and cortico-hippocampal (right) channel pairs for baseline (top) and post-high intensity stimulation (bottom) conditions for all experiments. Note relatively unaffected SO coherence for cortico-cortical comparisons and increases in cortico-hippocampal coherence post-stimulation for all experiments.

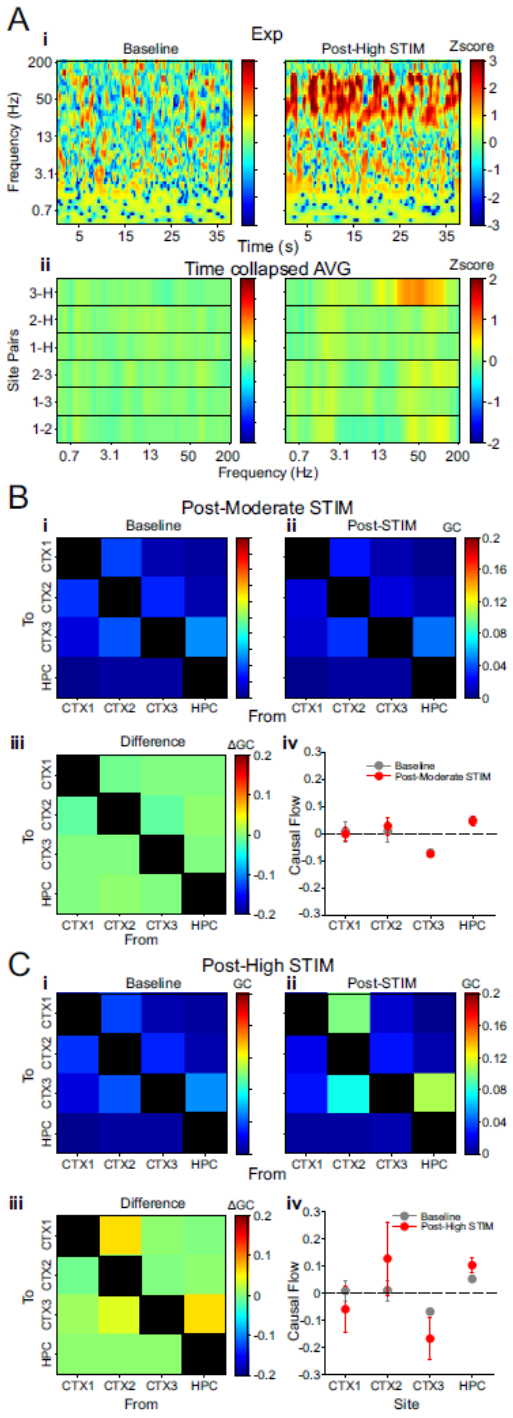

Figure 4.9 Following high intensity stimulation there is an increase in hippocampal-to-cortical gamma range coherence and Granger connectivity

A. Continuous wavelet coherence z-normalized to baseline for the bipolar experiments. i shows baseline (left) and post-high intensity stimulation (right) wavelet coherence for the

posterior cortical site and HPC channel pair z-normalized to a different baseline epoch for a single experiment (Exp). Note strong (> 2SD) z-coherence values in the gamma range following high-intensity stimulation. ii shows grand average (AVG) wavelet coherence plots that have been collapsed across time for all bipolar site comparisons. Note enhancement in gamma range coherence specific to the posterior cortical site (CTX3) and HPC channel pair following high intensity stimulation. **B.** Granger connectivity relationships at the gamma frequency range (30 – 45 Hz) following moderate intensity stimulation for CTX (sites 1, 2 and 3), and HPC in the bipolar experiments. i shows the grand average Granger causality matrix during the baseline condition, ii shows the Granger matrix following stimulation and iii is the difference between the two. iv shows average Granger flow (± SEM) for each site for both baseline and stimulation conditions. Note no changes in Granger connectivity following moderate intensity stimulation. **C.** Same as in B but following high intensity stimulation. Note slight (non-significant) increase in gamma range Granger causality from HPC to CTX3 as well as increase in Granger flow for HPC suggesting enhancement in hippocampal-to-cortical gamma communication.

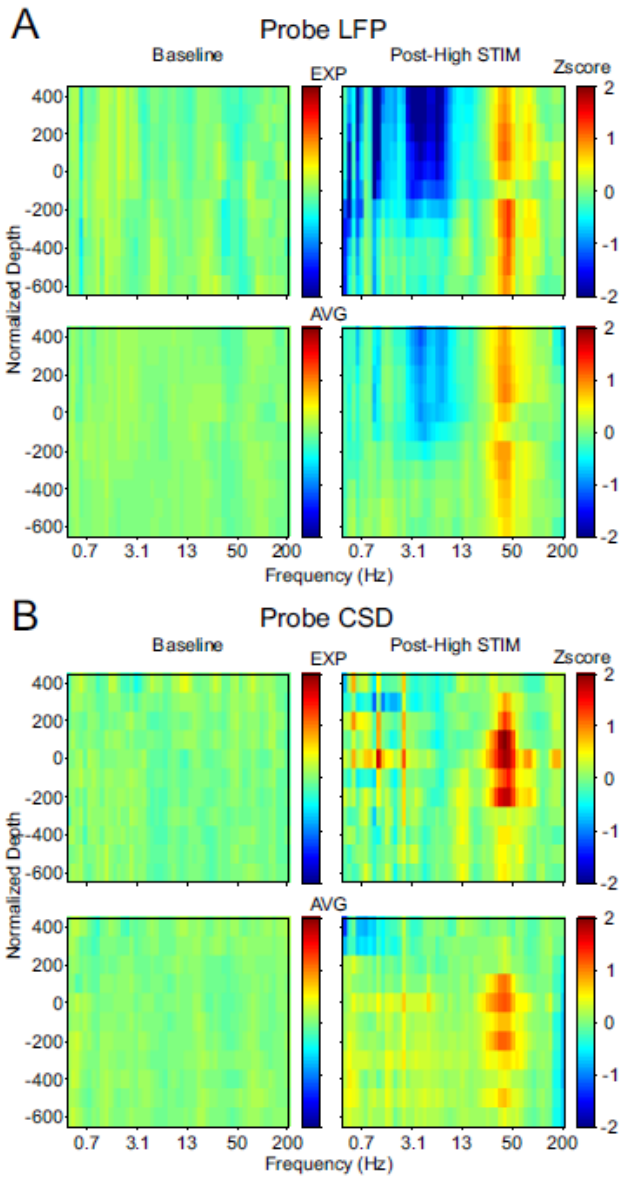

Figure 4.10 Enhanced hippocampo-neocortical gamma synchrony is observed across the hippocampal depth profile following the cessation of high intensity stimulation

A. Time-collapsed wavelet coherence on LFP traces for baseline (left) and following high intensity stimulation (right) for a single experiment (top) and grand average (bottom) comparing each contact across the normalized hippocampal depth to CTX. Note high average z-score values in the gamma range across depth with no enhancement observed around the theta reversal contact (depth of 0). **B.** Same as in A but computed on the hippocampal CSD traces. Note more spatially specific gamma range coherence enhancement

following high intensity stimulation compared to the LFP analysis. The strongest HPC-CTX coherence enhancement appeared at SPyr (depth of +100 μm).

5 Conclusion

In this thesis, my aim was to characterize spontaneous cortical and hippocampal dynamics at multiple local and longer-scale network levels during the SO and to apply rhythmic sinusoidal electrical stimulation at frontal cortical sites in attempt to modulate these dynamics in a fashion that may be relevant for memory consolidation. In Chapter 2 we used a simple 3-channel linear array across rat M1 and found two main propagation patterns along the anterior-posterior plane that competed for expression. Sinusoidal stimulation entrained slow and fast activity and biased propagation towards the anterior-to-posterior directional pattern in an intensity-dependent fashion. In Chapter 3, we expanded this model by using VSD imaging in a bilateral mouse cortical preparation and once again detected two main propagation patterns traveling along a lateral anterior to medial posterior axis. The applied stimulation altered propagation trajectories by creating stereotyped patterns having various initiation zones and a highly consistent termination zone in the somatosensory cortex. In Chapter 4 we introduced hippocampal probe recordings in the rat and found that sinusoidal stimulation enhanced cortico-hippocampal interplay in a number of ways. Moderate intensity stimulation increased hippocampal ripples and cortical spindles, while following the cessation of high intensity stimulation, SO and gamma-band relationships were enhanced particularly in the hippocampal-cortical direction. Taken together, the results from this thesis suggest that rhythmic field stimulation can significantly alter SO dynamics both within and across cortical and hippocampal networks.

Given that various forms of transcranial electrical stimulation have been used to successfully enhance a number of cognitive parameters (Boggio et al., 2007; Ferrucci et al., 2008; Neuling et al., 2013), and particularly memory consolidation (Barham et al., 2016; Goder et al., 2013; Marshall et al., 2006; Prehn-Kristensen et al., 2014), this thesis has

important mechanistic implications for such effects. Transcranial electrical stimulation, and specifically tACS, is an attractive tool for physiological and behavioral manipulation since it has been suggested to modulate the neuronal membrane potential without affecting gross functional properties such as firing rate (Reato et al., 2010, 2013). The results of this thesis show that this type of electrical field application can effectively alter two major functional properties during the SO: 1) cortical SO propagation patterns and 2) cortico-hippocampal relationships. These seemingly unrelated effects have recently been implicated in the mechanism for SO-dependent memory consolidation during which cortical propagation patterns determine directions of plasticity across cortical networks and in turn hippocampal events alter these cortical propagation dynamics (Wei et al., 2016).

5.1 Spontaneous cortical SO propagation dynamics

In this work we systematically characterized spontaneous SO propagation dynamics using the Hilbert transform to track SO on a cycle by cycle basis (Chapters 2 & 3). Cortico-cortical SO was highly coherent across cortical sites in accordance with research showing that membrane potential fluctuations during the SO are consistent across widespread regions (Steriade et al., 1993d; Volgushev et al., 2011). Using our simplified electrode array in Chapter 2 we found two main oppositional direction propagation patterns across M1 in the rat. Remarkably, our results in Chapter 3 using VSD imaging in a wide cortical window in the mouse revealed an average of 14 main propagation patterns with the two most common patterns also showing oppositional directions. The increased spatial information available in this study allowed us to observe that these patterns existed on an angled axis along an anterior lateral (including motor and somatosensory areas) to posterior medial (including

visual and retrosplenial areas) plane; rather than a linear plane as suggested by the first study (Chapter 2) with a limited electrode array.

Furthermore, we addressed the issue of pattern evolution over time. Previous work suggested that on any given cycle a new focal point of SO initiation can emerge (Massimini et al., 2004), but to our knowledge there has not been any systematic examination of whether future pattern occurrence can be predicted based on the past history of patterns. We showed that a given pattern had an increased probability of repeating itself on the subsequent cycle but not on any further cycles thereafter (Chapters 2 & 3). Interestingly, transitions between patterns occurred during the SO OFF state which is associated with network inactivity via disfacilitation (i.e., the removal of synaptic activity) rather than active inhibition (Contreras and Steriade, 1995; Contreras et al., 1996b; Timofeev et al., 2001). This finding suggests that the OFF state may offer a unique opportunity for dynamic events to occur at a time of network quiescence where an alternate hub has the possibility of taking over the initiation and propagation of activity for the next cycle.

In terms of propagation trajectory, human studies generally point to a smooth linear path of propagation initiating from a single focal point (Massimini et al., 2004; Nir et al., 2011) while most animal studies that examined propagation on a finer linear scale suggest a more complex trajectory with multiple peaks of activity (Hangya et al., 2011; Huang et al., 2004; Mohajerani et al., 2010). Our results appear intermediate to these contrasting findings. In Chapter 2 we detected linear propagation across M1 using our 3-channel array for the two major patterns along the anterior-posterior plane, however, non-sequential SO propagation that could not be explained with this simple array made up almost half of all detected patterns. Similarly in Chapter 3 using a large bilateral cortical VSD imaging preparation, the

two major patterns also appeared linear, yet on an angled plane relative to the midline, but more complex patterns were also present. Unlike previous research, however, (Mohajerani et al., 2010), we detected very few patterns that had multiple propagation initiation zones, but a relatively notable amount (~ 15 %) of patterns with multiple termination zones. The discrepancy may be due to the differing filtering ranges used, since we filtered specifically around a tight band-width to focus on the SO whereas the study by Mohajerani and colleagues used a wide filtering band encompassing faster activities. Another difference may be due to our cycle-by-cycle definition of SO propagation with no such segregation performed in the Mohajerani study.

As previously shown (Isomura et al., 2006; Wolansky et al., 2006), we discussed in Chapter 4 the existence of a hippocampal SO that was moderately coherent with the neocortical SO (~ 1 Hz). The hippocampal SO also displayed an independent slower component (~ 0.4 Hz) which likely comes about through cycle skipping of the cortical SO inputs (Hahn et al., 2012; Whitten, 2015). This skipping may be a result of medial EC (MEC) layer III cells with persistent activity outlasting the cortical UP state and thus delaying the DOWN state at its CA1 SLM target area (Hahn et al., 2012). Another possibility is the interaction between the cortical SO and an intrinsic slow hippocampal rhythm recently named “iota” (0.1 - 0.5 Hz) that is present during both activated and deactivated hippocampal states (Whitten, 2015). The interaction between the cortical SO and the hippocampal SO has been shown to involve propagation from the cortex to the hippocampus (Nir et al., 2011), and our results are in line with this notion as our Granger analysis revealed that under spontaneous conditions the SO-related activity flowed from the cortex at any given recording site to the hippocampus (Chapter 4).

5.2 Entrainment of slow and fast activity by sinusoidal stimulation

Throughout all experiments discussed in this thesis (Chapters 2-4), we applied sinusoidal rhythmic field stimulation at frontal cortical regions and assessed the effect of this manipulation on cortical and cortico-hippocampal SO dynamics. The stimulation successfully entrained LFP and MUA activity at all recorded cortical regions in M1 (Chapter 2) in an intensity-dependent fashion, with stronger intensities resulting in stronger entrainment. When expanding to a bilateral VSD preparation, we once again confirmed that all regions of the cortex were entrained to the stimulation, with the effect somewhat reduced for regions further away from the site of stimulation (V1, Chapter 3). Likewise, hippocampal probe recordings showed that hippocampal activity was entrained across depth (Chapter 4).

These findings are in accordance with previous work in rats showing that rhythmic stimulation entrains LFP and single-unit activity in the cortex and hippocampus (Ozen et al., 2010) , and is also in line with human work showing phase reset following the cessation of stimulation which is suggestive of entrainment (Marshall et al., 2006). Our stimulation frequency of 1.67 Hz was chosen to be close to the endogenous SO frequency (~ 1 Hz) while remaining different enough to spectrally separate SO and stimulation related effects. It has been shown that entrainment caused by rhythmic stimulation can be explained by an "Arnold tongue" phenomenon in which the closer the stimulation frequency is to the endogenous frequency, the less stimulation intensity is required for successful entrainment (Ali et al., 2013; Frohlich and McCormick, 2010). Therefore, we suppose that our chosen frequency provided a balance between a frequency different enough to assess stimulation effects and the required intensity for successful entrainment.

5.3 Effects of sinusoidal stimulation on SO propagation dynamics

One of the major goals of this thesis was to examine whether rhythmic stimulation can not only entrain local networks to a new rhythm but also bias or alter the dynamic interregional relationships during the SO. Although it has been previously shown that it is possible to electrically evoke slow-waves that propagate in a similar fashion to endogenous slow-waves from the site of stimulation, (Vyazovskiy et al., 2009), we are the first to our knowledge to examine the effect of rhythmic electric fieldstimulation on propagation dynamics. In Chapter 2, using the linear electrode array, electric field application biased propagation towards the anterior-to-posterior pattern in an intensity-dependent fashion and stereotyped its expression by continuously repeating this pattern and reducing the number of dynamic pattern alternations. In Chapter 3, the use of a large cortical window allowed us to define an unlimited number of 2-D propagation patterns and our clustering algorithm showed that stimulation produced a novel propagation pattern that did not exist under spontaneous conditions. This pattern was likewise stereotyped through consequential repetitions cycle after cycle and reduction in the variety of propagation patterns available for expression in comparison to baseline conditions. Interestingly, although the limited array in Chapter 2 prevented us from being able to consider the stimulation related propagation pattern as a completely separate pattern, when we assessed the stimulation-related pattern in Chapter 3 from the viewpoint of M1 (the area examined in Chapter 2), we would also come to the conclusion that this pattern appears to travel in an anterior-to-posterior direction (see appendix A).

5.4 Effects of sinusoidal stimulation on cortico-hippocampal communication

Field stimulation that was applied to frontal regions of the cortex remarkably affected not only cortico-cortical dynamics (Chapters 2 & 3) but also hippocampal and cortico-hippocampal dynamics (Chapter 4). Stimulation increased hippocampal SPW-R events and cortical spindles both during and immediately following the cessation of stimulation (Chapter 4). SPW-R events are thought to reflect replay of cellular patterns associated with prior spatial experiences (Sutherland and McNaughton, 2000; Wilson and McNaughton, 1994) and are modulated by the SO rhythm (Battaglia et al., 2004; Isomura et al., 2006; Molle et al., 2006; Siapas and Wilson, 1998; Sirota et al., 2003). Cortical spindles, on the other hand, are thought to prime cortical networks for plastic modification (Neske, 2015; Rosanova and Ulrich, 2005; Timofeev et al., 2002) and are likewise modulated by the SO (Steriade, 2006). Therefore, spindles and ripples may act in parallel, brought together in time by the SO in order to consolidate distributed cellular ensembles that represent the neural engram. In support of this, it has been shown that ripples are nested into individual spindle cycles (Clemens et al., 2007; Siapas and Wilson, 1998) and that both of these rhythms are modulated by learning experiences (Clemens et al., 2007; Mölle, 2009; Siapas and Wilson, 1998; Wierzynski et al., 2009).

The effects of stimulation on both SO and gamma-band dynamics suggested that the cortico-hippocampal interactions were not simply enhanced, but were also reversed in their directionality of information flow. Cortico-hippocampal SO was moderately coupled during spontaneous conditions at the cortical SO frequency of ~ 1 Hz. Following high intensity stimulation, cortical activity slowed and became highly coherent with the slower hippocampal component (~ 0.4 Hz). These effects were paralleled by findings of reversed

information flow using Granger analysis, with the hippocampus leading the cortex (Chapter 4). This was further supported by the finding of a reduced SO temporoammonic input to CA1 (the major source of cortical input to the HPC) using ICA analysis that separated out this individual component (Chapter 4).

A nearly identical pattern of results emerged for the gamma-band analysis. In Chapter 2 we showed that stimulation enhances cortico-cortical gamma band coupling and we extended this finding in Chapter 4 to show an increase in cortico-hippocampal gamma band coherence following high intensity stimulation. The strongest gamma coupling with the cortex appeared at the level of SPyr, the output layer of the hippocampus and the Granger analysis once again suggested increased causal flow from the hippocampus to the cortex for gamma frequencies. Taken together, these findings suggest that stimulation may reverse functional relationships between the cortex and hippocampus, perhaps in favour of further reinforcing newly acquired hippocampal memories and their integration with existing cortical representations (Born, 2010; Diekelmann and Born, 2010; Ji and Wilson, 2007; Rasch et al., 2007).

5.5 After-effects of sinusoidal stimulation

Most of the effects of stimulation on cortico-hippocampal dynamics mentioned above, such as cortical slowing and reversal of SO and gamma-band directional communication, occurred following the cessation of stimulation. Furthermore, in Chapter 3, following the cessation of stimulation, the cortical VSD signal was severely depressed for up to 30 minutes and SO propagation was impaired. This effect may be in accordance with the cortical slowing observed in Chapter 4, although it is difficult to compare given the different

species used (mouse in Chapter 3 and rat in Chapter 4) and the potentially different level of injected current as voltage was kept constant. Stimulation-related after-effects have been previously reported for tDCS including increases in firing rate and the influence on gene expression (Bindman et al., 1964; Paulus et al., 2013), yet virtually nothing is known about after-effects related to tACS. Therefore, this work provides important clues suggesting that rhythmic field stimulation has profound effects on cortico-hippocampal interplay that outlast the stimulation period.

5.6 Effects of various stimulation intensities on network dynamics

An important issue that was brought to light by the results of this thesis pertains to the use of various stimulation intensities and the associated consequences on network dynamics. We demonstrated that cortico-cortical SO coherence was progressively disrupted with increasing stimulation intensity while coherence of each cortical site with the stimulation frequency was increasingly enhanced (Chapter 2). This effect suggests a gradual trade-off between the size of the network entrained to the endogenous rhythm and that which becomes progressively entrained to the imposed stimulation rhythm. In line with this idea, we also showed that the modulation of local gamma by the SO phase was disrupted in an intensity-dependent fashion as gamma became instead modulated by the phase of the stimulation (Chapter 2). Therefore, moderate intensities of stimulation create a situation which is potentially disrupting to normal brain function as large parts of the network are entrained either to the endogenous rhythm or to the stimulation, thus dissociating these networks.

Our results are in accordance with previous work showing that stronger intensities of rhythmic stimulation entrain increasingly more units in both the neocortex and hippocampus (Ozen et al., 2010). In this prior study, moderate intensities entrained less than a quarter of neocortical and CA1neurons to the stimulation rhythm (Ozen et al., 2010). This dissociation of entrained and non-entrained units may cause altered cortico-hippocampal interactions, which could explain our results showing a reversal in cortico-hippocampal information flow (Chapter 4). Therefore, there is a complex relationship between stimulation intensity and entrainment, and future research should assess which intensities may benefit or disrupt memory function on a behavioral level.

5.7 Novel methods for removing and avoiding stimulation related electrical artifacts

Examining the effects of rhythmic electrical stimulation on network dynamics are complicated by the presence of large electrical artifacts in field recordings which mask the underlying brain activity. Therefore previous research has examined short stimulus-free epochs interleaved between stimulation sessions, most commonly using a 5-minute stimulation session with 1-minute stimulation-free blocks in between each session (Del Felice et al., 2015; Marshall et al., 2006; Marshall et al., 2004; Prehn-Kristensen et al., 2014; Sahlem et al., 2015). However, this approach potentially neglects important stimulus-related effects that are restricted to the stimulation period. To circumvent this problem, this thesis developed two novel approaches to subtract the stimulus artifact (Chapters 2 & 4). In Chapter 2 we used post-mortem channel-specific recordings of the stimulation artifact to obtain the artifact waveform for cycle-by-cycle artifact subtraction (PMA method). In Chapter 4, we used ICA analysis to detect the artifact component and remove this

component from the time-series (ICA method). We further systematically compared these two subtraction methods and found them to be virtually equivalent in their extraction of an artifact waveform that was highly similar in power, phase, and site-to-site coherence (Chapter 4). There were slight differences present in the artifact subtracted LFP when comparing the application of both methods, however, none of these differences changed the results of stimulation-related effects on network dynamics (Chapter 4). In Chapter 3, we addressed the issue of stimulation artifact using another novel approach; by performing VSD imaging which we hypothesized would be less sensitive to electrical artifacts. Indeed, the application of electrical stimulation under the influence of activity blockers (CNQX+MK-801 or lidocaine) and following brain death, showed a negligible artifact component remaining in the signal which did not propagate. This thesis therefore points to multiple novel approaches for obviating the issue of electrical artifact during sinusoidal stimulation to allow for more precise evaluation of stimulation-related effects on neural function.

5.8 Future directions

The results of this thesis point to several important avenues for future research to better understand the effects of rhythmic electrical stimulation on network dynamics and behavior. Throughout all experiments presented in this work, stimulation was applied near frontal regions of the cortex and SO propagation was biased in a specific stereotyped manner. It would be important for future work to use various stimulation location points and configurations, such as placed at occipital regions, and to examine whether the direction of SO propagation bias could be reversed or altered.

Another unresolved issue pertains to the entrainment of hippocampal activity to the stimulation. We showed that moderate intensity stimulation entrained hippocampal activity across multiple layers of CA1 and brief constant-current shocks to the stimulation sites triggered a strong evoked potential at the level of SLM (Chapter 4). Therefore, it is possible that field stimulation entrains cortical networks which then reach the hippocampus by way of the temporoammonic pathway that terminates at the level of SLM. Another possibility, however, is via the thalamic nucleus reuniens which receives inputs from the prefrontal cortex and also terminates at the level of SLM (Amaral and Lavenex, 2007). Future investigations may decipher between these two possibilities.

Our observation of stimulation after-effects, such as the reversal of information flow from the hippocampus to the cortex, suggests that stimulation may induce long-term functional changes to specific networks. Future research may dissect which part of the cortico-hippocampal circuit could be modified following stimulation. For example, it is possible that CA1 output to the EC may be strengthened resulting in enhanced hippocampal-cortical connectivity and/or that the input from the EC, by way of the temporoammonic pathway, to the CA1 is weakened, as suggested by our ICA temporoammonic component analysis (Chapter 4).

Finally, all of our results were performed on urethane-anesthetised rodents. Although urethane is considered an excellent model for sleep (Clement et al., 2008; Pagliardini et al., 2013; Sceniak and Maciver, 2006; Wolansky et al., 2006), future work should replicate our results in a naturally-sleeping animal. Furthermore, the most important future avenue would be to extend these findings to a chronic behavioral preparation and examine the corresponding effects on memory consolidation.

5.9 Conclusion

Neuroscience has come a long way since the early twentieth century at a time when Berger first performed human EEG recordings (Niedermeyer et al., 2005) and "Electrosleep" studies were taking place in attempt to alter behavioral state by injecting current into the brain (Guleyupoglu et al., 2013). Today, neuroscience has matured to a stage where investigations are trying to marry our knowledge of neural function - from the single cell to network levels, neural structure, normal and pathological behavior, and the consequences of manipulations at multiple levels. This thesis fills a small piece of this gigantic puzzle in demonstrating that rhythmic electrical field stimulation can be used to manipulate large-scale network interactions during sleep-like states in ways potentially beneficial for memory consolidation. Future work may develop optimal stimulation paradigms and assess their efficacy on memory function both in experimental and clinical settings.

References

Alhaj, H., Wisniewski, G., McAllister-Williams, R.H., 2011. The use of the EEG in measuring therapeutic drug action: focus on depression and antidepressants. J Psychopharmacol 25, 1175-1191.

Ali, M.M., Sellers, K.K., Frohlich, F., 2013. Transcranial alternating current stimulation modulates large-scale cortical network activity by network resonance. J Neurosci 33, 11262-11275.

Amaral, D.G., Lavenex, P., 2007. Hippocampal Neuroanatomy. In: Anderson, P., Morris, R., Amaral, D.G., Bliss, T., O'Keefe, J. (Eds.), The Hippocampus Book. Oxford University Press, New York, New York, pp. 37 - 114.

Amzica, F., Steriade, M., 1995a. Disconnection of intracortical synaptic linkages disrupts synchronization of a slow oscillation. J Neurosci 15, 4658-4677.

Amzica, F., Steriade, M., 1995b. Short- and long-range neuronal synchronization of the slow (< 1 Hz) cortical oscillation. J Neurophysiol 73, 20-38.

Annese, J., Schenker-Ahmed, N.M., Bartsch, H., Maechler, P., Sheh, C., Thomas, N., Kayano, J., Ghatan, A., Bresler, N., Frosch, M.P., Klaming, R., Corkin, S., 2014. Postmortem examination of patient H.M.'s brain based on histological sectioning and digital 3D reconstruction. Nat Commun 5, 3122.

Anokhin, A., Steinlein, O., Fischer, C., Mao, Y., Vogt, P., Schalt, E., Vogel, F., 1992. A genetic study of the human low-voltage electroencephalogram. Hum Genet 90, 99-112.

Aroniadou, V.A., Keller, A., 1993. The patterns and synaptic properties of horizontal intracortical connections in the rat motor cortex. J Neurophysiol 70, 1553-1569.

Axmacher, N., Elger, C.E., Fell, J., 2008. Ripples in the medial temporal lobe are relevant for human memory consolidation. Brain 131, 1806-1817.

Barham, M.P., Enticott, P.G., Conduit, R., Lum, J.A., 2016. Transcranial electrical stimulation during sleep enhances declarative (but not procedural) memory consolidation: Evidence from a meta-analysis. Neurosci Biobehav Rev 63, 65-77.

Basu, J., Siegelbaum, S.A., 2015. The Corticohippocampal Circuit, Synaptic Plasticity, and Memory. Cold Spring Harb Perspect Biol 7.

Battaglia, F.P., Sutherland, G.R., McNaughton, B.L., 2004. Hippocampal sharp wave bursts coincide with neocortical "up-state" transitions. Learn Mem 11, 697-704.

Bell, A.J., Sejnowski, T.J., 1995. An information-maximization approach to blind separation and blind deconvolution. Neural Comput 7, 1129-1159.

Beltramo, R., D'Urso, G., Dal Maschio, M., Farisello, P., Bovetti, S., Clovis, Y., Lassi, G., Tucci, V., De Pietri Tonelli, D., Fellin, T., 2013. Layer-specific excitatory circuits differentially control recurrent network dynamics in the neocortex. Nat Neurosci 16, 227-234.

Bendor, D., Wilson, M.A., 2012. Biasing the content of hippocampal replay during sleep. Nat Neurosci 15, 1439-1444.

Benito, N., Fernandez-Ruiz, A., Makarov, V.A., Makarova, J., Korovaichuk, A., Herreras, O., 2014. Spatial modules of coherent activity in pathway-specific LFPs in the hippocampus reflect topology and different modes of presynaptic synchronization. Cereb Cortex 24, 1738-1752.

Bestmann, S., de Berker, A.O., Bonaiuto, J., 2015. Understanding the behavioural consequences of noninvasive brain stimulation. Trends Cogn Sci 19, 13-20.

Bi, G.Q., Poo, M.M., 1998. Synaptic modifications in cultured hippocampal neurons: dependence on spike timing, synaptic strength, and postsynaptic cell type. J Neurosci 18, 10464-10472.

Binder, S., Baier, P.C., Molle, M., Inostroza, M., Born, J., Marshall, L., 2012. Sleep enhances memory consolidation in the hippocampus-dependent object-place recognition task in rats. Neurobiol Learn Mem 97, 213-219.

Binder, S., Berg, K., Gasca, F., Lafon, B., Parra, L.C., Born, J., Marshall, L., 2014a. Transcranial slow oscillation stimulation during sleep enhances memory consolidation in rats. Brain Stimul 7, 508-515.

Binder, S., Rawohl, J., Born, J., Marshall, L., 2014b. Transcranial slow oscillation stimulation during NREM sleep enhances acquisition of the radial maze task and modulates cortical network activity in rats. Front Behav Neurosci 7, 220.

Bindman, L.J., Lippold, O.C., Redfearn, J.W., 1964. The Action of Brief Polarizing Currents on the Cerebral Cortex of the Rat (1) during Current Flow and (2) in the Production of Long-Lasting after-Effects. J Physiol 172, 369-382.

Boggio, P.S., Bermpohl, F., Vergara, A.O., Muniz, A.L., Nahas, F.H., Leme, P.B., Rigonatti, S.P., Fregni, F., 2007. Go-no-go task performance improvement after anodal transcranial DC stimulation of the left dorsolateral prefrontal cortex in major depression. J Affect Disord 101, 91-98.

Boggio, P.S., Khoury, L.P., Martins, D.C., Martins, O.E., de Macedo, E.C., Fregni, F., 2009. Temporal cortex direct current stimulation enhances performance on a visual recognition memory task in Alzheimer disease. J Neurol Neurosurg Psychiatry 80, 444-447.

Boggio, P.S., Sultani, N., Fecteau, S., Merabet, L., Mecca, T., Pascual-Leone, A., Basaglia, A., Fregni, F., 2008. Prefrontal cortex modulation using transcranial DC stimulation reduces alcohol craving: a double-blind, sham-controlled study. Drug Alcohol Depend 92, 55-60.

Born, J., 2010. Slow-wave sleep and the consolidation of long-term memory. World J Biol Psychiatry 11 Suppl 1, 16-21.

Born, J., Rasch, B., Gais, S., 2006. Sleep to remember. Neuroscientist 12, 410-424.

Brown, R.E., Basheer, R., McKenna, J.T., Strecker, R.E., McCarley, R.W., 2012. Control of sleep and wakefulness. Physiol Rev 92, 1087-1187.

Bruns, A., 2004. Fourier-, Hilbert- and wavelet-based signal analysis: are they really different approaches? J Neurosci Methods 137, 321-332.

Burwell, R.D., Witter, M.P., Amaral, D.G., 1995. Perirhinal and postrhinal cortices of the rat: a review of the neuroanatomical literature and comparison with findings from the monkey brain. Hippocampus 5, 390-408.

Buzsáki, G., 1998. Memory consolidation during sleep: a neurophysiological perspective. J Sleep Res 7 Suppl 1, 17-23.

Buzsáki, G., 2006. Rhythms of the brain. Oxford University Press, Oxford ; New York.

Buzsáki, G., Draguhn, A., 2004. Neuronal oscillations in cortical networks. Science 304, 1926-1929.

Buzsáki, G., Geisler, C., Henze, D.A., Wang, X.J., 2004. Interneuron Diversity series: Circuit complexity and axon wiring economy of cortical interneurons. Trends Neurosci 27, 186-193.

Buzsáki, G., Horvath, Z., Urioste, R., Hetke, J., Wise, K., 1992. High-frequency network oscillation in the hippocampus. Science 256, 1025-1027.

Buzsáki, G., Logothetis, N., Singer, W., 2013. Scaling brain size, keeping timing: evolutionary preservation of brain rhythms. Neuron 80, 751-764.

Buzsáki, G., Moser, E.I., 2013. Memory, navigation and theta rhythm in the hippocampal-entorhinal system. Nat Neurosci 16, 130-138.

Buzsáki, G., Silva, F.L., 2012. High frequency oscillations in the intact brain. Prog Neurobiol 98, 241-249.

Buzsáki, G., Wang, X.J., 2012. Mechanisms of gamma oscillations. Annu Rev Neurosci 35, 203-225.

Canolty, R.T., Edwards, E., Dalal, S.S., Soltani, M., Nagarajan, S.S., Kirsch, H.E., Berger, M.S., Barbaro, N.M., Knight, R.T., 2006. High gamma power is phase-locked to theta oscillations in human neocortex. Science 313, 1626-1628.

Canolty, R.T., Knight, R.T., 2010. The functional role of cross-frequency coupling. Trends Cogn Sci 14, 506-515.

Caplan, J.B., Madsen, J.R., Raghavachari, S., Kahana, M.J., 2001. Distinct patterns of brain oscillations underlie two basic parameters of human maze learning. J Neurophysiol 86, 368-380.

Cardin, J.A., Carlen, M., Meletis, K., Knoblich, U., Zhang, F., Deisseroth, K., Tsai, L.H., Moore, C.I., 2009. Driving fast-spiking cells induces gamma rhythm and controls sensory responses. Nature 459, 663-667.

Carr, M.F., Karlsson, M.P., Frank, L.M., 2012. Transient slow gamma synchrony underlies hippocampal memory replay. Neuron 75, 700-713.

Castellanos, N.P., Makarov, V.A., 2006. Recovering EEG brain signals: artifact suppression with wavelet enhanced independent component analysis. J Neurosci Methods 158, 300-312.

Chan, A.W., Mohajerani, M.H., LeDue, J.M., Wang, Y.T., Murphy, T.H., 2015. Mesoscale infraslow spontaneous membrane potential fluctuations recapitulate high-frequency activity cortical motifs. Nat Commun 6, 7738.

Chauvette, S., Crochet, S., Volgushev, M., Timofeev, I., 2011. Properties of slow oscillation during slow-wave sleep and anesthesia in cats. J Neurosci 31, 14998-15008.

Chauvette, S., Seigneur, J., Timofeev, I., 2012. Sleep oscillations in the thalamocortical system induce long-term neuronal plasticity. Neuron 75, 1105-1113.

Chauvette, S., Volgushev, M., Timofeev, I., 2010. Origin of active states in local neocortical networks during slow sleep oscillation. Cereb Cortex 20, 2660-2674.

Clemens, Z., Fabo, D., Halasz, P., 2005. Overnight verbal memory retention correlates with the number of sleep spindles. Neuroscience 132, 529-535.

Clemens, Z., Molle, M., Eross, L., Barsi, P., Halasz, P., Born, J., 2007. Temporal coupling of parahippocampal ripples, sleep spindles and slow oscillations in humans. Brain 130, 2868-2878.

Clement, E.A., Richard, A., Thwaites, M., Ailon, J., Peters, S., Dickson, C.T., 2008. Cyclic and sleep-like spontaneous alternations of brain state under urethane anaesthesia. PLoS One 3, e2004.

Colgin, L.L., Moser, E.I., 2010. Gamma oscillations in the hippocampus. Physiology (Bethesda) 25, 319-329.

Contreras, D., Destexhe, A., Sejnowski, T.J., Steriade, M., 1996a. Control of spatiotemporal coherence of a thalamic oscillation by corticothalamic feedback. Science 274, 771-774.

Contreras, D., Destexhe, A., Sejnowski, T.J., Steriade, M., 1997. Spatiotemporal patterns of spindle oscillations in cortex and thalamus. J Neurosci 17, 1179-1196.

Contreras, D., Steriade, M., 1995. Cellular basis of EEG slow rhythms: a study of dynamic corticothalamic relationships. J Neurosci 15, 604-622.

Contreras, D., Timofeev, I., Steriade, M., 1996b. Mechanisms of long-lasting hyperpolarizations underlying slow sleep oscillations in cat corticothalamic networks. J Physiol 494 (Pt 1), 251-264.

Corkin, S., 2002. What's new with the amnesic patient H.M.? Nat Rev Neurosci 3, 153-160.

Cragg, B.G., 1960. Responses of the hippocampus to stimulation of the olfactory bulb and of various afferent nerves in five mammals. Exp Neurol 2, 547-572.

Crane, J.W., Windels, F., Sah, P., 2009. Oscillations in the basolateral amygdala: aversive stimulation is state dependent and resets the oscillatory phase. J Neurophysiol 102, 1379-1387.

Crick, F., 1990. What Mad Pursuit: A Personal View of Scientific Discovery. Basic Books, New York.

Crunelli, V., Hughes, S.W., 2010. The slow (<1 Hz) rhythm of non-REM sleep: a dialogue between three cardinal oscillators. Nat Neurosci 13, 9-17.

Dan, Y., Poo, M.M., 2004. Spike timing-dependent plasticity of neural circuits. Neuron 44, 23-30.

David, F., Schmiedt, J.T., Taylor, H.L., Orban, G., Di Giovanni, G., Uebele, V.N., Renger, J.J., Lambert, R.C., Leresche, N., Crunelli, V., 2013. Essential thalamic contribution to slow waves of natural sleep. J Neurosci 33, 19599-19610.

De Gennaro, L., Marzano, C., Fratello, F., Moroni, F., Pellicciari, M.C., Ferlazzo, F., Costa, S., Couyoumdjian, A., Curcio, G., Sforza, E., Malafosse, A., Finelli, L.A., Pasqualetti, P., Ferrara, M., Bertini, M., Rossini, P.M., 2008. The electroencephalographic fingerprint of sleep is genetically determined: a twin study. Ann Neurol 64, 455-460.

Deans, J.K., Powell, A.D., Jefferys, J.G., 2007. Sensitivity of coherent oscillations in rat hippocampus to AC electric fields. J Physiol 583, 555-565.

DeFelipe, J., Farinas, I., 1992. The pyramidal neuron of the cerebral cortex: morphological and chemical characteristics of the synaptic inputs. Prog Neurobiol 39, 563-607.

Del Felice, A., Magalini, A., Masiero, S., 2015. Slow-oscillatory Transcranial Direct Current Stimulation Modulates Memory in Temporal Lobe Epilepsy by Altering Sleep Spindle Generators: A Possible Rehabilitation Tool. Brain Stimul 8, 567-573.

Delorme, A., Makeig, S., 2004. EEGLAB: an open source toolbox for analysis of single-trial EEG dynamics including independent component analysis. J Neurosci Methods 134, 9-21.

Dickson, C.T., 2010. Ups and downs in the hippocampus: the influence of oscillatory sleep states on "neuroplasticity" at different time scales. Behav Brain Res 214, 35-41.

Dickson, C.T., de Curtis, M., 2002. Enhancement of temporal and spatial synchronization of entorhinal gamma activity by phase reset. Hippocampus 12, 447-456.

Diekelmann, S., Born, J., 2010. The memory function of sleep. Nat Rev Neurosci 11, 114-126.

Dubljevic, V., Saigle, V., Racine, E., 2014. The rising tide of tDCS in the media and academic literature. Neuron 82, 731-736.

Dunmyre, J.R., Mashour, G.A., Booth, V., 2014. Coupled flip-flop model for REM sleep regulation in the rat. PLoS One 9, e94481.

Economist, T., 2015. Hacking your brain.

Ego-Stengel, V., Wilson, M.A., 2010. Disruption of ripple-associated hippocampal activity during rest impairs spatial learning in the rat. Hippocampus 20, 1-10.

Eichenbaum, H., 2013. What H.M. taught us. J Cogn Neurosci 25, 14-21.

Eschenko, O., Molle, M., Born, J., Sara, S.J., 2006. Elevated sleep spindle density after learning or after retrieval in rats. J Neurosci 26, 12914-12920.

Eschenko, O., Ramadan, W., Molle, M., Born, J., Sara, S.J., 2008. Sustained increase in hippocampal sharp-wave ripple activity during slow-wave sleep after learning. Learn Mem 15, 222-228.

Fell, J., Klaver, P., Lehnertz, K., Grunwald, T., Schaller, C., Elger, C.E., Fernandez, G., 2001. Human memory formation is accompanied by rhinal-hippocampal coupling and decoupling. Nat Neurosci 4, 1259-1264.

Fellin, T., Halassa, M.M., Terunuma, M., Succol, F., Takano, H., Frank, M., Moss, S.J., Haydon, P.G., 2009. Endogenous nonneuronal modulators of synaptic transmission control cortical slow oscillations in vivo. Proc Natl Acad Sci U S A 106, 15037-15042.

Fernandez-Ruiz, A., Herreras, O., 2013. Identifying the synaptic origin of ongoing neuronal oscillations through spatial discrimination of electric fields. Front Comput Neurosci 7, 5.

Ferrucci, R., Mameli, F., Guidi, I., Mrakic-Sposta, S., Vergari, M., Marceglia, S., Cogiamanian, F., Barbieri, S., Scarpini, E., Priori, A., 2008. Transcranial direct current stimulation improves recognition memory in Alzheimer disease. Neurology 71, 493-498.

Fogel, S.M., Smith, C.T., 2011. The function of the sleep spindle: a physiological index of intelligence and a mechanism for sleep-dependent memory consolidation. Neurosci Biobehav Rev 35, 1154-1165.

Fowler, M.J., Sullivan, M.J., Ekstrand, B.R., 1973. Sleep and memory. Science 179, 302-304.

Freeman, W.J., 1975. Mass action in the nervous system : examination of the neurophysiological basis of adaptive behavior through the EEG. Academic Press, New York.

Freeman, W.J., Burke, B.C., Holmes, M.D., 2003. Aperiodic phase re-setting in scalp EEG of beta-gamma oscillations by state transitions at alpha-theta rates. Hum Brain Mapp 19, 248-272.

Freund, T.F., Buzsáki, G., 1996. Interneurons of the hippocampus. Hippocampus 6, 347-470.

Fries, P., Nikolic, D., Singer, W., 2007. The gamma cycle. Trends Neurosci 30, 309-316.

Frohlich, F., McCormick, D.A., 2010. Endogenous electric fields may guide neocortical network activity. Neuron 67, 129-143.

Fucke, T., Suchanek, D., Nawrot, M.P., Seamari, Y., Heck, D.H., Aertsen, A., Boucsein, C., 2012. Stereotypical spatiotemporal activity patterns during slow-wave activity in the neocortex. J Neurophysiol 106, 3035-3044.

Fuentemilla, L., Miro, J., Ripolles, P., Vila-Ballo, A., Juncadella, M., Castaner, S., Salord, N., Monasterio, C., Falip, M., Rodriguez-Fornells, A., 2013. Hippocampus-dependent strengthening of targeted memories via reactivation during sleep in humans. Curr Biol 23, 1769-1775.

Gais, S., Born, J., 2004. Declarative memory consolidation: mechanisms acting during human sleep. Learn Mem 11, 679-685.

Gais, S., Molle, M., Helms, K., Born, J., 2002. Learning-dependent increases in sleep spindle density. J Neurosci 22, 6830-6834.

Girardeau, G., Benchenane, K., Wiener, S.I., Buzsáki, G., Zugaro, M.B., 2009. Selective suppression of hippocampal ripples impairs spatial memory. Nat Neurosci 12, 1222-1223.

Goder, R., Baier, P.C., Beith, B., Baecker, C., Seeck-Hirschner, M., Junghanns, K., Marshall, L., 2013. Effects of transcranial direct current stimulation during sleep on memory performance in patients with schizophrenia. Schizophr Res 144, 153-154.

Goodrich, G.B., 2010. We Do, Therefore We Think: Time, Motility, and Consciousness. Reviews in the Neurosciences 21, 331-361.

Granger, C.W.J., 1969. Investigating Causal Relations by Econometric Models and Cross-spectral Methods. Econometrica 37, 424-438.

Greenberg, A., Dickson, C.T., 2013. Spontaneous and electrically modulated spatiotemporal dynamics of the neocortical slow oscillation and associated local fast activity. Neuroimage 83C, 782-794.

Greenberg, A., Whitten, T.A., Dickson, C.T., 2016. Stimulating forebrain communications: Slow sinusoidal electric fields over frontal cortices dynamically modulate hippocampal activity and cortico-hippocampal interplay during slow-wave states. Neuroimage 133, 189-206.

Grenier, F., Timofeev, I., Steriade, M., 2001. Focal synchronization of ripples (80-200 Hz) in neocortex and their neuronal correlates. J Neurophysiol 86, 1884-1898.

Guleyupoglu, B., Schestatsky, P., Edwards, D., Fregni, F., Bikson, M., 2013. Classification of methods in transcranial electrical stimulation (tES) and evolving strategy from historical approaches to contemporary innovations. J Neurosci Methods 219, 297-311.

Hahn, T.T., McFarland, J.M., Berberich, S., Sakmann, B., Mehta, M.R., 2012. Spontaneous persistent activity in entorhinal cortex modulates cortico-hippocampal interaction in vivo. Nat Neurosci 15, 1531-1538.

Halassa, M.M., 2011. Thalamocortical dynamics of sleep: roles of purinergic neuromodulation. Semin Cell Dev Biol 22, 245-251.

Hangya, B., Tihanyi, B.T., Entz, L., Fabo, D., Eross, L., Wittner, L., Jakus, R., Varga, V., Freund, T.F., Ulbert, I., 2011. Complex propagation patterns characterize human cortical activity during slow-wave sleep. J Neurosci 31, 8770-8779.

Harris, K.D., Csicsvari, J., Hirase, H., Dragoi, G., Buzsáki, G., 2003. Organization of cell assemblies in the hippocampus. Nature 424, 552-556.

Huang, X., Troy, W.C., Yang, Q., Ma, H., Laing, C.R., Schiff, S.J., Wu, J.Y., 2004. Spiral waves in disinhibited mammalian neocortex. J Neurosci 24, 9897-9902.

Hubel, D.H., Wiesel, T.N., 1962. Receptive fields, binocular interaction and functional architecture in the cat's visual cortex. J Physiol 160, 106-154.

Hubel, D.H., Wiesel, T.N., 1963. Shape and arrangement of columns in cat's striate cortex. J Physiol 165, 559-568.

Huber, R., Ghilardi, M.F., Massimini, M., Ferrarelli, F., Riedner, B.A., Peterson, M.J., Tononi, G., 2006. Arm immobilization causes cortical plastic changes and locally decreases sleep slow wave activity. Nat Neurosci 9, 1169-1176.

Huber, R., Ghilardi, M.F., Massimini, M., Tononi, G., 2004. Local sleep and learning. Nature 430, 78-81.

Hughes, A.M., Whitten, T.A., Caplan, J.B., Dickson, C.T., 2012. BOSC: a better oscillation detection method, extracts both sustained and transient rhythms from rat hippocampal recordings. Hippocampus 22, 1417-1428.

Isomura, Y., Sirota, A., Ozen, S., Montgomery, S., Mizuseki, K., Henze, D.A., Buzsáki, G., 2006. Integration and segregation of activity in entorhinal-hippocampal subregions by neocortical slow oscillations. Neuron 52, 871-882.

Jauregui-Lobera, I., 2012. Electroencephalography in eating disorders. Neuropsychiatr Dis Treat 8, 1-11.

Ji, D., Wilson, M.A., 2007. Coordinated memory replay in the visual cortex and hippocampus during sleep. Nat Neurosci 10, 100-107.

Ketchum, K.L., Haberly, L.B., 1993. Synaptic events that generate fast oscillations in piriform cortex. J Neurosci 13, 3980-3985.

Kramer, M.A., Tort, A.B., Kopell, N.J., 2008. Sharp edge artifacts and spurious coupling in EEG frequency comodulation measures. J Neurosci Methods 170, 352-357.

Kuki, T., Ohshiro, T., Ito, S., Ji, Z.G., Fukazawa, Y., Matsuzaka, Y., Yawo, H., Mushiake, H., 2013. Frequency-dependent entrainment of neocortical slow oscillation to repeated optogenetic stimulation in the anesthetized rat. Neurosci Res 75, 35-45.

Kurth, S., Ringli, M., Geiger, A., LeBourgeois, M., Jenni, O.G., Huber, R., 2010. Mapping of cortical activity in the first two decades of life: a high-density sleep electroencephalogram study. J Neurosci 30, 13211-13219.

Le Bon-Jego, M., Yuste, R., 2007. Persistently active, pacemaker-like neurons in neocortex. Front Neurosci 1, 123-129.

Le Van Quyen, M., Bragin, A., 2007. Analysis of dynamic brain oscillations: methodological advances. Trends Neurosci 30, 365-373.

Le Van Quyen, M., Staba, R., Bragin, A., Dickson, C., Valderrama, M., Fried, I., Engel, J., 2010. Large-scale microelectrode recordings of high-frequency gamma oscillations in human cortex during sleep. J Neurosci 30, 7770-7782.

Lechner, H.A., Squire, L.R., Byrne, J.H., 1999. 100 years of consolidation--remembering Muller and Pilzecker. Learn Mem 6, 77-87.

Lee, A.K., Wilson, M.A., 2002. Memory of sequential experience in the hippocampus during slow wave sleep. Neuron 36, 1183-1194.

Lefebvre, H., 1992. Éléments de rythmanalyse. Introduction à la connaissance des rythmes. Éditions Syllepse, Paris.

Lefebvre, H., 2004. Rhythmanalysis: Space, Time and Everyday Life. Bloomsbury Academic London, UK.

Lemieux, M., Chauvette, S., Timofeev, I., 2015. Neocortical inhibitory activities and long-range afferents contribute to the synchronous onset of silent states of the neocortical slow oscillation. J Neurophysiol 113, 768-779.

Lemieux, M., Chen, J.Y., Lonjers, P., Bazhenov, M., Timofeev, I., 2014. The impact of cortical deafferentation on the neocortical slow oscillation. J Neurosci 34, 5689-5703.

Lewis, T.J., Rinzel, J., 2000. Self-organized synchronous oscillations in a network of excitable cells coupled by gap junctions. Network 11, 299-320.

Logothetis, N.K., Eschenko, O., Murayama, Y., Augath, M., Steudel, T., Evrard, H.C., Besserve, M., Oeltermann, A., 2012. Hippocampal-cortical interaction during periods of subcortical silence. Nature 491, 547-553.

Lorincz, M.L., Gunner, D., Bao, Y., Connelly, W.M., Isaac, J.T., Hughes, S.W., Crunelli, V., 2015. A distinct class of slow (~0.2-2 Hz) intrinsically bursting layer 5 pyramidal neurons determines UP/DOWN state dynamics in the neocortex. J Neurosci 35, 5442-5458.

Luczak, A., Bartho, P., Harris, K.D., 2009. Spontaneous events outline the realm of possible sensory responses in neocortical populations. Neuron 62, 413-425.

Luczak, A., Bartho, P., Marguet, S.L., Buzsáki, G., Harris, K.D., 2007. Sequential structure of neocortical spontaneous activity in vivo. Proc Natl Acad Sci U S A 104, 347-352.

Maharajh, K., Teale, P., Rojas, D.C., Reite, M.L., 2010. Fluctuation of gamma-band phase synchronization within the auditory cortex in schizophrenia. Clin Neurophysiol 121, 542-548.

Makeig, S., Bell, A.J., Jung, T.P., Sejnowski, T.J., 1996. Independent component analysis of electroencephalographic data. In: Touretzky, D., Mozer, M., Hasselmo, M. (Eds.), Advances in Neural Information Processing Systems MIT Press, Cambridge, MA, USA, pp. 145-151.

Marshall, L., Born, J., 2007. The contribution of sleep to hippocampus-dependent memory consolidation. Trends Cogn Sci 11, 442-450.

Marshall, L., Helgadottir, H., Molle, M., Born, J., 2006. Boosting slow oscillations during sleep potentiates memory. Nature 444, 610-613.

Marshall, L., Kirov, R., Brade, J., Molle, M., Born, J., 2011. Transcranial electrical currents to probe EEG brain rhythms and memory consolidation during sleep in humans. PLoS One 6, e16905.

Marshall, L., Molle, M., Hallschmid, M., Born, J., 2004. Transcranial direct current stimulation during sleep improves declarative memory. J Neurosci 24, 9985-9992.

Massimini, M., Amzica, F., 2001. Extracellular calcium fluctuations and intracellular potentials in the cortex during the slow sleep oscillation. J Neurophysiol 85, 1346-1350.

Massimini, M., Ferrarelli, F., Esser, S.K., Riedner, B.A., Huber, R., Murphy, M., Peterson, M.J., Tononi, G., 2007. Triggering sleep slow waves by transcranial magnetic stimulation. Proc Natl Acad Sci U S A 104, 8496-8501.

Massimini, M., Huber, R., Ferrarelli, F., Hill, S., Tononi, G., 2004. The sleep slow oscillation as a traveling wave. J Neurosci 24, 6862-6870.

Mathewson, K.E., Gratton, G., Fabiani, M., Beck, D.M., Ro, T., 2009. To see or not to see: prestimulus alpha phase predicts visual awareness. J Neurosci 29, 2725-2732.

McCormick, D.A., Bal, T., 1997. Sleep and arousal: thalamocortical mechanisms. Annu Rev Neurosci 20, 185-215.

McCormick, D.A., Pape, H.C., 1990. Properties of a hyperpolarization-activated cation current and its role in rhythmic oscillation in thalamic relay neurones. J Physiol 431, 291-318.

Miles, R., Wong, R.K., 1986. Excitatory synaptic interactions between CA3 neurones in the guinea-pig hippocampus. J Physiol 373, 397-418.

Mohajerani, M.H., Chan, A.W., Mohsenvand, M., LeDue, J., Liu, R., McVea, D.A., Boyd, J.D., Wang, Y.T., Reimers, M., Murphy, T.H., 2013. Spontaneous cortical activity alternates between motifs defined by regional axonal projections. Nat Neurosci 16, 1426-1435.

Mohajerani, M.H., McVea, D.A., Fingas, M., Murphy, T.H., 2010. Mirrored bilateral slow-wave cortical activity within local circuits revealed by fast bihemispheric voltage-sensitive dye imaging in anesthetized and awake mice. J Neurosci 30, 3745-3751.

Moll, M., 2014. Henry Molaison's (or HM) brain digitized to show how amnesia affects the brain. Tech Times.

Mölle, M., Eschenoka, O., Gais, S., Sara, S. J., & Born, J., 2009. The influence of learning on sleep slow oscillations and associated spindles and ripples in humans and rats. European Journal of Neuroscience 29, 1071-1081.

Mölle, M., Marshall, L., Gais, S., Born, J., 2002. Grouping of spindle activity during slow oscillations in human non-rapid eye movement sleep. J Neurosci 22, 10941-10947.

Mölle, M., Marshall, L., Gais, S., Born, J., 2004. Learning increases human electroencephalographic coherence during subsequent slow sleep oscillations. Proc Natl Acad Sci U S A 101, 13963-13968.

Molle, M., Yeshenko, O., Marshall, L., Sara, S.J., Born, J., 2006. Hippocampal sharp wave-ripples linked to slow oscillations in rat slow-wave sleep. J Neurophysiol 96, 62-70.

Montgomery, S.M., Buzsáki, G., 2007. Gamma oscillations dynamically couple hippocampal CA3 and CA1 regions during memory task performance. Proc Natl Acad Sci U S A 104, 14495-14500.

Mountcastle, V.B., 1997. The columnar organization of the neocortex. Brain 120 (Pt 4), 701-722.

Murphy, M., Riedner, B.A., Huber, R., Massimini, M., Ferrarelli, F., Tononi, G., 2009. Source modeling sleep slow waves. Proc Natl Acad Sci U S A 106, 1608-1613.

Neda, Z., Ravasz, E., Brechet, Y., Vicsek, T., Barabasi, A.L., 2000. The sound of many hands clapping. Nature 403, 849-850.

Neske, G.T., 2015. The Slow Oscillation in Cortical and Thalamic Networks: Mechanisms and Functions. Front Neural Circuits 9, 88.

Neuling, T., Rach, S., Herrmann, C.S., 2013. Orchestrating neuronal networks: sustained after-effects of transcranial alternating current stimulation depend upon brain states. Front Hum Neurosci 7, 161.

Newman, E.A., 2003. New roles for astrocytes: regulation of synaptic transmission. Trends Neurosci 26, 536-542.

Ngo, H.V., Martinetz, T., Born, J., Molle, M., 2013. Auditory closed-loop stimulation of the sleep slow oscillation enhances memory. Neuron 78, 545-553.

Niedermeyer, E., Lopes da Silva, F.H., Books@Ovid - York University., Ovid Technologies Inc., 2005. Electroencephalography basic principles, clinical applications, and related fields. Lippincott Williams & Wilkins, Philadelphia, pp. xiii, 1309 p.

Nir, Y., Staba, R.J., Andrillon, T., Vyazovskiy, V.V., Cirelli, C., Fried, I., Tononi, G., 2011. Regional slow waves and spindles in human sleep. Neuron 70, 153-169.

O'Neill, J., Senior, T.J., Allen, K., Huxter, J.R., Csicsvari, J., 2008. Reactivation of experience-dependent cell assembly patterns in the hippocampus. Nat Neurosci 11, 209-215.

Ozen, S., Sirota, A., Belluscio, M.A., Anastassiou, C.A., Stark, E., Koch, C., Buzsaki, G., 2011. Transcranial electric stimulation entrains cortical neuronal populations in rats. J Neurosci 30, 11476-11485.

Ozen, S., Sirota, A., Belluscio, M.A., Anastassiou, C.A., Stark, E., Koch, C., Buzsáki, G., 2010. Transcranial electric stimulation entrains cortical neuronal populations in rats. J Neurosci 30, 11476-11485.

Pagliardini, S., Gosgnach, S., Dickson, C.T., 2013. Spontaneous sleep-like brain state alternations and breathing characteristics in urethane anesthetized mice. PLoS One 8, e70411.

Paulus, W., Peterchev, A.V., Ridding, M., 2013. Transcranial electric and magnetic stimulation: technique and paradigms. Handb Clin Neurol 116, 329-342.

Pavlides, C., Winson, J., 1989. Influences of hippocampal place cell firing in the awake state on the activity of these cells during subsequent sleep episodes. J Neurosci 9, 2907-2918.

Paxinos, G., Watson, C., 1998. The rat brain in stereotaxic coordinates, 4th ed. Academic Press, San Diego.

Peyrache, A., Battaglia, F.P., Destexhe, A., 2011. Inhibition recruitment in prefrontal cortex during sleep spindles and gating of hippocampal inputs. Proc Natl Acad Sci U S A 108, 17207-17212.

Plihal, W., Born, J., 1997. Effects of early and late nocturnal sleep on declarative and procedural memory. J Cogn Neurosci 9, 534-547.

Poskanzer, K.E., Yuste, R., 2011. Astrocytic regulation of cortical UP states. Proc Natl Acad Sci U S A 108, 18453-18458.

Prehn-Kristensen, A., Munz, M., Goder, R., Wilhelm, I., Korr, K., Vahl, W., Wiesner, C.D., Baving, L., 2014. Transcranial oscillatory direct current stimulation during sleep improves declarative memory consolidation in children with attention-deficit/hyperactivity disorder to a level comparable to healthy controls. Brain Stimul 7, 793-799.

Ramadan, W., Eschenko, O., Sara, S.J., 2009. Hippocampal sharp wave/ripples during sleep for consolidation of associative memory. PLoS One 4, e6697.

Rasch, B., Born, J., 2013. About sleep's role in memory. Physiol Rev 93, 681-766.

Rasch, B., Buchel, C., Gais, S., Born, J., 2007. Odor cues during slow-wave sleep prompt declarative memory consolidation. Science 315, 1426-1429.

Rauchs, G., Desgranges, B., Foret, J., Eustache, F., 2005. The relationships between memory systems and sleep stages. J Sleep Res 14, 123-140.

Reato, D., Rahman, A., Bikson, M., Parra, L.C., 2010. Low-intensity electrical stimulation affects network dynamics by modulating population rate and spike timing. J Neurosci 30, 15067-15079.

Reato, D., Rahman, A., Bikson, M., Parra, L.C., 2013. Effects of weak transcranial alternating current stimulation on brain activity-a review of known mechanisms from animal studies. Front Hum Neurosci 7, 687.

Rockstroh, B.S., Wienbruch, C., Ray, W.J., Elbert, T., 2007. Abnormal oscillatory brain dynamics in schizophrenia: a sign of deviant communication in neural network? BMC Psychiatry 7, 44.

Rodriguez, R., Haberly, L.B., 1989. Analysis of synaptic events in the opossum piriform cortex with improved current source-density techniques. J Neurophysiol 61, 702-718.

Rolls, E.T., 2000. Hippocampo-cortical and cortico-cortical backprojections. Hippocampus 10, 380-388.

Ros, H., Sachdev, R.N., Yu, Y., Sestan, N., McCormick, D.A., 2009. Neocortical networks entrain neuronal circuits in cerebellar cortex. J Neurosci 29, 10309-10320.

Rosanova, M., Ulrich, D., 2005. Pattern-specific associative long-term potentiation induced by a sleep spindle-related spike train. J Neurosci 25, 9398-9405.

Sahlem, G.L., Badran, B.W., Halford, J.J., Williams, N.R., Korte, J.E., Leslie, K., Strachan, M., Breedlove, J.L., Runion, J., Bachman, D.L., Uhde, T.W., Borckardt, J.J., George, M.S., 2015. Oscillating Square Wave Transcranial Direct Current Stimulation (tDCS) Delivered During Slow Wave Sleep Does Not Improve Declarative Memory More Than Sham: A Randomized Sham Controlled Crossover Study. Brain Stimul 8, 528-534.

Sanchez-Vives, M.V., McCormick, D.A., 2000. Cellular and network mechanisms of rhythmic recurrent activity in neocortex. Nat Neurosci 3, 1027-1034.

Sceniak, M.P., Maciver, M.B., 2006. Cellular actions of urethane on rat visual cortical neurons in vitro. J Neurophysiol 95, 3865-3874.

Schall, K.P., Kerber, J., Dickson, C.T., 2008. Rhythmic constraints on hippocampal processing: state and phase-related fluctuations of synaptic excitability during theta and the slow oscillation. J Neurophysiol 99, 888-899.

Scheffer-Teixeira, R., Belchior, H., Leao, R.N., Ribeiro, S., Tort, A.B., 2013. On high-frequency field oscillations (>100 Hz) and the spectral leakage of spiking activity. J Neurosci 33, 1535-1539.

Schomburg, E.W., Fernandez-Ruiz, A., Mizuseki, K., Berenyi, A., Anastassiou, C.A., Koch, C., Buzsáki, G., 2014. Theta Phase Segregation of Input-Specific Gamma Patterns in Entorhinal-Hippocampal Networks. Neuron.

Schroeder, C.E., Lakatos, P., 2009. Low-frequency neuronal oscillations as instruments of sensory selection. Trends Neurosci 32, 9-18.

Scoville, W.B., 1954. The limbic lobe in man. J Neurosurg 11, 64-66.

Scoville, W.B., Milner, B., 1957. Loss of recent memory after bilateral hippocampal lesions. J Neurol Neurosurg Psychiatry 20, 11-21.

Sederberg, P.B., Schulze-Bonhage, A., Madsen, J.R., Bromfield, E.B., McCarthy, D.C., Brandt, A., Tully, M.S., Kahana, M.J., 2007. Hippocampal and neocortical gamma oscillations predict memory formation in humans. Cereb Cortex 17, 1190-1196.

Sejnowski, T.J., Destexhe, A., 2000. Why do we sleep? Brain Res 886, 208-223.

Sejnowski, T.J., Paulsen, O., 2006. Network oscillations: emerging computational principles. J Neurosci 26, 1673-1676.

Seth, A.K., 2010. A MATLAB toolbox for Granger causal connectivity analysis. J Neurosci Methods 186, 262-273.

Sheroziya, M., Timofeev, I., 2015. Moderate Cortical Cooling Eliminates Thalamocortical Silent States during Slow Oscillation. J Neurosci 35, 13006-13019.

Siapas, A.G., Wilson, M.A., 1998. Coordinated interactions between hippocampal ripples and cortical spindles during slow-wave sleep. Neuron 21, 1123-1128.

Siegel, J.M., 2001. The REM sleep-memory consolidation hypothesis. Science 294, 1058-1063.

Singer, W., Gray, C., Engel, A., Konig, P., Artola, A., Brocher, S., 1990. Formation of cortical cell assemblies. Cold Spring Harb Symp Quant Biol 55, 939-952.

Singer, W., Gray, C.M., 1995. Visual feature integration and the temporal correlation hypothesis. Annu Rev Neurosci 18, 555-586.

Sirota, A., Csicsvari, J., Buhl, D., Buzsáki, G., 2003. Communication between neocortex and hippocampus during sleep in rodents. Proc Natl Acad Sci U S A 100, 2065-2069.

Squire, L.R., 2004. Memory systems of the brain: a brief history and current perspective. Neurobiol Learn Mem 82, 171-177.

Squire, L.R., Bayley, P.J., 2007. The neuroscience of remote memory. Curr Opin Neurobiol 17, 185-196.

Stagg, C.J., Nitsche, M.A., 2011. Physiological basis of transcranial direct current stimulation. Neuroscientist 17, 37-53.

Staresina, B.P., Bergmann, T.O., Bonnefond, M., van der Meij, R., Jensen, O., Deuker, L., Elger, C.E., Axmacher, N., Fell, J., 2015. Hierarchical nesting of slow oscillations, spindles and ripples in the human hippocampus during sleep. Nat Neurosci 18, 1679-1686.

Steriade, M., 2006. Grouping of brain rhythms in corticothalamic systems. Neuroscience 137, 1087-1106.

Steriade, M., Amzica, F., Nunez, A., 1993a. Cholinergic and noradrenergic modulation of the slow (approximately 0.3 Hz) oscillation in neocortical cells. J Neurophysiol 70, 1385-1400.

Steriade, M., Contreras, D., Amzica, F., Timofeev, I., 1996. Synchronization of fast (30-40 Hz) spontaneous oscillations in intrathalamic and thalamocortical networks. J Neurosci 16, 2788-2808.

Steriade, M., Contreras, D., Curro Dossi, R., Nunez, A., 1993b. The slow (< 1 Hz) oscillation in reticular thalamic and thalamocortical neurons: scenario of sleep rhythm generation in interacting thalamic and neocortical networks. J Neurosci 13, 3284-3299.

Steriade, M., Nunez, A., Amzica, F., 1993c. Intracellular analysis of relations between the slow (< 1 Hz) neocortical oscillation and other sleep rhythms of the electroencephalogram. J Neurosci 13, 3266-3283.

Steriade, M., Nunez, A., Amzica, F., 1993d. A novel slow (< 1 Hz) oscillation of neocortical neurons in vivo: depolarizing and hyperpolarizing components. J Neurosci 13, 3252-3265.

Stickgold, R., 1998. Sleep: off-line memory reprocessing. Trends Cogn Sci 2, 484-492.

Stopfer, M., Bhagavan, S., Smith, B.H., Laurent, G., 1997. Impaired odour discrimination on desynchronization of odour-encoding neural assemblies. Nature 390, 70-74.

Strange, B.A., Witter, M.P., Lein, E.S., Moser, E.I., 2014. Functional organization of the hippocampal longitudinal axis. Nat Rev Neurosci 15, 655-669.

Stroh, A., Adelsberger, H., Groh, A., Ruhlmann, C., Fischer, S., Schierloh, A., Deisseroth, K., Konnerth, A., 2013. Making waves: initiation and propagation of corticothalamic Ca2+ waves in vivo. Neuron 77, 1136-1150.

Sullivan, D., Mizuseki, K., Sorgi, A., Buzsáki, G., 2014. Comparison of sleep spindles and theta oscillations in the hippocampus. J Neurosci 34, 662-674.

Sutherland, G.R., McNaughton, B., 2000. Memory trace reactivation in hippocampal and neocortical neuronal ensembles. Curr Opin Neurobiol 10, 180-186.

Takahashi, K., Kayama, Y., Lin, J.S., Sakai, K., 2010. Locus coeruleus neuronal activity during the sleep-waking cycle in mice. Neuroscience 169, 1115-1126.

Tamminen, J., Payne, J.D., Stickgold, R., Wamsley, E.J., Gaskell, M.G., 2010. Sleep spindle activity is associated with the integration of new memories and existing knowledge. J Neurosci 30, 14356-14360.

Tavel, M.E., Fisch, C., 1964. Repetitive Ventricular Arrhythmia Resulting from Artificial Internal Pacemaker. Circulation 30, 493-500.

Thomson, A.M., Bannister, A.P., 2003. Interlaminar connections in the neocortex. Cereb Cortex 13, 5-14.

Timofeev, I., Chauvette, S., 2011. Thalamocortical oscillations: local control of EEG slow waves. Curr Top Med Chem 11, 2457-2471.

Timofeev, I., Grenier, F., Bazhenov, M., Houweling, A.R., Sejnowski, T.J., Steriade, M., 2002. Short- and medium-term plasticity associated with augmenting responses in cortical slabs and spindles in intact cortex of cats in vivo. J Physiol 542, 583-598.

Timofeev, I., Grenier, F., Bazhenov, M., Sejnowski, T.J., Steriade, M., 2000a. Origin of slow cortical oscillations in deafferented cortical slabs. Cereb Cortex 10, 1185-1199.

Timofeev, I., Grenier, F., Steriade, M., 2000b. Impact of intrinsic properties and synaptic factors on the activity of neocortical networks in vivo. J Physiol Paris 94, 343-355.

Timofeev, I., Grenier, F., Steriade, M., 2001. Disfacilitation and active inhibition in the neocortex during the natural sleep-wake cycle: an intracellular study. Proc Natl Acad Sci U S A 98, 1924-1929.

Timofeev, I., Steriade, M., 1996. Low-frequency rhythms in the thalamus of intact-cortex and decorticated cats. J Neurophysiol 76, 4152-4168.

Timofeev, I., Steriade, M., 1997. Fast (mainly 30-100 Hz) oscillations in the cat cerebellothalamic pathway and their synchronization with cortical potentials. J Physiol 504 (Pt 1), 153-168.

Tucker, M.A., Hirota, Y., Wamsley, E.J., Lau, H., Chaklader, A., Fishbein, W., 2006. A daytime nap containing solely non-REM sleep enhances declarative but not procedural memory. Neurobiol Learn Mem 86, 241-247.

Turchin, P., Nefedov, S.A., 2009. Secular cycles. Princeton University Press, Princeton, N.J.

Valderrama, M., Crepon, B., Botella-Soler, V., Martinerie, J., Hasboun, D., Alvarado-Rojas, C., Baulac, M., Adam, C., Navarro, V., Le Van Quyen, M., 2012. Human gamma oscillations during slow wave sleep. PLoS One 7, e33477.

van Strien, N.M., Cappaert, N.L., Witter, M.P., 2009. The anatomy of memory: an interactive overview of the parahippocampal-hippocampal network. Nat Rev Neurosci 10, 272-282.

Vanderwolf, C.H., 1975. Neocortical and hippocampal activation relation to behavior: effects of atropine, eserine, phenothiazines, and amphetamine. J Comp Physiol Psychol 88, 300-323.

Varela, C., Kumar, S., Yang, J.Y., Wilson, M.A., 2014. Anatomical substrates for direct interactions between hippocampus, medial prefrontal cortex, and the thalamic nucleus reuniens. Brain Struct Funct 219, 911-929.

Vertes, R.P., Hoover, W.B., Szigeti-Buck, K., Leranth, C., 2007. Nucleus reuniens of the midline thalamus: link between the medial prefrontal cortex and the hippocampus. Brain Res Bull 71, 601-609.

Volgushev, M., Chauvette, S., Mukovski, M., Timofeev, I., 2006. Precise long-range synchronization of activity and silence in neocortical neurons during slow-wave oscillations [corrected]. J Neurosci 26, 5665-5672.

Volgushev, M., Chauvette, S., Timofeev, I., 2011. Long-range correlation of the membrane potential in neocortical neurons during slow oscillation. Prog Brain Res 193, 181-199.

Vyazovskiy, V.V., Faraguna, U., Cirelli, C., Tononi, G., 2009. Triggering slow waves during NREM sleep in the rat by intracortical electrical stimulation: effects of sleep/wake history and background activity. J Neurophysiol 101, 1921-1931.

Vyazovskiy, V.V., Olcese, U., Hanlon, E.C., Nir, Y., Cirelli, C., Tononi, G., 2011. Local sleep in awake rats. Nature 472, 443-447.

Walker, M.P., Stickgold, R., 2004. Sleep-dependent learning and memory consolidation. Neuron 44, 121-133.

Watts, D.J., Strogatz, S.H., 1998. Collective dynamics of 'small-world' networks. Nature 393, 440-442.

Wei, Y., Krishnan, G.P., Bazhenov, M., 2016. Synaptic Mechanisms of Memory Consolidation during Sleep Slow Oscillations. J Neurosci 36, 4231-4247.

Wester, J.C., Contreras, D., 2012. Columnar interactions determine horizontal propagation of recurrent network activity in neocortex. J Neurosci 32, 5454-5471.

Whitten, T.A., 2015. Coordination of hippocampal input and output pathways during sleep-like states. Neuroscience and Mental Health Institute. University of Alberta.

Whitten, T.A., Hughes, A.M., Dickson, C.T., Caplan, J.B., 2011. A better oscillation detection method robustly extracts EEG rhythms across brain state changes: the human alpha rhythm as a test case. Neuroimage 54, 860-874.

Whitten, T.A., Wolansky, T., Dickson, C.T., 2014. The beats of different drummers: differential phase relationships of hippocampal pathways with the cortical slow oscillation. 9th FENS Forum, Milan, Italy.

Wierzynski, C.M., Lubenov, E.V., Gu, M., Siapas, A.G., 2009. State-dependent spike-timing relationships between hippocampal and prefrontal circuits during sleep. Neuron 61, 587-596.

Wiggers, C.J., Wegma, R., 1940. Ventricular fibrillation due to single, localized induction and condenser shocks applied during the vulnerable phase of ventricular systole. American Journal of Physiology 128.

Wilson, C.J., Groves, P.M., 1981. Spontaneous firing patterns of identified spiny neurons in the rat neostriatum. Brain Res 220, 67-80.

Wilson, M.A., McNaughton, B.L., 1994. Reactivation of hippocampal ensemble memories during sleep. Science 265, 676-679.

Wolansky, T., Clement, E.A., Peters, S.R., Palczak, M.A., Dickson, C.T., 2006. Hippocampal slow oscillation: a novel EEG state and its coordination with ongoing neocortical activity. J Neurosci 26, 6213-6229.

Yanovsky, Y., Ciatipis, M., Draguhn, A., Tort, A.B., Brankack, J., 2014. Slow oscillations in the mouse hippocampus entrained by nasal respiration. J Neurosci 34, 5949-5964.

Zaghi, S., Acar, M., Hultgren, B., Boggio, P.S., Fregni, F., 2010. Noninvasive brain stimulation with low-intensity electrical currents: putative mechanisms of action for direct and alternating current stimulation. Neuroscientist 16, 285-307.

Zar, J.H., 1999. Biostatistical analysis, 4th ed. Prentice Hall, Upper Saddle River, N.J.

Appendix A

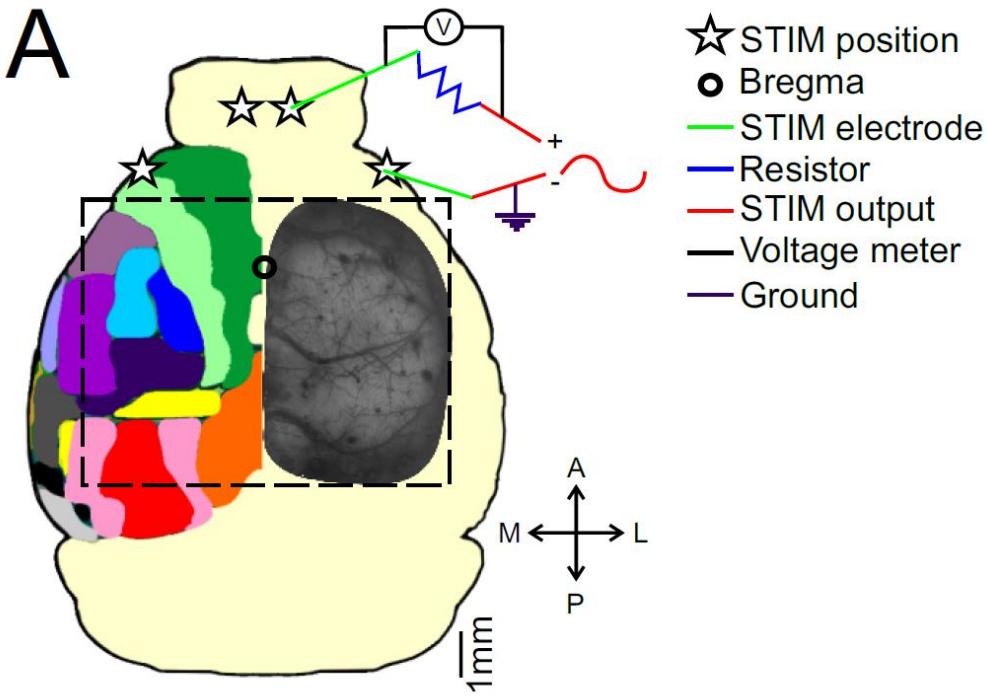

Figure A.1 Hemisphere specific current measurement circuit

A. Standardized mouse cortical map with colored regions indicating cortical areas as in Figure 3.1 A. Open circle indicates position of bregma. Stars indicate stimulation electrode positions. Dotted square indicates size of craniotomy. Depicted circuit shows a resistor (blue) which was connected to the frontal stimulation electrode (green) and to the stimulation output (red). The posterior stimulation electrode (green) was connected to the other stimulation output. The stimulator was also conncted to ground (purple). The voltage recorded across the resistor divided by the known resistance yielded a measure of the current passing across the given hemisphere. Only one hemisphere is shown here but an identical circuit was used for both hemispheres.

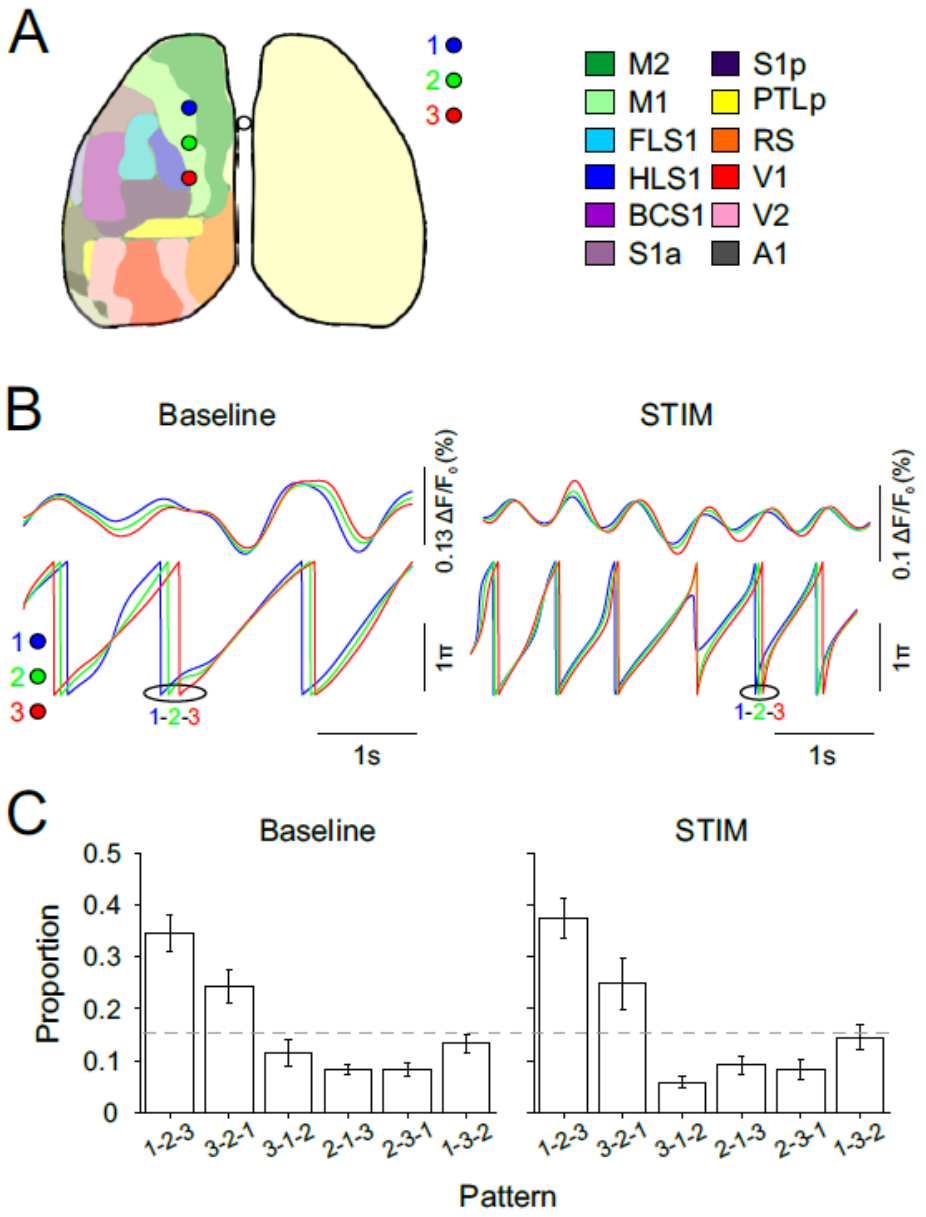

Figure A.2 Restricted SO propagation across M1

A. Schematic of mouse brain (left) showing three cortical sites chosen for a restricted propagation model analogous to the cortical sites in the rat brain recordings in Chapter 2. The colored areas show the cortical functional areas with the corresponding legend on the right. **B.** SO filtered (0.3 – 1.5 Hz; left) and STIM filtered (1.1 – 1.9 Hz; right) example traces (top) and corresponding Hilbert phase (bottom) for a single experiment during

baseline (left) and stimulation (right) conditions for the three cortical sites depicted in A. An example cycle is circled showing an anterior-to-posterior (sites 1-2-3) propagation pattern during both baseline and stimulation conditions. C. Grand average histogram across experiments showing the proportion of cycles expressing all possible 6 propagation patterns using the three cortical sites depicted in A for baseline (left) and stimulation (right) conditions. Note highest proportion of the anterior-to-posterior (1-2-3) pattern during the baseline condition with a non-significant increase for that pattern during stimulation. Grey dotted line shows chance level pattern expression gives three sites and 6 possible patterns.